EFFECT OF FIRE ON THE REINFORCED CONCRETE MEMBERS UNDER LOADED CONDITIONS

ABDULLAH - HIL - BAKI

DEPARTMENT OF CIVIL ENGINEERING

BANGLADESH UNIVERSITY OF ENGINEERING & TECHNOLOGY
DHAKA, BANGLADESH.

September, 2018

EFFECT OF FIRE ON THE REINFORCED CONCRETE MEMBERS UNDER LOADED CONDITIONS

by

ABDULLAH - HIL - BAKI
(Student ID: F0412042339)

Submitted in partial fulfillment of the requirements for the degree of

MASTER OF SCIENCE IN CIVIL ENGINEERING (STRUCTURAL)

DEPARTMENT OF CIVIL ENGINEERING
BANGLADESH UNIVERSITY OF ENGINEERING & TECHNOLOGY
DHAKA, BANGLADESH.

September, 2018

The thesis titled **EFFECT OF FIRE ON THE REINFORCED CONCRETE MEMBERS UNDER LOADED CONDITIONS** submitted by ABDULLAH - HIL - BAKI, Student ID: F0412042339, Session: April, 2012 has been accepted as satisfactory in partial fulfillment of the requirement for the degree of Master of Science in Civil Engineering (Structural) on the 25th of September, 2018.

1. Dr. Raquib Ahsan Professor Department of Civil Engineering Bangladesh University of Engineering & Technology, Dhaka.	*Chairman*
2. Dr. Ahsanul Kabir Professor & Head Department of Civil Engineering Bangladesh University of Engineering & Technology, Dhaka.	25.9.18 *Member* *(Ex-Officio)*
3. Dr. Tanvir Manzur Professor Department of Civil Engineering Bangladesh University of Engineering & Technology, Dhaka.	*Member*
4. Dr. Md. Tarek Uddin, PEng. Professor Department of Civil & Environmental Engineering Islamic University of Technology, Gazipur.	*Member* *(External)*

CANDIDATE'S DECLARATION

It is hereby declared that,

a. The study in this thesis is the result of work by author, except for the contents where specific reference has been made to the work of others.

b. This thesis or any part of it has not been submitted elsewhere for the award of any degree or diploma.

Abdullah Hil Baki

Abdullah - Hil - Baki

DEDICATION

I like to dedicate this work to my family members, specially my parents who loved, raised and guided me in every single step of my life; to my beloved wife for her sacrifice and support; to my lovely daughter and my brother for their endless motivation.

ACKNOWLEDGEMENT

In the name of Almighty Allah the most beneficent and most merciful, the author expresses his profound gratitude to Allah for giving him opportunity to undergo the Master of Science in Civil Engineering programme and complete this thesis. The author expresses his sincere gratitude to his honourable supervisor, Dr. Raquib Ahsan, Professor, Department of Civil Engineering, Bangladesh University of Engineering & Technology (BUET) for his exemplary support, motivation, guidance and encouragement for this study and research.

The author wishes to express his deep appreciation to the National Housing Authority (NHA) for its support and allowing the author to complete the Master of Science programme successfully and special thanks to the Chairman, NHA, the Executive Engineers, Dhaka Division-2 and Mirpur Housing & Settlement Division-2 for their cordial and wholehearted support to the research programme. The author gratefully acknowledge the cooperation of all concerned persons of the Department of Civil Engineering, Center for Advanced Studies and Research (CASR) and BUET Central Library for their assistance.

The author is also thankful to his family and friends for providing necessary mental support.

ABSTRACT

In this modern era of rapid development and technological advancement, frequent fire phenomenon are the most dangerous man made catastrophe in the metropolis. Dhaka, the center of development of Bangladesh, is marked by its rapid development of commercial buildings and high rise buildings, which are mostly unplanned in respect of urban planning and prone to fire accidents. Since reinforced concrete is the main building material used in most of the cases in this mega city, a detailed study on the reinforced concrete member is needed to mitigate the scale of destruction of fire in case of accident. With this point kept in mind, a parametric study was performed to understand the effect of fire on the reinforced concrete members, especially on beam as it is the primal load bearing component of any structure in general.

In the unidirectional coupled field analyses, *i.e.* thermal to structural coupling, in ANSYS, concrete compressive strength (28MPa, 35MPa and 42MPa), steel yield strength (400MPa and 500MPa), beam cover (37.5mm, 50mm, 62.5mm and 75mm) and reinforcement ratio (minimum, intermediate and maximum value) were combined in analytical modelling with different temperature (300°C, 600°C and 900°C) and duration of burning (30minutes, 60minutes, 90minutes and 120minutes) to observe the developed stress levels inside the beam. To imitate real life scenario, the temperature effect was observed in loaded condition during the simulation. The constitutive laws of concrete and reinforcing bars were for the loading stage only, no information on unloading stage was input.

The results obtained show that the stresses in concrete and reinforcement increases with the increase in temperature and time, though the maximum load the member can withstand is gradually decreasing. The results of the simulations suggest the safe use of reinforcing steel for any temperature for initial 30 minutes of burning. On the contrary, the preparation and selection of concrete strength must be carefully chosen since after the first 60 minutes of burning the concrete was found stressed drastically close to its plastic limit. The result also indicates, if the member is loaded at 20 percent of its maximum capacity, it can withstand temperature as high as 900°C for a duration as long as two hours.

TABLE OF CONTENTS

ACKNOWLEDGEMENT vi

ABSTRACT vii

TABLE OF CONTENTS viii

LIST OF ABBREVIATIONS xi

Chapter 1: INTRODUCTION 1

1.1 General 1

1.2 Background and Present Status of the Problem 1

1.3 Objectives 2

1.4 Scope of the Research 2

1.5 Research Methodology 2

1.6 Organization of the Report 3

1.7 Summary 3

Chapter 2: LITERATURE REVIEW 4

2.1 Introduction 4

2.2 Test Methods of RCC under Elevated Temperature 4

2.2.1 Idealized test methods 4

2.2.2 Common test methods 6

2.3 Past Studies: At A Glance 7

2.3.1 Concrete test by Castillo et al. (1990) 7

2.3.2 Concrete test by Hertz (1984, 1991) 10

2.3.3 Unstressed concrete test by Hammer 13

2.3.4 Full scale experiment by Bailey (2001) 15

2.3.5 Strength test by Morita et al. (1992) 17

2.3.6 Strength test by Furumura et al. (1995) 19

2.3.7 Beam test by Felicetti et al. (1996) 21

2.3.8 Strength test by Noumowé et al. (1996) 26

2.3.9 Beam test by Jensen et al. (1995) 27

2.3.10 Beam test by Sanjayan et al. (1991) 30

2.3.11 Column test by Diederichs et al. (1995) 32

2.3.12 Beam test by Rashidi (2013) 33

2.3.13 Beam test by Kadhum (2014) 34

2.3.14 Numerical Beam Modelling by Kodur et al. (2008) 36
2.3.15 Concrete test by Mundhada et al. (2015) 38
2.3.16 Column test by Lee et al. (2015) 40
2.4 Review on Past Studies 42
2.4.1 Concrete material tests 42
2.4.2 Element and full scale test 43
2.5 Summary 44

Chapter 3: RESEARCH METHODOLOGY 45
3.1 Introduction 45
3.2 Material Properties 45
3.2.1 Concrete 45
3.2.2 Reinforcing steel 48
3.2 Member Profiles 50
3.4 Application of Temperature 51
3.5 Validation of Model 52
3.6 Summary 54

Chapter 4: RESULTS AND DISCUSSION 55
4.1 Introduction 55
4.2 Results of Beam Model 55
4.2.1 Temperature profiles 55
4.2.2 Effect of duration of burning 56
4.2.3 Effect of concrete cover 64
4.2.4 Effect of concrete strength 75
4.2.5 Effect of steel strength 85
4.2.6 Effect of reinforcement ratio 93
4.2.7 Maximum applied load comparison 97
4.3 Results of Portal Frame Models 99
4.3.1 Temperature profiles 99
4.3.2 Lateral sway 103
4.4 Summary 104

Chapter 5: CONCLUSION AND SUGGESTIONS 105
5.1 General 105

5.2 Conclusion 105

5.3 Suggestions 106

REFERENCES **107**

APPENDIX-A **109**

APPENDIX-B **114**

APPENDIX-C **134**

LIST OF ABBREVIATIONS

BUET	=	Bangladesh University of Engineering & Technology
BFSCDA	=	Bangladesh Fire Service and Civil Defense Authority
BSEC	=	Bangladesh Steel and Engineering Corporation
DCC	=	Dhaka City Corporation
USA	=	United States of America
HSC	=	High Strength Concrete
NSC	=	Normal Strength Concrete
RCC	=	Reinforced Cement Concrete
R.H.	=	Relative Humidity
MPa	=	Mega Pascal
ISO	=	International Organization for Standardization
ACI	=	American Concrete Institute
APDL	=	ANSYS Parametric Design Language
BS	=	British Standards
EN	=	European Norms

Chapter 1
INTRODUCTION

1.1 General

Fire, though the most significant driving force of the civilization on the history of mankind, is also one of the most ancient disasters the human race faced. The disaster was natural mainly when men could not control fire, but for past few decades, it is mainly a manmade disaster caused by accidents resulting from lack of proper knowledge of ignition of fire. As a densely populated and rapidly developing country, Bangladesh has suffered from severe fire incidents in recent years. Again, as center of development and administrative body, the capital city of Dhaka has undergone the majority of fire incidents recently. According to Bangladesh Fire Service and Civil Defense Authority, Dhaka has faced 11.2%, 13.79% and 12% of all the fire incidents in all around Bangladesh in 2004, 2005 and 2006 according to *Islam and Adri* [1]. Fire accidents in BSEC building on 2008, Bashundhara City on 2009, Nimtali on 2010 and Gulshan DCC market on 2017 are some mentionable ones in Dhaka among recent years. Though man has the equipment to cause fire and control it to some extent, he does not have the capacity to control the destructive force of it yet in the most advanced era. Fire may break out any time anywhere and destroy lives, properties and leave a most traumatic memory on the survivors. Fire on structures are important to study because fire incidents in structures are usually the horrific ones. To deduce safer combination of reinforced concrete and vulnerability of existing structure during fire, a detailed parametric study was the most intended.

1.2 Background and Present Status of the Problem

Researches on fire phenomenon all over the world got accelerated soon after the destruction of World Trade Centre Twin Tower on 9/11 in New York, USA. Though some guidelines were present before the incident, the researchers looked for the effect of fire on various materials and structures ever since. With the development of High Strength Concrete (HSC) and Steel, it is imperative to understand their vulnerability in fire since minimizing damage is the most prior concern. A lot of experimental tests were performed on cooled down heated members, it is very difficult to replicate a fire incident in loaded condition. Hence, it is imperative to simulate the structural fire in different combinations of parameters. A lot of numerical study on fire from every possible aspects of the incident can give a more accurate guidance to minimize the destruction of fire.

1.3 Objectives

The objective the study is to identify the behavioral pattern of concrete and reinforcing steel of variable strength having different cover dimension under fire load in order:

i. To observe the effect of material strengths on the behavior of pre-loaded concrete beams during fire phenomenon.

ii. To observe the effect of concrete cover on the behavior of loaded concrete beams during fire.

iii. To observe the effect of reinforcement ratio on the behavior of loaded concrete beams during fire.

iv. To observe the range and duration of temperatures on the behavior of stressed concrete beams on fire.

v. To observe the behavior of simple reinforced concrete portal frame during fire incidents under loaded condition.

1.4 Scope of the Research

This research work is aimed at analyses of different beam models with appropriate mechanical and thermal properties. The loaded analyses were performed in one directional coupling of thermal-structural module *i.e.* only coupled field analyses of thermal to structural modules were done. As mechanical properties of material, only the loading stage of the stress-strain constitutive laws were considered. The material strength in both elastic and plastic range was defined to sufficiently understand the effect of temperature on reinforced concrete members. The temperature rise followed the curved defined as standard time-temperature curve as per guidelines of Article-3.2.1 of BS-EN 1992-1-2:2002. Only the tensile and compressive stresses of both concrete and reinforcement regions were the targeted output of the study.

1.5 Research Methodology

The research work is planned to be performed primarily on ANSYS software for structural and thermal analysis of reinforced concrete members. The material modelling of concrete and steel may include density, thermal conductivity, specific heat, thermal elongation and respective stress-strain constitutive laws in different elevated temperatures, all selected as per established building code. Application of fire is planned to be simulated by inducing temperature-time graph suggested as per code.

1.6 Organization of the Report

This thesis report consists 5 (Five) chapters.

Chapter 1 briefly outlines the background, objectives, scopes and research methodology of the study.

Chapter 2 reviews the past studies related to this research. The past studies encompasses both the analytical and experimental research works.

Chapter 3 elaborates the research procedures in details. It mostly illustrates the fundamental properties of materials in various temperatures, the application of thermal loading etc. In addition, this chapter describes the verification of model by comparing the temperature profiles suggested by codes.

Chapter 4 represents the output data in various combinations of input parameters. The strength of concrete and steel, the sectional dimension including cover, reinforcement ratio, level of temperature and duration of burning are the main input parameters. The compressive and tensile stresses of both concrete and steel are compared to these inputs.

Chapter 5 comprises brief concluding remarks and some recommendations regarding the findings and future researches.

1.7 Summary

Though the incident of fire is a prehistoric element, the understanding of its effect on day-to-day materials is still going on. As the most common building material in the more fire-prone regions of Bangladesh, the reinforced concrete member especially beam was analyzed numerically for better understanding of the effect of fire on the developed stress levels.

Chapter 2
LITERATURE REVIEW

2.1 Introduction

Concrete is used as the building materials since 300BC when the Romans first used the admixture with some pink sand-like material obtained from Pozzuoli lime-based mixture to find a strong building material, according to *Lambert* [2]. The most significant developments in using pozzolans were occurred in the 18th century, when James Smeaton in 1756 developed the first hydraulic lime product by calcining Blue Lias limestone containing clay and mixing of an Italian pozzolanic earth from Civita Vecchia and found a very strong building material, as cited by *Isaac* [3]. Later James Parker produced Roman cement or natural cement in 1796. Fiber reinforcement in concrete was introduced in 1970s. In 1824, Joseph Aspdin patented Portland cement, because the render made from it was in color similar to the prestigious Portland stone quarried on the Isle of Portland, Dorset, England. However, Aspdin's cement was nothing like modern Portland cement but was a first step in its development, called a proto-Portland cement, according to *Blezard* [4]. After 1985, production of high strength concrete accelerated the construction technology to greater advancement. With advancement in material technology, the vulnerability of these construction materials to various natural forces including fire is tested in various medium of environments.

2.2 Test Methods of RCC under Elevated Temperatures

Consulting the mode of various experiments conducted by different writers or institutions in determining the mechanical property of RCC at elevated temperature, a number of different types experiments can be listed together which can be grouped into two broad categories as the Idealized Test Method and the Common Test Method. Each of the categories is discussed in the subsequent paragraphs.

2.2.1 Idealized test methods

There are six idealized test methods for testing concrete at high temperature. Four of which belong to the category of the steady state temperature test and two belong to the category of the transient temperature tests as cited by *Schneider* [5], *Phan* [6]. Each test method is designed to yield the particular data required by the test program. Typically, steady state temperature tests are characterized by a particular period during which the specimen is heated to target temperature, followed by a period during which the target temperature is maintained until a steady state condition is developed. Load is applied after the steady-state condition has been attained. Whereas, transient temperature test are characterized either by one of the following, simultaneous application of heating and loading, the load may be applied before heating or the load may be developed during heating, such as by restraint against thermal expansion. These six test methods are summarized below to aid in better understanding the procedure for fire testing of HSC and NSC.

A. Steady State Test Methods

(i) Stress Rate Controlled Test: The test specimen is heated to the specified temperature with a constant heating rate and then the temperature is maintained all through. The specimen is then subjected to a constant rate of loading until the ultimate load is achieved. Data from this type of test can be used to determine various mechanical properties of concrete.

(ii) Strain Rate Controlled Test: The test specimen is heated to the specified temperature with a constant heating rate. When the specimen has reached a steady state condition, it is loaded at a constant strain rate. This kind of test allows the complete stress-strain curve to be developed, which is possible to determine the mechanical energy dissipated be the specimen up to complete failure.

(iii) Steady State Creep Test: The test specimen is slowly heated to the target temperature and a steady state condition is allowed to develop. After the steady state condition is reached, the load is applied. Both the target temperature and the load are kept constant during the test period, which is typically longer than the test period of other types of tests. The measured results are creep deformation due to sustained constant load at different temperature.

(iv) Relaxation Test: The test specimen is heated to target temperature, and a steady state condition is allowed to develop prior to application of load. The initial, elastic strain resulting immediately from the application of load is recorded. The specimen is maintained at this initial strain during the duration of the test, and measurements of stress as a function of time are recorded.

B. Transient Test Methods

(i) Transient Creep Test: The specimen is subjected to a constant applied load, usually a percentage of the specimen's ultimate strength measured at room temperature, prior to heating. The specimen is then heated at a constant rate until failure occurs. The measurements result in a family of strain versus time curves corresponding to different applied loads.

(ii) Transient Relaxation Test: Load is applied to the specimen prior to heating, and an initial strain is recorded. This initial strain is maintained for the duration of the test by adjusting the applied load while the specimen is heated at a specified rate. The test is terminated when the applied stress level falls to zero. The measurements can be expressed as stress versus time relationships for different initial strain levels.

2.2.2 Common test methods

Most of the test programs reviewed in this thesis did not follow strictly the idealized test methods outlined above. Rather, the test methods that were used may be described as being derived from the above idealized test methods. Three test methods, commonly referred to as stressed, unstressed and unstressed residual strength tests, have been used in most experimental programs on the fire performance of HSC. These tests methods are described below:

A. Stressed Test: A preload, often in the range of 20% to 40% of ultimate compressive strength at ambient temperature is applied to the specimen prior to heating and maintained during heating. Heat is applied at a constant rate until a target temperature is reached, and the temperature is maintained until a thermal steady state is achieved. Load or strain is then increased at a prescribed rate until the specimen fails.

B. Unstressed Test: The specimen is heated, without preload at a constant rate to the target temperature, which is maintained until a thermal steady state is reached within the specimen. Load or strain is then applied at a prescribed rate until failure occurs. The test method is somehow identical to the steady state temperature, stress or strain rate controlled test.

C. **Unstressed Residual Strength Test:** The specimen is heated without preload at a prescribed rate to the target temperature, which is maintained until a thermal steady state is reached within the specimen. The specimen is then allowed to cool, also following a prescribed rate, at room temperature. Load or strain is applied at room temperature until the specimen fails. The unstressed residual strength test differs from all the test methods described above and its results are most suitable for assessing the post-fire properties of concrete.

2.3 Past Studies: at a Glance

A number of studies both numerical and experimental were performed to determine the effect of fire on concrete structures. Some tested only the materials, some tested on small building components and some experimented on full structures, all to understand the interaction of temperature and concrete structures.

2.3.1 Concrete test by Castillo et al. (1990)

Castillo et al. [7] conducted experiment on two types of concrete, one of NSC with water cement ratio (w/c) = 0.68, compressive strength (f_c') = 27.6 MPa and the other HSC with w/c = 0.327, f_c' = 62.1 MPa for the temperature range from 100° to 800° C with 100° interval. For each type of concrete, two types of test were performed: stressed and unstressed, on the sample cylinders of 51 x 102 mm dimension with maximum aggregate size 9.5 mm. For each set of cylinders tested at a given temperature, three specimens from the same batch were also tested at room temperature to provide reference values. Molds were removed from the specimens 24 hrs after casting, and the specimens were stored in a moist room at 23 °C and 100 percent relative humidity (R.H.) for a period of 60 to 90 days. Two weeks prior to testing, the specimens were removed from the moist room and kept at room temperature with 55 to 65 percent R.H. until the time of test.

During the heating period, moisture in the specimens was allowed to escape freely. The moisture content of the specimens at the time of testing was not measured. In the unstressed tests, the specimens were heated to the desired temperature, which was maintained for 5 to 10 minutes to attain a steady state condition at the center of the specimen.

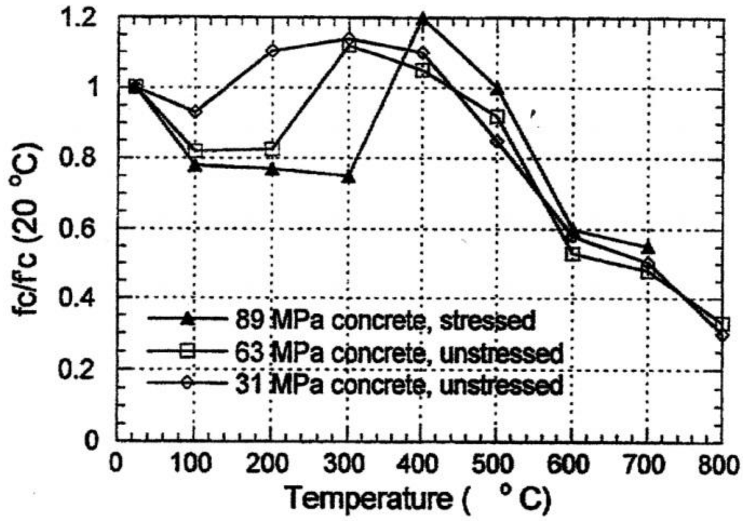

Figure-2.1: Compressive Strength Ratio Vs Temperature [7]

The specimens were then loaded until failure. In the stressed tests, 40 percent of the ultimate compressive strength at room temperature was applied to the specimens and sustained during the heating period.

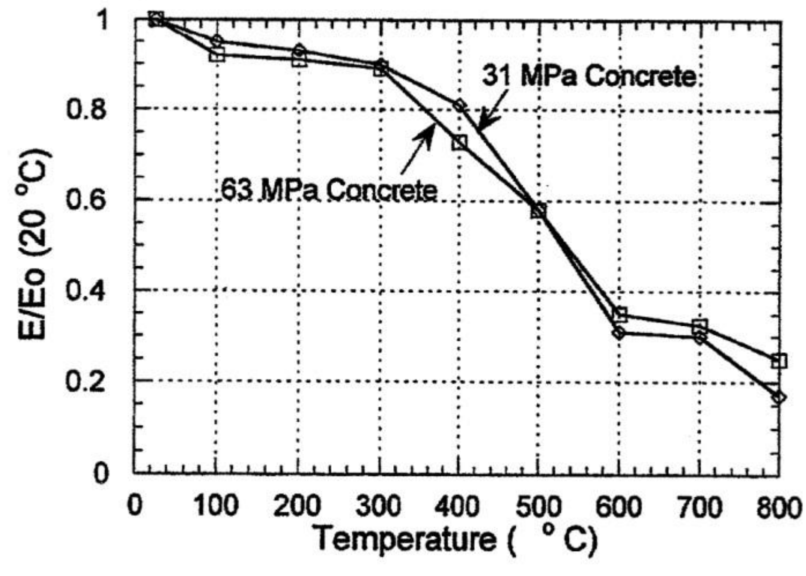

Figure-2.2: Modulus of Elasticity Ratio Vs Temperature [7]

After the temperature reached the steady state, the load was increased at the prescribed rate until the specimen failed.

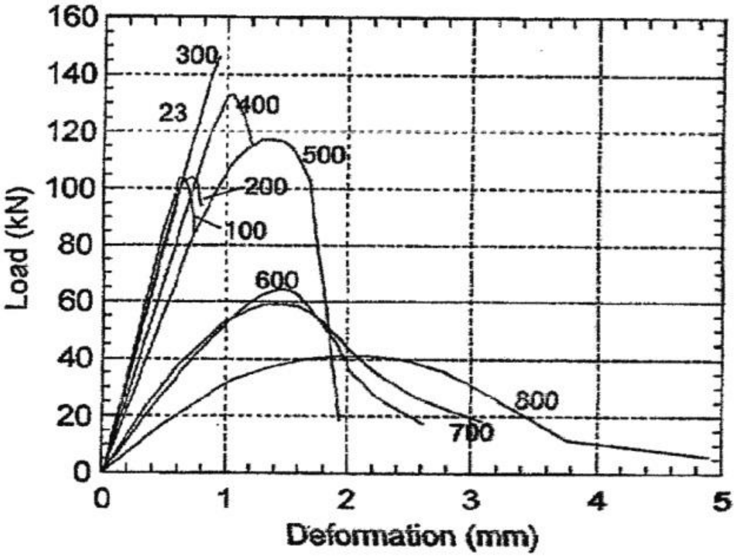

Figure-2.3: Load-Deformation Behaviour of HSC at High Temperature [7]

The control specimens were tested at room temperature on the day of the high-temperature tests. The results of both test methods are plotted in the form of normalized compressive strengths and moduli of elasticity versus temperature shown in Figures 2.1 and 2.2, the loaded formation curves at different temperatures shown in Figures 2.3 and 2.4.

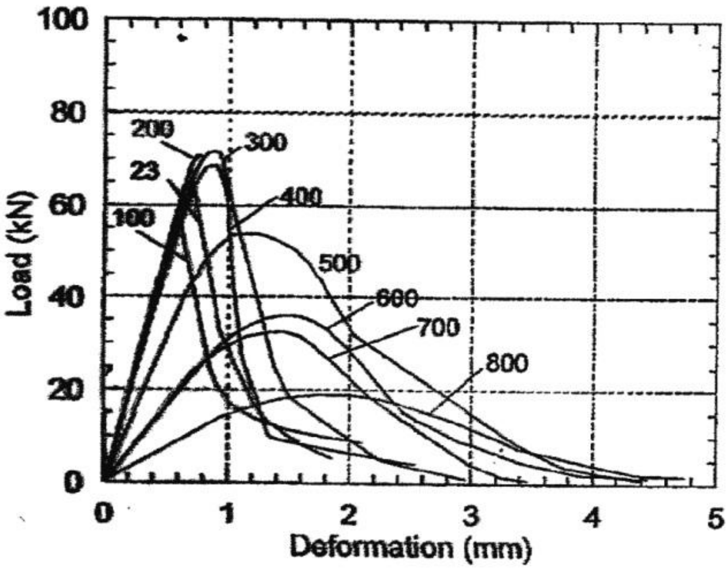

Figure-2.4: Load-Deformation Behaviour of NSC at High Temperature [7]

The authors summarized the results on the following aspects:

1. When exposed to temperatures in the range of 100 to 300°C, HSC showed a 15 to 20 percent loss of compressive strength. Whereas the NSC showed

no such strength loss. As the strength of concrete increased, the loss of strength from exposure to high temperature also increased.

2. After an initial loss of strength, HSC recovered its strength between 300 and 400°C, reaching a maximum value of 8 to 13 percent above the room temperature strength. As the strength of concrete increased, the recovery in strength also occurred at a higher temperature.

3. At temperatures above 400°C, HSC progressively lost its compressive strength which dropped to about 30 percent of the room temperature strength at 800°C. This decrease was similar to that of the NSC.

4. None of the preloaded specimens were able to sustain the load beyond 700°C. About one-third of these specimens failed in an explosive manner in the temperature range of 320 to 360°C while being heated under a constant preload.

5. The modulus of elasticity of the HSC decreased by 5 to 10 percent when exposed to temperatures in the range of 100 to 300°C. At 800°C, the modulus of elasticity was only 20 to 25 percent of the value at room temperature. Similar variations of modulus of elasticity were observed for HSC and NSC. Beyond 300°C, the elastic modulus decreased at a faster rate with increase in temperatures.

2.3.2 Concrete test by Hertz (1984, 1991)

Hertz [8], *Hertz* [9] conducted two test series, one in 1984 and other in 1991on 100 x 200 mm HSC cylinder samples. The 1st test series applied unstressed residual strength test of the specimens. The compressive strength of the sample was 150 MPa. The specimens were heated to 20°, 150°, 350°, 450° and 650° C where each temperature level was maintained for 2 hr for thermal steady state, then cooled at 1°C/min rate.

After seven days of cooling load was applied at constant rate for three samples of each set. The observed result is expressed in Figures 2.5 and 2.6. According to the test the strength increased up to 350°C and then lowered for the higher temperature. 4 out of the 15 samples exploded where one at 350°C, two at 450°C and one at 650°C.

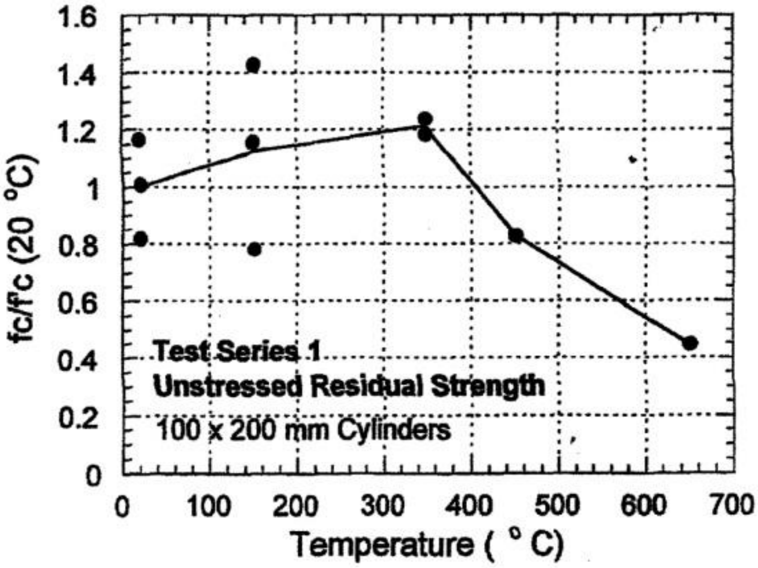

Figure-2.5: Variation of Compressive Strength with Temperature [8]

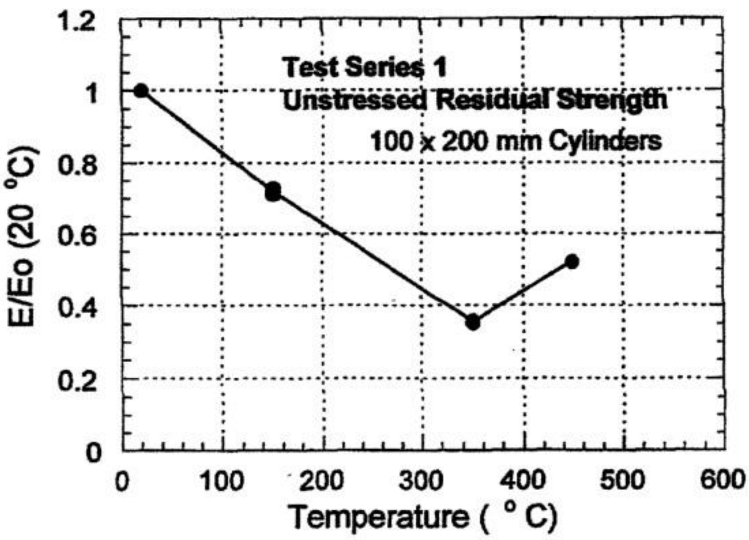

Figure-2.6: Variation of Elastic Modulus with Temperature [8]

The 2nd test was also based on unstressed residual strength test of three sized cylinders, 100 x 200 mm, 57 x 100 mm and 28 x 52 mm, all had 24 pieces of samples with light weight aggregate of burned bauxite. The results are shown in Figures 2.7 and 2.8.

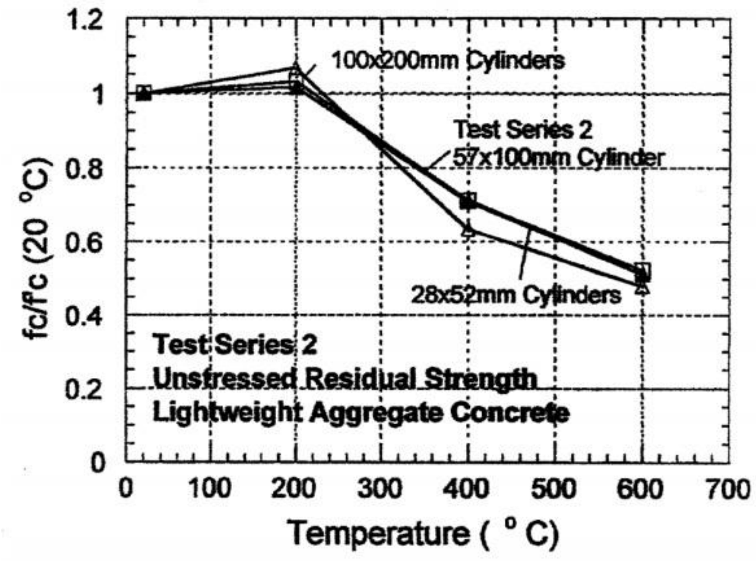

Figure-2.7: Variation of Residual Strength with Temperature [9]

The study was summarized as:

1. Concrete densified by means of Silica fume may explode during heating.
2. Presence of steel fibre does not reduce the risk of explosion.
3. Light weight concrete is not recommended in place of normal weight concrete when spalling is concerned.

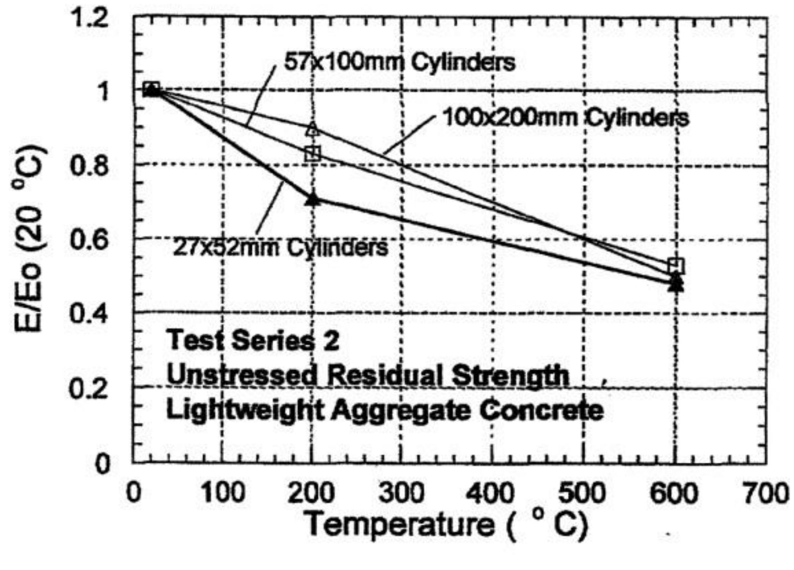

Figure-2.8: Variation of Residual Elastic Modulus with Temperature [9]

2.3.3 Unstressed concrete test by Hammer

Hammer conducted an unstressed (stress rate controlled) test to study the effect on the fire performance of HSC in 1995 for variable combination of concrete compressive strength (between 69MPa to 118MPa), aggregate type (lightweight aggregate vs. normal weight crushed gravels) and heating temperature, cited in *Phan* [6].

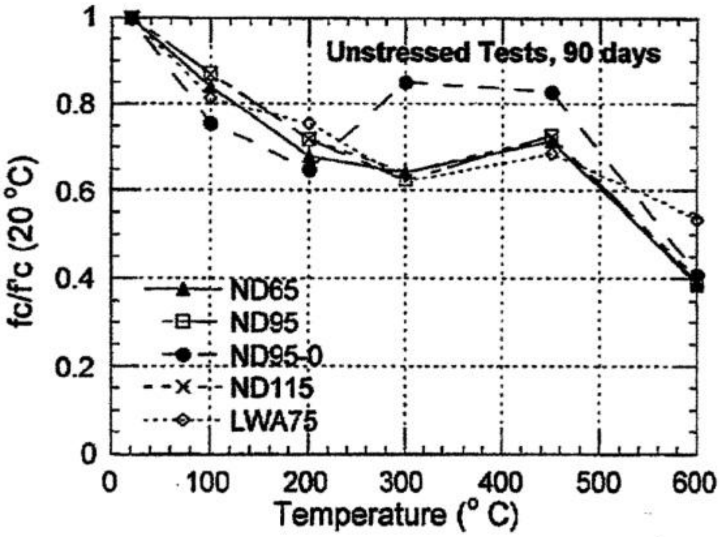

Figure-2.9: Compressive Strength of 90-days Concrete Vs Temperature [6]

He heated 100 x 310 mm cylinder samples at 20°, 100°, 200°, 300°, 450° and 600°C and samples were prepared with varying silica fume (0% to 5%) and water content (w/c = 0.27 to 0.50). Two samples were tested for each temperature level, one on 90th day and the other on 150th day. Samples were heated using steel tube covered by a heating element. The graphical results of 90 days experiment are shown in Figures 2.9 and 2.10.

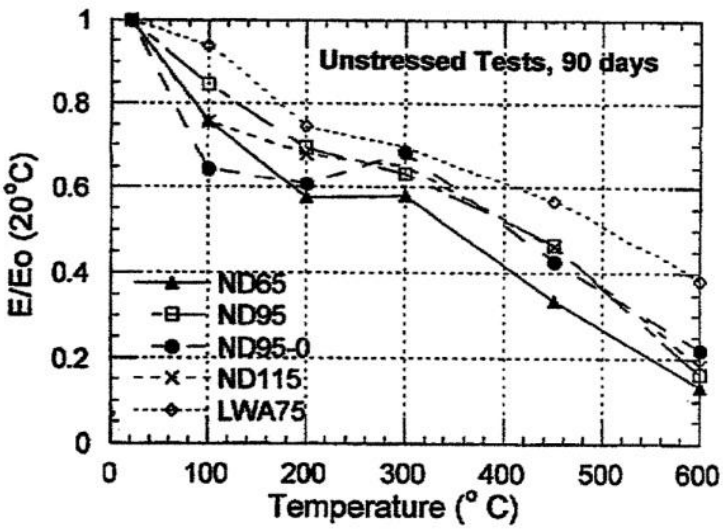

Figure-2.10: Elastic Modulus of 90-days Concrete Vs Temperature [6]

The graphical results of 150 days are shown in Figures 2.11 and 2.12.

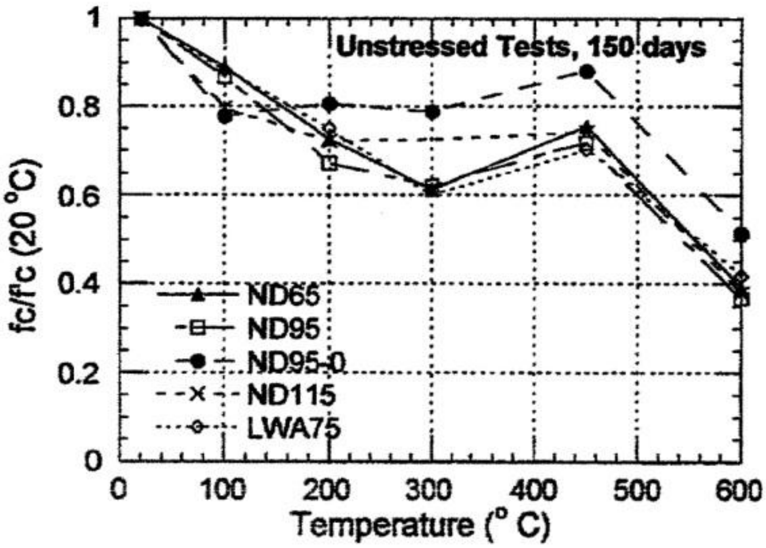

Figure-2.11: Compressive Strength of 150-days Concrete Vs Temperature [6]

The study revealed that:

1. The difference in terms of strength loss with increasing temperature, examined in this study was insignificant, except for samples with no silica fume which showed a gain in strength between 200 to 300°C.
2. A typical "breakpoint" in the strength-temperature curves was observed at 300°C. The study reported that, at this temperature an explosive failure followed by the release of a lot of steam was observed. No such explosive failure or steam release was observed at the other temperatures. The author speculated that the reason for the reduced strength even at low temperatures (between 100 to 300 °C), is the high internal pressure due to the reduced ability of moisture to escape from HSC.

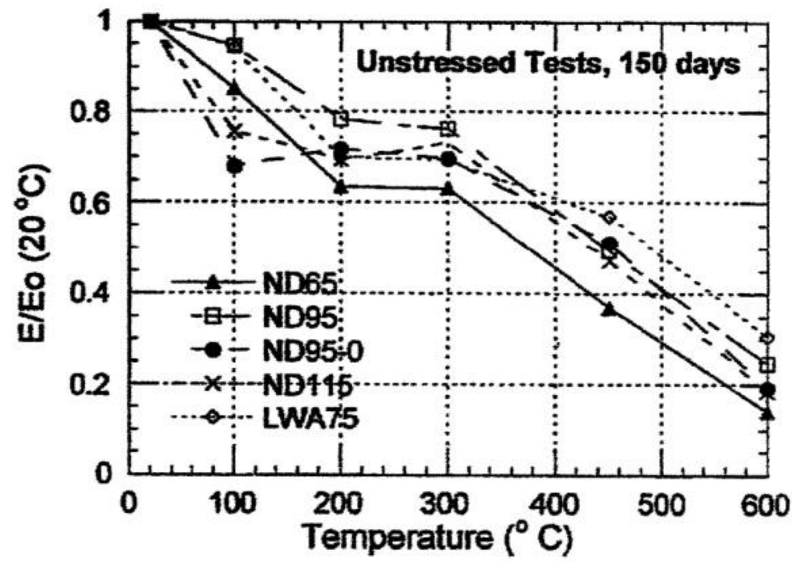

Figure-2.12: Elastic Modulus of 150-days Concrete Vs Temperature [6]

3. An increase in compressive strength was observed for all concretes, except for no silica fume samples, between 300 to 450°C. For silica fume free samples, the strength increase occurred earlier, between 200 to 300°C.
4. Moduli of elasticity of all concretes decreased at a faster rate at temperature above 300°C.
5. Concrete without silica fume show slightly better performance in terms of lower strength loss.
6. The replacement of normal weight coarse aggregate with light-weight aggregate does not seem to affect the temperature dependent strength loss.

2.3.4 Full scale experiment by Bailey (2001)

Bailey [10] conducted a full scale test to study the behaviour of a concrete building when subjected to fire. The 07 storied tested building was constructed using elements formed from NSC and HSC and was designed for 60 min fire resistance following UK design code. HSC having Polypropylene fiber was used for the column within the firing compartment. Fire was applied in the ground floor according to the Figure 2.13. During the experiment despite of adequate safety massive fire escaped through 325 mm vent within first 18 minutes and damaged the overall instrument network causing instrumental malfunction. Thereby the data beyond 18 minutes were unobtainable.

The effects of the fire experiment are shown in the Figure 2.14. However, this study satisfied the European Number (EN) version of the Euro code Part 1.2 regarding the spalling ignoring of structure, since the slab continued to support the load. It also expressed compressive membrane action can only occur at small displacement and can occur in flat slab.

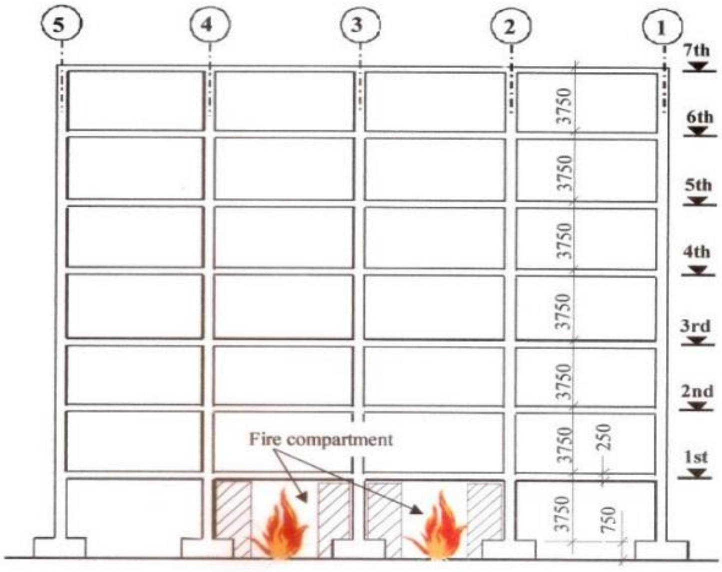

Figure-2.13: Design of Fire [10]

Figure-2.14: Effect of Fire on the Ceiling [10]

At large displacement tensile membrane action occurs but its effects are small in flat slab where only vertical support is at the column. It also stated for tensile membrane action, the reinforcing bar supports the load and therefore need to retain their strength during a fire, which can only be achieved if sufficient concrete cover to the bar is maintained.

The author also discussed that lateral movement of the heated slab was significant, resulting in buckling of the steel cross-bracing and lateral displacement of the external columns. The buckling of the steel cross-bracing reduced the restraint slightly to the heated slab whereas concrete shear wall would cause greater restraint resulting severity in spalling. He further suggested that the designer should be aware of the behaviour and consider that column can withstand likely lateral displacement during fire.

2.3.5 Strength test by Morita et al. (1992)

Morita et al. [11] conducted unstressed residual strength tests on cylinders made from three mixtures with target compressive strengths of 19.6, 39.2, and 58.8MPa in 1992. The cylinders, 100 x 200 mm, were heated at a rate of 1 °C/min to temperatures of 200, 350, and 500°C. The heat was maintained for 60 minute at these temperatures to allow a steady state to be reached, then the cylinders were allowed to cool to room temperature at a rate of 1°C/min. For each temperature level, three specimens were tested. Test results, in terms of variation of compressive strength and modulus of elasticity with respect to temperature, are shown in Figures 2.15 to 2.18, respectively.

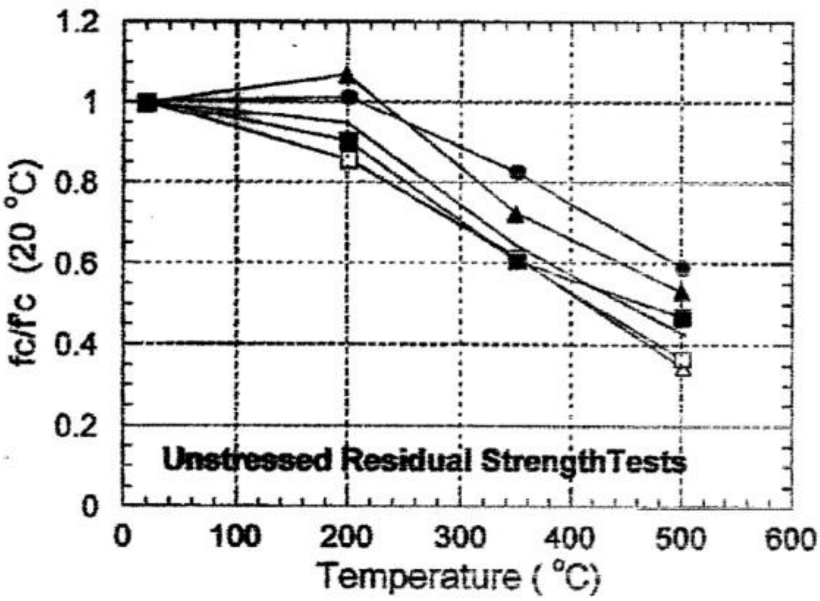

Figure-2.15: Residual Normalized Strength Vs Temperature [11]

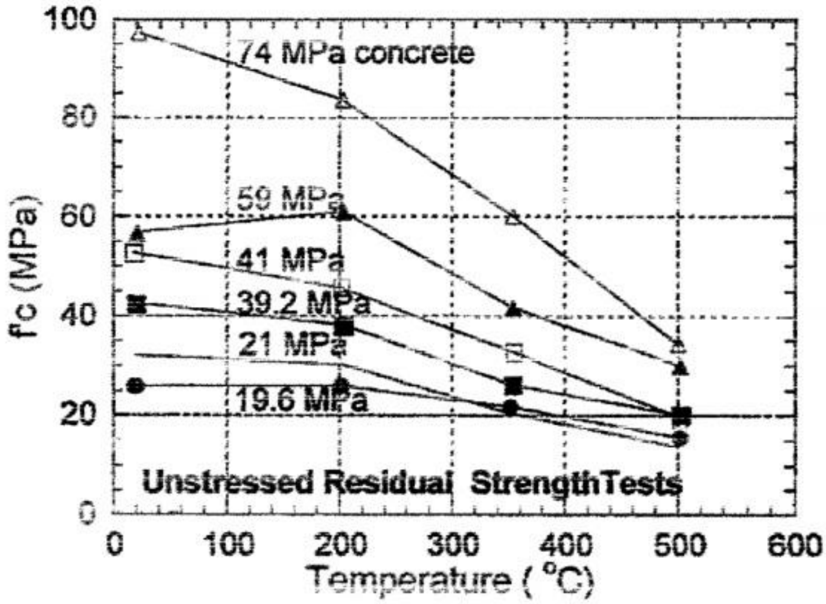

Figure-2.16: Residual Compressive Strength Vs Temperature [11]

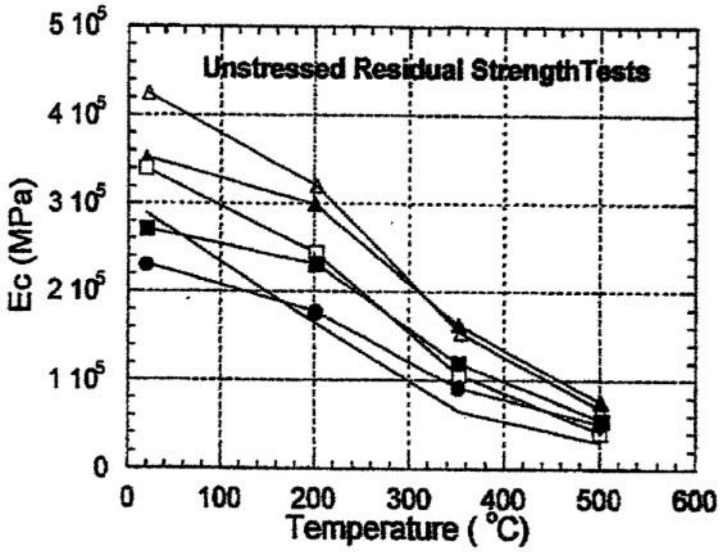

Figure-2.17: Residual Elastic Modulus Vs Temperature [11]

The study concluded that high strength concretes have a higher rate of reduction in residual compressive strength and modulus of elasticity than normal strength concrete after being exposed to temperatures up to 500 °C. The study did not report any spalling problems during heating.

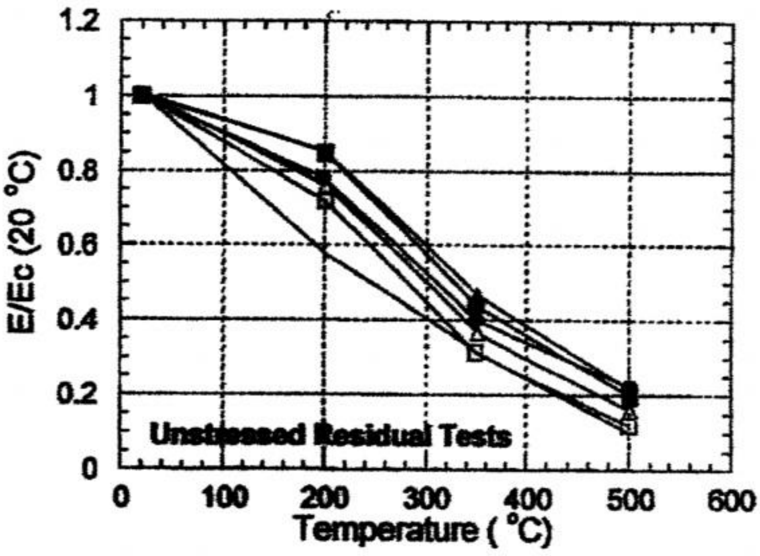

Figure-2.18: Residual Normalized Elastic Modulus Vs Temperature [11]

2.3.6 Strength test by Furumura et al. (1995)

Furumura et al. [12] performed unstressed tests and unstressed residual strength tests on 50 x 100 mm concrete cylinders using three compressive strength levels: 21MPa, 42MPa and 60MPa. The concrete was made from ordinary Portland cement. Each specimen was subjected to constant temperatures, within the range from 100 to 700°C with an increment of 100°C. Three specimens were tested at each temperature level. All specimens were heated at a rate of 1°C/min and the target temperatures were maintained for two hours to achieve a steady state.

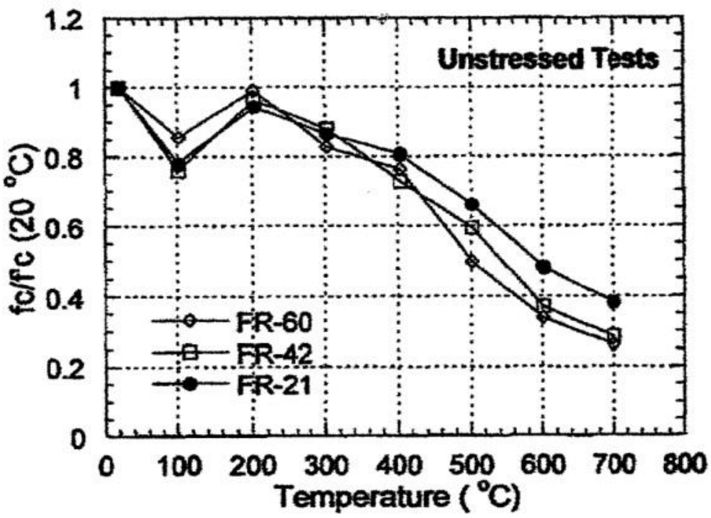

Figure-2.19: Compressive Strength Vs Temperature [12]

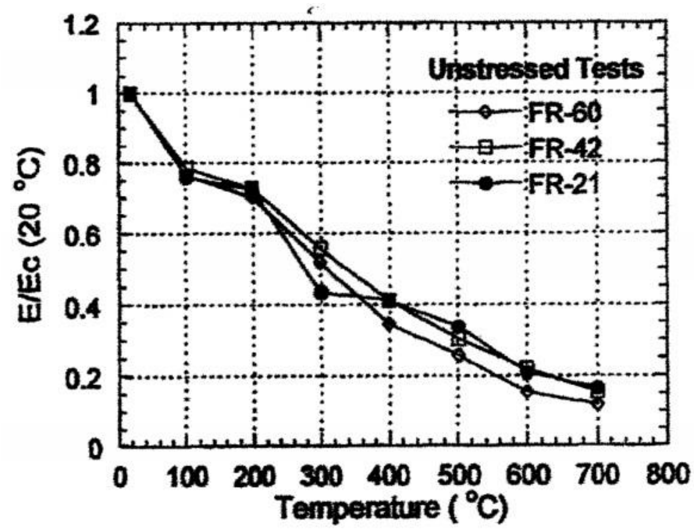

Figure-2.20: Elastic Modulus Vs Temperature [12]

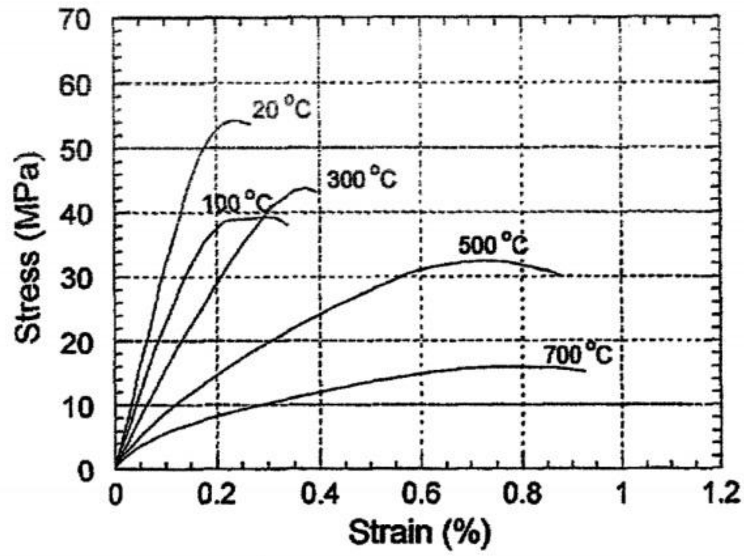

Figure-2.21: Typical Stess-Strain Relationship for 42MPa Concrete [12]

The results of the unstressed tests, in terms of average compressive strength versus temperature, average modulus of elasticity versus temperature, and typical concrete stress strain relationships, are shown in Figures 2.19 to 2.22.

Furumura et al. [12] observed that, for the unstressed tests, the compressive strength decreased at 100°C, recovered to the room temperature strength at 200°C, and then decreased monotonically with increasing temperature beyond 200°C. For the unstressed residual strength tests, the compressive strength decreased gradually with increasing temperature for the entire temperature range without any recovery. The modulus of elasticity, in general, decreased gradually with increasing temperature.

The difference between unstressed tests and unstressed residual strength tests were reduced with increasing temperature. The stress-strain curves for HSC are quite different than those of the normal strength concrete (Figure-2.22).

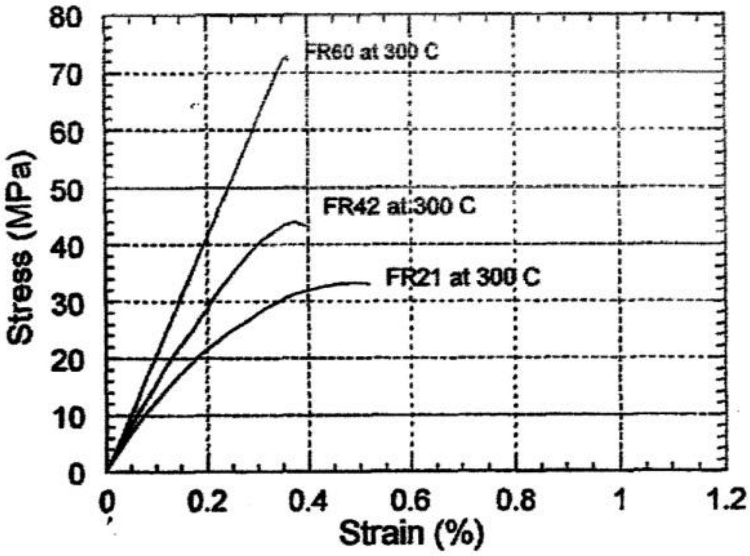

Figure-2.22: Comparison of Stess-Strain Relationship for Concretes at 300°C [12]

HSC series 42MPa and 60MPa exhibited steeper slopes than the NSC at temperature up to 300 to 400°C in the unstressed test. Spalling failure of the 60MPa-concrete specimens was observed at temperatures up to 300°C.

2.3.7 Beam test by Felicetti et al. (1996)

Felicetti et al. [13] performed unstressed residual strength (strain rate controlled) tests on silica fume based HSC specimens with specified strengths of 72MPa and 95MPa. Both concretes used siliceous aggregates, consisting mostly of crushed lint particles, with maximum size of 25 mm. The specimens included cylinders of two different sizes: 100 x 300 mm and 100 x 150 mm; and deep beams with dimensions of 80 x 275 x 500 mm. The 100 x 300 mm cylinders (37 specimens) were tested in uniaxial compression. The 100 x 150 mm cylinders (20 specimens) were notched at mid-height and tested in direct tension. The deep beams (3 reinforced and 3 unreinforced) were tested in bending and shear. For uniaxial compression tests, batches of 2 to 4 cylinders were exposed to temperatures of 20, 105, 250, 400, and 500°C. For direct tension tests, batches of 2 to 3 cylinders were exposed to the same temperatures but only up to 400°C.

All specimens were cured under water for one week and stored in air for three weeks at 20°C and 92% R.H. and one month at 20°C and 65% R.H. Specimens heated to 105°C were kept at this temperature for 7 days in an oven, and then allowed to cool to room temperature in the closed oven. For specimens exposed to higher temperatures, a heating rate of 12°C/min was used to heat the specimens to target temperatures, which were maintained for 12 hr. A cooling rate of 12°C/min was used to cool the specimens to room temperature. Figures 2.23 and 2.24 express the residual compressive strength and elasticity results of uniaxial compression tests for both 95MPa and 72MPa.

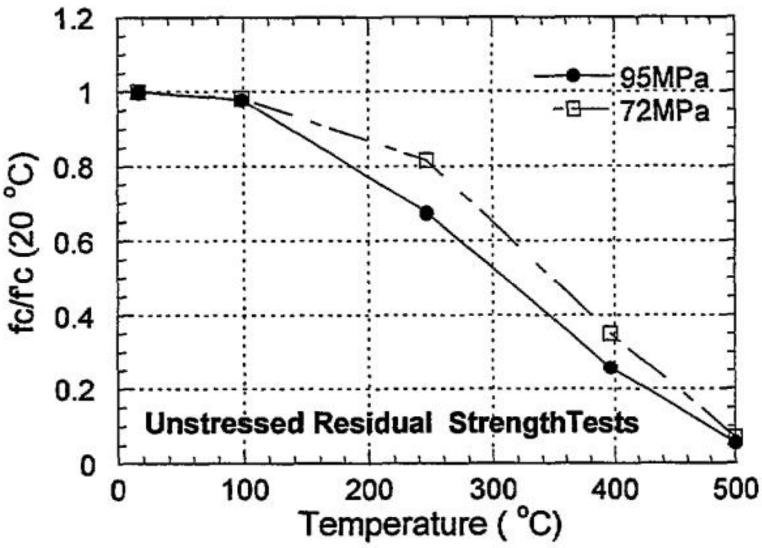

Figure-2.23: Residual Concrete Strength Vs Temperature [13]

Figures 2.25 and 2.26 summarize the results of the uniaxial compression stress-strain tests, Figures 2.27 and 2.28 summarize the results of the direct tension tests and Figures 2.29 and 2.30 summarize the results of the beam tests for each 95MPa and 72MPa.

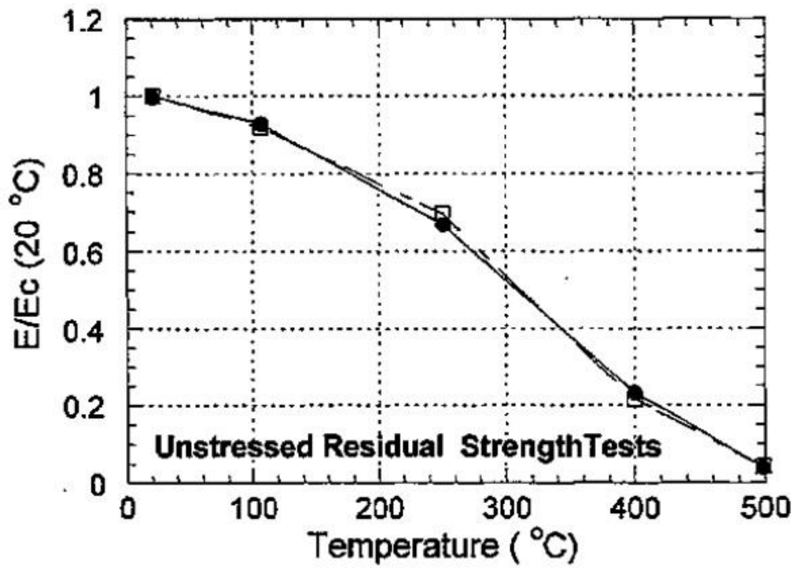

Figure-2.24: Residual Elastic Modulus Vs Temperature [13]

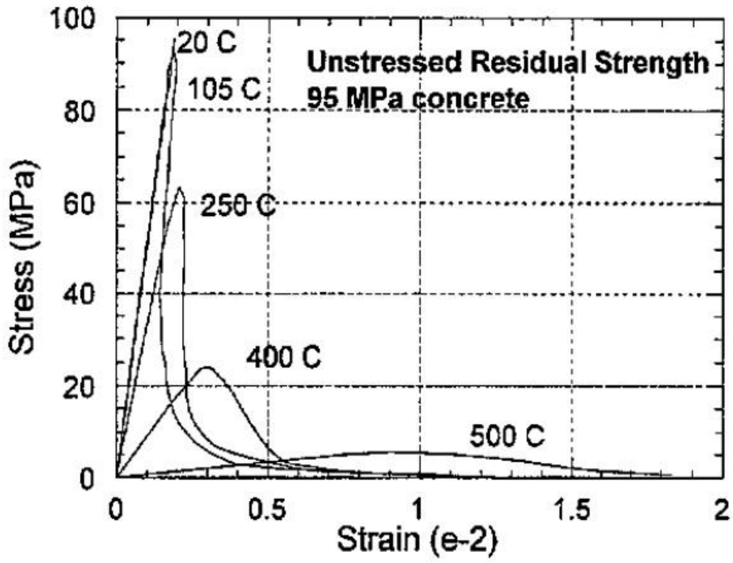

Figure-2.25: Stress-Strain Curve for 95MPa Concrete after Heating to Exposure Temperature [13]

The study revealed similar trends of reductions in compressive strength and modulus of elasticity with increasing temperatures as was observed in other test programs.

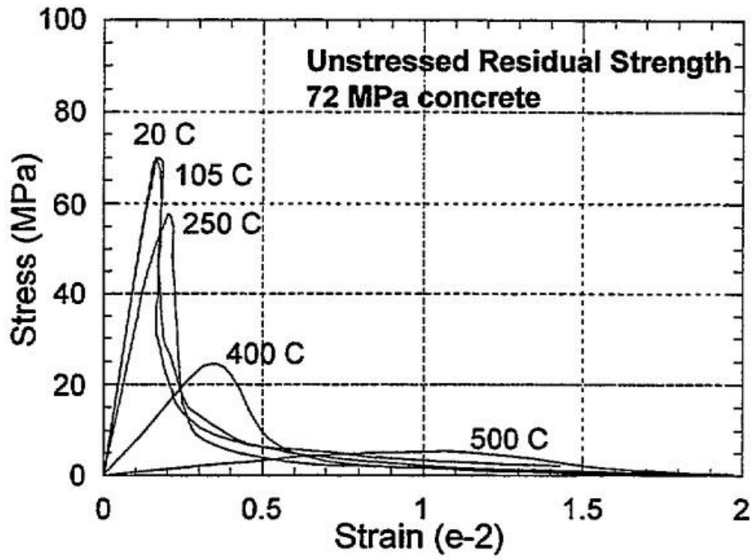

Figure-2.26: Stress-Strain Curve for 72MPa Concrete after Heating to Exposure Temperature [13]

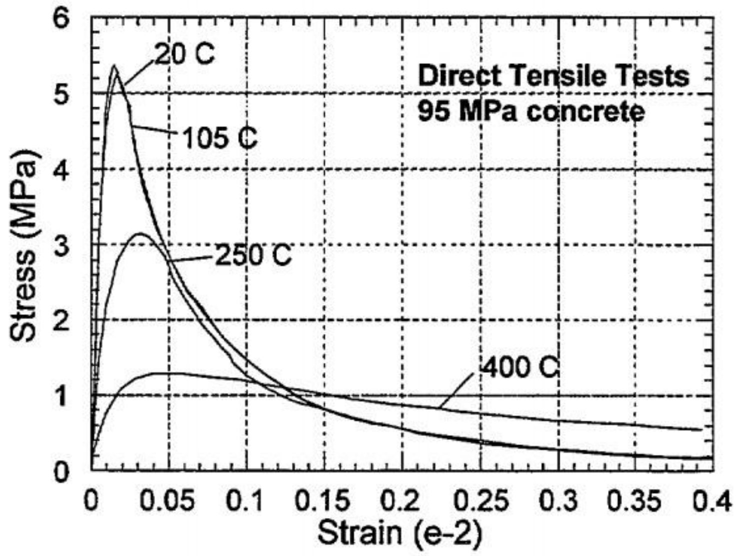

Figure-2.27: Tensile Stress-Strain Curve for 95MPa Concrete after Heating to Exposure Temperature [13]

An exposure temperature of 250°C appears to be the level which marks the higher rate of strength and modulus reduction. At 400 to 500°C, most of the flint aggregates appeared cracked or split, with a different color compared with aggregates not exposed to heat.

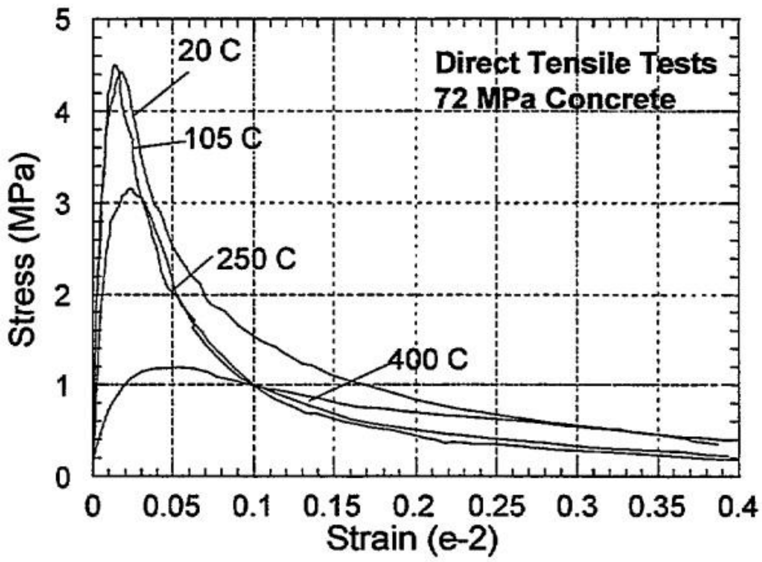

Figure-2.28: Tensile Stress-Strain Curve for 72Pa Concrete after Heating to Exposure Temperature [13]

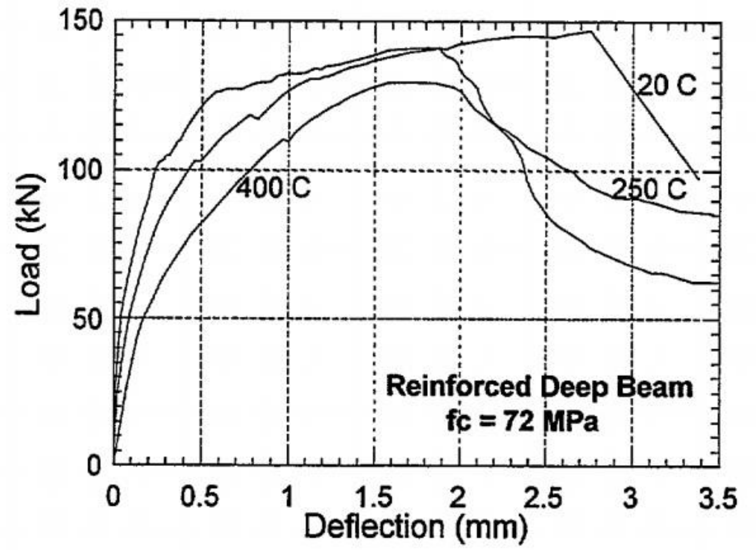

Figure-2.29: Load-Deflection Response of Reinforced Beams Vs Temperature [13]

Results of the unreinforced beam tests indicated that the peak load was less sensitive to high temperature than implied by the marked reduction in tensile strength observed in the direct tension tests.

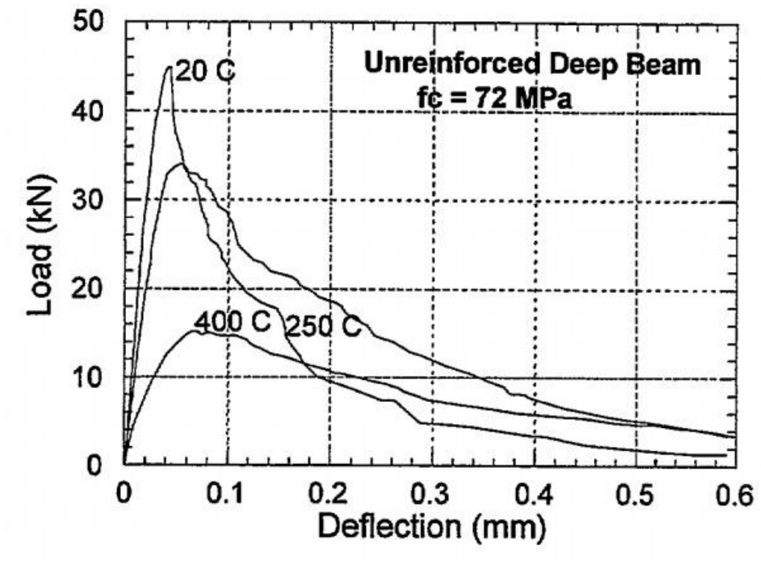

Figure-2.30: Load-Deflection Response of Unreinforced Beams Vs Temperature [13]

For reinforced concrete beams, the peak load was only marginally decreased up to 400°C. This later finding reflects the fact that in a RC beam, the flexural capacity is governed primarily by the area of steel and not concrete strength.

2.3.8 Strength test by Noumowé et al. (1996)

Noumowé et al. [14] conducted a study on performance of HSC exposed to high temperatures which included experimental and analytical parts. The experimental part consisted of unstressed residual strength tests of normal strength and HSC cylinders (160 x 320 mm) and prisms (100 x 100 x 400 mm). A normal strength (38.1MPa) and a high-strength (61.1MPa) mixture were used. The prisms had enlarged ends and were used to measure tensile strength. Both concretes used calcareous aggregates. The specimens were cured at 22 °C and 95% R.H. until the time of testing (at 2 months). The specimens were heated at a rate of 1°C/min to target temperatures of 150, 300, 450, 500, and 600°C, which was maintained for 1 hour, and then allowed to cool at 1 °C/min to room temperature. Uniaxial compressive, splitting tensile and direct tensile tests were performed to obtain residual compressive strength, modulus of elasticity, and residual tensile strength versus temperature relationships. The latter two relationships are shown in Figures 2.31 and 2.32.

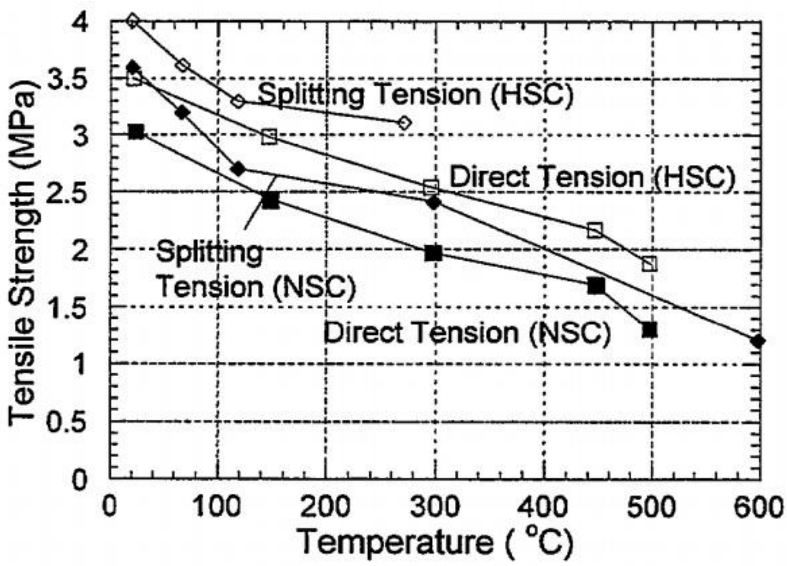

Figure-2.31: Residual Tensile Strength of HSC and NSC Vs Temperature [14]

The experimental results show that residual tensile strengths for both normal strength and HSC decreased similarly and almost linearly with increasing temperatures. Tensile strengths of HSC at all temperatures were approximately 15% higher than those of normal strength concrete.

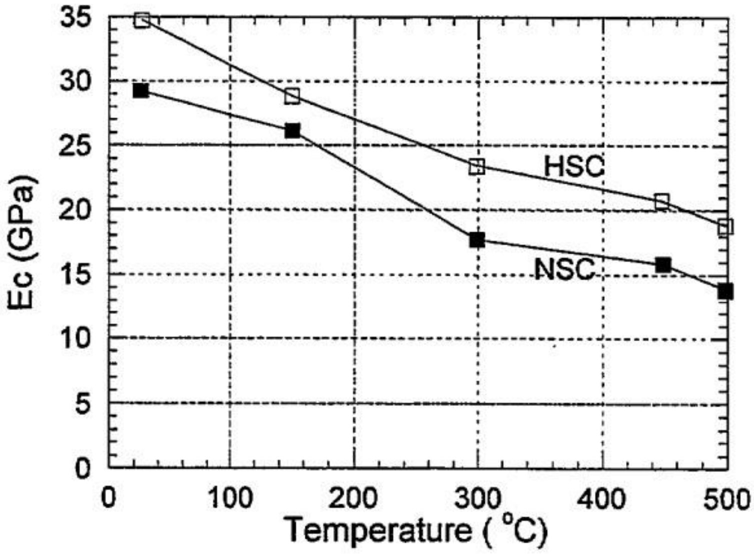

Figure-2.32: Elastic Modulus of HSC and NSC Vs Temperature [14]

Also, tensile strengths measured by the splitting tensile tests were consistently higher than by the direct tensile tests. The residual moduli of elasticity of HSC remained approximately 10-25% higher than those of normal strength concrete for the entire temperature range. Porosity measurements indicated that between 25 and 120°C, the porosity of both concretes were not altered. As temperatures increased, normal strength concrete became increasingly more porous compared with HSC. Mass losses in both concretes were also similar up to 110°C (less than 1%). Highest rate of mass loss occurred in temperature range of 110 to 350°C. The rate of weight loss stabilized at temperatures above 350°C. At any temperature, mass loss in normal strength concrete was higher than that in HSC.

2.3.9 Beam test by Jensen et al. (1995)

Jensen et al. [15] conducted three series of beam under Norwegian Fire Research Laboratory. The test specimens were reinforced and prestressed concrete beams having dimensions of 150 x 200 x 2850 mm. Three types of concretes were used: ND (normal density), LWA (lightweight aggregate - Liapor aggregate), and LWAF (lightweight aggregate with fibers - Fibrin fiber type 1823). The concretes were designed to have target 28-day cube strengths (100 x 100 x 100 mm cubes) of 75MPa and 95MPa. In addition, some beams were provided with a coating of Lightcem concrete as passive fire protection, and two of the beams in test series 2 were made of lightweight aggregate LightCem concrete with a target 28-day cube strength of 50MPa. Standard bars of quality K500TS according to the requirements of Norwegian

Standard NS 3570 were used as reinforcement. The longitudinal reinforcing bars were 20 mm and 32 mm, and the stirrups were 8 mm. For prestressing, 26 mm, Dywidag bars, of the type St 835/1030 were used. A prestress force of 300kN was centrically applied at the ends of the beams, resulting in a mean prestress of approximately 10MPa.

Table-2.1: Concrete Material Properties [15]

Type	Beam ID	f_c (28d) MPa	f_{cc} (28d) MPa	E_c (28d) GPa	Density kg/m^3	Age at Fire Test (days)	Moist Content (%)
ND95	(11), 12 61, 62	83.4 89.6	73.4 72.5	32.4 30.4	2457 2450	85 64	3.9 3.7
LWA75	(20), 21, 22	75.8	69.2	24.7	1936	48/ 92	6.9
LWAF75	31, 41, 42[1], 43, (30), 32[1], 35, 33, (34)	68.9 78.2 70.1	61.8 75.3 60.1	23.8 24.7 23.9	1906 1913 1970	56 54 86	6.5 6.0 8.9
LWAC	51, 52[1]	46.6	42.4	18.2	-	77	-

[1] Loaded at midspan with a concentrated vertical load of 30kN. The load was applied in 6 steps of 5kN each, by means of a hydraulic cylinder connected to a steel frame in a self-supporting system.

Test series 1 and 2 consisted of 7 beams each. Series 3 was a reference series for evaluation of residual strength of the fire exposed beams, and consisted of 2 beams. Series 1 included 7 reinforced LWA concrete beams with a nominal 28-day cube strength of 75MPa. Series 2 included 4 reinforced beams (2 of ND concrete and 2 of LWA concrete), 3 prestressed beams (1 of ND concrete, 1 of LWA concrete, and 1 of LWA concrete with fibers). Series 3 includes 2 reference beams. Information on concrete material properties and other test information are summarized in Table-2.9.1.

Fire tests were performed in an oil-heated furnace. The furnace has horizontal exposure openings with dimensions of 2500 mm x 5000 mm and a depth of 1500 mm. In test series 1 and 2, the concrete beams were exposed to a hydrocarbon fire on three sides. The heating regime followed the standard time-temperature curve prescribed by International Organization for Standardization (ISO) 834 for a hydrocarbon fire. The test procedure was also in accordance with ISO 834. Thermocouples were installed on the longitudinal and shear reinforcement at two locations in each beam. The beams were exposed to the ISO 834 hydrocarbon fire for 2 hour, and the maximum oven temperature reached approximately 1100°C. The furnace temperature history and the period when spalling were observed are shown in Figure 2.33. Table 2.2 summarizes the results of the tests.

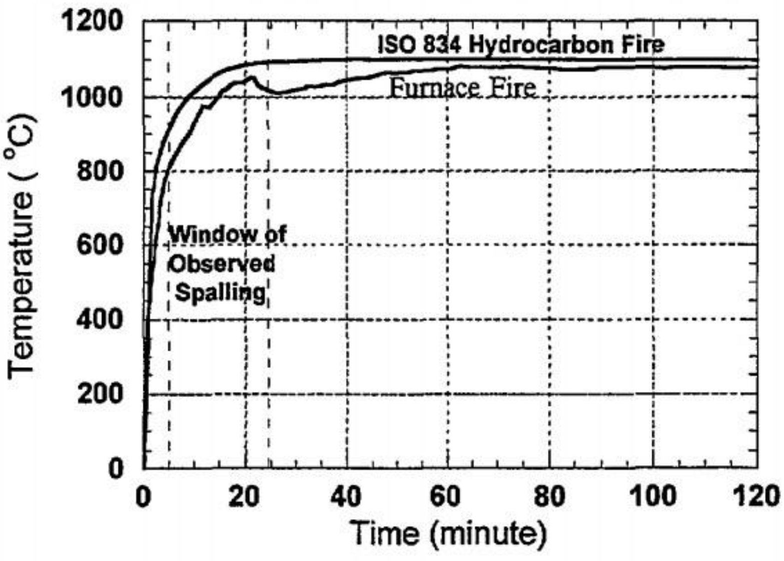

Figure-2.33: ISO Hydrocarbon Fire Curve, Furnace Temperature and Time When Spalling was Observed [15]

Sounds of spalling were reported to begin at approximately 5 to 6 minutes into the tests, and they stopped at 25 minute for test series 1 and 20 minute for test series 2. According to the hydrocarbon fire curve, the spalling began at a furnace temperature of 800°C and ended when the furnace reached its steady state temperature of 1100°C.

The following conclusions were drawn from this study:

1. Severe spalling (exposed reinforcement) occurred more in the higher strength lightweight aggregate beams as observed in reinforced and prestressed LWA75 beams, while spalling without exposed reinforcement occurred more in high-strength, normal weight ND beams.

2. Shallow or no spalling was observed for higher strength lightweight concrete beams with fibers (LWAF).

3. No spalling was observed for the lightweight beams with fibers and the passive protective coating (LWAFP75).

Table-2.2: Summary of Observation of Test [15]

Concrete Type	No Spalling	Shallow Spalling No Exposed Reinforcement	Severe Spalling Exposed Reinforcement	Collapse
LWAF75	32[1], 33[2]	31	35[3]	-
LWAF75P	41, 42[1], 43	-	-	-
LWA75	-	-	21, 22[2]	-
LightCem	52[1]	51	-	-
ND95	-	61, 62	-	12[2]

[1] Beam tested with vertical load;

[2] Prestressed beam;

[3] Spalling was limited to the bottom of this beam and no spalling occurred on the sides. The study reported this spalling as likely being caused by poor concreting.

2.3.10 Beam test by Sanjayan et al. (1991)

Two full-scale T-beams, one made of high-strength concrete with silica fume (105MPa) and one made of normal strength concrete (27MPa) were fire tested by *Sanjayan et al.* [16]. The beams were 2.5 m long and the flanges were 1.2 m wide. Different flange thicknesses of 200 mm and 150 mm were cast on each side of the web. The web depth was 450 mm from the top surface, and the web was 250 mm wide. To study the effect of reinforcement cover, the cover to the steel in the 200-mm flange was 75 mm, and for the 150-mm flange the cover was 25 mm. In addition, the main bars in the web were staggered diagonally to obtain reinforcement covers of 25, 50, and 75 mm along the web.

Moisture contents of the test beams were determined by drying concrete sections which had the same cross section as the test specimens and which were cast together with the test specimens. Thermocouples were installed at regular intervals inside the specimens to monitor the temperature distributions during the fire tests. To determine the intensity of spalling, the weights of the specimens were monitored with load cells while the test was in progress. Temperatures measured at 25, 50, and 75 mm from the bottom of the web, and weight losses versus time for both specimens are shown in the Figures 2.34 and 2.35, respectively.

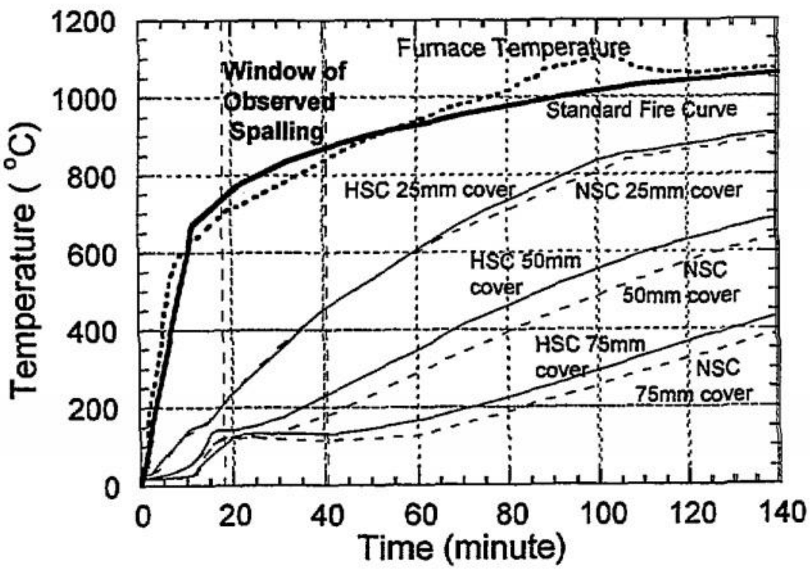

Figure-2.34: Temperature vs Time at Different Location of the Specimen [16]

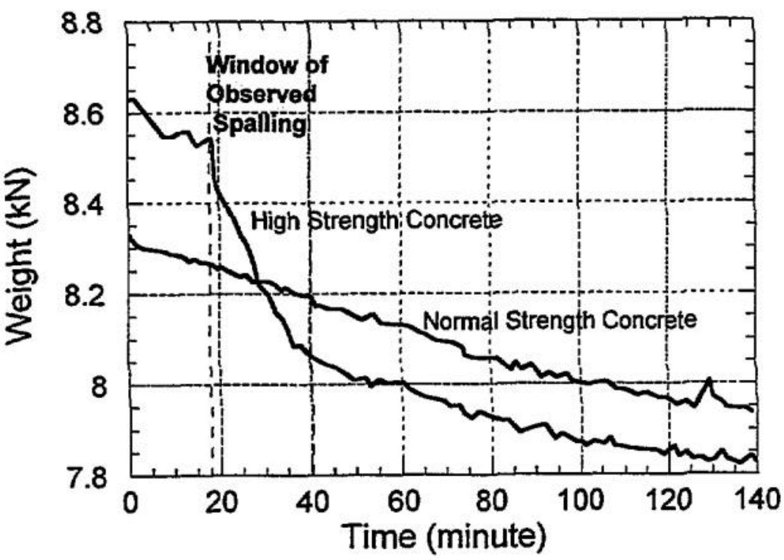

Figure-2.35: Specimen Loss vs Time for HSC and NSC Specimen [16]

About 15 min into the test, with the furnace temperature averaging 691°C, moisture began to dip from several vertical cracks in both specimens. A larger quantity of moisture dripped from the high-strength concrete specimen. There was no spalling until 18 min into the test, with furnace temperature averaging 715°C. Severe explosive spalling of the high-strength concrete beam started when a large piece dislodged from the 200-rnm flange. The concrete temperature at a depth of 25 mm, where spalling occurred, averaged 128°C. Explosive spalling of small pieces of the high-strength concrete specimen from the 200-mm flange continued with increasing intensity until about 40 min into the test. Between 20 and 40 min there was a large rate of weight loss corresponding to the spalling. No spalling was observed in the NSC specimen, even though the temperatures inside the normal strength concrete specimen were only slightly lower than in the HSC specimen.

Since this involved only one replicate specimen for each type of concrete, it is difficult to draw definite conclusions. However, the following observations were reported:

1. High-strength concrete appears to be more prone to spalling in a fire than normal strength concrete.
2. Spalling occurred in the thicker 200-mm flange where the cover of the steel was large (75 mm). In the 150-mm flange, the cover was 25 mm and there was no spalling. No explanation was given for this observation.
3. No spalling occurred in the web, possibly because (1) in the web, the concrete was exposed to three sides and therefore the distance for the moisture to escape was much shorter; and (2) the existence of wider flexural cracks in the web.
4. The higher moisture content found in the high strength concrete indicates that high strength concrete has slower drying rate than normal strength concrete.

2.3.11 Column test by Diederichs et al. (1995)

Diederichs et al. [17] reported general information on fire tests of three short HSC columns (250 x 250 x 1000 mm), tests by the VTT Fire Technology Laboratory (Finland) of ten short HSC columns (150 x 150 x 900 mm), and a fire test on a full scale column (400 x 500 x 5590 mm) by the Institute fur Baustoffe, Massivbau und Brandschutz.

The three columns tested by *Diederichs et al.* [17] were made of three different concrete mixtures (I, II, and III). Mixture I had a specified cube strength of 101MPa and contained fibers (not clearly specified). Mixture II had specified cube strength of 105MPa and contained no fibers. Mixture III had a specified cube strength of 90MPa and contained fibers. The columns were subjected to 100% of the design load prior to fire testing. The two columns with fibers experienced minor spalling (mixture I) and no spalling (mixture III) during fire tests. Fire tests on these columns were terminated at 125 minutes after the start of the tests. The mixture II column (without fibers) experienced spalling at about 6 minutes into the fire test. Spalling continued until 30 minutes into the test when it reached the longitudinal reinforcement at the edges of the column. The test was terminated at 45 minutes, which is significantly less than the time of 125 minutes for specimens with fibers.

In the VTT fire tests, the ten HSC specimens were made of three different concrete mixtures, all contained variable fiber contents:

1. Group 1: Portland Cement PZ55F with concrete cube strength of 85 MPa.
2. Group 2: Portland Cement PZ55F with concrete cube strength of 105 MPa.
3. Group 3: Portland Cement PZ45F with concrete cube strength of 45 MPa.

VTT's fire tests were conducted according to the German Standard DIN 4102 (similar to International Standard ISO 834). None of the columns experienced spalling. All columns were reported to have failed due to loss of compressive strength at high temperature. The fire resistance times were 51 minutes for the HSC columns (Groups 1 and 2) and 72 minutes for the NSC columns (Group 3).

In the full scale column test, the specimen was made of concrete with a specified cube compressive strength of 110 MPa and contained fibers. The column was eccentrically loaded with 100% of its design load and exposed to ISO 834 standard fire from all four sides. Shallow spalling occurred at about 10 minutes after starting the test and stopped after 30 minutes. At 181 minutes, the column collapsed due to compressive failure of the concrete near the maximum stressed cross section.

The report by *Diederichs et al.* [17] indicated that the use of capillary forming fibers help reduce the potential for spalling in HSC columns and suggested that further studies be conducted on the effects of variations in fiber contents.

2.3.12 Beam test by Rashidi (2013)

Rashidi [18] experimented a total of 120 pieces reinforced concrete beams with twelve different compositions under ten different conditions. The compressive strength, clear cover and the strength of reinforcing steel have been the prime variables for difference in compositions. The testing conditions varied in burning temperatures and durations apart from the ambient one basing on different realistic fire accidents. A full scale natural gas furnace has been constructed in this research having integral gas line. Both element and material testing have been conducted in this research. After completion of the fire test all the beams were checked for different physical properties and the data have been recorded and maintained.

The results obtained from the experiments have been evaluated under four analytical studies. The high strength concrete displayed better performances as regards to spalling effect and the reserve strength than the normal strength concrete. Though thicker clear cover provides better protection to the reinforcement, on the contrary, it has adverse effect against fire and causes severe damage in terms of spalling and loss of the residual strength. Strength of reinforcing steel has exhibited a twofold property countering each other. High strength steel exhibited higher performance in case of reserve strength but inferior in case of spalling. These parametric studies also suggested a good number of graphical guidelines for designing better fire endurable flexural members within commonly used concrete compressive strengths.

The research proposed two separate methods: one for designing superior fire durable structure and the other for evaluating pre/post fire state of structures. The fire design method consults a group of charts those have been formulated from the experimental results.

2.3.13 Beam test by Kadhum (2014)

Reduced scale beam models (2250×375×375 mm) were tested by *Kadhum* [19] in a flame of temperature of 25-750°C. At age of 60 days of beam casting, two temperature levels of 400 and 750°C were chosen with exposure duration of 1.5 hours.

Test results indicated remarkable reduction in the ultrasonic pulse velocity and rebound number of the rigid beams cooled in water were (2-5%) more than the rigid beam specimens cooled in air (Figures 2.36 and 2.37).

Based on the study, *Kadhum* [19] concluded:

1. The ultrasonic pulse velocity tested showed a response to the effect of fire flame, the reduction in (U.P.V) was (28 and 33%) and (52 and 54%) for beams cooled in air and water at 400 and 750°C respectively. It appears that this non-destructive test gives good predicted values for the residual strength.

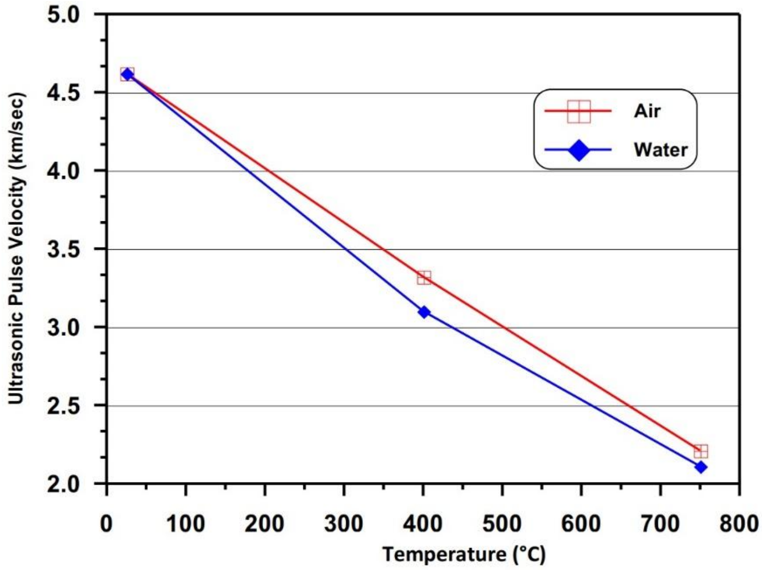

Figure-2.36: The effect of fire flame on the Ultrasonic Pulse Velocity [19]

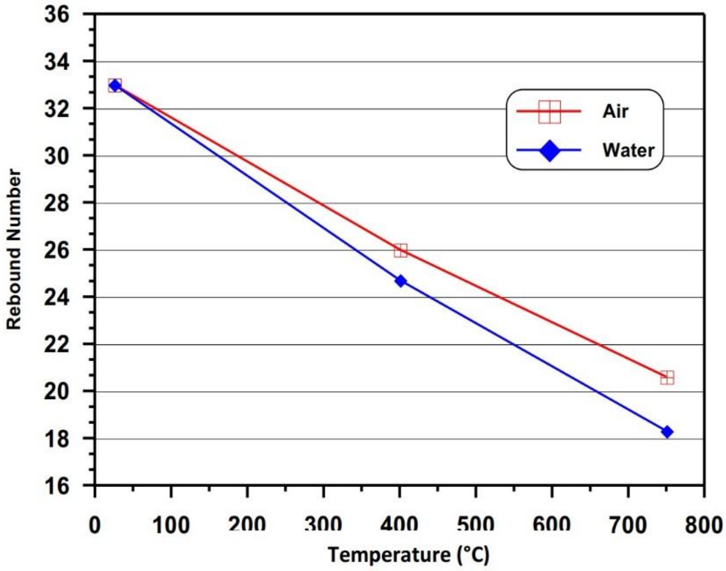

Figure-2.37: The effect of fire on the rebound number [19]

2. The reduction in rebound number was (22 and 27%) and (42 and 45%) for beams cooled in air and water at 400 and 750°C respectively. The decrease in the rebound number with increasing in fire temperature can be attributed to the fact that fire causes damage to the surface of concrete rigid beams rather than to concrete in the core of the member.

3. Sudden cooling concrete caused additional strength loss for RC beam specimens.

4. It was found that the ultimate load capacity of rigid beam specimens decreases significantly when subjected to burning by fire flame.

5. In this study, it is noticed that the load-deflection relation of RC rigid beam specimens exposed to fire flame temperature around 750°C are more leveled indicating softer load-deflection behavior than that of the control beams. This can be attributed to the early cracks and lower modulus of elasticity.

6. The ACI and B.S Codes predict ultimate moment capacity after exposure to 750°C fire flame temperature conservatively.

7. The experimental results clearly indicate that the crack width in reinforced concrete beams that are subjected to fire flame are higher than the beams that are not burned at identical loads.

8. Fire temperature has significant effect on the flexural performance of RC rigid beams. The ultimate and serviceable bearing capacities of RC specimens decrease with the increase of fire temperature.

2.3.14 Numerical beam modelling by Kodur et al. (2008)

Kodur et al. [20] used moment-curvature relationships to trace the response of an RC beam in the entire range of loading up to collapse under fire. The model considered the case of loading where the bending moment was the dominant action on the beam and the effect of both shear force and axial force was neglected. The temperatures and strength capacities for each segment, and computed deflections in the beam were used to evaluate failure of the beam at each time step. At every time step, each beam segment was checked against pre-determined failure criteria, which include thermal and structural considerations. The time increments continued until a certain point at which the thermal failure criterion is met or the capacity (or deflection) reaches its limit state. At this point, the beam was assumed to have failed. The time to reach this failure point is the fire resistance of the beam. The model generated various critical output parameters, such as temperatures, stresses, strains, deflections and moment capacities at various given fire exposure times.

Results from the analysis were used to demonstrate the behavior of a typical RC beam under fire conditions. To illustrate the thermal predictions from the model, the temperature variation was plotted as a function of fire exposure time at various locations of the beam cross section. The temperature at various depths of concrete, as well as in rebar, increased with fire exposure time (Figure 2.38). The moment capacity of the beam decreases with increasing time of fire exposure (Figure 2.39).

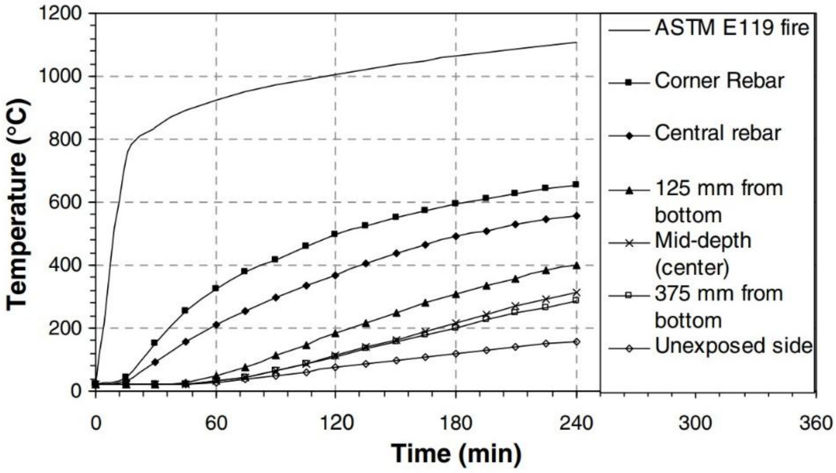

Figure-2.38: Time-Temperature graph [20]

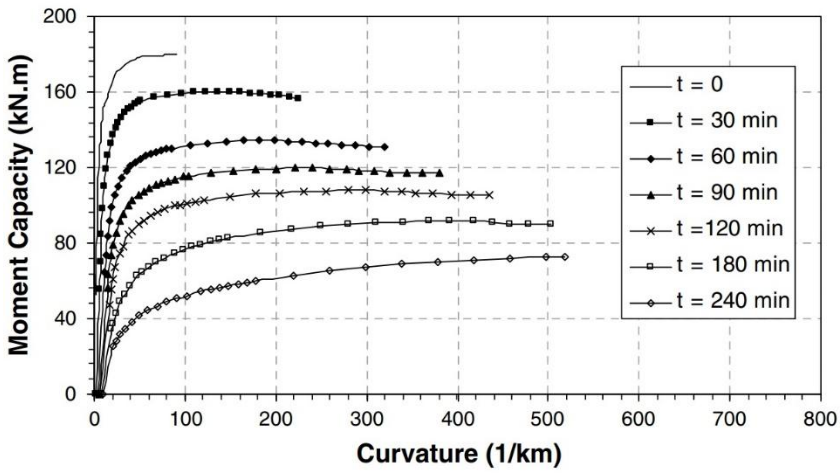

Figure-2.39: Moment-Curvature graph [20]

Based on the results of this study, the following conclusions were drawn:

1. There is limited information on the fire performance of reinforced concrete beams, especially under design fire and realistic loading scenarios.

2. The moment–curvature based macroscopic finite element model, presented in this study, is capable of predicting the fire behavior of reinforced concrete beams, in the entire range: from pre-fire stage to collapse stage, with an accuracy that is adequate for practical purposes. Using the model

the fire resistance of a reinforced concrete beam can be evaluated for any value of significant parameters such as beam length, type of aggregate, section dimensions, without the necessity of testing.

3. The limiting criterion, used for determining failure of a reinforced concrete beam exposed to fire, has significant influence on the fire resistance values. The conventional failure criterion such as limiting rebar temperature or strength consideration may not be conservative under some scenarios. The deflection and rate of deflection failure criterion should be considered in evaluating fire resistance of reinforced concrete beams.

2.3.15 Concrete test by Mundhada et al. (2015)

Mundhada et al. [21] cast ninety concrete cubes of 150 mm size, divided equally over three different grades of design mix concrete viz. M: 30, M: 25 & M: 20. After 28 days' curing & 24 hours' air drying, the cubes were subjected to different temperatures in the range of 200°C to 800°C, for two different exposure times viz. 1 hour & 2 hours in an electric furnace. The heated cubes were cooled at room temperature for 24 hours & then subjected to cube compressive strength test. Results revealed fairly robust performance up to 500°C, with strength coming down only slightly. Up to this stage, the fire affected structural members remain serviceable although the factor of safety would come down. Affected structure/ structural members would require minor repairs & patchwork to recuperate. At or after 650°C, the fall in concrete strength would be a cause for concern. Major retrofitting might be required. At or beyond 650°C, concrete stood completely decimated. The result was presented as shown in Figures 2.40 and 2.41.

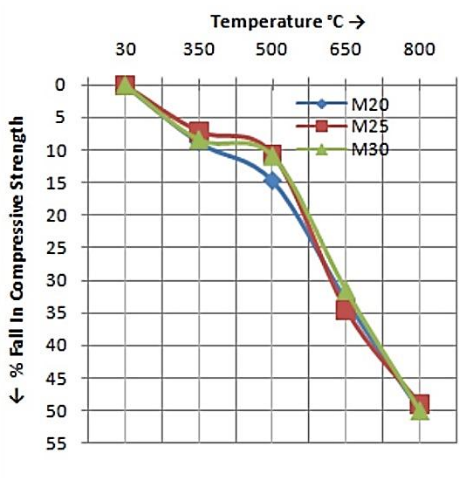

Figure-2.40: Fall in compressive strength after 1 hour [21]

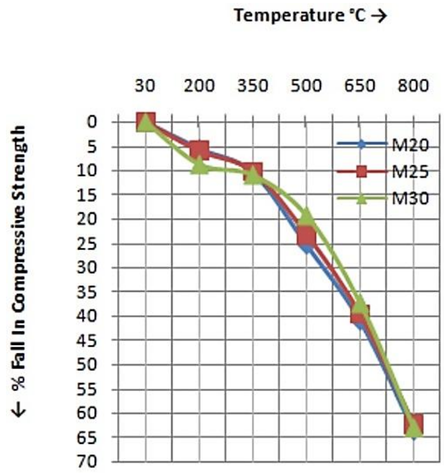

Figure-2.41: Fall in compressive strength after 2 hour [21]

Based on the results & their scrutiny, the following conclusions were drawn:

1. Up to 350°C, concrete remains almost unaffected in appearance & strength.
2. At 500°C, quality of concrete suffers slightly & strength too comes down. Structure/ structural members remain serviceable although the factor of safety comes down. Affected structure/ structural members will require minor repairs & patchwork to recuperate.
3. At or after 650°C, the fall in concrete quality & strength becomes a cause for concern. Major retrofitting might be required.
4. Beyond 650°C, concrete stands decimated on all accounts. Affected members/portion will require replacement.
5. Higher exposure time results in greater damage. This calls for active measures to limit exposure time.
6. Within the ambit of NSC (Normal strength concrete), higher grade concrete performs better in absolute terms.

2.3.16 Column test by Lee et al. (2015)

Lee et al. [22] tested high strength concrete columns exposed to high heat flux to clarify the reasons for explosive spalling. Small column shaped specimens (100x100x400mm) were made of 1000MPa compressive strength concrete. Two types of concrete mix designs were used: one with fibre reinforcement at 1.5kg/m^3 and other is without fibre reinforcements. The moisture content was adjusted by differing the curing conditions either in water or in air. Resultant moisture content was 2.7-4.2% by weight for specimens cured in air, 4.1-5.0% by weight for specimens cured in water. The conditioned specimens were heated either partially (by two surfaces, F2-specimens) or entirely (by four surfaces, F4-specimens). The degree of spalling, shape of failure surfaces and fragments were analyzed. By the analysis of volume and weight loss, the effects of partial / total heating and moisture content were examined.

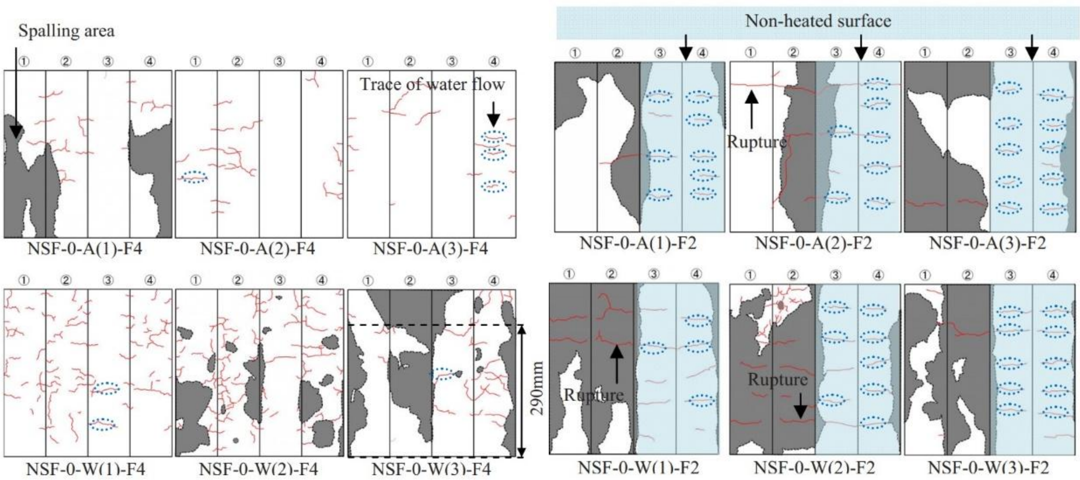

Figure-2.42: Planner figure of specimens without fibre after heating test [22]

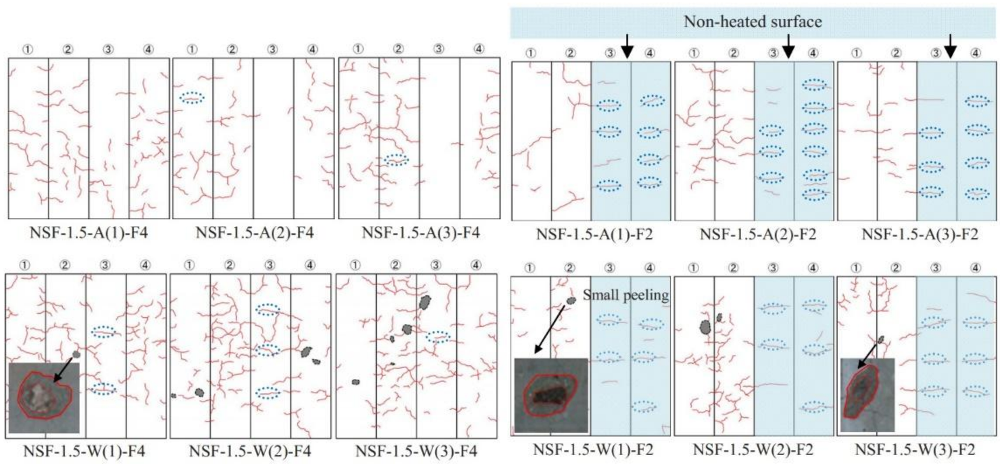

Figure-2.43: Planner figure of specimens with fibre after heating test [22]

Experimental results showed that the spalling of the F2-specimens covers a wide range compared to that of the F4-specimens. Many of the cracks in the F2-specimens occurred horizontally from heated surface to non-heated surface. Some of them are caused by the rupture of concrete (Figures 2.42 and 2.43).

The trace of the water flow was also observed on the cracks of non-heated surfaces. On the other hand, there were not large spallings in the fibre-reinforced concrete specimens. However, crack patterns occurred in the fibre-reinforced concrete F2-specimens were similar to that of F2-specimens without fibre. It was confirmed that there are small peelings where aggregates always exist in the center of peelings. It might be caused by the expansion of inner aggregates.

The followings are the findings of this research:

1. The crack, rupture and spalling are severe on partially heated specimens than the entirely heated specimens. As a quantitative terms, the volume loss, weight loss and spalling area are lager on partially heated specimens than entirely heated specimens. In this context, it can be clarified that the uneven heating would increase the spalling.

2. The effect of moisture content on spalling is not clear. However, volume loss and spalling area are slightly increased at more than 4% of moisture content in the entirely heated specimens. At large moisture contents, small peeling has occurred on the surface. The aggregate was found at the center of peeling. It could be considered that peelings are caused by expansion of aggregate close to surface.

3. Deep spalling took place at totally heated corner and partially heated corner. It was also found that the fragment shape differs according to the spalling location. The length/thickness ratio of fragments comes from totally heated corner and partially heated corner are larger than the ratio of fragments comes from middle of corner. And the length/width ratio is large for a fragment comes from totally heated corner.

2.4 Review on Past Studies

Fire test on concrete and RCC can be conducted in nine different ways and in two broad categories. Among these, the Idealized Test Methods possess six ways of testing which are relatively rigorous in nature, demanding sophisticated and complex instruments and three ways in the Common Tests Methods for testing, relatively flexible in nature. Twelve different experiments conducted have been reviewed in this chapter. Among these twelve tests, eight were material test, three were structural element tests and one was a full scale test on seven storied building.

2.4.1 Concrete material tests

The material tests were conducted on cylinders and cubes of different standard sizes. Six tests were Unstressed Residual Strength tests conducted by *Hertz* [8], *Hertz* [9] and *Felicetti et al.* [13] on HSC, *Morita et al.* [11], *Furumura et al.* [12] and *Noumowé et al.* [14] on NSC and HSC. *Castillo et al.* [7] conducted stressed and unstressed test on NSC and HSC and Hammer conducted unstressed strength test on HSC in 1995. Among all these *Hertz* [8], *Hertz* [9], *Hammer*, *Felicetti et al.* [13] and *Noumowé et al.* [14] used silica fume concrete for HSC. The observations on the material tests are summarized as:

1. *Castillo et al.* [7] observed almost similar pattern of strength loss for both NSC and HSC except HSC suffered initial strength loss from 100 to 300ºC followed by a strength recovery between 300 to 400ºC.

2. *Hertz* [8], *Hertz* [9] summarized that, silica fume concretes are likely to explode during heating, steel fiber do not resist explosion.

3. Hammer observed insignificant strength loss of samples in the experiment except strength regain occurred in sample without silica between 200 to 300 ºC and for silica contained samples between 300 to 450ºC, slightly better performance was observed in the samples without silica fume.

4. *Morita et al.* [11], *Furumura et al.* [12] observed regular and insignificant strength loss patterns of the samples except *Furumura et al.* [12] witnessed regain of strength between 100 to 200ºC.

5. *Felicetti et al.* [13] and *Noumowé et al.* [14] both tested siliceous concrete in which *Felicetti et al.* [13] observed similar reduction of strength and

modulus of elasticity for the two different HSC. *Noumowé et al.* [14] had no different observation in respect of the compressive strength of NSC and HSC but he observed that tensile strength of both the concrete were similar and almost linear with the increase of temperature in which HSC demonstrated almost 15% higher losses than the NSC. He also observed that modulus of elasticity of HSC remained 10% to 25% higher than that of NSC but the NSC was more porous as the temperature increased up to the last.

2.4.2 Element and full scale test

Among three element tests there were two beam tests, one by *Jensen et al.* [15] and the other by *Sanjayan et al.* [16] and one column test by *Diederichs et al.* [17]. A full scale fire test was conducted by *Bailey* [10] on a seven storied building.

In addition to material tests, *Felicetti et al.* [13] also tested reinforced and unreinforced deep beams of siliceous aggregates for bending and shear. *Jensen et al.* [15] tested reinforced HSC with difference in aggregate types and *Sanjayan et al.* [16] tested T-beams of NSC and HSC with silica fume.

1. *Felicetti et al.* [13] concluded that for RC beams, the flexural capacity is governed primarily by the steel area, not the concrete strength.

2. *Jensen et al.* [15] observed sever spalling exposing reinforcements in HSC beams with lightweight aggregate, spalling without exposing reinforcement for the NSC beams and presence of fiber drastically reduces the spalling.

3. *Sanjayan et al.* [16] observed HSC appeared to more prone to spalling than NSC and 75 mm clear cover suffered the spalling but no spalling occurred in 25 mm clear cover. He also observed higher level of moisture content in HSC than NSC.

4. *Diederichs et al.* [17] in the HSC column test observed that columns collapsed due failure of the compressive strength, he further indicated that the use of capillary forming fibres help the potential for spalling in HSC column.

5. *Bailey* [10], in his full scale structural test suggested about occurrence of compressive membrane action in the flat slab for small displacement only but for large displacement, tensile membrane action occurs that effects less in flat slab. He mentioned sufficient concrete cover helps the reinforcing bars strength to withstand in supporting the load against tensile membrane action. He observed significant lateral displacement of the column due to the displacement of the heated slab and suggested proper apprehension of the designer about the columns movement under fire incidents.

2.5 Summary

The effect of fire on both high strength and normal strength concrete were tested for years to get a generalized constitutive law. Though a full scale test was conducted [9], it partially imitated the real scenario since the structure was not loaded. Loaded concrete beams and columns were simulated but their number is very little. For full understanding of the effect of fire, every parameters combined with every possible combination must be analyzed in loaded condition numerically and cross checked by some field tests.

Chapter 3
RESEARCH METHODOLOGY

3.1 Introduction

The research is outlined to simulate the behaviour of structurally loaded reinforced concrete beams subjected to high temperatures for a definite period of time. Since the fire hazard scenario was modelled with controlled parameters of material properties, the simulation process allowed to examine the results in Stress Rate Controlled Steady State Idealized Test condition in this research work. Detailed studies were performed on thermally loaded members by exerting loads at a uniform rate and without any load at all.

3.2 Material Properties

The numerical modeling in this research involves two materials: Concrete and Reinforcing Steel. Both of the fundamental materials were modelled by the thermal and structural characteristics defined in BS-EN 1992-1-2:2004 as stated in Appendix-A. For accurate simulation of structural components, the whole stress-strain curve at a certain temperature has been defined in the model. The mechanical and thermal analysis was done by using ANSYS Parametric Design Language (APDL) of the ANSYS v14.5 software with the help of its underlying structural principals as described in brief in the Appendix-B. The detailed material properties used in the study is presented in the subsequent paragraphs.

3.2.1 Concrete

Concrete is a composite material composed of fine and coarse aggregate bonded together with a fluid cement (cement paste) that hardens over time. It is distinguished from other, non-cementitious types of concrete all binding some form of aggregate together, including asphalt concrete with a bitumen binder, which is frequently used for road surfaces, and polymer concretes that use polymers as a binder. The main properties of concrete dependent on temperatures are density, specific heat, thermal conductivity, thermal elongation/ strain, the stress-strain curve etc. The general and structural properties defined in the modelling under consideration of high temperature are stated in the following tables. As defined in Table 3.1, the density of concrete reduces with the elevation of temperature. The thermal conductivity also reduces with the increase in temperature as shown in Table 3.2. But marked increase in specific heat and thermal elongation/ strain is noticed with rise in temperature as depicted in Tables 3.3 and 3.4, respectively.

Table-3.1: Density of Concrete at different Temperatures

Temperature (°C)	Density (kg/m³)
0	2400
115	2400
200	2352
400	2280
1200	2112

Table-3.2: Thermal Conductivity of Concrete at different Temperatures

Temperature (°C)	Thermal Conductivity ($Wm^{-1}K^{-1}$)
0	2.000
100	1.7656
400	1.1908
700	0.8086
1000	0.6190
1200	0.5996

Table-3.3: Specific Heat of Concrete with 1.5% moisture at different Temperatures

Temperature (°C)	Specific Heat ($JKg^{-1}K^{-1}$)
0	900
100	900
101	1470
115	1470
200	1000
400	1100
1200	1100

Table-3.4: Thermal Elongation of Concrete at different Temperatures

Temperature (°C)	Elongation ($\Delta L/L_0$)
20	1.84×10^{-7}
250	2.43×10^{-3}
500	7.20×10^{-3}
700	1.40×10^{-2}
1200	1.40×10^{-2}

The stress-strain constitutive law of concrete at elevated temperatures are defined in the models as per Article-3.2.2 of BS-EN 1992-1-2:2004. In the analytical model, concrete with 3 (Three) different compressive strength is considered, *i.e.* 28 MPa, 35

MPa and 42 MPa. The respective constitutive laws of concrete were set according to the guideline of BS-EN 1992-1-2:2004 as stated in Tables 3.5 to 3.10.

Table-3.5: Mechanical Properties of 28MPa Concrete at different Temperatures

Temperature (°C)	$f_{c,\theta}$ (MPa)	$E_{c,\theta}$ (GPa)	$f_{cr,\theta}$ (MPa)	$G_{c,\theta}$ (GPa)
20	28.00	24.87	3.28	10.36
100	28.00	24.87	3.28	10.36
300	23.80	22.93	3.02	9.55
600	12.60	16.68	2.20	6.95
900	2.20	7.03	0.93	2.93
1200	0.00	0.00	0.00	0.00

Table-3.6: Stress-Strain Properties of 28MPa Concrete at different Temperatures

T = 20°C		T = 100°C		T = 300°C		T = 600°C		T = 900°C	
Stain	Stress (MPa)	Stain	Stress (MPa)	Stain	Stress (MPa)	Stain	Stress (MPa)	Stain	Stress (MPa)
0.0000	0.000	0.0000	0.000	0.0000	0.000	0.0000	0.000	0.0000	0.000
0.0010	16.279	0.0008	8.367	0.0014	7.112	0.0050	3.765	0.0050	0.669
0.0015	22.744	0.0016	16.279	0.0042	19.332	0.0150	10.235	0.0150	1.819
0.0020	26.752	0.0028	25.096	0.0056	22.739	0.0175	11.293	0.0200	2.140
0.0023	27.702	0.0036	27.702	0.0063	23.547	0.0225	12.466	0.0225	2.216
0.0025	28.000	0.0040	28.000	0.0070	23.800	0.0250	12.600	0.0250	2.240
0.0200	0.000	0.0225	0.000	0.0275	0.000	0.0350	0.000	0.0425	0.000

Table-3.7: Mechanical Properties of 35MPa Concrete at different Temperatures

Temperature (°C)	$f_{c,\theta}$ (MPa)	$E_{c,\theta}$ (GPa)	$f_{cr,\theta}$ (MPa)	$G_{c,\theta}$ (GPa)
20	35.00	27.81	3.67	11.59
100	35.00	27.81	3.67	11.59
300	29.80	25.64	3.38	10.68
600	15.80	18.65	2.46	7.77
900	2.80	7.87	1.04	3.28
1200	0.00	0.00	0.00	0.00

Table-3.8: Stress-Strain Properties of 35MPa Concrete at different Temperatures

T = 20°C		T = 100°C		T = 300°C		T = 600°C		T = 900°C	
Stain	Stress (MPa)	Stain	Stress (MPa)	Stain	Stress (MPa)	Stain	Stress (MPa)	Stain	Stress (MPa)
0.0000	0.000	0.0000	0.000	0.0000	0.000	0.0000	0.000	0.0000	0.000
0.0010	20.349	0.0008	10.458	0.0014	8.889	0.0050	4.706	0.0050	0.837
0.0015	28.430	0.0016	20.349	0.0042	24.165	0.0150	12.793	0.0150	2.274
0.0020	33.439	0.0028	31.370	0.0056	28.424	0.0175	14.167	0.0200	2.675

0.0023	34.628	0.0036	34.628	0.0063	19.434	0.0225	15.583	0.0225	2.770
0.0025	35.000	0.0040	35.000	0.0070	29.750	0.0250	15.750	0.0250	2.800
0.0200	0.000	0.0225	0.000	0.0275	0.000	0.0350	0.000	0.0425	0.000

Table-3.9: Mechanical Properties of 42MPa Concrete at different Temperatures

Temperature (°C)	$f_{c,\theta}$ (MPa)	$E_{c,\theta}$ (GPa)	$f_{cr,\theta}$ (MPa)	$G_{c,\theta}$ (GPa)
20	42.00	30.46	4.02	12.69
100	42.00	30.46	4.02	12.69
300	35.70	28.08	3.70	11.70
600	18.90	20.43	2.70	8.51
900	3.40	8.62	1.14	3.59
1200	0.00	0.00	0.00	0.00

Table-3.10: Stress-Strain Properties of 42MPa Concrete at different Temperatures

T = 20°C		T = 100°C		T = 300°C		T = 600°C		T = 900°C	
Stain	Stress (MPa)	Stain	Stress (MPa)	Stain	Stress (MPa)	Stain	Stress (MPa)	Stain	Stress (MPa)
0.0000	0.000	0.0000	0.000	0.0000	0.000	0.0000	0.000	0.0000	0.000
0.0010	24.419	0.0008	12.550	0.0014	10.667	0.0050	5.647	0.0050	1.004
0.0015	34.116	0.0016	24.419	0.0042	28.998	0.0150	15.352	0.0150	2.729
0.0020	40.127	0.0028	37.644	0.0056	34.108	0.0175	16.940	0.0200	3.210
0.0023	41.554	0.0036	41.554	0.0063	35.321	0.0225	18.699	0.0225	3.324
0.0025	42.000	0.0040	42.000	0.0070	35.700	0.0250	18.900	0.0250	3.360
0.0200	0.000	0.0225	0.000	0.0275	0.000	0.0350	0.000	0.0425	0.000

The values of thermal conductivity, density and specific heat were input in the thermal module and those of thermal elongation/ strain and stress-strain points were defined in the subsequent structural module.

3.2.2 Reinforcing steel

Reinforcing steel is a steel bar or mesh of steel wires used as a tension device in reinforced concrete and reinforced masonry structures to strengthen and aid the concrete under tension. Concrete is strong under compression, but has weak tensile strength. Reinforcing bar significantly increases the tensile strength of the structure. The thermal elongation/ strain and the stress-strain curve are the main properties of reinforcing steel susceptible to change with the increase in temperature as shown in Table 3.11.

The stress-strain constitutive law of reinforcing steel at elevated temperatures are defined in the models as per Article-3.2.3 of BS-EN 1992-1-2:2004, where different reduction factors are suggested for different temperatures, showing gradually declining trend with higher temperatures.

Table-3.11: Thermal Elongation of Reinforcing Steel at different Temperatures

Temperature (°C)	Elongation ($\Delta L/L_0$)
20	$1.55x10^{-20}$
250	$3.01x10^{-3}$
500	$6.76x10^{-3}$
750	$1.10x10^{-2}$
860	$1.10x10^{-2}$
1200	$1.78x10^{-2}$

At 1200°C of temperature, the steel loses its strength completely. In the analytical model, reinforcing steel with 2 (Two) different yield strength is considered, *i.e.* 400 MPa and 500 MPa. The respective constitutive laws of steel were set according to the guideline of BS-EN 1992-1-2:2004 as stated in Tables 3.12 to 3.15.

Table-3.12: Mechanical Properties of 400MPa Steel at different Temperatures

Temperature (°C)	$f_{sy,\theta}$ (MPa)	$E_{s,\theta}$ (GPa)	$f_{sp,\theta}$ (MPa)	$\varepsilon_{sp,\theta}$	$G_{s,\theta}$ (GPa)
20	400.00	200.00	400.00	0.0020	76.92
100	400.00	200.00	400.00	0.0020	76.92
300	400.00	160.00	244.00	0.0015	61.54
600	188.00	62.00	72.00	0.0012	23.85
900	24.00	14.00	16.00	0.0011	5.38
1200	0.00	0.00	0.00	0.0000	0.00

Table-3.13: Stress-Strain Properties of 400MPa Steel at different Temperatures

T = 20°C		T = 100°C		T = 300°C		T = 600°C		T = 900°C	
Stain	Stress (MPa)	Stain	Stress (MPa)	Stain	Stress (MPa)	Stain	Stress (MPa)	Stain	Stress (MPa)
0.0000	0.00	0.0000	0.00	0.0000	0.00	0.0000	0.00	0.0000	0.00
0.0020	400.00	0.0020	400.00	0.0015	244.00	0.0012	72.00	0.0011	16.00
0.0050	400.00	0.0050	400.00	0.0050	331.53	0.0050	137.33	0.0050	20.75
0.0150	400.00	0.0150	400.00	0.0150	393.85	0.0150	183.38	0.0150	23.70
0.0200	400.00	0.0200	400.00	0.0200	400.00	0.0200	188.00	0.0200	24.00
0.1500	400.00	0.1500	400.00	0.1500	400.00	0.1500	188.00	0.1500	24.00
0.2000	0.00	0.2000	0.00	0.2000	0.00	0.2000	0.00	0.2000	0.00

Table-3.14: Mechanical Properties of 500MPa Steel at different Temperatures

Temperature (°C)	$f_{sy,\theta}$ (MPa)	$E_{s,\theta}$ (GPa)	$f_{sp,\theta}$ (MPa)	$\varepsilon_{sp,\theta}$	$G_{s,\theta}$ (GPa)
20	500.00	200.00	500.00	0.0025	76.92
100	500.00	200.00	500.00	0.0025	76.92
300	500.00	160.00	305.00	0.0019	61.54

600	235.00	62.00	90.00	0.0015	23.85
900	30.00	14.00	20.00	0.0014	5.38
1200	0.00	0.00	0.00	0.0000	0.00

Table-3.15: Stress-Strain Properties of 500MPa Steel at different Temperatures

T = 20°C		T = 100°C		T = 300°C		T = 600°C		T = 900°C	
Stain	Stress (MPa)	Stain	Stress (MPa)	Stain	Stress (MPa)	Stain	Stress (MPa)	Stain	Stress (MPa)
0.0000	0.00	0.0000	0.00	0.0000	0.00	0.0000	0.00	0.0000	0.00
0.0025	500.00	0.0025	500.00	0.0019	305.00	0.0015	90.00	0.0014	20.00
0.0050	500.00	0.0050	500.00	0.0050	408.03	0.0050	167.17	0.0050	25.73
0.0150	500.00	0.0150	500.00	0.0150	491.86	0.0150	228.86	0.0150	29.62
0.0200	500.00	0.0200	500.00	0.0200	500.00	0.0200	235.00	0.0200	30.00
0.1500	500.00	0.1500	500.00	0.1500	500.00	0.1500	235.00	0.1500	30.00
0.2000	0.00	0.2000	0.00	0.2000	0.00	0.2000	0.00	0.2000	0.00

The values of thermal elongation/ strain and stress-strain points were defined in the subsequent structural module of reinforcing steel.

3.3 Member Profiles

The thermal effect on beams are done for 2 (Two) types of sections, *i.e.* 300mm x 400mm and 300mm x 600mm. The 300mm x 400mm beams are modelled with single type of reinforcement ratio but with 2 (Two) values for concrete cover, *i.e.* 50mm and 75mm. Figure 3.1 and Table 3.16 summarizes the input parameters used in the numerical models.

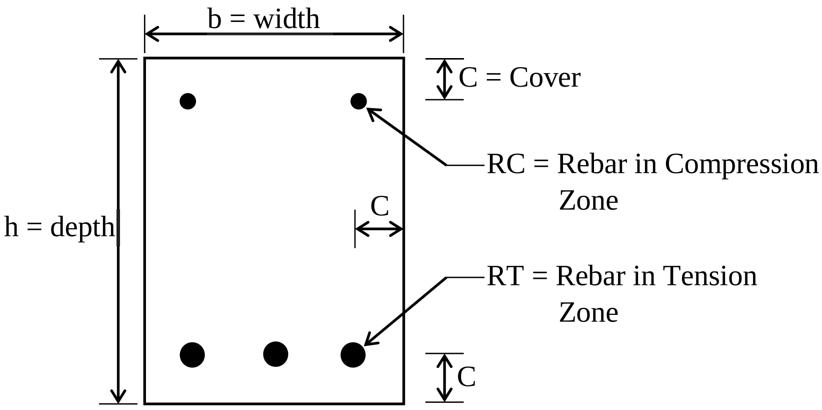

Figure-3.1: A typical beam section with parameters

Table-3.16: Sectional Properties of Reinforced Concrete Beams

b x h (mm)	Span (m)	C (mm)	RC	RT	f_y (MPa)	f_c' (MPa)	ρ
300x400	6.00	50.00	2-Ø12mm	3-Ø20mm	400/ 500	28/ 35/ 42	0.0090
300x400	6.00	75.00	2-Ø12mm	3-Ø20mm	400/	28/ 35/	0.0090

					500	42	
300x600	6.00	50.00	2-Ø12mm	3-Ø16mm	400	28	0.0037
300x600	6.00	50.00	2-Ø12mm	3-Ø20mm	400	28	0.0057
300x600	6.00	50.00	2-Ø12mm	3-Ø36mm	400	28	0.0185

Table-3.16: Sectional Properties of Reinforced Concrete Beams (Continued)

b x h (mm)	Span (m)	C (mm)	RC	RT	f_y (MPa)	f_c' (MPa)	ρ
300x600	6.00	50.00	2-Ø12mm	3-Ø17mm	400	42	0.0041
300x600	6.00	50.00	2-Ø12mm	3-Ø20mm	400	42	0.0057
300x600	6.00	50.00	2-Ø12mm	3-Ø41mm	400	42	0.0240

* N.B.: ρ = reinforcement ratio

The beams with 300mm x 400mm were modelled to check the effect of temperature without altering the reinforcement ratio, while beams 300mm x 600mm were modelled to check the temperature effect with varying reinforcement ratio.

A simple portal frame was modelled with a beam of 300mm x 400mm spanning 6.00m and two 4.00m high columns of 300mm x 400mm. In the portal frame model, the beam was reinforced with 3-Ø20mm tensile and 2-Ø12mm compressive rebar; while columns were reinforced with 4-Ø20mm rebar in each one.

3.4 Application of Temperature

The relevant design fire scenarios and the associated design fires should be determined on the basis of a fire risk assessment. The temperature in the thermal module was increased gradually to the target temperature following the standard time-temperature curve as per guidelines of Article-3.2.1 of BS-EN 1992-1-2:2002. Then the temperature of a particular model was kept constant for the desired time period as shown in Figures 3.2 to 3.4. The subsequent nodal temperature throughout the section was recorded.

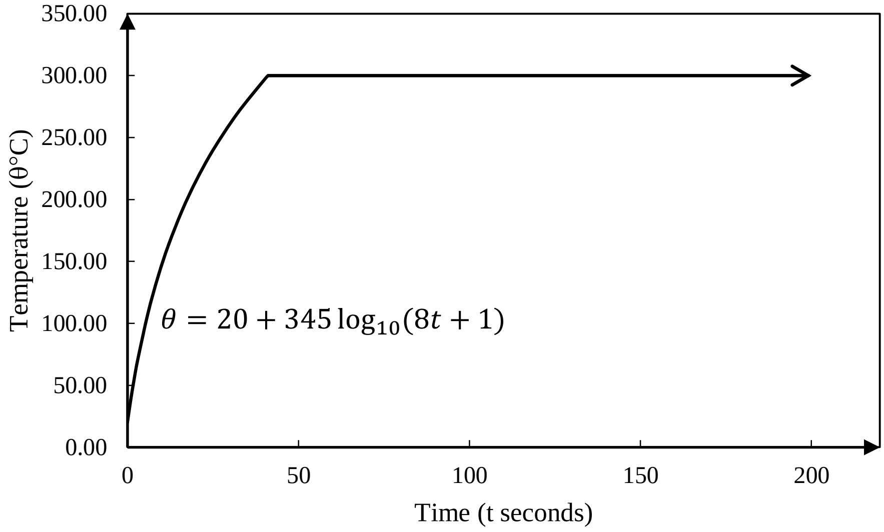

Figure-3.2: Temperature increase over time to attain 300°C

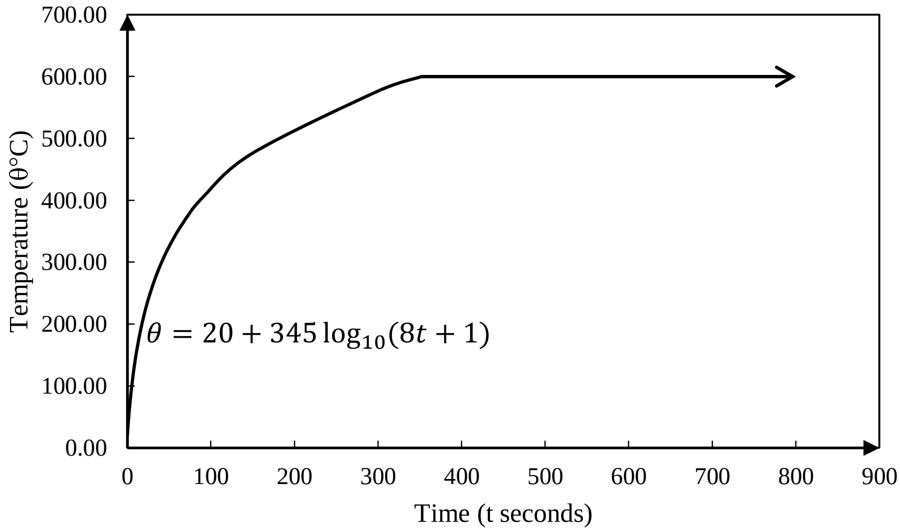

Figure-3.3: Temperature increase over time to attain 600°C

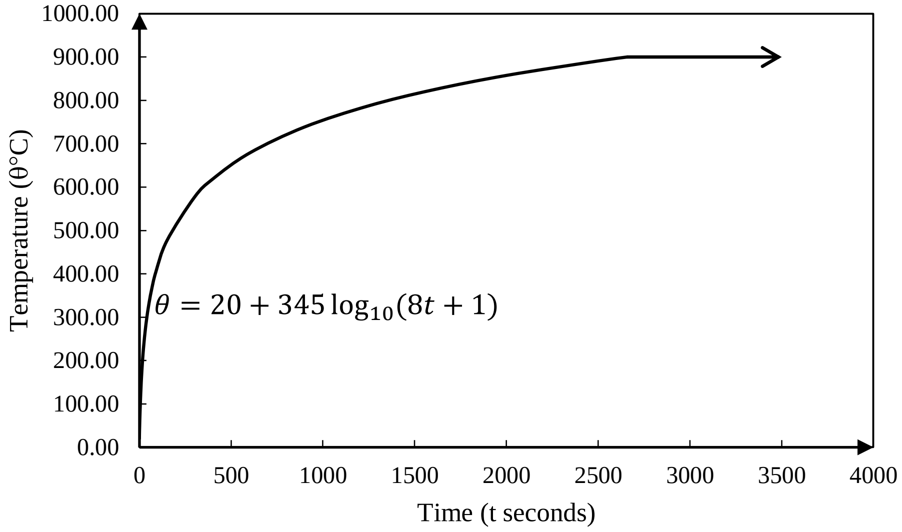

Figure-3.4: Temperature increase over time to attain 900°C

Temperature all around the longitudinal section of beam was applied in accordance with the Figures 3.2 to 3.4. In case of portal frame, all sides of the portal accept the joint were heated following the same pattern.

3.5 Validation of Model

The numerical modelling procedures was checked by comparing the obtained temperature profiles from a 160mm x 300mm beam heated in accordance with the standard temperature-time equation as stated in Article-3.2.1 of BS-EN 1992-1-2:2002. The result from the subsequent model was plot in contour diagram and was compared to the temperature profiles given in Appendix-A of BS-EN 1992-1-2:2004. In Figures 3.5 to 3.7, the result from the simulation and the profiles from the code are presented for comparison.

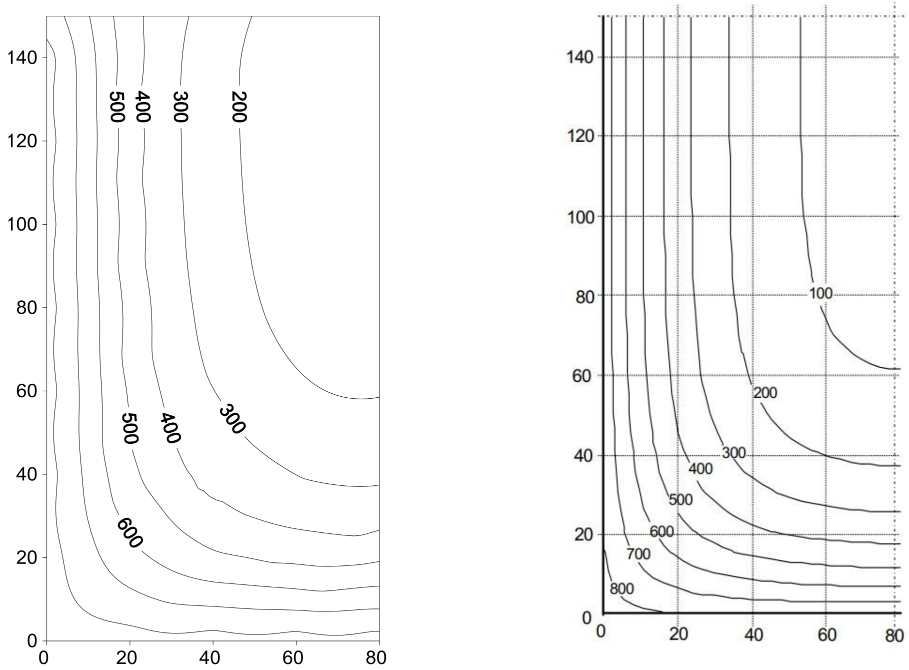

(a) From Model *(b) From BS-EN 1992-1-2:2004*

Figure-3.5: Temperature profiles of a 160mm x 300mm beam after 30minutes of burning

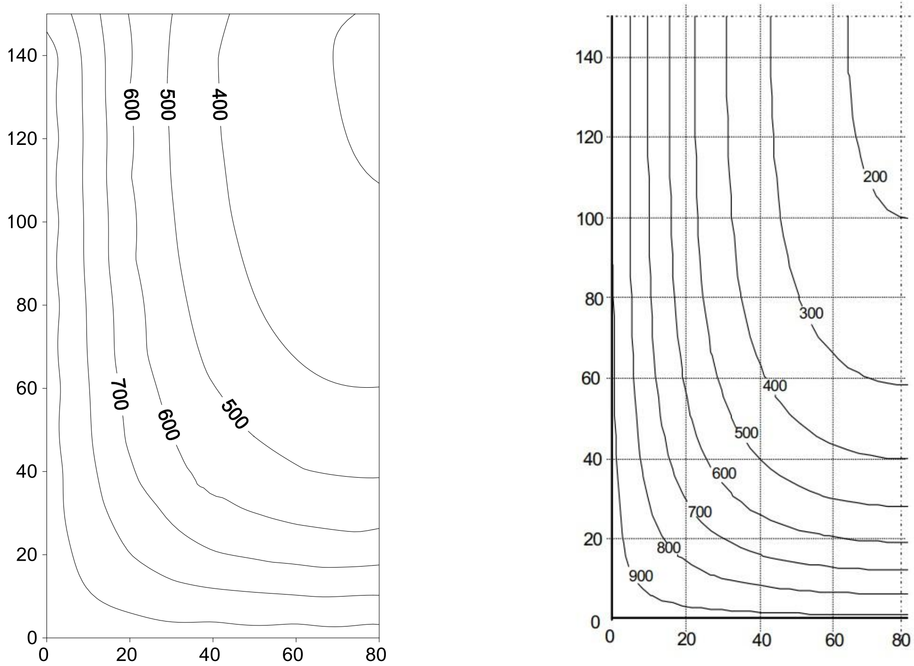

(a) From Model *(b) From BS-EN 1992-1-2:2004*

Figure-3.6: Temperature profiles of a 160mm x 300mm beam after 60minutes of burning

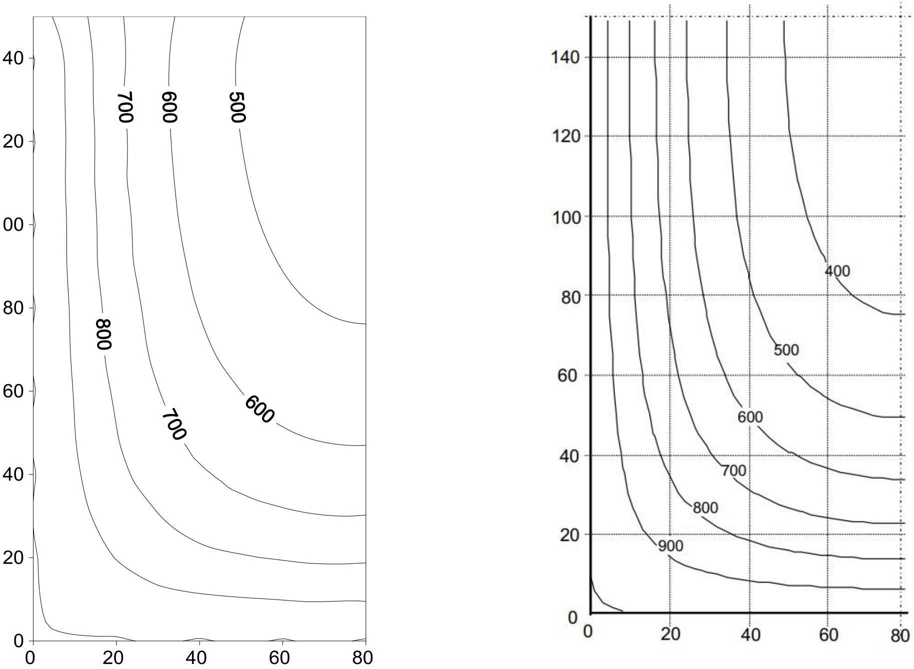

(a) From Model *(b) From BS-EN 1992-1-2:2004*

Figure-3.7: Temperature profiles of a 160mm x 300mm beam after 90minutes of burning

From Figures 3.5 to 3.7, it is clear that the temperature profile found in the analytical modelling is nearly similar to that from the code BS-EN 1992-1-2:2004. Though a small deviation from the code was observed, the model was considered okay for further simulation since the temperatures found from the simulation were more conservative than those from the code.

3.6 Summary

The numerical modelling was done with carefully chosen values and properties from international code. The general properties and mechanical properties of material *i.e.* concrete and reinforcements were selected with reasonable interpolation of data found in code. Since the temperature profiles found in the current method is more conservative than that of the code, it is safe to assume the parametric analysis can be advanced and safely recommended for further studies.

Chapter 4
RESULTS AND DISCUSSION

4.1 Introduction

The effect of fire on reinforced concrete members was tested in this research by numerical modelling of beams and a simple portal with varying sets of strength, rebar percentage, sectional dimensions and temperature duration as described in Chapter 4 of this report. For any definite beam section, 3 (Three) temperature models with 300°C, 600°C and 900°C were performed in ANSYS v14.5. The nodal temperature data was then transferred to the structural analysis and simultaneous structural loads were applied to obtain the results. The obtained results were plotted with appropriate parameters in SURFER v13, a three-dimensional mapping software, to find the contour variations of data.

4.2 Results of Beam Models

In this parametric study of beam, since the material strength, *i.e.* steel strength and concrete strength, cover dimension, temperature, duration of burning and reinforcement ratios were used as input parameters, all the obtained results were presented graphically against each of these parameters. Effects of each parameter on results recorded, *i.e.* the compressive and tensile stress of both steel and concrete, are discussed in these sections.

4.2.1 Temperature profiles

The numerical modelling of fire incident was done following the standard time-temperature model as described in Article-3.4 of this report. Rising temperature pattern was applied up to target temperature, but a steady temperature was maintained then for the desired duration of burning. The temperature profiles are formed from the nodal temperature data throughout the section. Temperature profiles at 300°C after a duration of 0, 60 and 120 minutes for 300mm x 400mm beam with 50mm cover are presented in Figure 4.1.

Temperature distribution throughout the cross section at the time of reaching the outside temperature of 300°C is shown in Figure 4.1(a). At this point:

i. Temperature profile only infiltrate about 25mm inside the beam section.

ii. The reinforcement region does not show any rise in temperature yet.

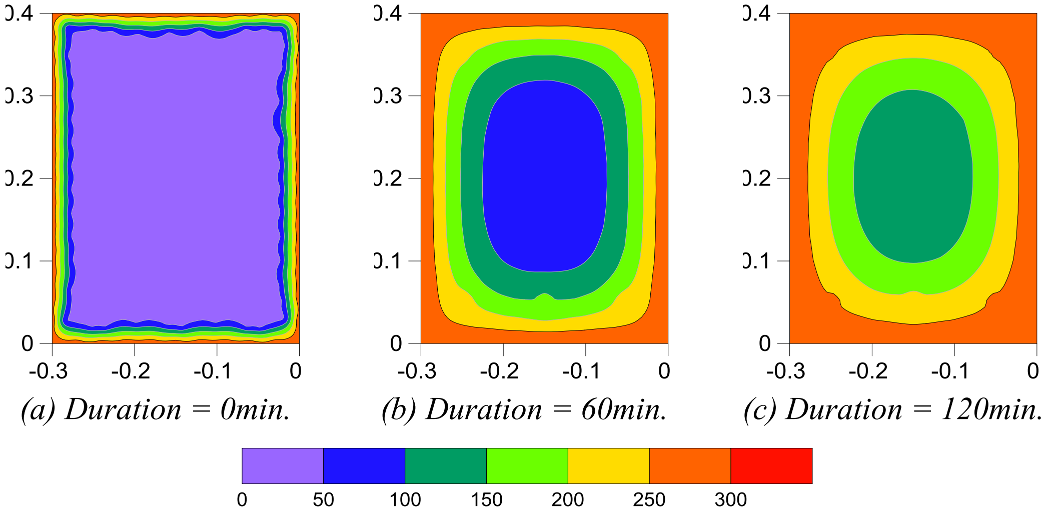

Figure-4.1: Temperature profiles for beam (size: 300mm x 400mm, cover = 50mm) for applied temperature of 300°C

After 60minutes of burning in 300°C, significant changes are noticed:

i. Temperature profile propagates throughout the entire section. The core temperature is 50°C.

ii. The reinforcement of both tension and compression zone shows temperature of 150°C to 250°C.

After 120minutes of burning in 300°C, the scenario is more severe:

i. Temperature profile propagates violently throughout the entire section. The core temperature is about 150°C.

ii. The reinforcement of both tension and compression zone shows temperature of 250°C to 300°C.

More graphical presentation of temperature profiles with different sectional properties as well as temperature properties are shown in Article-C.2 of Appendix-C in this report.

4.2.2 Effect of duration of burning

The target temperatures are fixed for 4 (Four) different duration up to 120 minutes to observe its effect. A detailed discussions on the effect of covers is outlined here comparing the results obtained in the numerous models performed in this research.

A. Effect on Compressive Stress of Concrete

The flexural compressive stress was obtained at the maximum loading at different duration of burning for same temperature with varying steel strength and concrete strength. The compressive stress of concrete beam at maximum possible loads is obtained from the compression zone of the concrete. The resulting compressive force acts as one force of the couple. The higher the couple force, the more the section is capable of resisting the flexural loads. The compressive stress of concrete found in the models are graphed below in Figures 4.2 and 4.3.

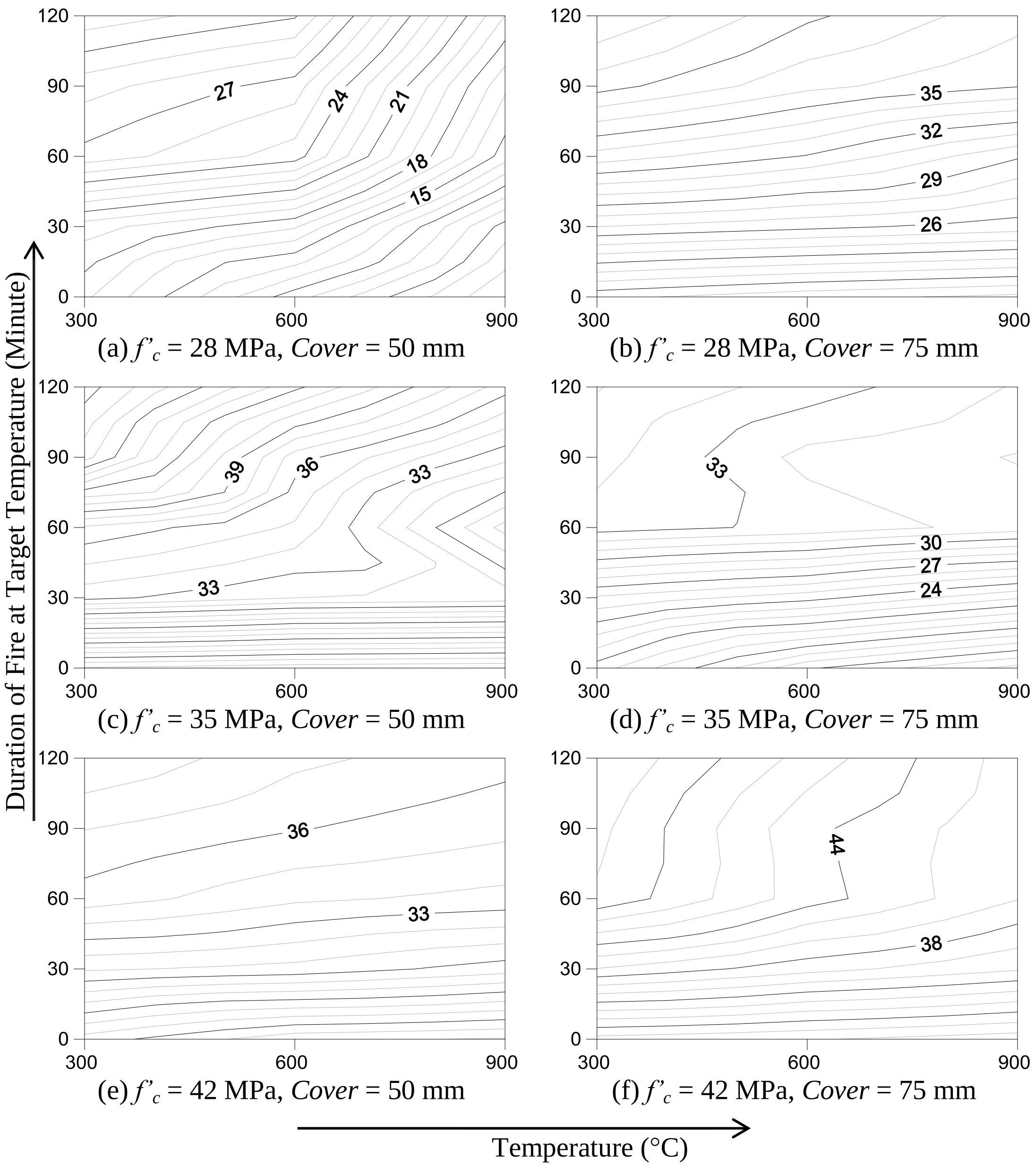

Figure-4.2: Compressive stress (MPa) variation in concrete at different temperature and duration of fire for F_y = 400 MPa

In Figure 4.2, steel yield strength of 400MPa is used and in Figure 4.3, steel yield strength of 500MPa is used. For each steel category and temperature, values of compressive stress of concrete are extracted and plotted for same set of steel, concrete and cover dimension.

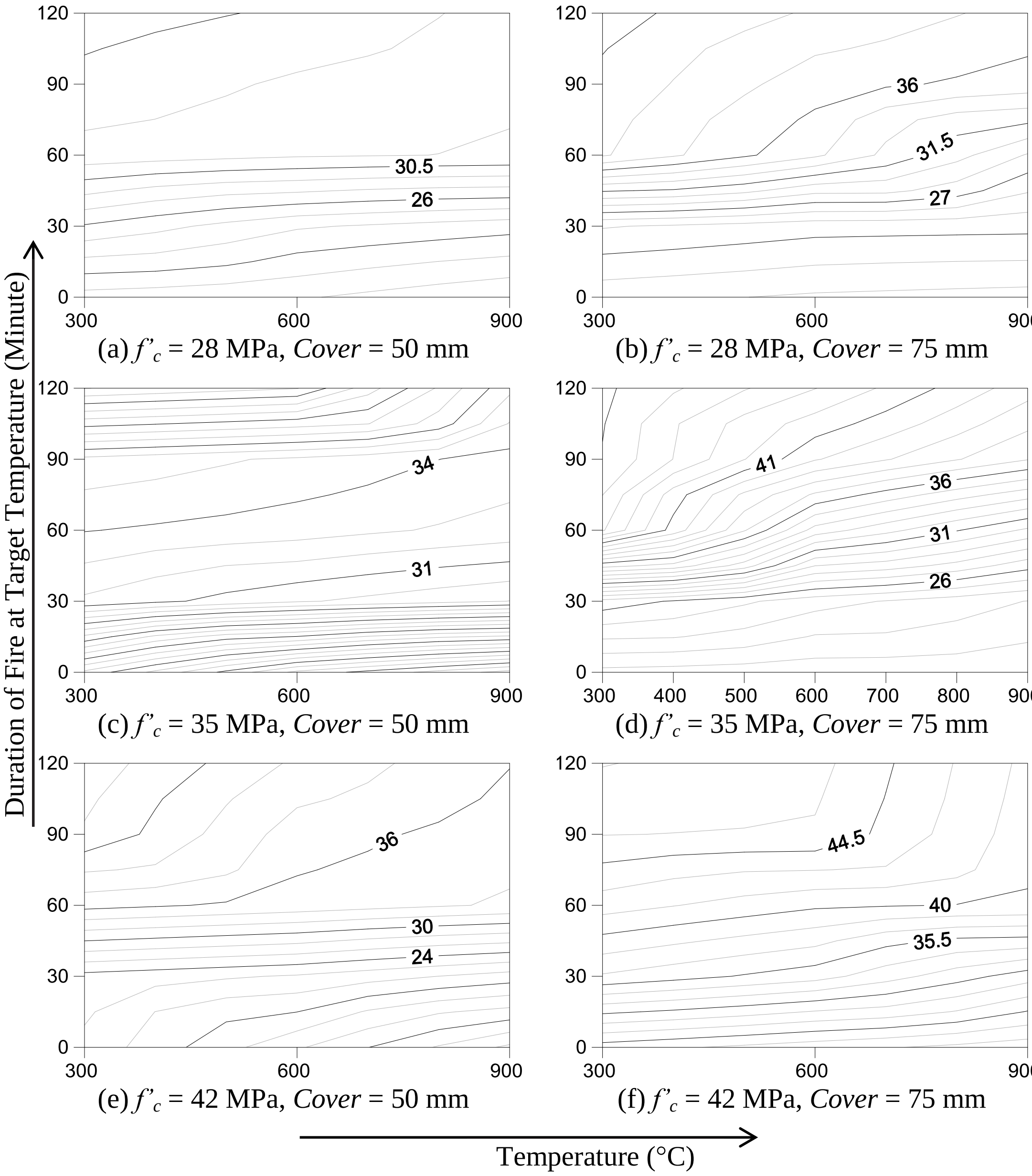

Figure-4.3: Compressive stress (MPa) variation in concrete at different temperature and duration of fire for F_y = 500 MPa

From Figures 4.2 and 4.3, the following discussions are outlined:

i. For same steel strength, concrete strength and concrete cover to steel, the compressive stress of concrete increases with the increase in duration of burning. This phenomena occurred since the concrete is stressed more with temperature effect as duration increases. The concrete in compression thus need to counteract more stress developed from the thermal effect, hence, showed a rising compressive stress trends over duration of burning.

ii. The compressive stress of concrete increases at a faster rate in first 60 minutes of burning.

B. Effect on Tensile Stress of Concrete

The tensile stress in concrete was obtained at the maximum loading at different duration of burning for same temperature with varying steel strength and concrete strength. In Figure 4.4, steel yield strength of 400MPa is used and in Figure 4.5, steel yield strength of 500MPa is used. For each steel category and temperature, values of compressive stress of concrete are extracted and plotted for same set of steel, concrete and cover dimension.

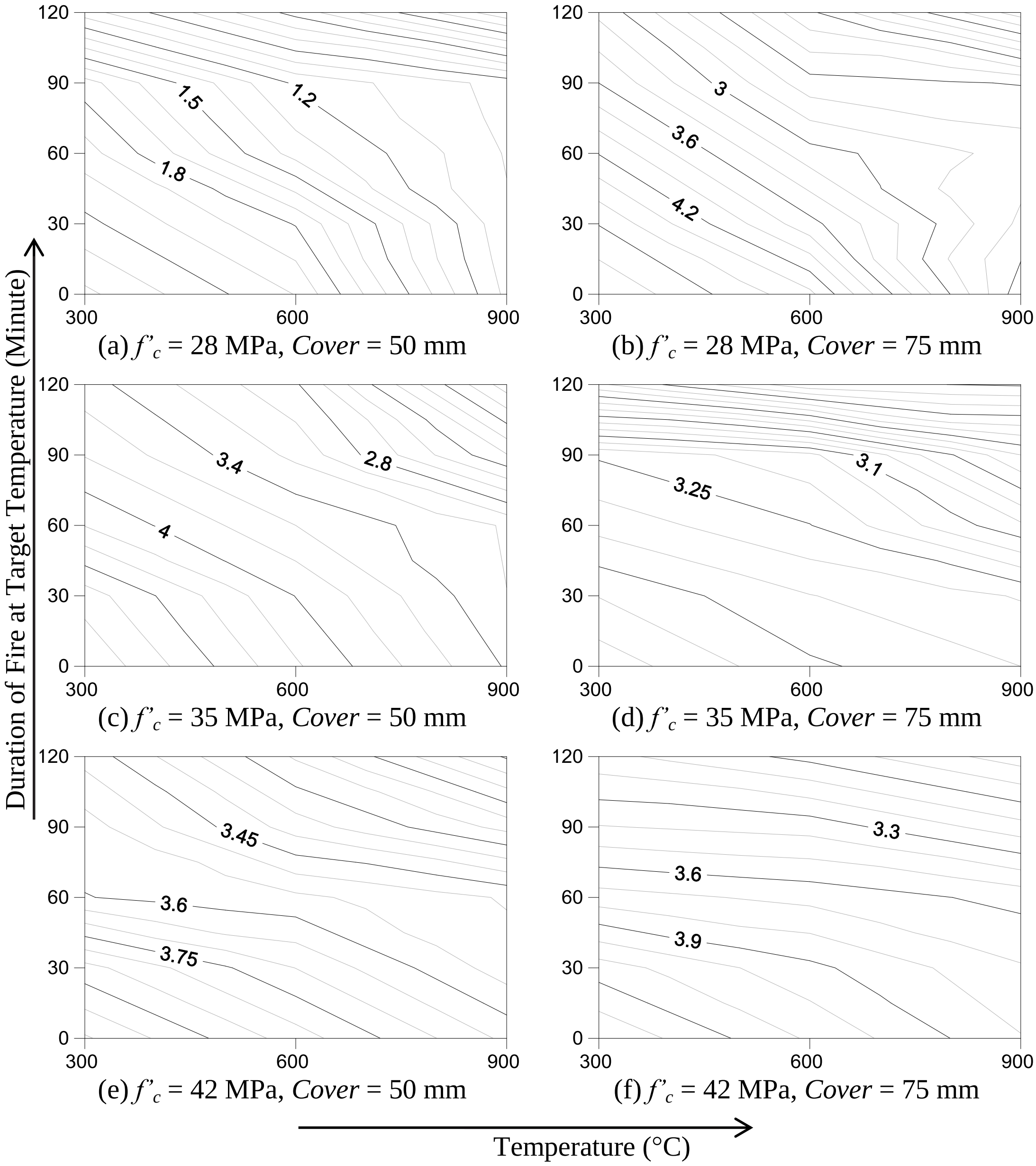

Figure-4.4: Tensile stress (MPa) variation in concrete at different temperature and duration of fire for F_y = 400 MPa

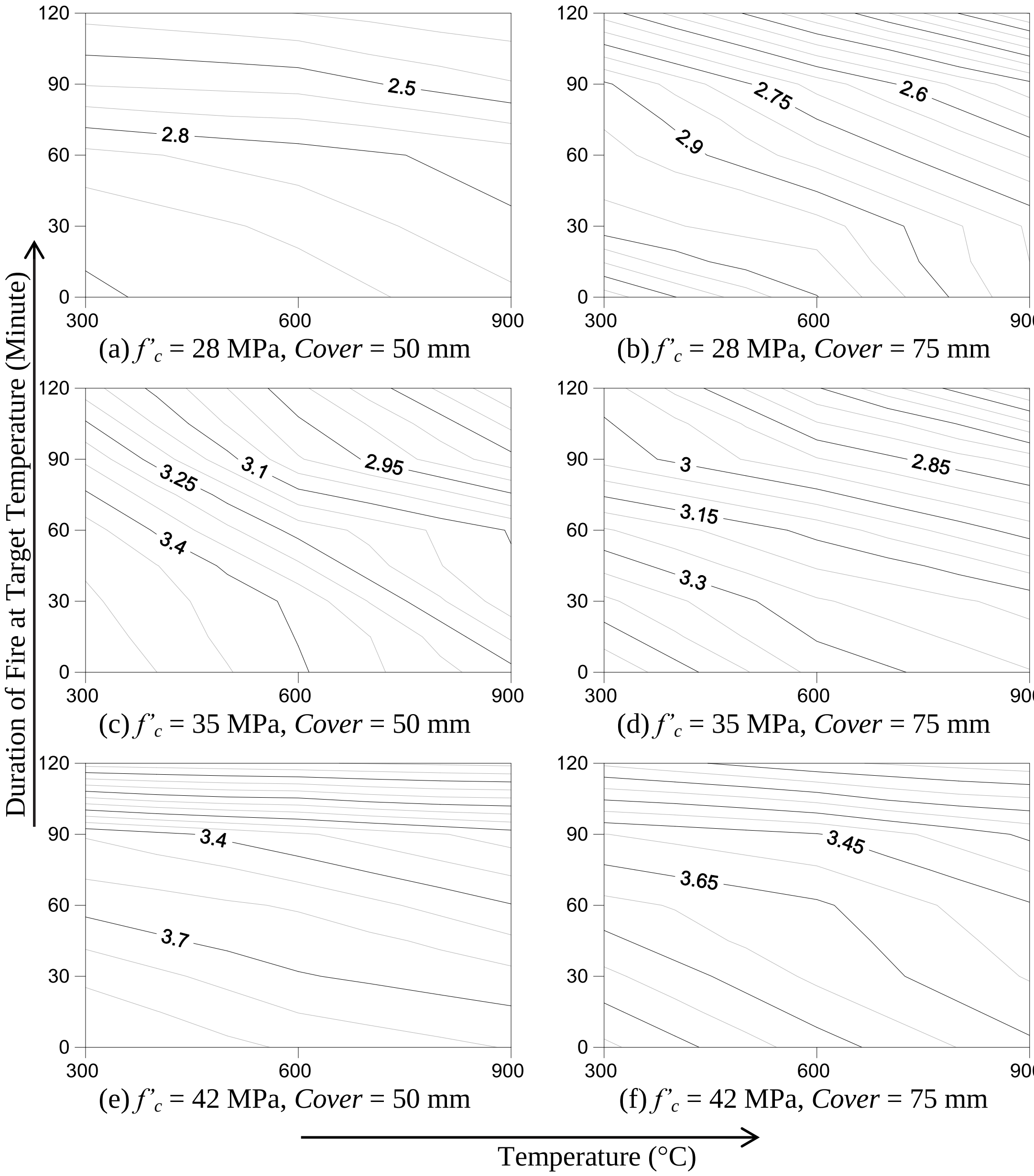

Figure-4.5: Tensile stress (MPa) variation in concrete at different temperature and duration of fire for F_y = 500 MPa

From Figures 4.4 and 4.5, the following discussions are outlined:

i. For same steel strength, concrete strength and concrete cover to steel, the tensile stress of concrete increases with the decrease in duration of burning.

ii. The tensile stress of concrete decreases faster after 90 minutes of burning.

C. Effect on Tensile Stress of Steel

The tensile stress in reinforcing steel was extracted at the maximum loading at different duration of burning. The extracted data are presented in Figures 4.6 and 4.7. Figure 4.6 represents the beams with 400MPa steels and Figure 4.7 represents those with 500MPa steel.

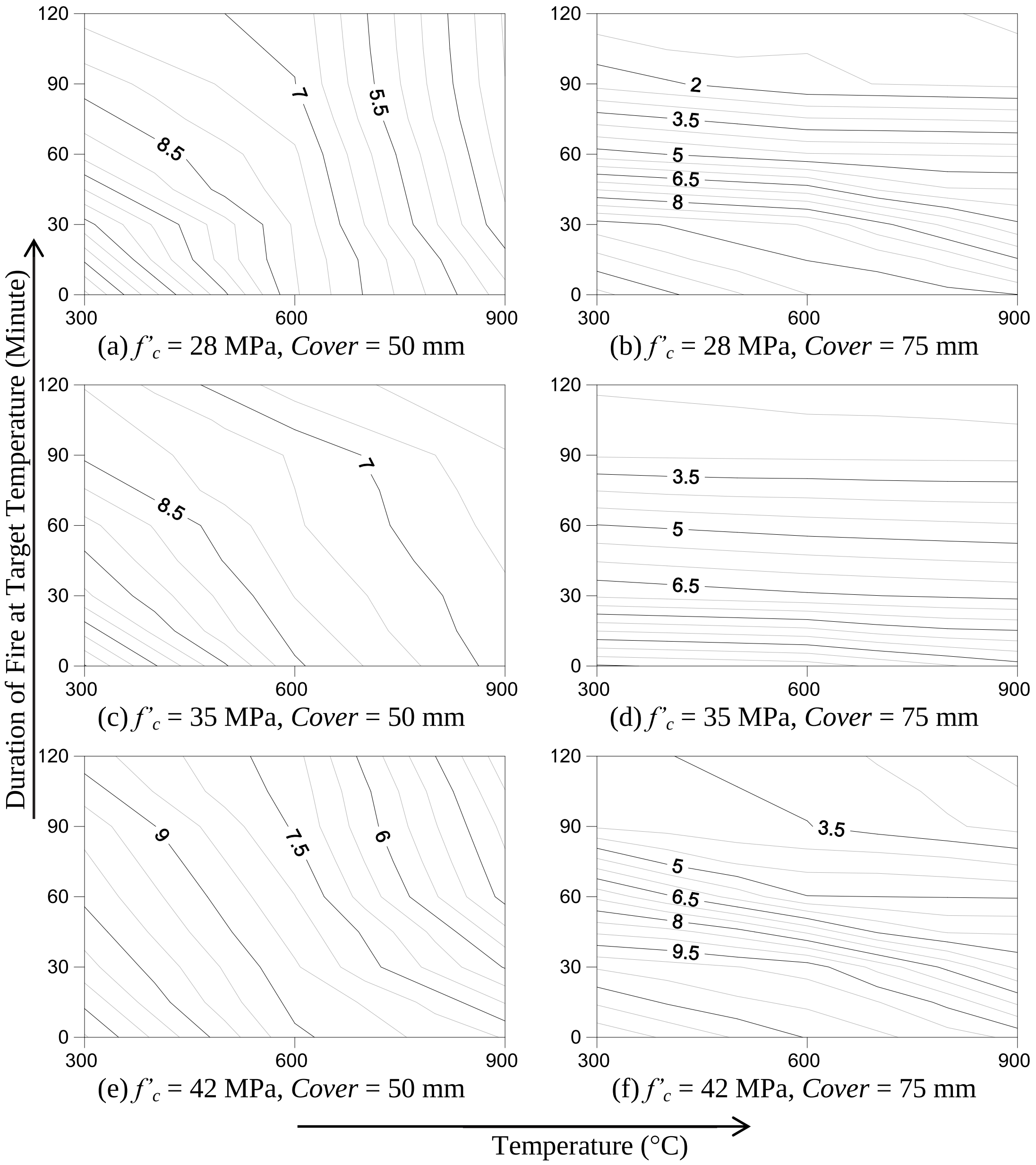

Figure-4.6: Tensile stress (MPa) variation in reinforcement at different temperature and duration of fire for F_y = 400 MPa

From Figures 4.6 and 4.7, the subsequent points are noticed:

i. For same steel strength, concrete strength and effective depth of beam, the observed tensile stress in steel decreases with the increase in duration of burning.

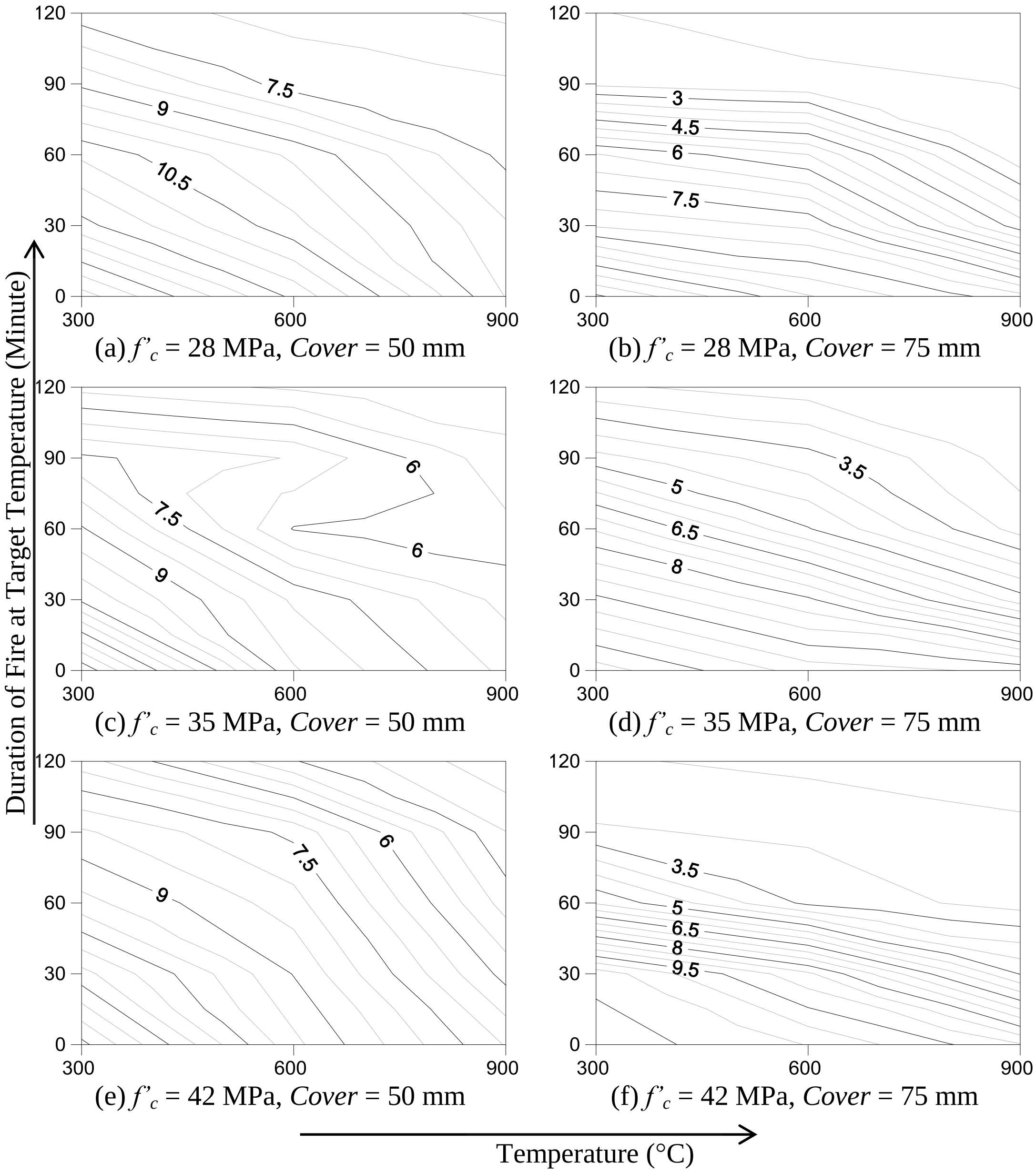

Figure-4.7: Tensile stress (MPa) variation in reinforcement at different temperature and duration of fire for F_y = 500 MPa

ii. For cover as high as 75mm, the rate of decrement of tensile stress in steel is high up to first 90 minutes of burning.

D. Effect on Compressive Stress of Steel

Applying maximum loading at different duration of burning, the compressive stress of steel was recorded in each model. The extracted data are presented in Figures 4.8 and 4.9 with 400MPa steels and 500MPa steel respectively.

From Figures 4.8 and 4.9, these points are noted:

i. The observed compressive stress in steel increases with the increase in duration of burning for same steel strength, concrete strength and effective depth of beam.

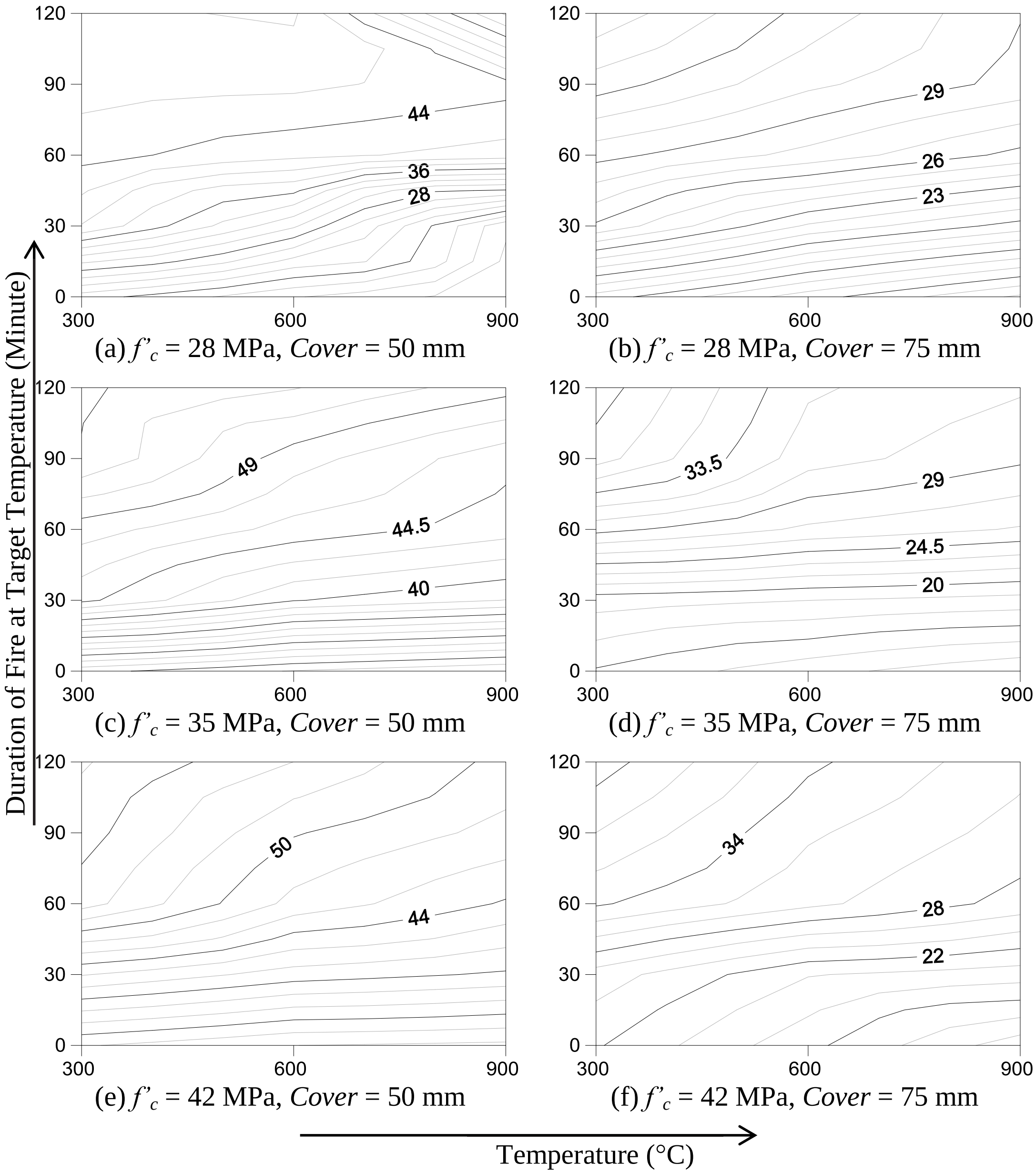

Figure-4.8: Compressive stress (MPa) variation in reinforcement at different temperature and duration of fire for F_y = 400 MPa

ii. Up to first 60 minutes of burning in any temperature above 300°C, the compressive stress of steel rapidly increase with time.

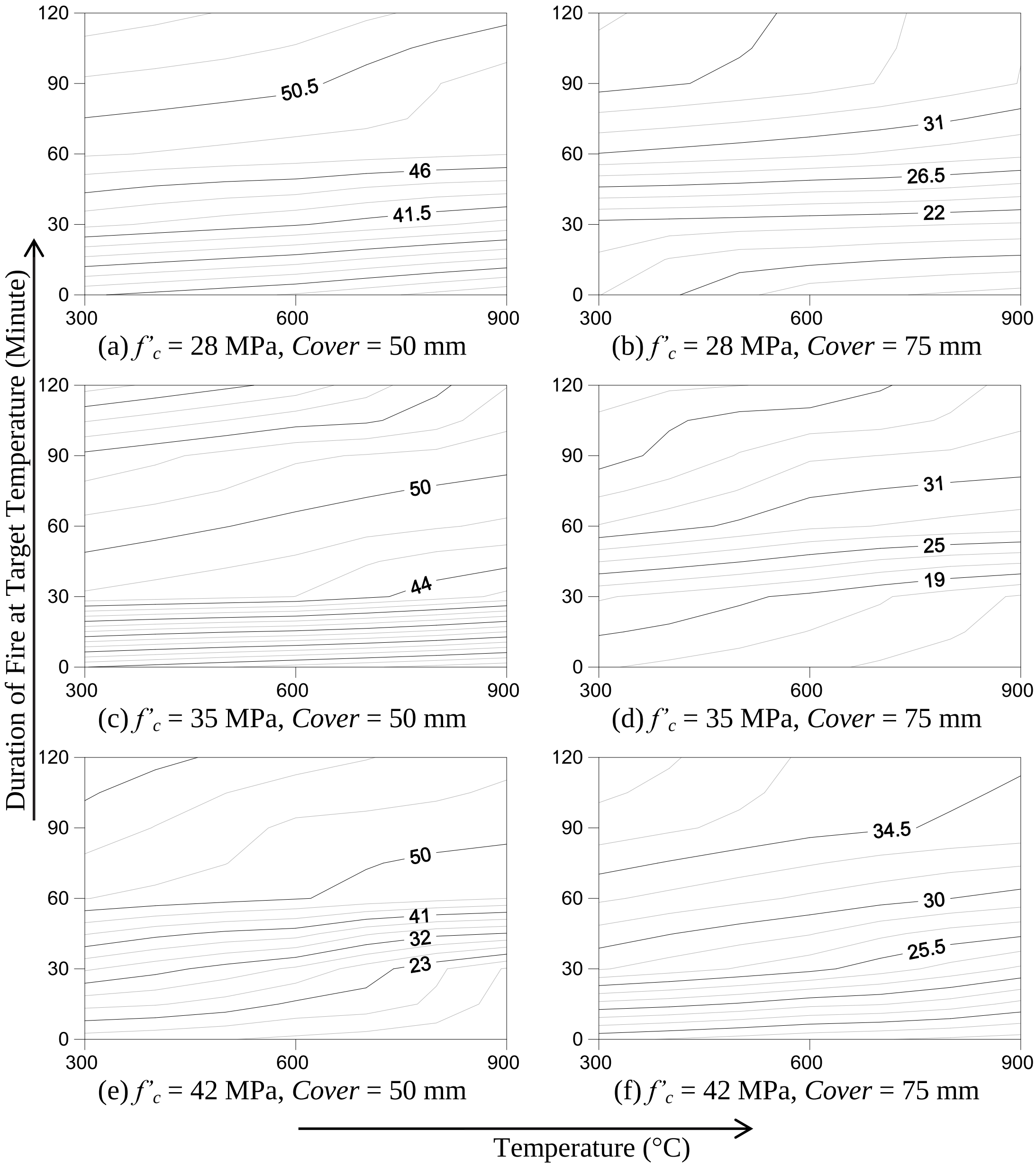

Figure-4.9: Compressive stress (MPa) variation in reinforcement at different temperature and duration of fire for F_y = 500 MPa

4.2.3 Effect of concrete cover

The concrete covers are varied to check the effect of effective depth in case of fire on beam. A detailed discussions on the effect of covers is outlined here comparing the results obtained in the numerous models performed in this research.

A. Effect on Compressive Stress of Concrete

The flexural compressive stress of concrete was obtained at the maximum loading of different burning temperatures and burning durations with varying steel strength and concrete strength. The compressive stress of concrete found in the models are graphed below in Figures 4.10 and 4.11.

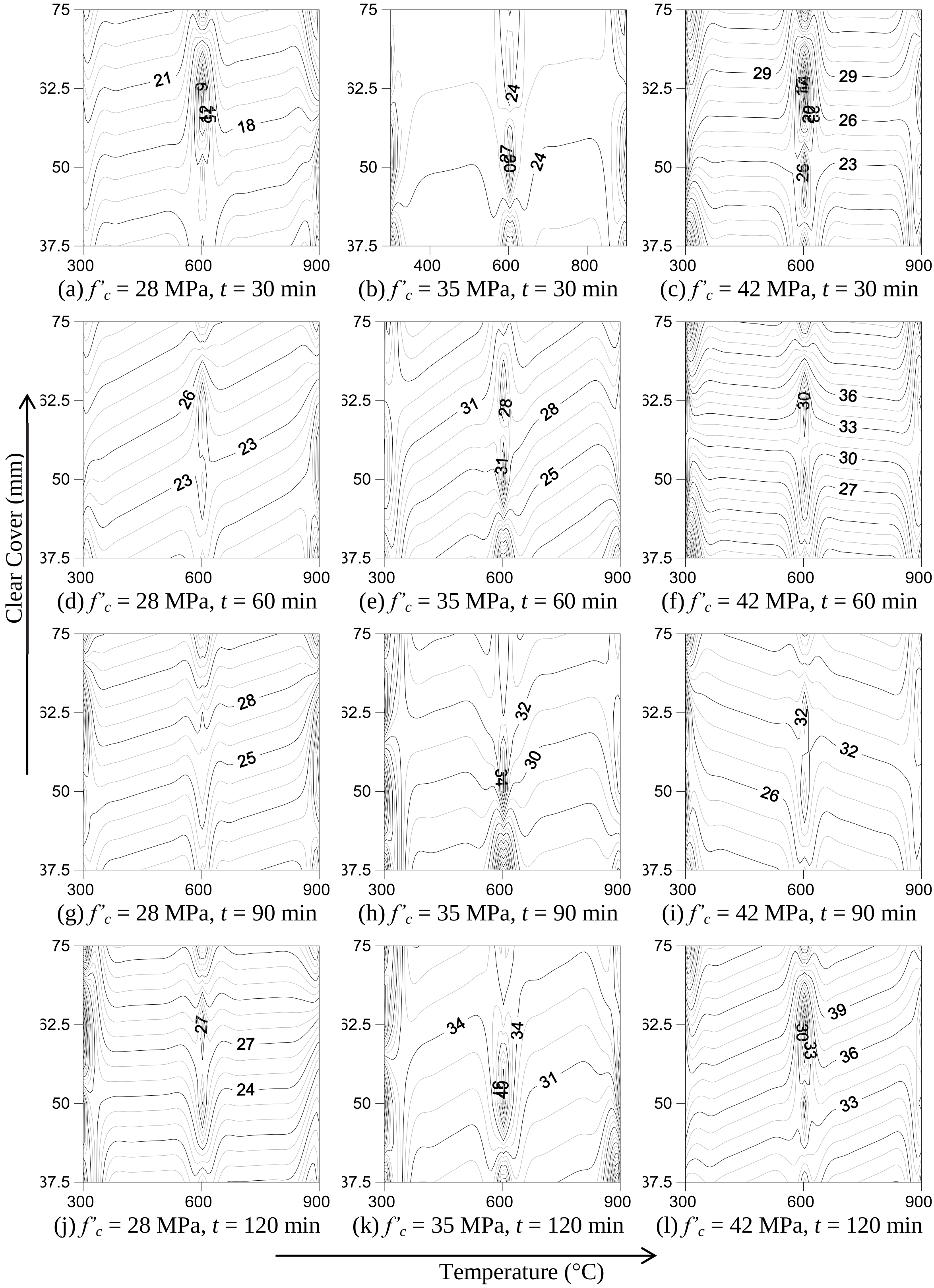

Figure-4.10: Compressive stress (MPa) variation in concrete at different temperature and clear cover for F_y = 400 MPa

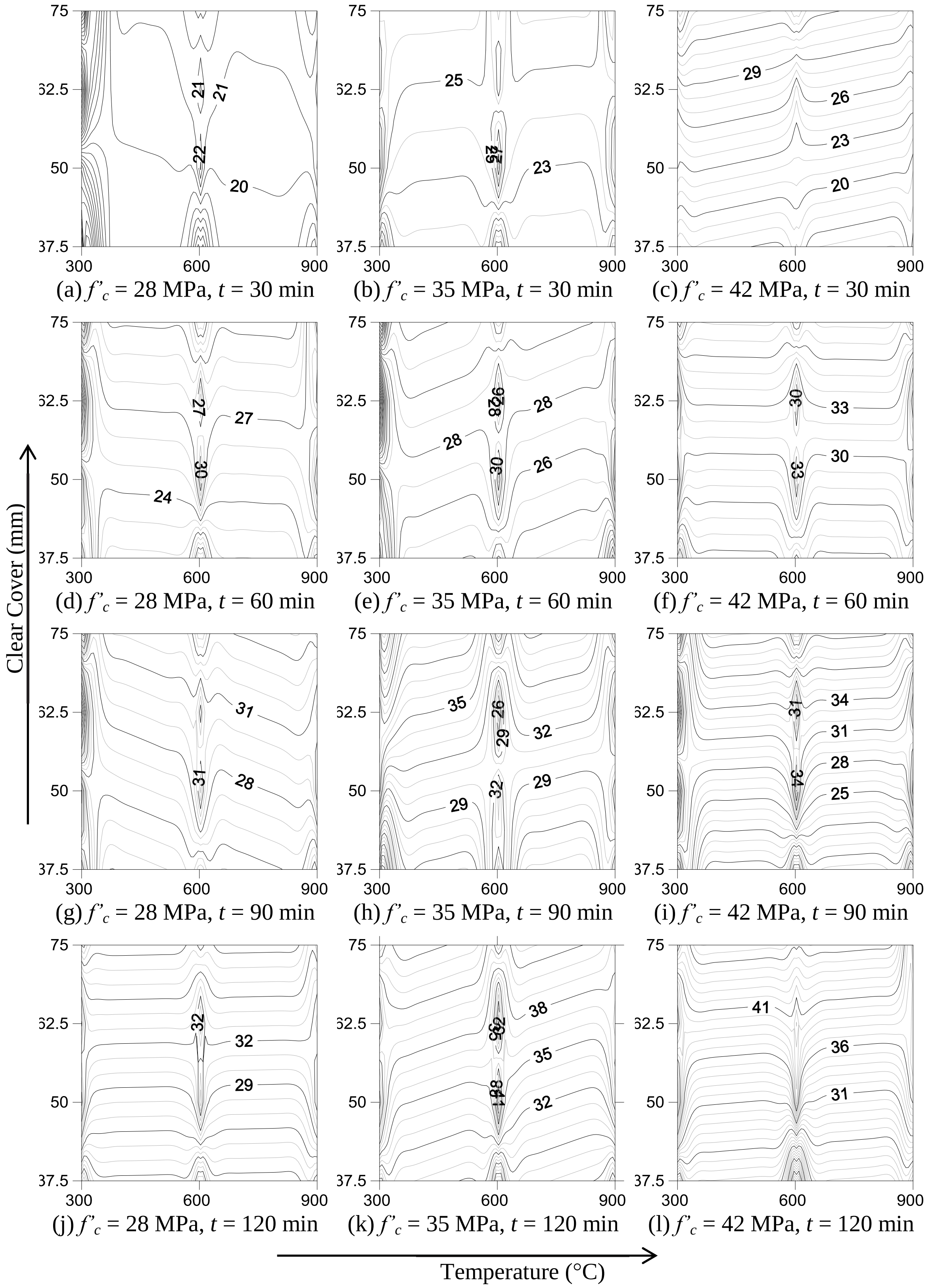

(a) f'_c = 28 MPa, t = 30 min (b) f'_c = 35 MPa, t = 30 min (c) f'_c = 42 MPa, t = 30 min

(d) f'_c = 28 MPa, t = 60 min (e) f'_c = 35 MPa, t = 60 min (f) f'_c = 42 MPa, t = 60 min

(g) f'_c = 28 MPa, t = 90 min (h) f'_c = 35 MPa, t = 90 min (i) f'_c = 42 MPa, t = 90 min

(j) f'_c = 28 MPa, t = 120 min (k) f'_c = 35 MPa, t = 120 min (l) f'_c = 42 MPa, t = 120 min

Figure-4.11: Compressive stress (MPa) variation in concrete at different temperature and clear cover for F_y = 500 MPa

From Figures 4.10 and 4.11, the following discussions are outlined:

i. The maximum compressive stress of the concrete increases with the increase in cover for 28MPa and 42MPa concrete.

ii. For 35MPa concrete, the maximum compressive stress decreases over the increase in cover.

iii. With 28MPa and 35MPa concrete, the maximum compressive force occurred near the supports at bottom. Since this region is prone to thermal compressive stress, the 28MPa concrete could not resist the required amount of force from temperature effect but 35MPa concrete could resist it, hence, showing an opposite pattern of maximum compressive stress for higher cover dimension.

iv. In case of 42MPa concrete, the maximum compressive force occurred at the top-center of beam. This zone is susceptible to mechanical compressive force, thus with high concrete strength the concrete mechanically resist more force with higher cover since the steel in this compression region resist less force in the same variation of cover.

v. The maximum compressive stress of concrete decreases with the increase in temperature for same concrete, steel and duration of burning combination.

B. Effect on Tensile Stress of Concrete

The tensile stresses of concrete found from the model are graphed below in Figures 4.12 and 4.13. From these graphs it is evident that:

i. The maximum tensile stress in concrete increases with the increase in cover for 28MPa and 42 MPa concrete but decrease for 35MPa concrete.

ii. With 28MPa and 35MPa concrete, the resultant tensile force in concrete occurred near bottom-center of the beam. Since this region is prone to thermal compressive stress, the 28MPa concrete could not resist the required amount of force from temperature effect but 35MPa concrete could resist it, hence, showing an opposite pattern of maximum tensile stress for higher cover dimension.

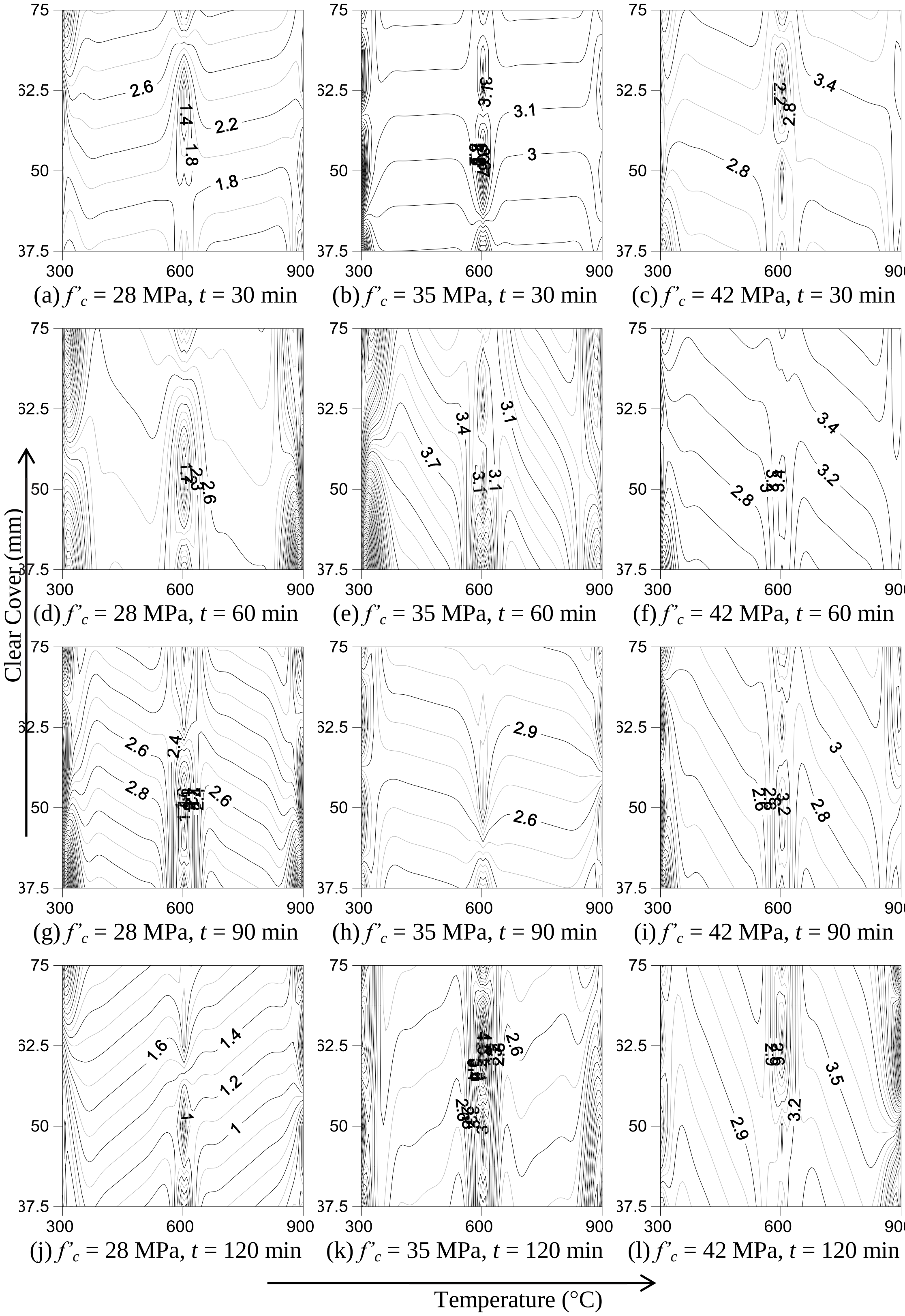

(a) f'_c = 28 MPa, t = 30 min (b) f'_c = 35 MPa, t = 30 min (c) f'_c = 42 MPa, t = 30 min

(d) f'_c = 28 MPa, t = 60 min (e) f'_c = 35 MPa, t = 60 min (f) f'_c = 42 MPa, t = 60 min

(g) f'_c = 28 MPa, t = 90 min (h) f'_c = 35 MPa, t = 90 min (i) f'_c = 42 MPa, t = 90 min

(j) f'_c = 28 MPa, t = 120 min (k) f'_c = 35 MPa, t = 120 min (l) f'_c = 42 MPa, t = 120 min

Figure-4.12: Tensile stress (MPa) variation in concrete at different temperature and clear cover for F_y = 400 MPa

iii. In case of 42MPa concrete, the maximum tensile force occurred at the top of beam near supports. This zone is susceptible to mechanical tensile force, thus with high concrete strength the concrete mechanically resist more force with higher cover since the steel in this tension region resist less force in the same variation of cover.

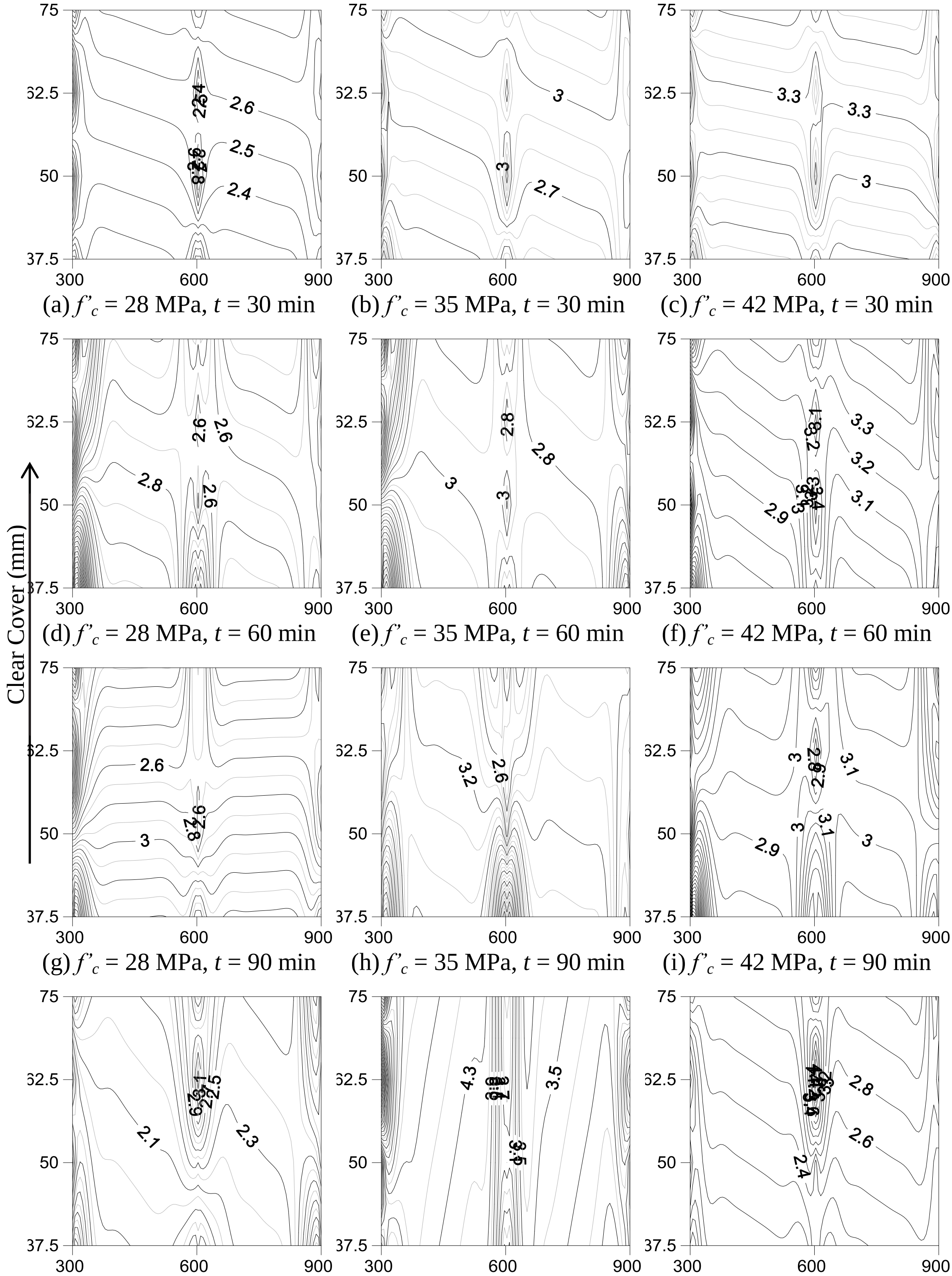

(a) f'_c = 28 MPa, t = 30 min (b) f'_c = 35 MPa, t = 30 min (c) f'_c = 42 MPa, t = 30 min

(d) f'_c = 28 MPa, t = 60 min (e) f'_c = 35 MPa, t = 60 min (f) f'_c = 42 MPa, t = 60 min

(g) f'_c = 28 MPa, t = 90 min (h) f'_c = 35 MPa, t = 90 min (i) f'_c = 42 MPa, t = 90 min

(j) f'_c = 28 MPa, t = 120 min (k) f'_c = 35 MPa, t = 120 min (l) f'_c = 42 MPa, t = 120 min

Temperature (°C)

Figure-4.13: Tensile stress (MPa) variation in concrete at different temperature and clear cover for F_y = 500 MPa

C. Effect on Tensile Stress of Steel

The tensile stress of reinforcing bars with different cover dimension are shown in Figures 4.14 and 4.15.

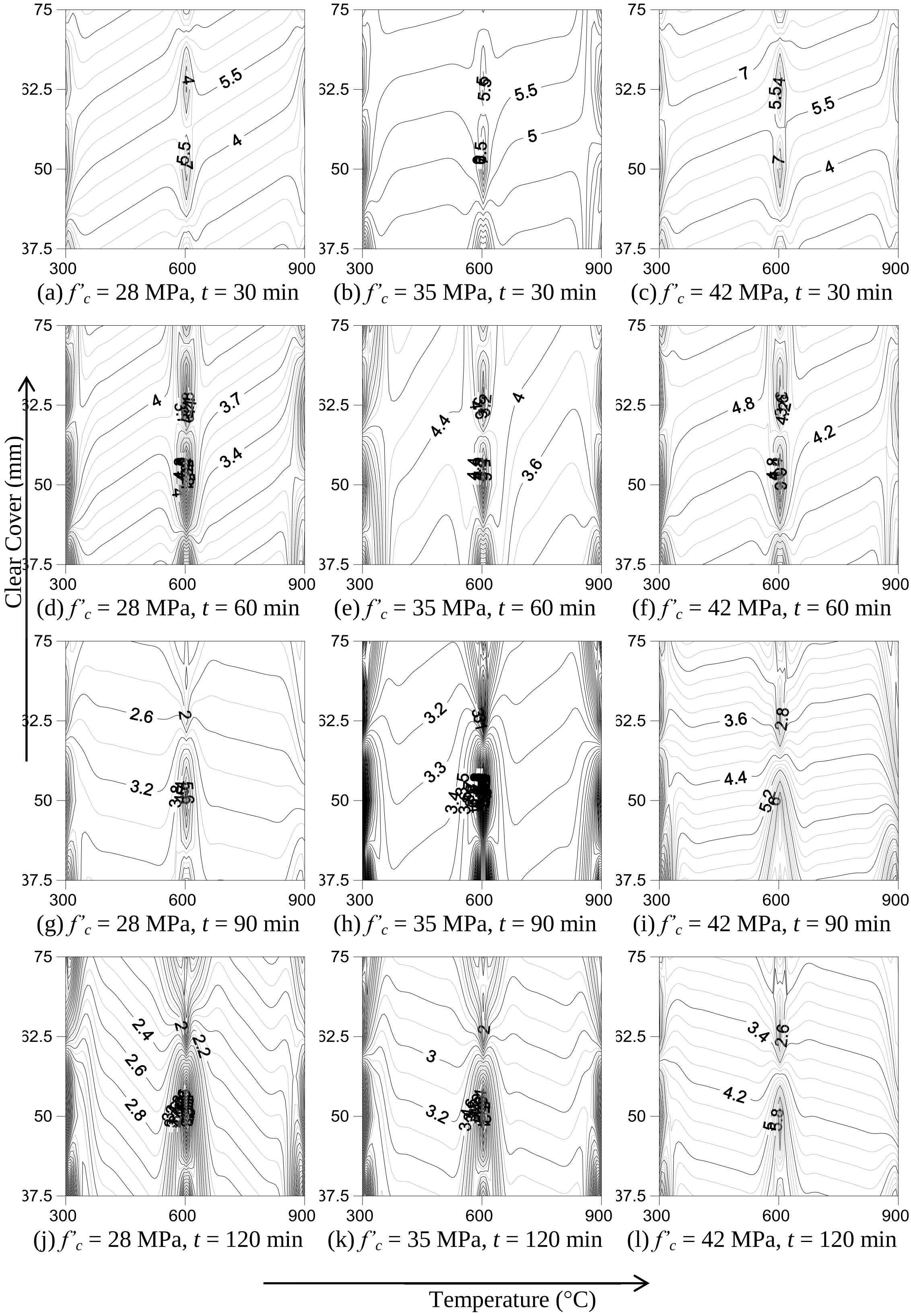

(a) f'_c = 28 MPa, t = 30 min (b) f'_c = 35 MPa, t = 30 min (c) f'_c = 42 MPa, t = 30 min

(d) f'_c = 28 MPa, t = 60 min (e) f'_c = 35 MPa, t = 60 min (f) f'_c = 42 MPa, t = 60 min

(g) f'_c = 28 MPa, t = 90 min (h) f'_c = 35 MPa, t = 90 min (i) f'_c = 42 MPa, t = 90 min

(j) f'_c = 28 MPa, t = 120 min (k) f'_c = 35 MPa, t = 120 min (l) f'_c = 42 MPa, t = 120 min

Figure-4.14: Tensile stress (MPa) variation in reinforcement at different temperature and clear cover for F_y = 400 MPa

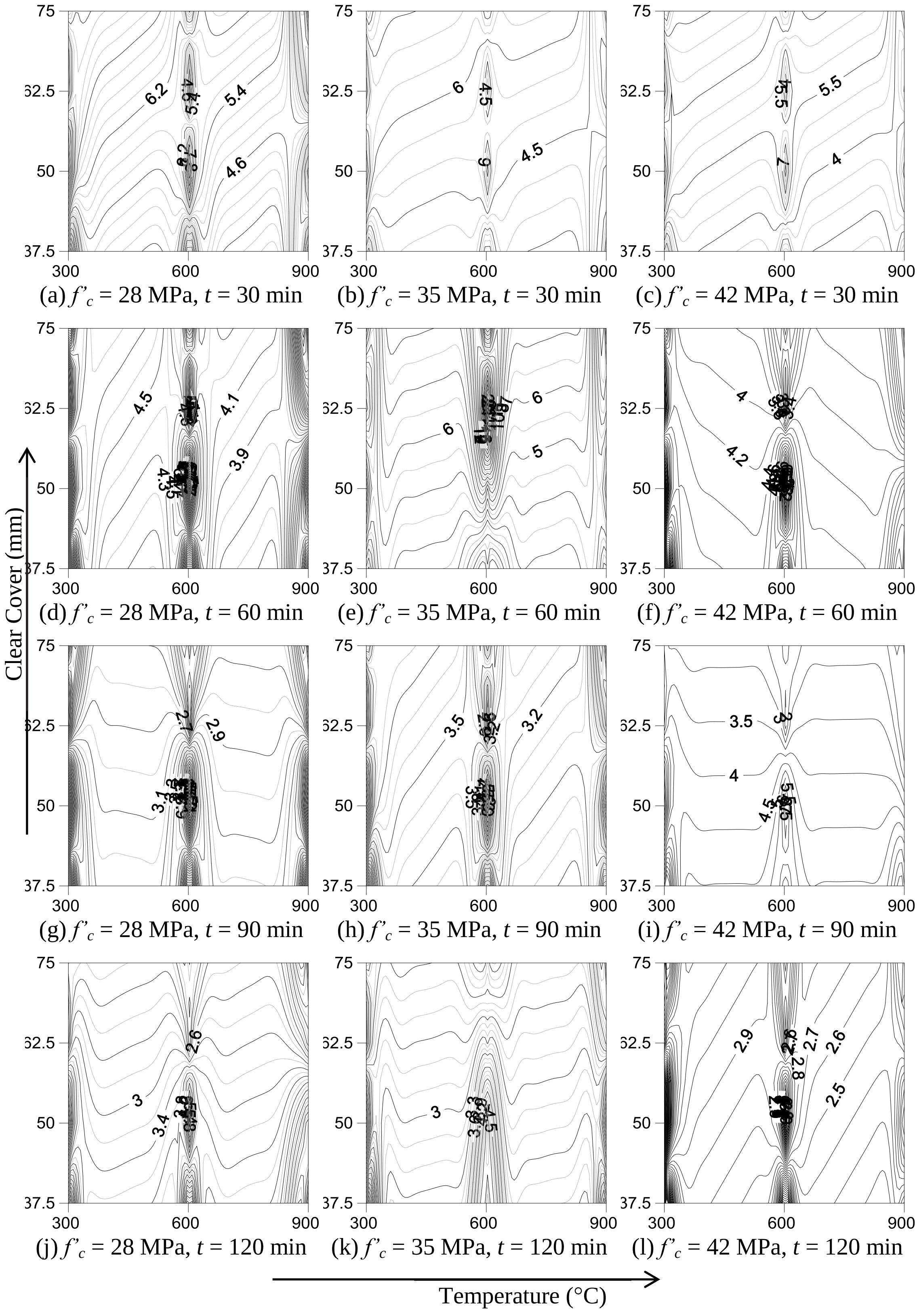

(a) f'_c = 28 MPa, t = 30 min (b) f'_c = 35 MPa, t = 30 min (c) f'_c = 42 MPa, t = 30 min
(d) f'_c = 28 MPa, t = 60 min (e) f'_c = 35 MPa, t = 60 min (f) f'_c = 42 MPa, t = 60 min
(g) f'_c = 28 MPa, t = 90 min (h) f'_c = 35 MPa, t = 90 min (i) f'_c = 42 MPa, t = 90 min
(j) f'_c = 28 MPa, t = 120 min (k) f'_c = 35 MPa, t = 120 min (l) f'_c = 42 MPa, t = 120 min

Figure-4.15: Tensile stress (MPa) variation in reinforcement at different temperature and clear cover for F_y = 500 MPa

Analyzing the contour patterns found on Figures 4.14 and 4.15, the following conclusions may be drawn:

i. At 30minutes duration of burning, the tensile stress in reinforcing bars has no or little effect from the change in cover for temperature above 600°C.

ii. At any period after 30minutes of burning, the tensile stress in rebar generally reduce with higher cover dimensions.

iii. The tensile stress variation of steel showed consistency to mechanical action since higher cover dimension ends in lower tensile stress in steel as effective depth is lower.

D. Effect on Compressive Stress of Steel

The compressive stress is recorded throughout the steel portion of beam. Then the maximum compressive stress found in each model is plotted against temperature variation keeping other parameters unchanged in Figures 4.16 and 4.17 for 400MPa and 500MPa steel respectively.

The patterns in Figures 4.16 and 4.17 suggests that:

i. With higher concrete cover dimension, the compressive stress in steel is less for a particular duration, material strength and temperature.

ii. Thermal action is very significant compared to the mechanical effect in case of compressive stress in steel. Because, mechanically, steel in compression has less effective depth or less cover resulting into less mechanical compressive force. But in the analyses, the pattern is just the opposite, showing more compliance to thermal action than to mechanical action.

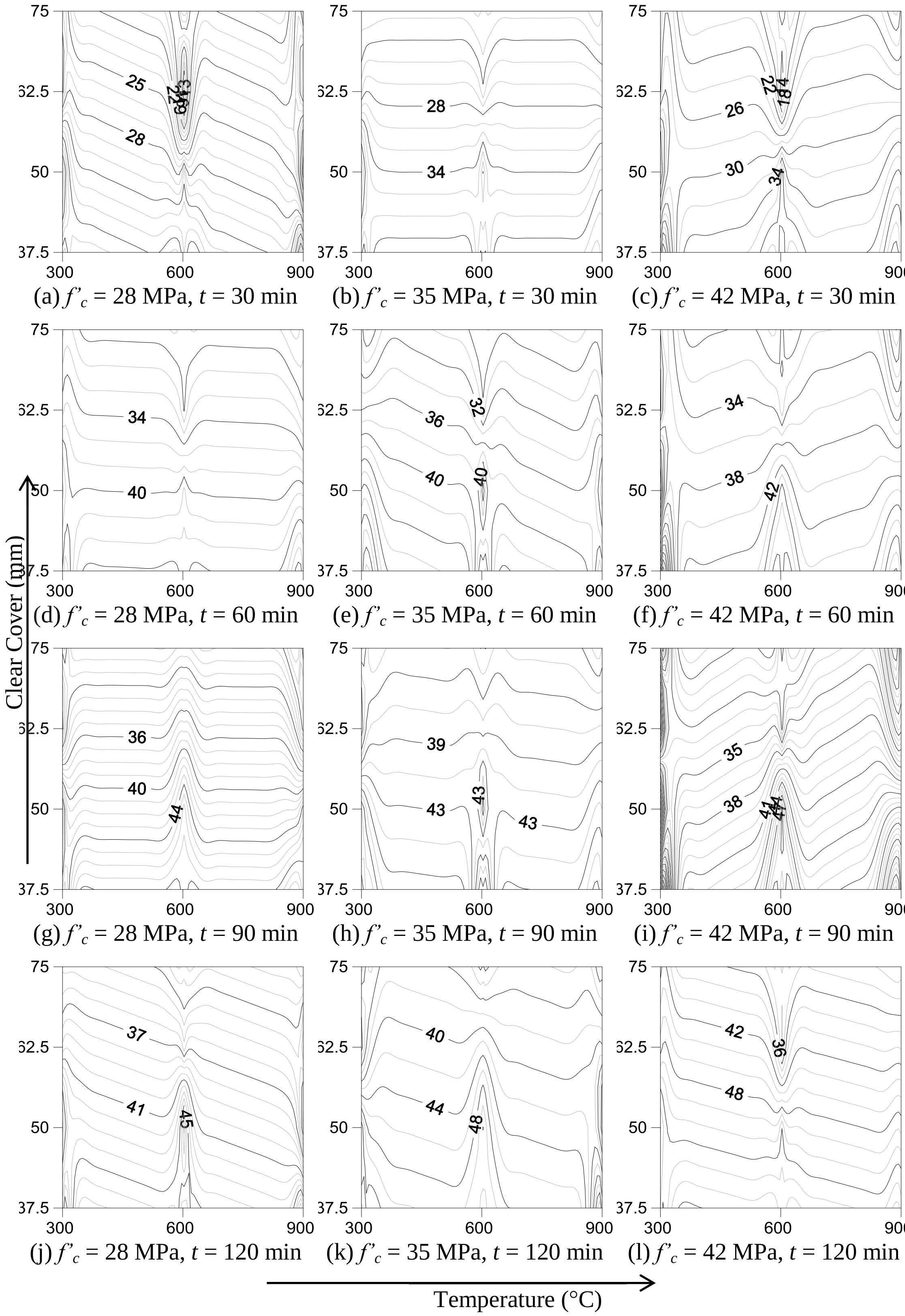

(a) f'_c = 28 MPa, t = 30 min (b) f'_c = 35 MPa, t = 30 min (c) f'_c = 42 MPa, t = 30 min

(d) f'_c = 28 MPa, t = 60 min (e) f'_c = 35 MPa, t = 60 min (f) f'_c = 42 MPa, t = 60 min

(g) f'_c = 28 MPa, t = 90 min (h) f'_c = 35 MPa, t = 90 min (i) f'_c = 42 MPa, t = 90 min

(j) f'_c = 28 MPa, t = 120 min (k) f'_c = 35 MPa, t = 120 min (l) f'_c = 42 MPa, t = 120 min

Figure-4.16: Compressive stress (MPa) variation in reinforcement at different temperature and clear cover for F_y = 400 MPa

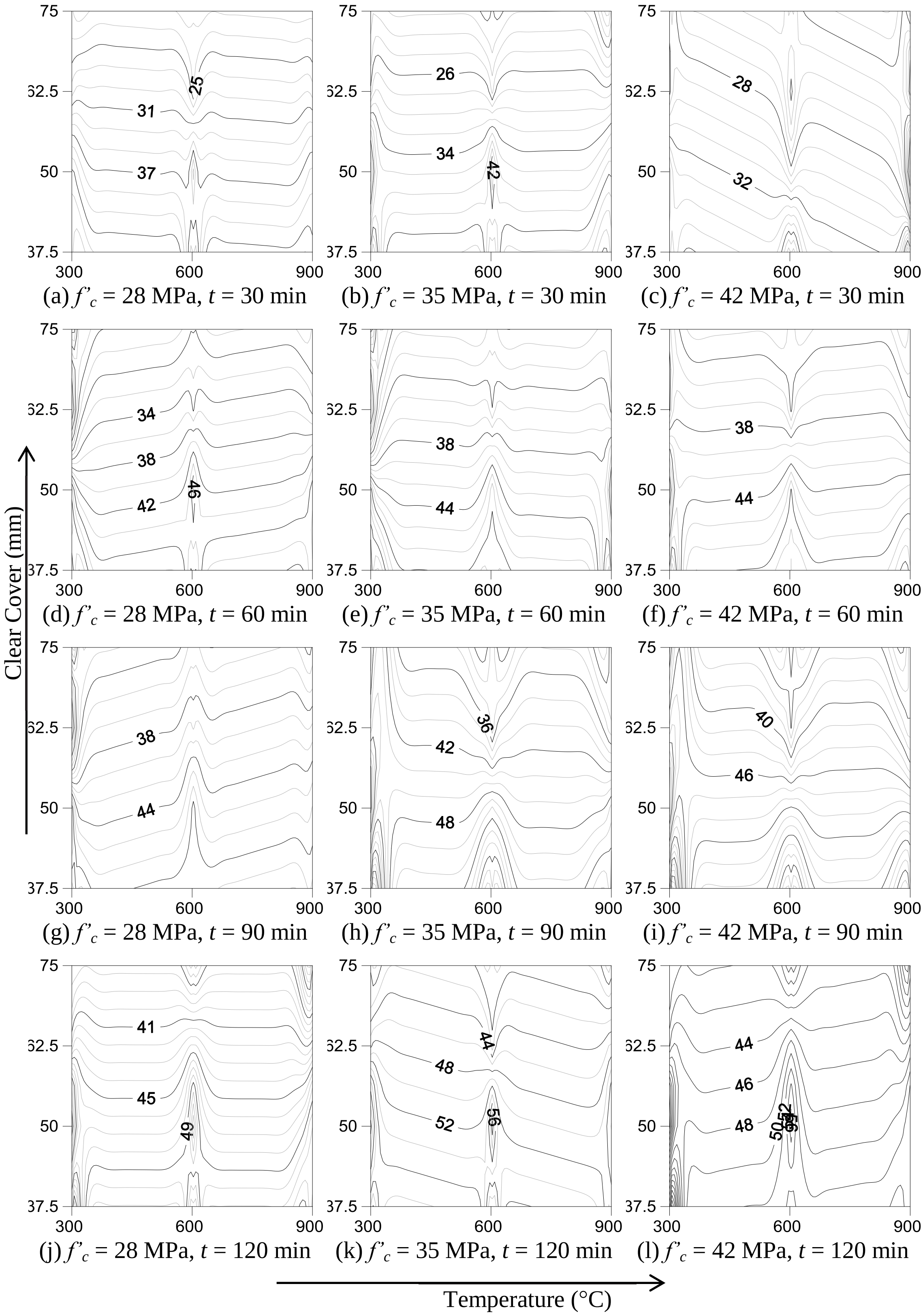

Figure-4.17: Compressive stress (MPa) variation in reinforcement at different temperature and clear cover for F_y = 500 MPa

4.2.4 Effect of concrete strength

The beams in this research are modelled with 3 (Three) concrete strengths to observe the effect of concrete strength during fire phenomena. All four extracted outputs are plotted in strength-temperature surface to find the subsequent patterns.

A. Effect on Compressive Stress of Concrete

The flexural compressive stress of concrete was obtained at the maximum loading of different burning temperatures and burning durations with varying steel strength and concrete strength. In Figures 4.18 and 4.19, the graphs are plotted for 400MPa and 500MPa steel respectively.

From Figures 4.18 and 4.19, it is summarized that:

i. Up to 35MPa concrete strength, the compressive stress of concrete due to resultant force increases with the increase of concrete strength.

ii. For concrete strength more than 35MPa, the compressive stress decreases with the increase of concrete strength.

iii. As per BS-EN 1992-1-2:2004 as stated in Article-3.2.1 of this report, up to 30 minutes of burning duration, no concrete is in plastic state. But, after 30 minutes of burning concrete enters into the plastic state.

iv. Mechanically, concrete stress should rise with the rise in concrete strength. Hence, Up to 35MPa concrete, the results showed mechanical action governs, whereas after 35 MPa thermal action governs. The thermal action intensifies with duration of burning.

v. When the compressive stress of concrete is in plastic state, the change of stress level with concrete strength becomes very slow.

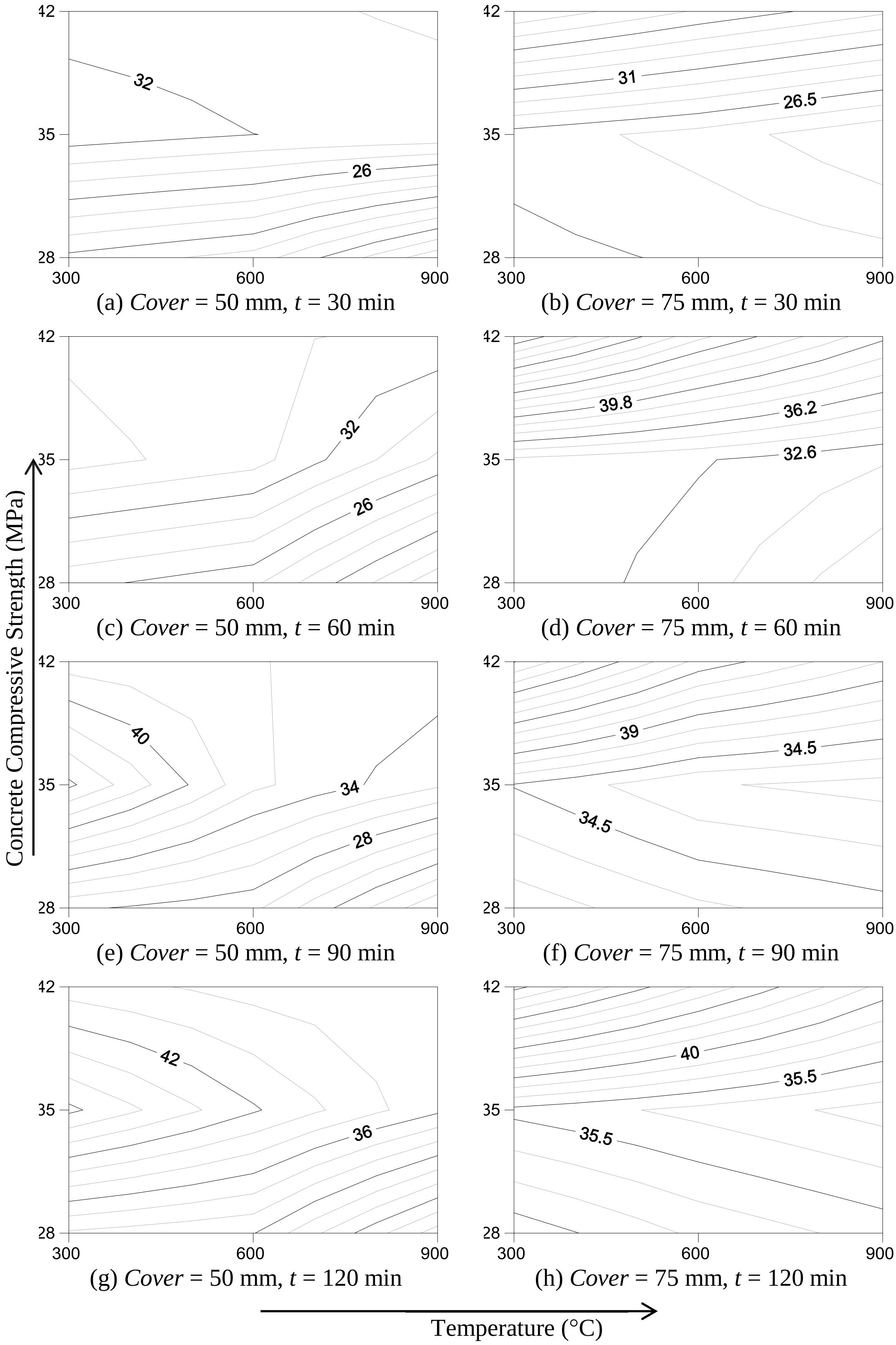

Figure-4.18: Compressive stress (MPa) variation in concrete at different temperature and concrete compressive strength for F_y = 400 MPa

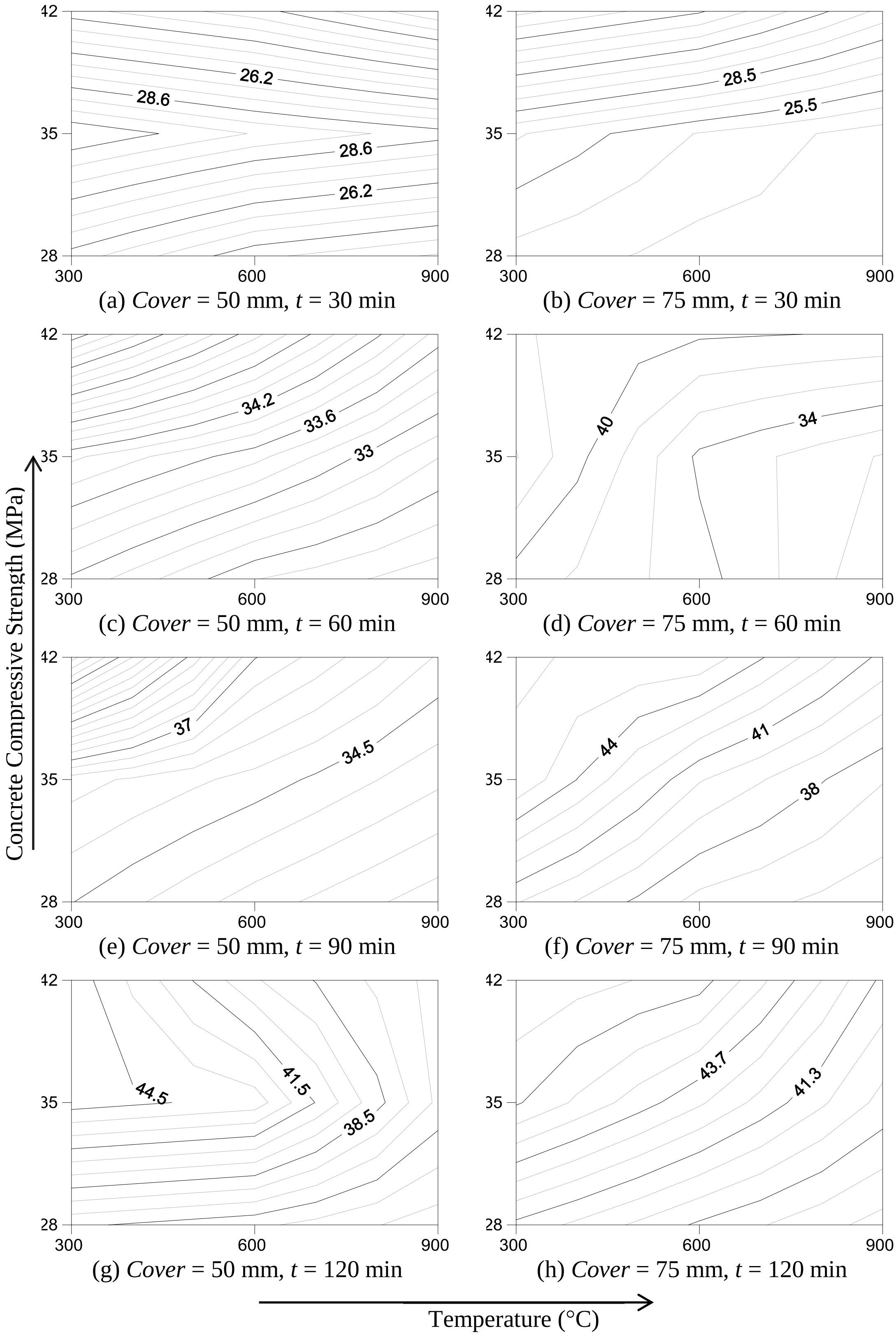

Figure-4.19: Compressive stress (MPa) variation in concrete at different temperature and concrete compressive strength for F_y = 500 MPa

B. Effect on Tensile Stress of Concrete

The tensile stress of all concrete area were recorded and the maximum of these are plotted in graphs. Figures 4.20 and 4.21 show the change in tensile stress of concrete resulted from different concrete strength.

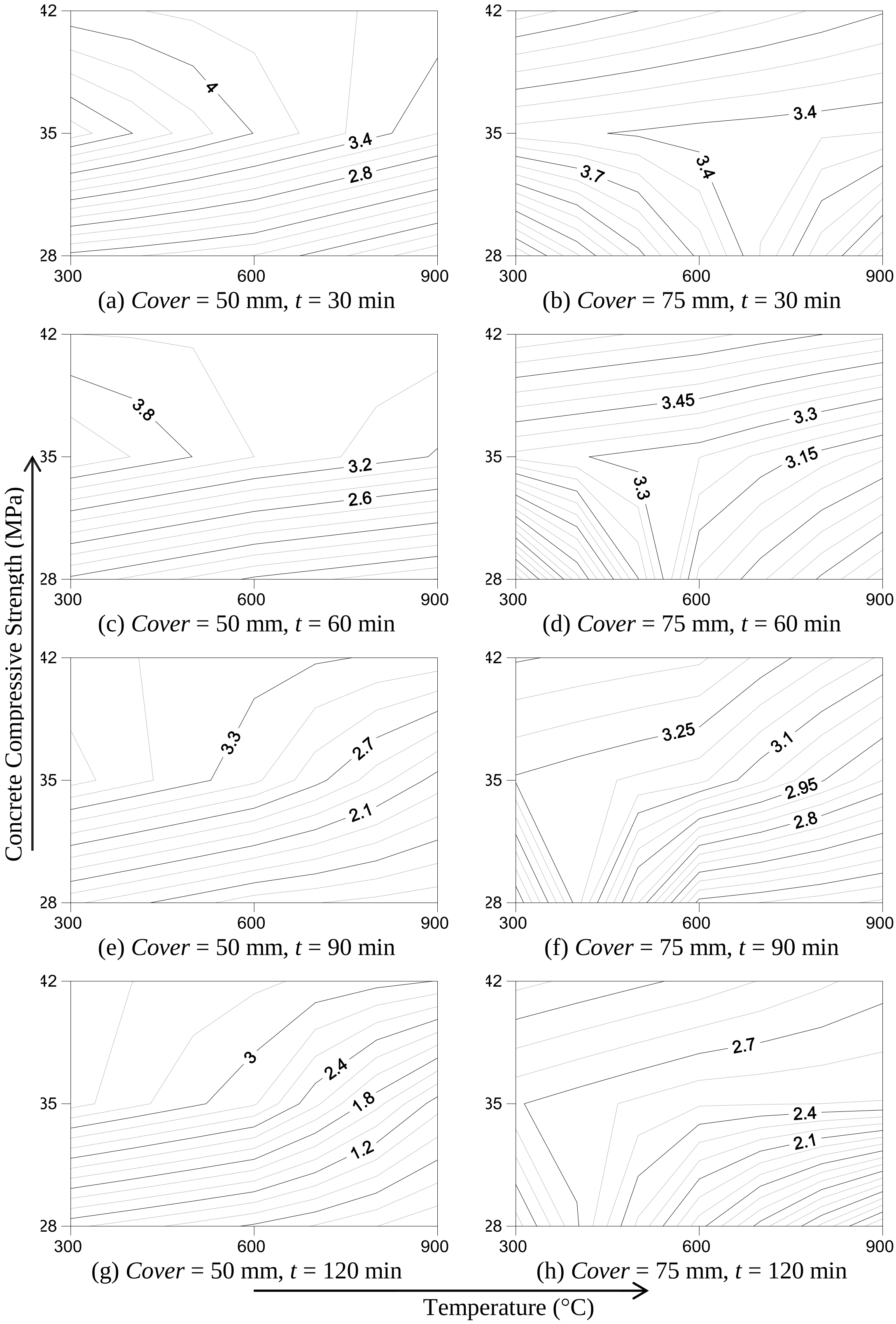

Figure-4.20: Tensile stress (MPa) variation in concrete at different temperature and concrete compressive strength for F_y = 400 MPa

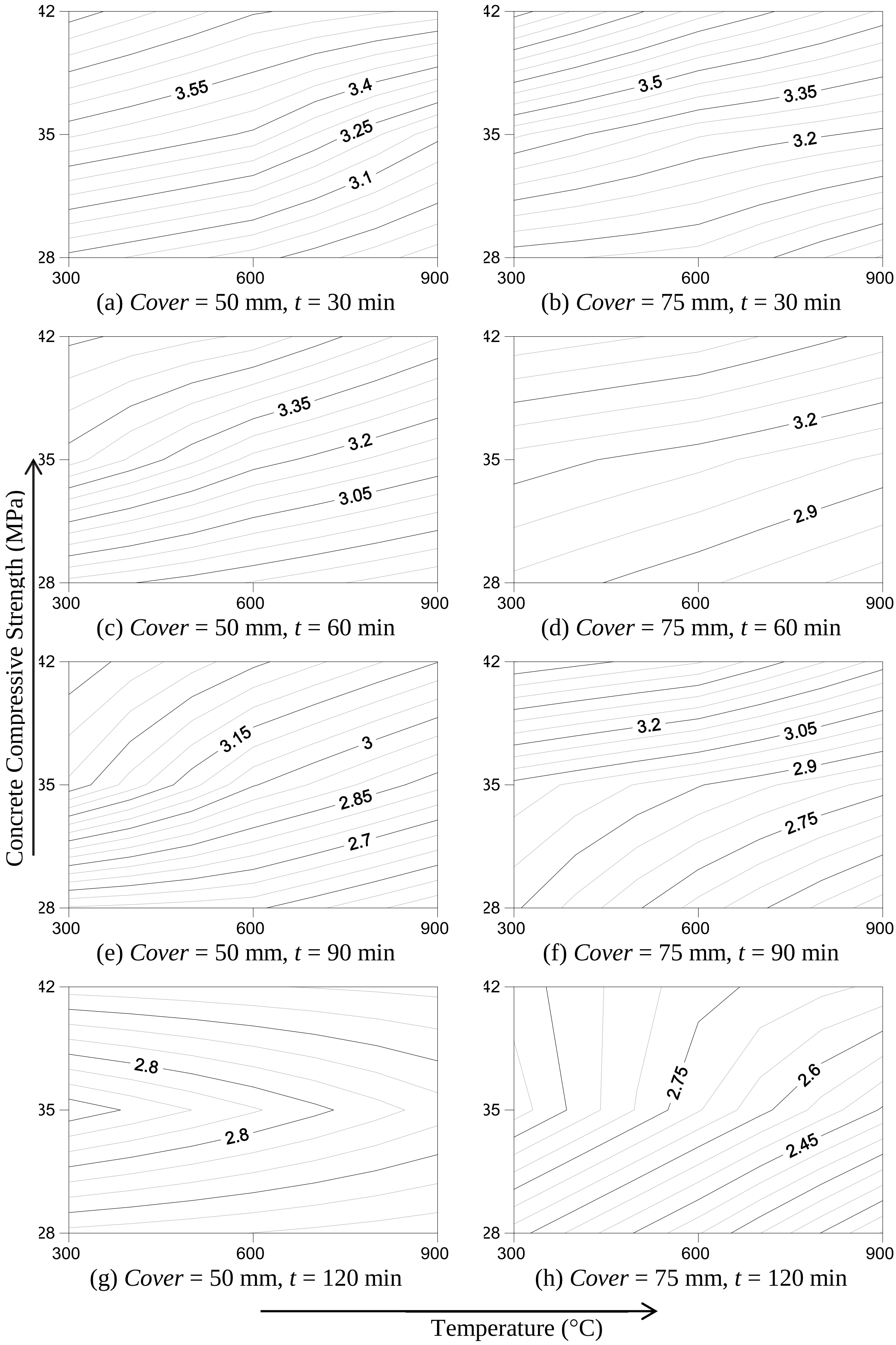

(a) *Cover* = 50 mm, *t* = 30 min (b) *Cover* = 75 mm, *t* = 30 min

(c) *Cover* = 50 mm, *t* = 60 min (d) *Cover* = 75 mm, *t* = 60 min

(e) *Cover* = 50 mm, *t* = 90 min (f) *Cover* = 75 mm, *t* = 90 min

(g) *Cover* = 50 mm, *t* = 120 min (h) *Cover* = 75 mm, *t* = 120 min

Figure-4.21: Tensile stress (MPa) variation in concrete at different temperature and concrete compressive strength for F_y = 500 MPa

The Figures 4.20 and 4.21 show some significant information regarding the tension developed in concrete area under fire loading:

i. The maximum concrete tensile stress, developed from the resultant of mechanical and thermal action, increases with the increase in concrete strength.

ii. The tensile stress variation over concrete strength is very slight. Hence, it can be concluded that in compression controlled sections, the tensile stress of concrete is the one of the least affected outputs.

C. Effect on Tensile Stress of Steel

The tensions developed from the flexural effect of applied mechanical loads and the thermal actions were extracted from the models analyzed. The data are plotted to understand the effect of concrete strength over the tensile stress of steel in beams. Figures 4.22 and 4.23 suggest:

i. Generally, the tension on steel increases over the increase of concrete strength.

ii. The increment of tensile stress is subtle at temperature up to 500°C.

iii. With the increase in concrete strength, the beam section can take more flexure hence, tensile stress of steel is expected to increase mechanically.

iv. The analyses depicts that steel in tension has little or no effect for the thermal action, since the mechanical action governs.

v. Conventional mechanics of reinforced concrete flexural members may be applied at elevated temperatures.

vi. In compression controlled sections, the tensile stress of steel is the one of the least affected by the increase of temperature.

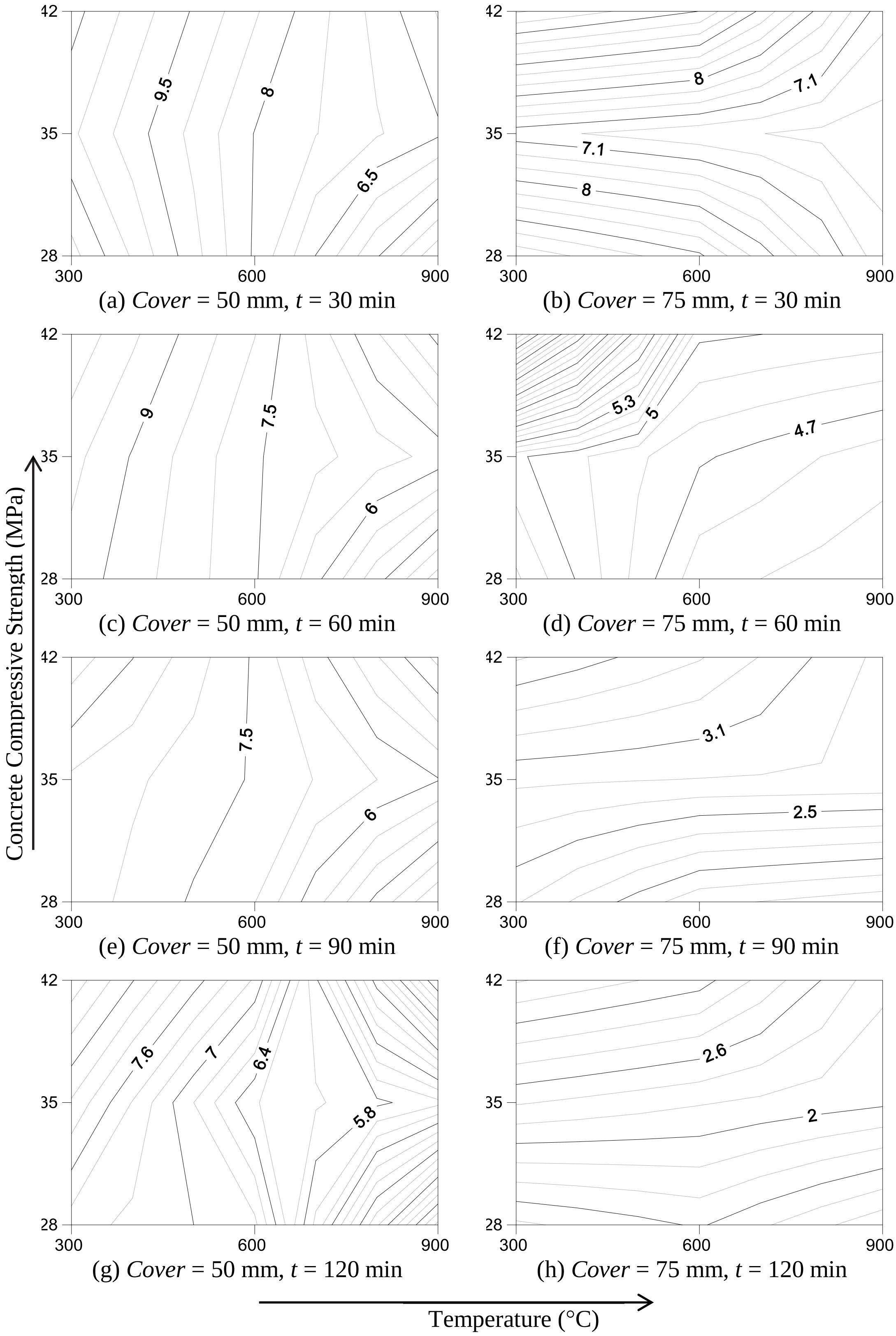

(a) *Cover* = 50 mm, *t* = 30 min
(b) *Cover* = 75 mm, *t* = 30 min
(c) *Cover* = 50 mm, *t* = 60 min
(d) *Cover* = 75 mm, *t* = 60 min
(e) *Cover* = 50 mm, *t* = 90 min
(f) *Cover* = 75 mm, *t* = 90 min
(g) *Cover* = 50 mm, *t* = 120 min
(h) *Cover* = 75 mm, *t* = 120 min

Figure-4.22: Tensile stress (MPa) variation in reinforcement at different temperature and concrete compressive strength for F_y = 400 MPa

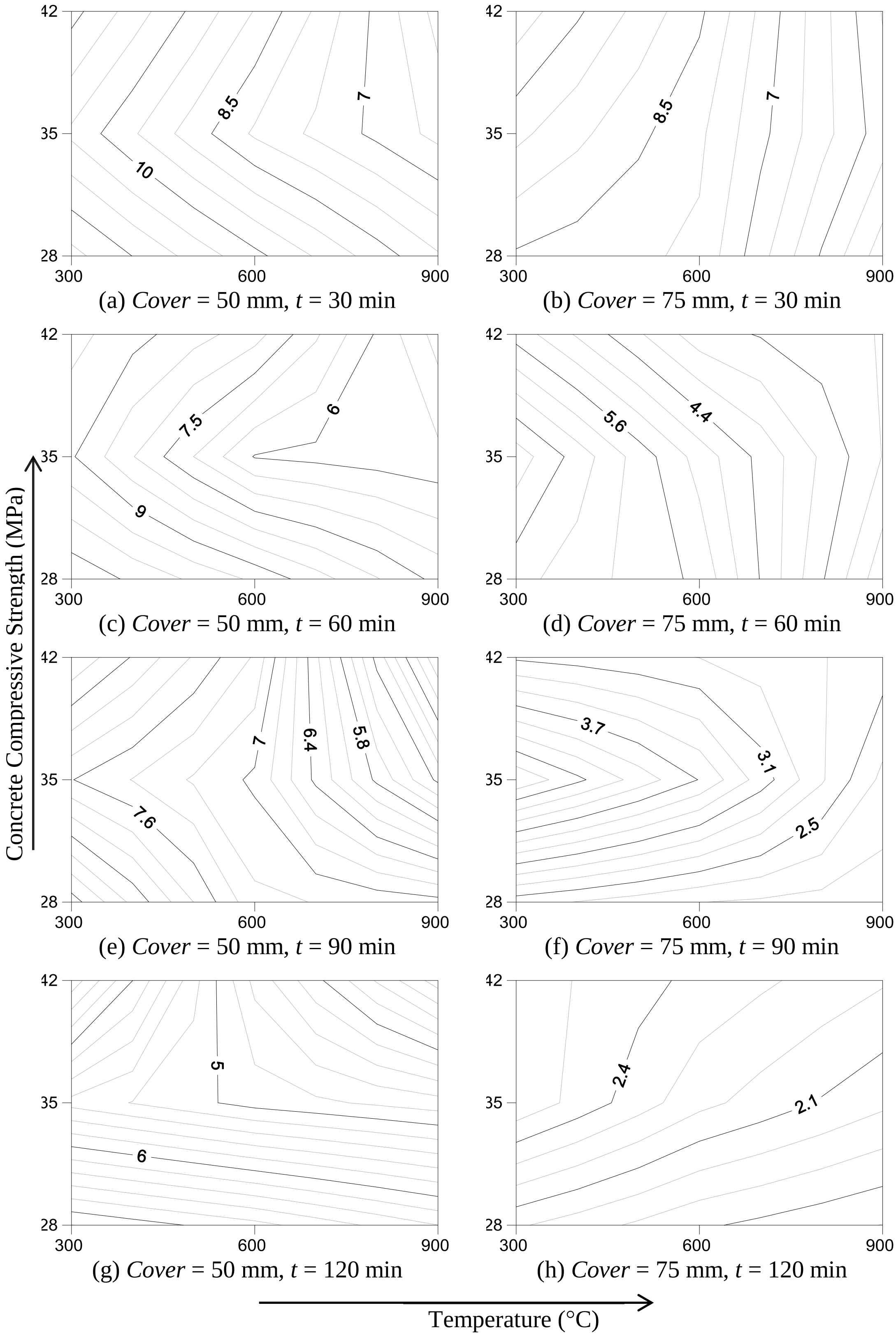

Figure-4.23: Tensile stress (MPa) variation in reinforcement at different temperature and concrete compressive strength for F_y = 500 MPa

D. Effect on Compressive Stress of Steel

The steel in compression zones are observed and the maximum compressive stress of steel is plotted in strength-temperature surface (Figures 4.24 and 4.25).

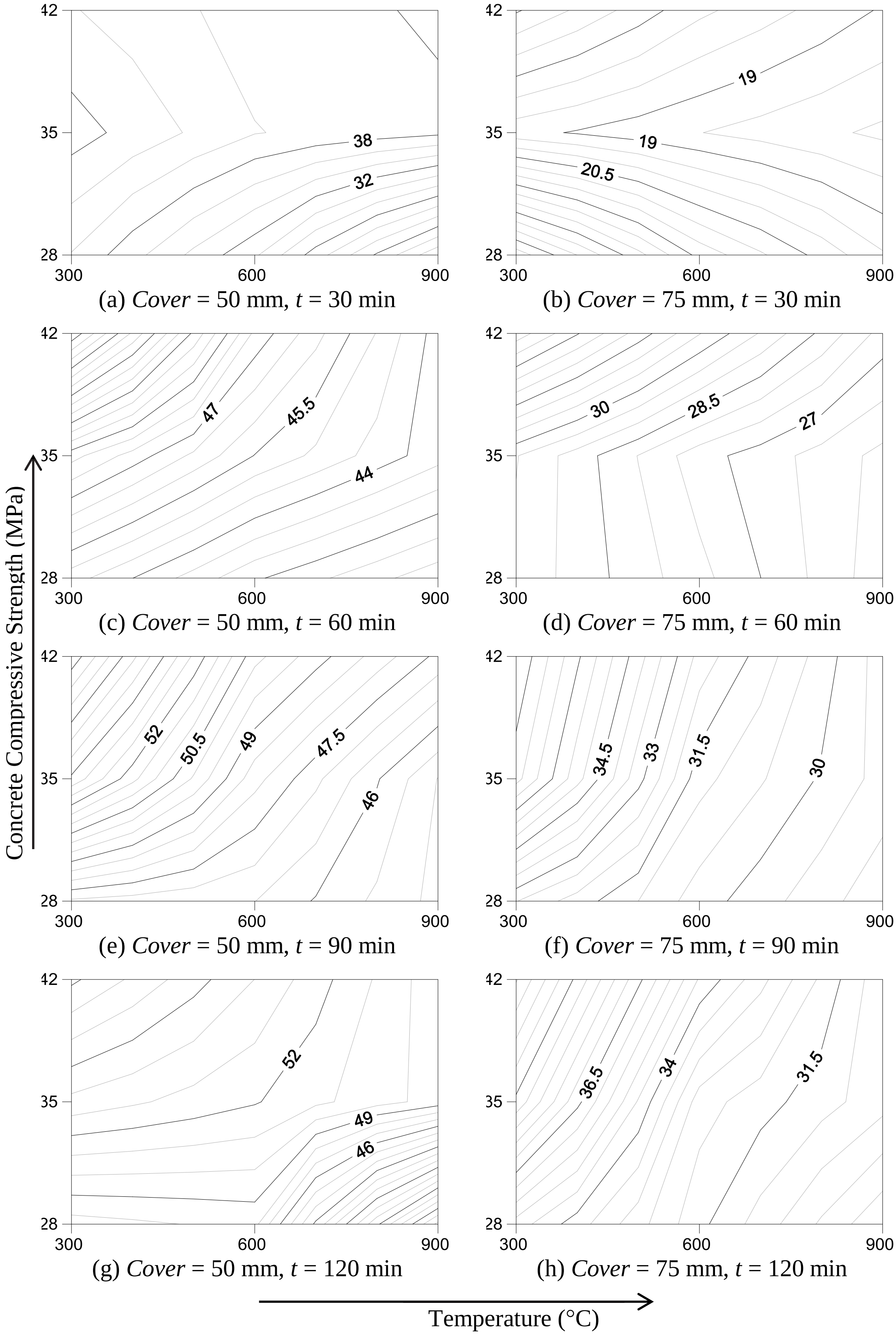

Figure-4.24: Compressive stress (MPa) variation in reinforcement at different temperature and concrete compressive strength for F_y = 400 MPa

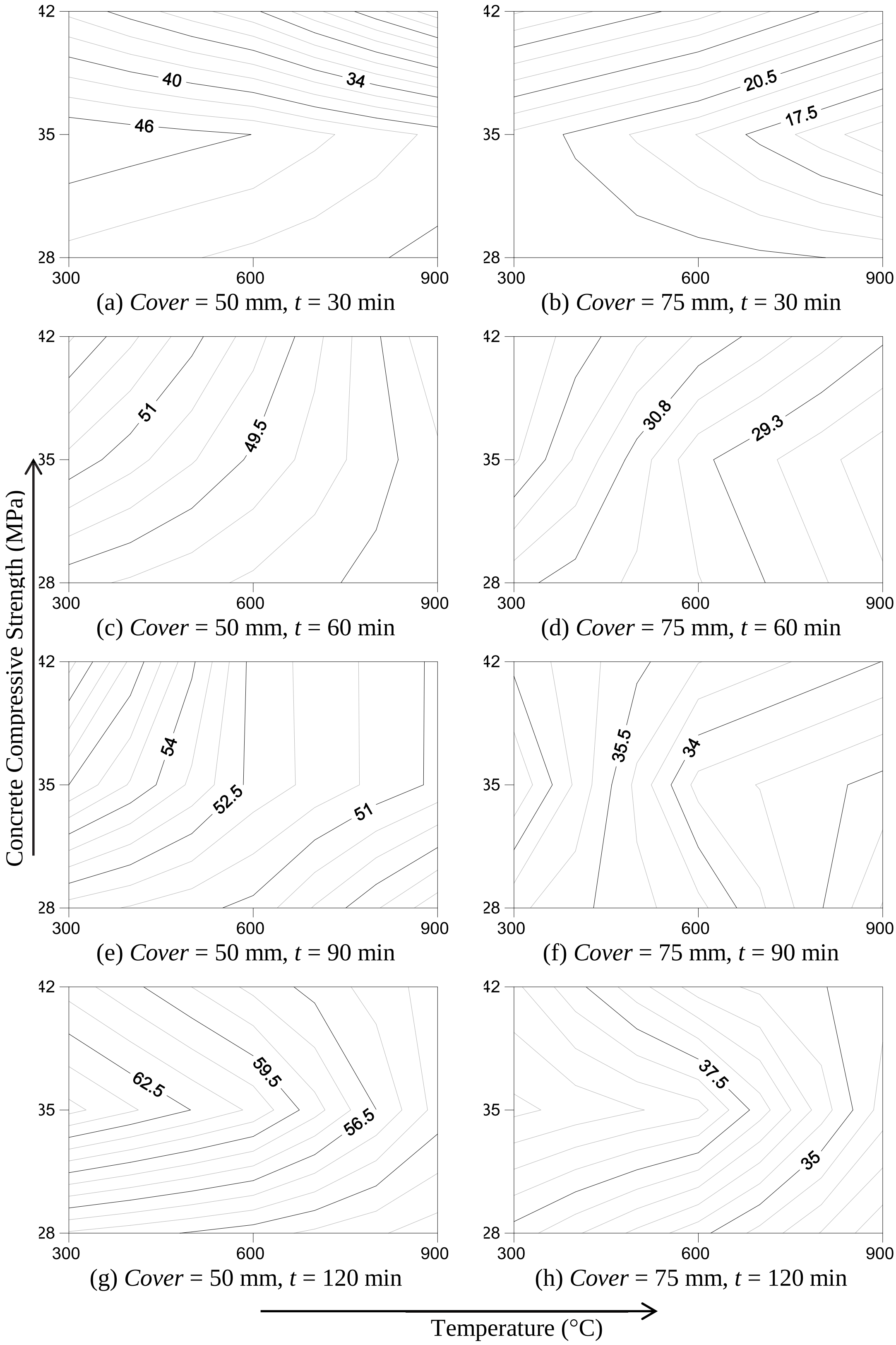

Figure-4.25: Compressive stress (MPa) variation in reinforcement at different temperature and concrete compressive strength for F_y = 500 MPa

The Figures dictate:

i. Compressive stress of steel increased over the increase in concrete strength.

4.2.5 Effect of steel strength

The beams in this research are modelled with reinforcing steel of 2 (Two) yields strengths to observe the effect of steel strength during fire phenomena. All four extracted outputs are plotted in strength-temperature surface to find the subsequent patterns.

A. Effect on Compressive Stress of Concrete

The maximum compressive stress found in the analytical models are plotted in Figures 4.26 and 4.27 for 28MPa and 42 MPa concrete respectively.

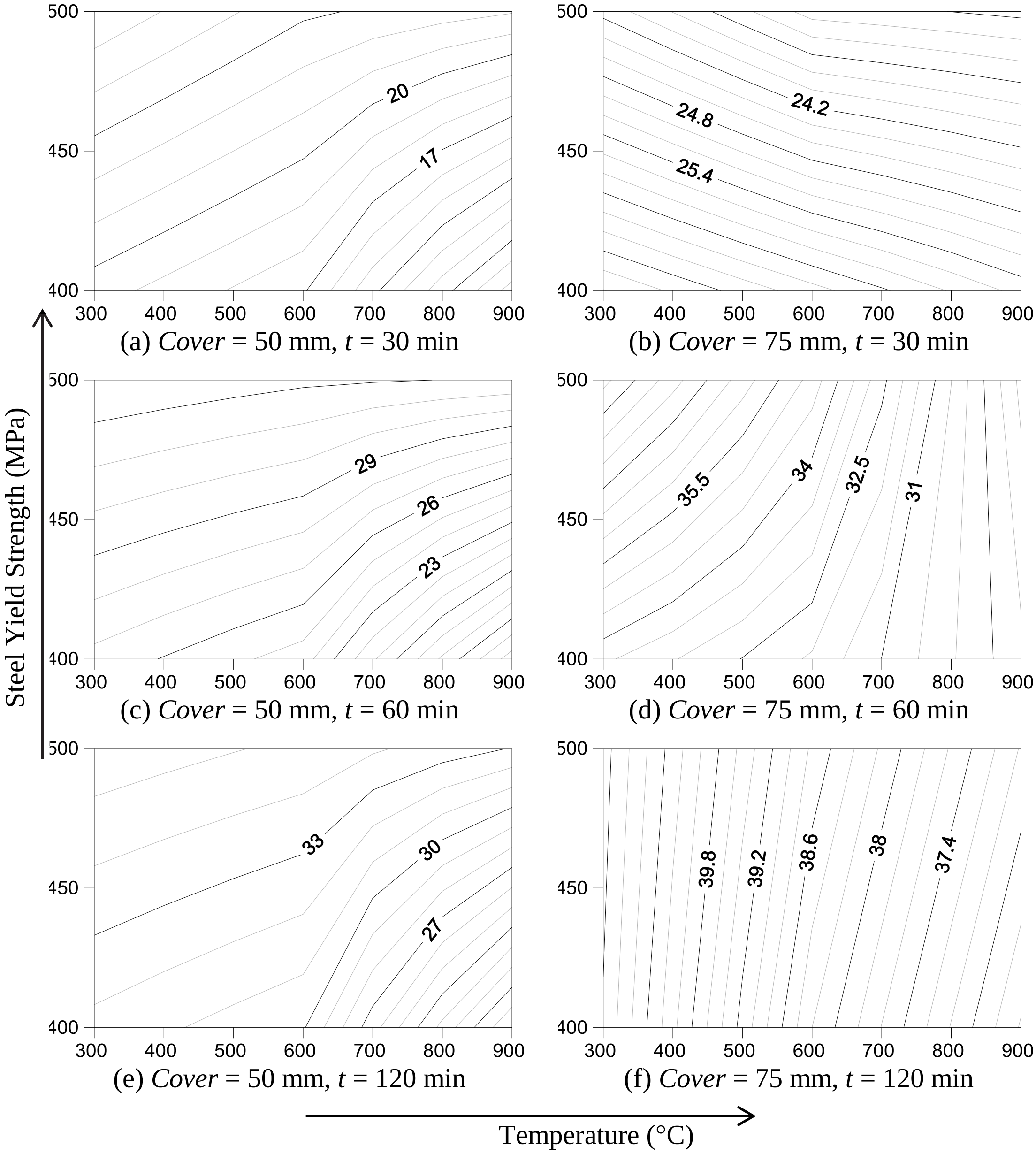

Figure-4.26: Compressive stress (MPa) variation in concrete at different temperature and steel strength for f'$_c$ = 28 MPa

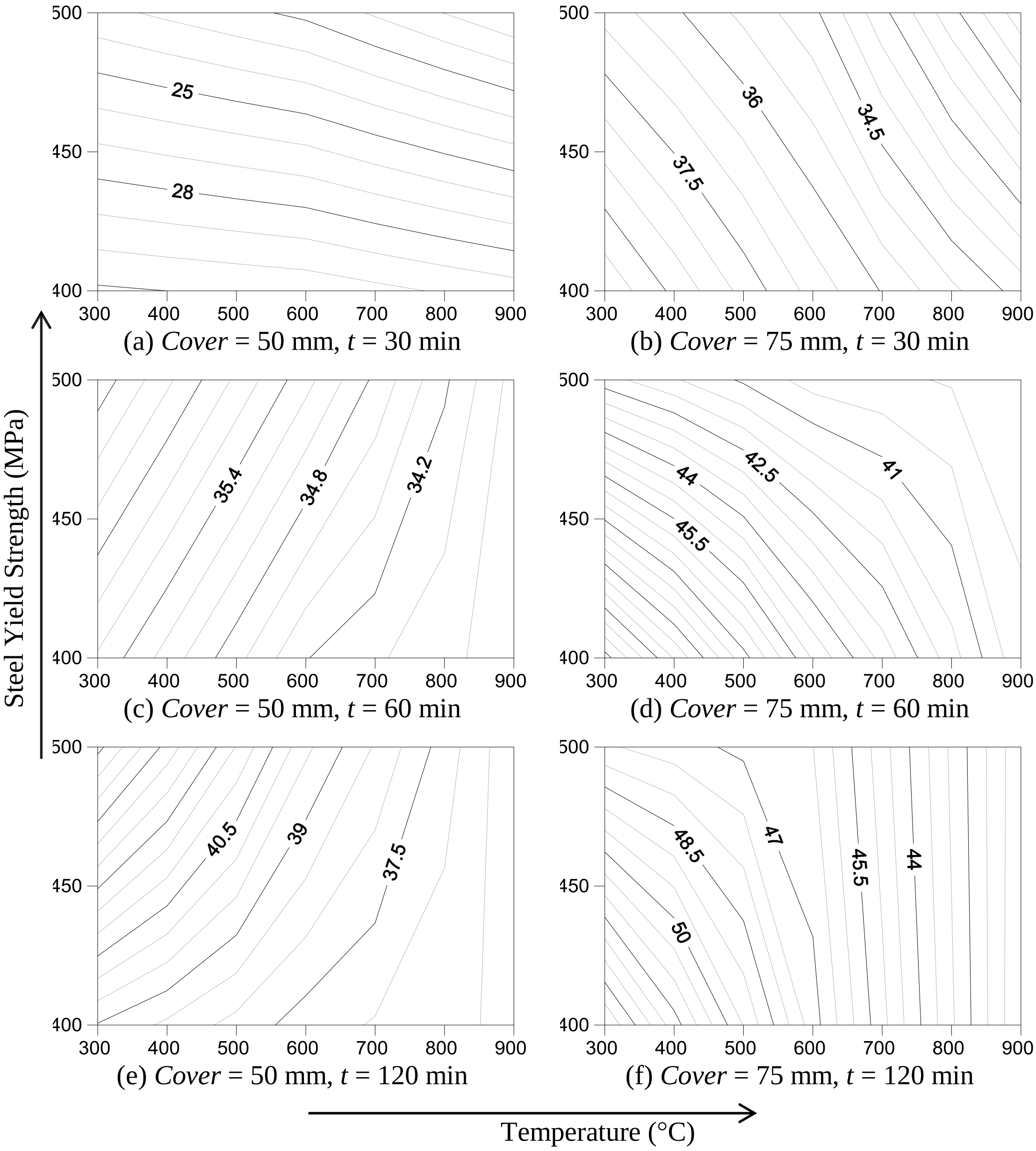

Figure-4.27: Compressive stress (MPa) variation in concrete at different temperature and steel strength for f'$_c$ = 42 MPa

From Figures 4.26 and 4.27, it is evident that:

i. The compressive stress in concrete increased slightly as the steel strength increased.

ii. On high covers, yield strength of concrete has little effect on the compressive stress of concrete if the reinforced concrete section is a compression controlled one.

B. Effect on Tensile Stress of Concrete

The maximum tensile stress of concrete nodes is recorded for each case and plotted in Figures 4.28 and 4.29 to get a comparative pictures of the effect of steel strength. For a definite concrete strength, cover and duration of burning, the contours are plotted in steel strength-temperature surface.

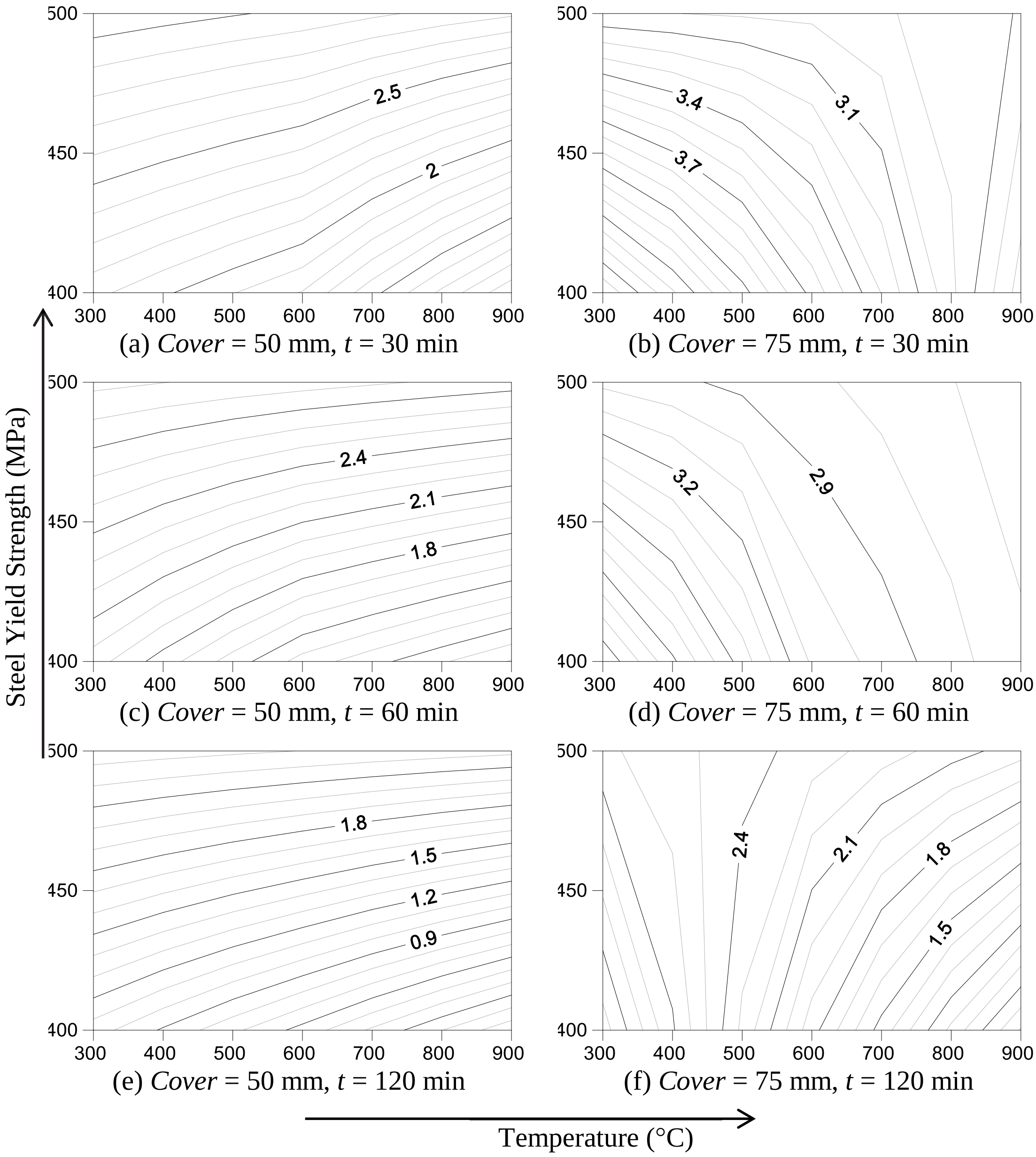

Figure-4.28: Tensile stress (MPa) variation in concrete at different temperature and steel strength for f'_c = 28 MPa

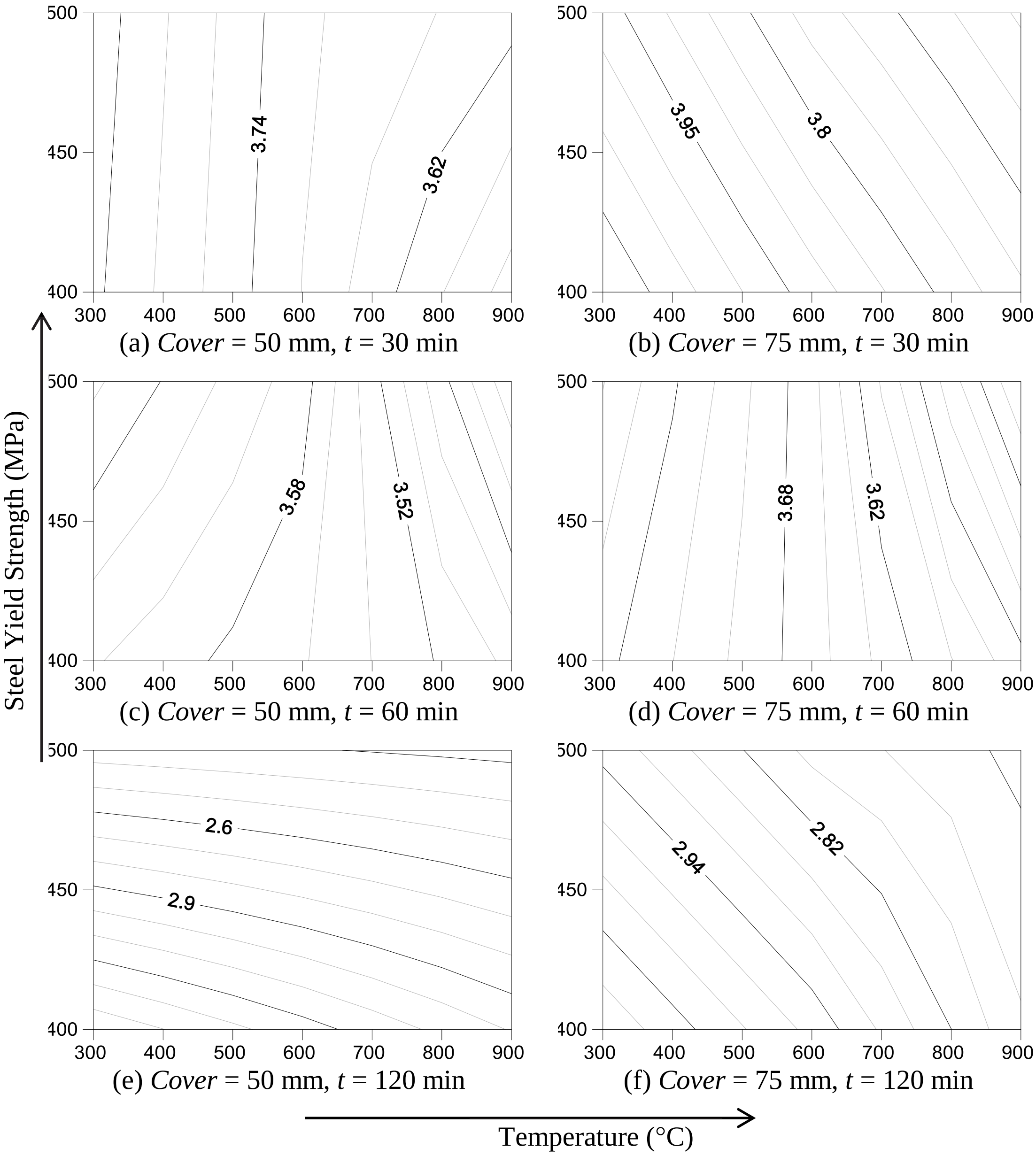

Figure-4.29: Tensile stress (MPa) variation in concrete at different temperature and steel strength for f'_c = 42 MPa

The patterns found in Figures 4.28 and 4.29 dictate that:

i. The tensile stress in concrete slightly increase with the increase in steel yield strength.

ii. Steel yield strength has almost no effect on the tensile stress change in concrete.

C. Effect on Tensile Stress of Steel

The simulated reinforced concrete beams were analyzed by varying the concrete strength, cover dimension and steel strength. They were then analyzed by exerting their respective maximum load by varying temperature and duration of burning. The maximum tensile stress developed from the thermal and mechanical action simultaneously, is plotted in graphical form in Figures 4.30 and 4.31.

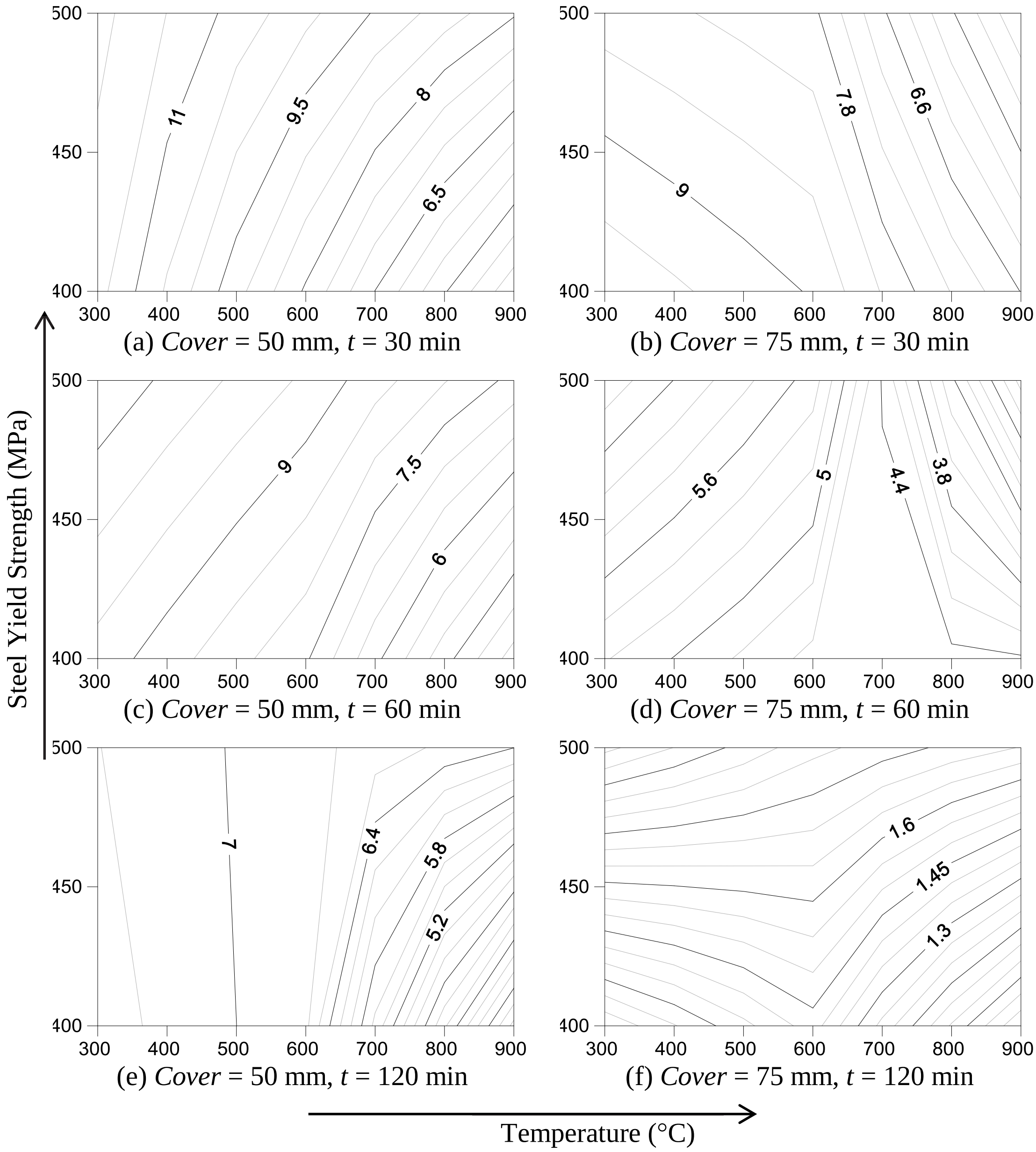

Figure-4.30: Tensile stress (MPa) variation in reinforcement at different temperature and steel strength for f'_c = 28 MPa

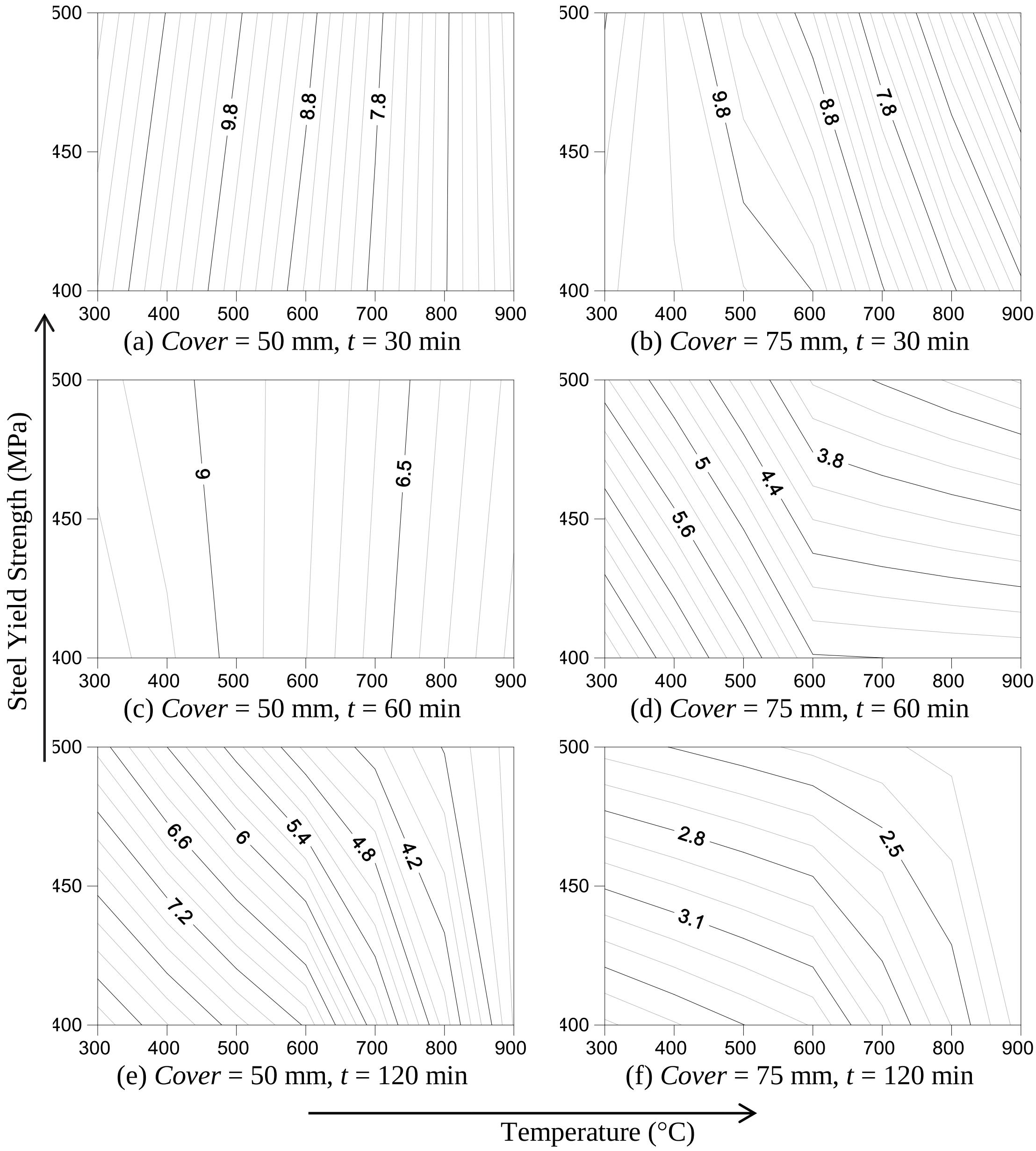

Figure-4.31: Tensile stress (MPa) variation in reinforcement at different temperature and steel strength for f'_c = 42 MPa

The Figures 4.30 and 4.31 clearly show that:

i. The steel strength had little or no effect on the developed tensile stress of the beams. It might happen for the beams had failed in crushing of concrete, hence, steel were not significantly stressed in tension.

D. Effect on Compressive Stress of Steel

The models had shown different compressive stress level of steel, the maximum of which in each case is plotted in Figures 4.32 and 4.33.

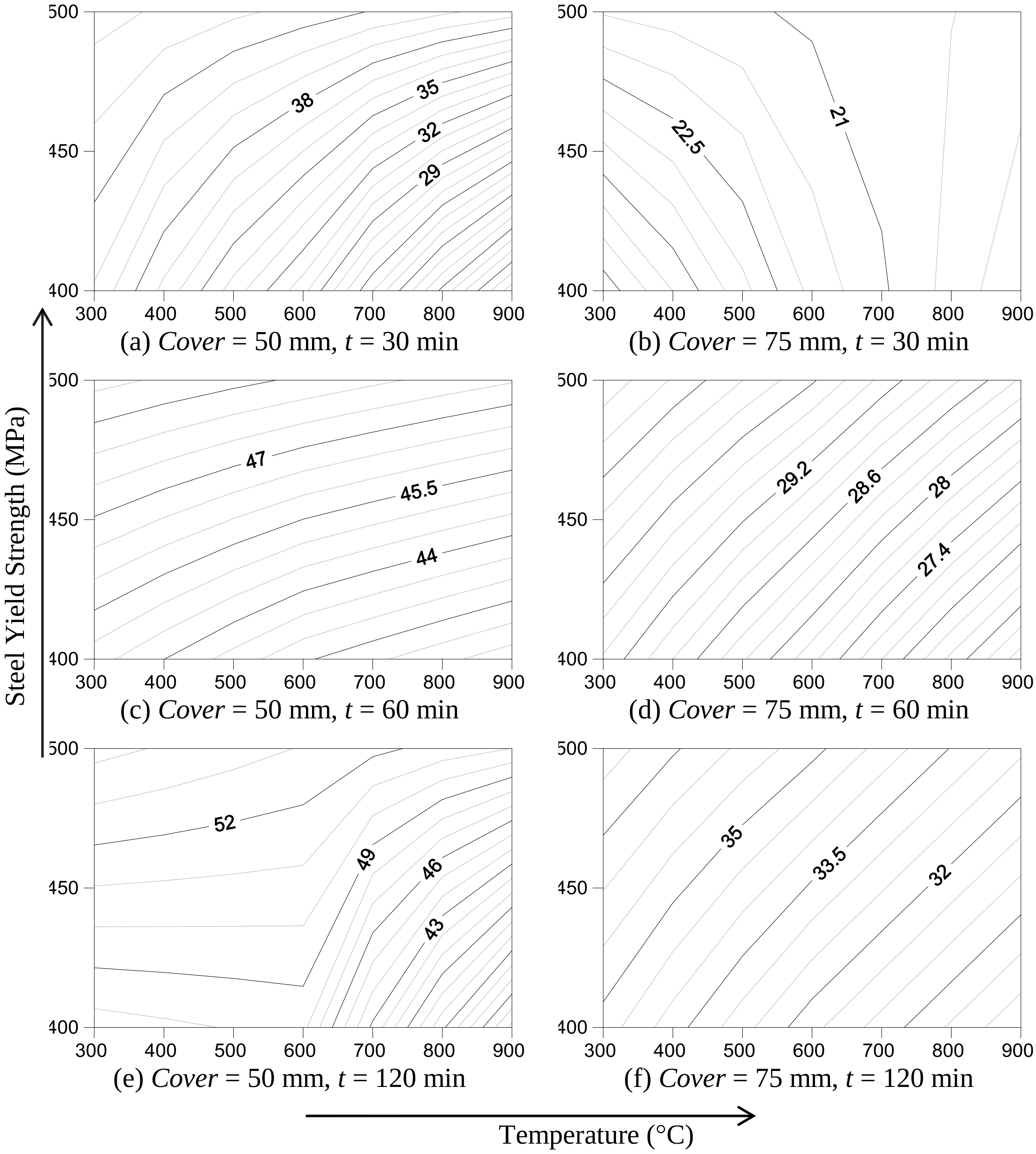

Figure-4.32: Compressive stress (MPa) variation in reinforcement at different temperature and steel strength for f'$_c$ = 28 MPa

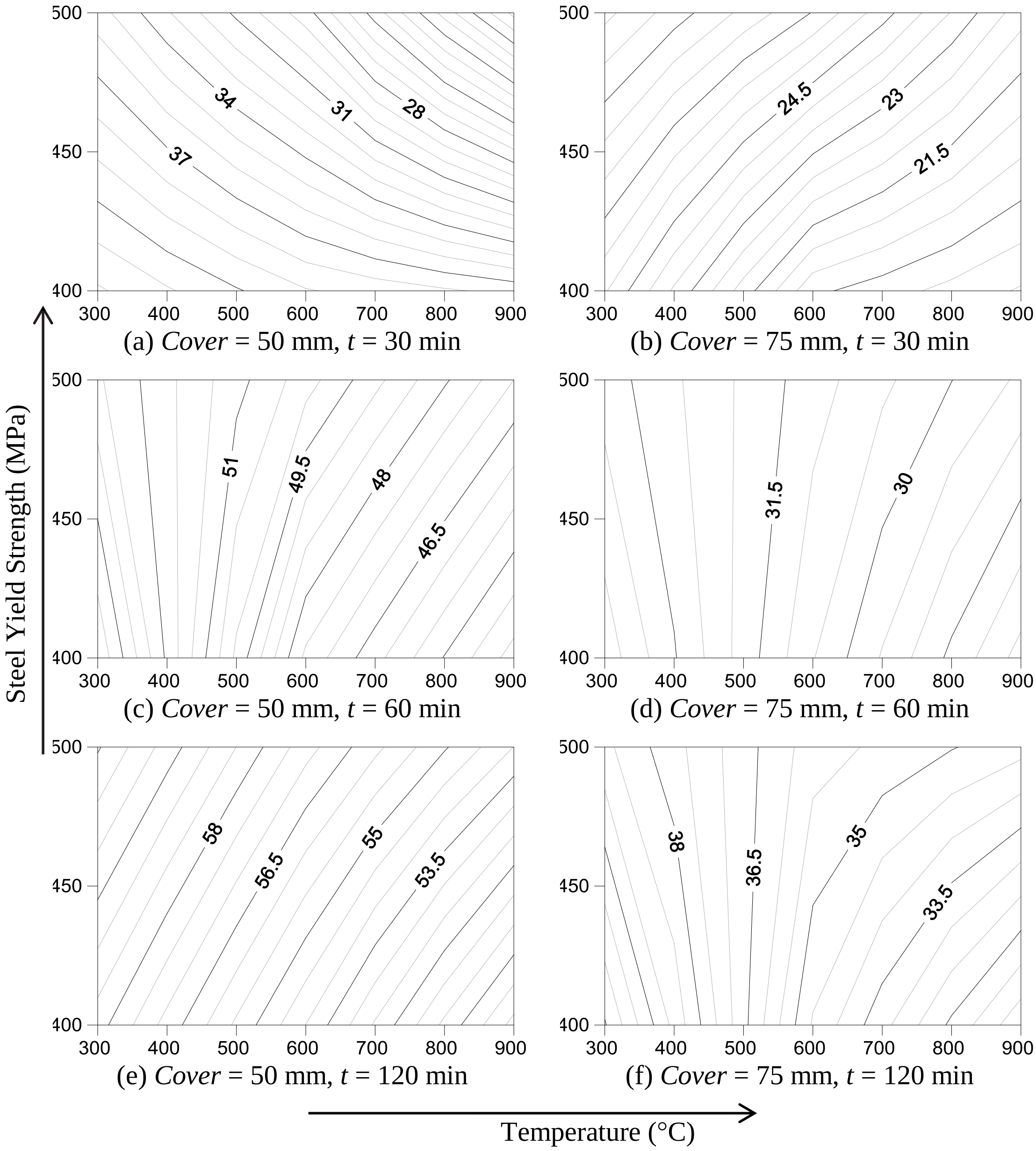

Figure-4.33: Compressive stress (MPa) variation in reinforcement at different temperature and steel strength for f'_c = 42 MPa

The results plotted in Figures 4.32 and 4.33 have revealed that:

i. The maximum compressive stress in reinforcement increases with the increase in steel yield strength.

4.2.6 Effect of reinforcement ratio

The reinforcement ratio plays a vital role in mechanical action of beams. The beams in numerical model are analyzed with different reinforcement ratio to find the correlation of steel ratio with the fire scenario.

A. Effect on Compressive Stress of Concrete

The compressive stress of concrete found from the analyses is plotted in Figure 4.34.

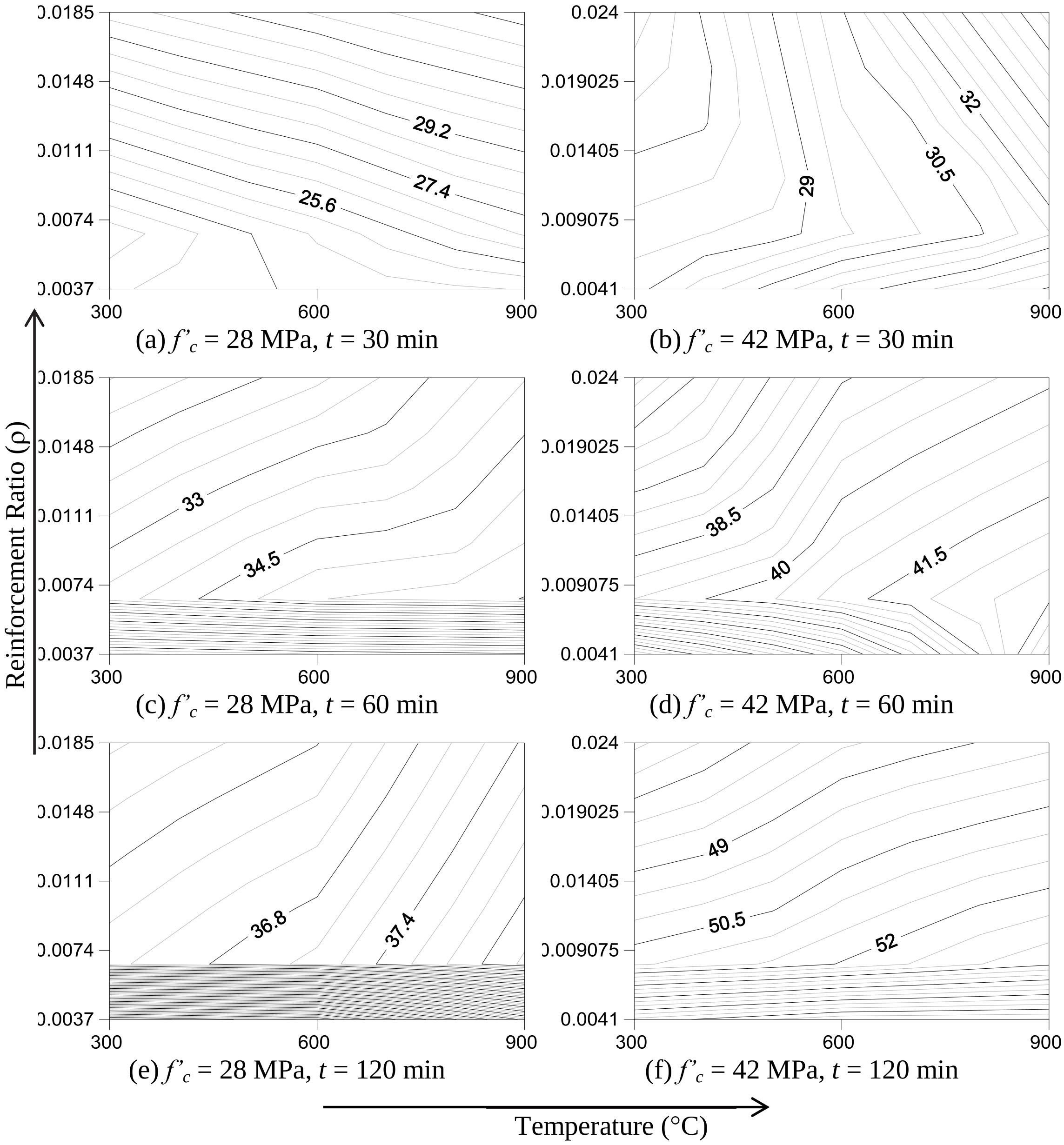

Figure-4.34: Compressive stress (MPa) variation in concrete at different temperature and reinforcement ratio for F_y = 400 MPa, cover = 50mm

Some points can be noted from the patterns in Figure 4.34:

i. For duration below 30minutes, the compressive stress of concrete increases with the increase in reinforcement ratio.

ii. But at higher duration of burning, where the steel is effected by temperature, up to 25% of (ρ_{max} - ρ_{min}) from the ρ_{min}, the compressive stress increased with rebar ratio increment, which is because mechanical action governed in these case. The higher reinforcement ratio showed the opposite effect as thermal action governed there.

B. Effect on Tensile Stress of Concrete

The tensile stress of concrete is plotted in Figure 4.35 below to compare the obtained results.

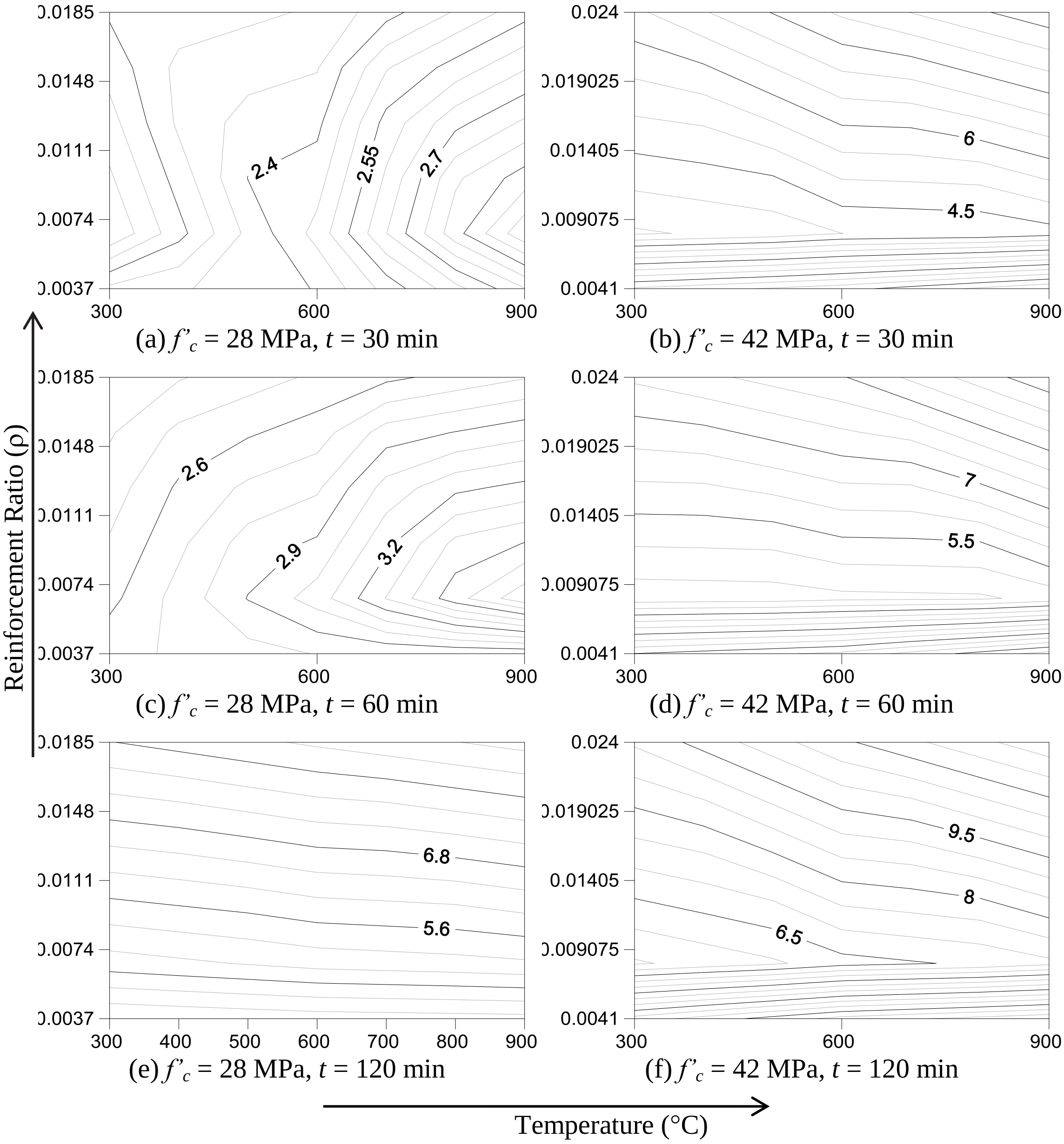

Figure-4.35: Tensile stress (MPa) variation in concrete at different temperature and reinforcement ratio for F_y = 400 MPa, cover = 50mm

It can be noted that:

i. The tensile stress increased slightly with the increase in reinforcement ratio.

C. Effect on Tensile Stress of Steel

The maximum tensile stress found in each case is plotted on rebar percentage-temperature surface in Figure 4.36.

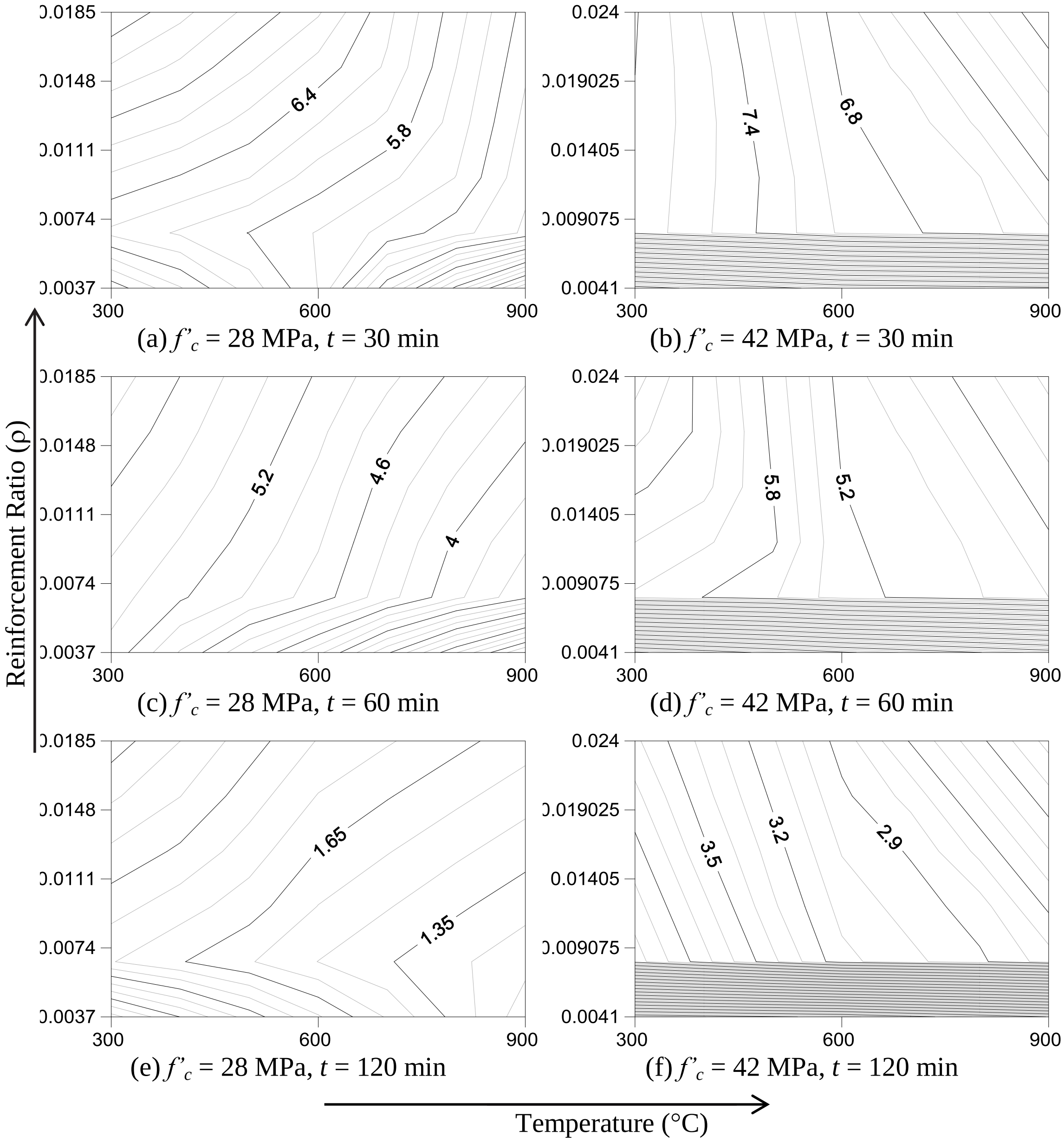

Figure-4.36: Tensile stress (MPa) variation in reinforcement at different temperature and reinforcement ratio for F_y = 400 MPa, cover = 50mm

Figure 4.36 indicates that:

i. Tensile stress in rebar increases very slightly with reinforcement ratio.

D. Effect on Compressive Stress of Steel

The flexural compressive stress of steel found maximum in the numerical analyses are graphed in Figure 4.37.

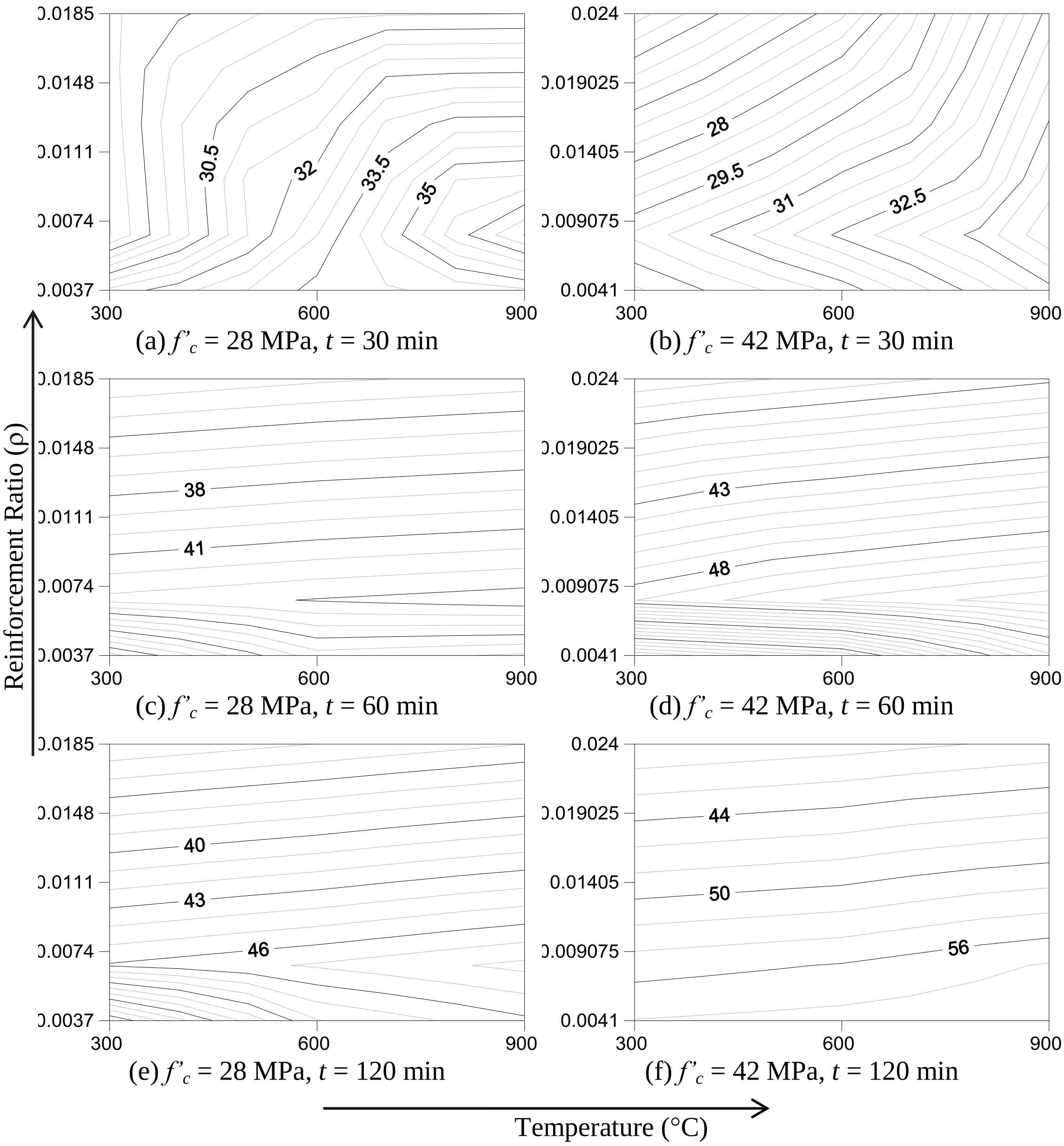

Figure-4.37: Compressive stress (MPa) variation in reinforcement at different temperature and reinforcement ratio for F_y = 400 MPa, cover = 50mm

From Figure 4.37 it is outlined that:

i. With the increase in reinforcement ratio the maximum compressive strength of the reinforcement decreases.

4.2.7 Maximum applied load comparison

The beams modelled were loaded up to maximum capacity. For each combination of parameters, a percentage of P/P_0 was plotted against temperature for a definite rating of fire, where P = Maximum Load Applied at a Temperature for a Definite Time, P_0 = Maximum Load Applied at 20°C. The graphs are plotted in Figures 4.38 to 4.39.

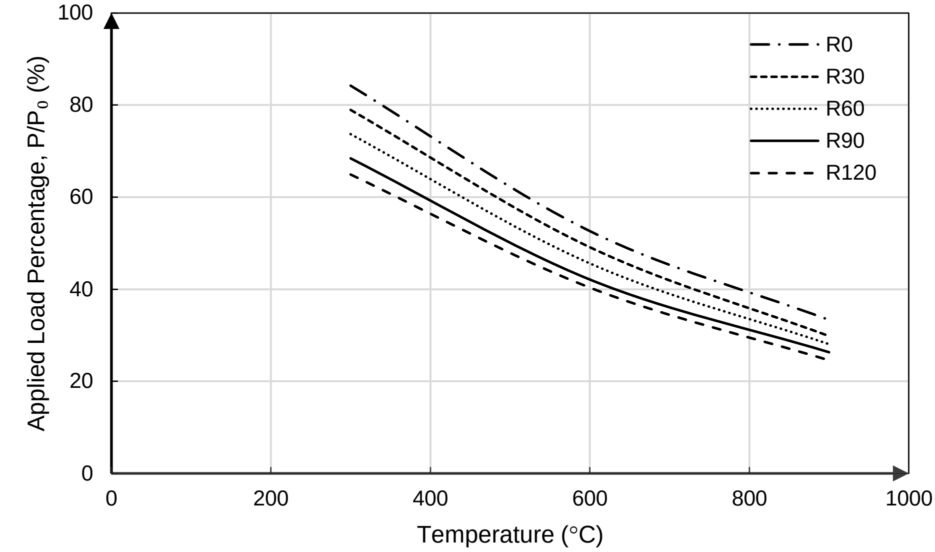

(a) f'_c = 28MPa, Cover = 50mm

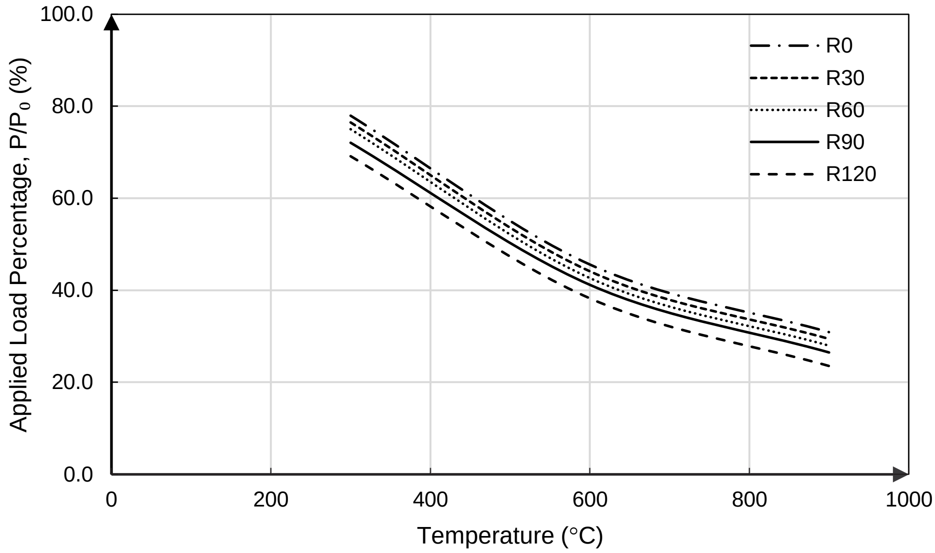

(b) f'_c = 42MPa, Cover = 50mm

Figure-4.38: Applied Load Percentage Vs Temperature Graph for F_y = 400MPa

Figures 4.38 and 4.39 clearly points that:

i. With the increase in temperature, the concrete member can withstand temperature for less time period *i.e.* the rating for fire decreases.

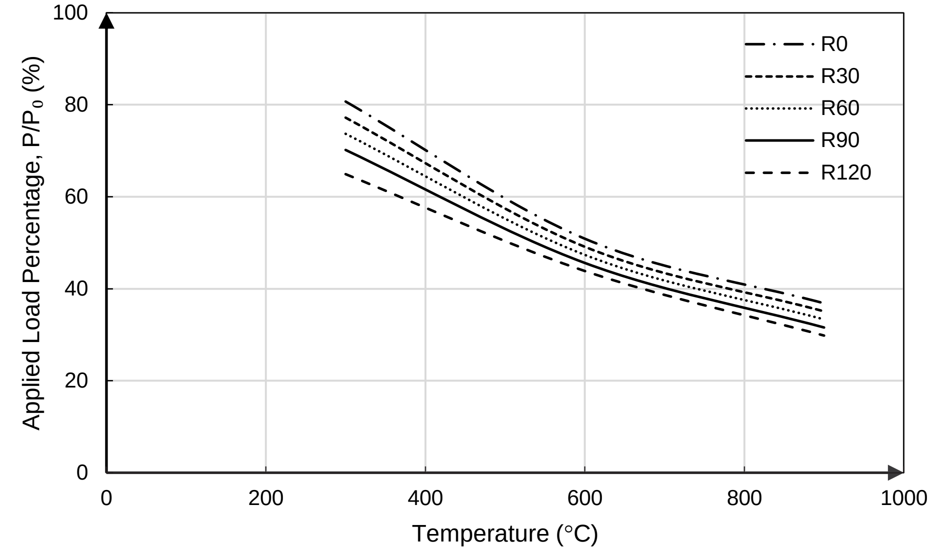

(a) f'c = 28MPa, Cover = 50mm

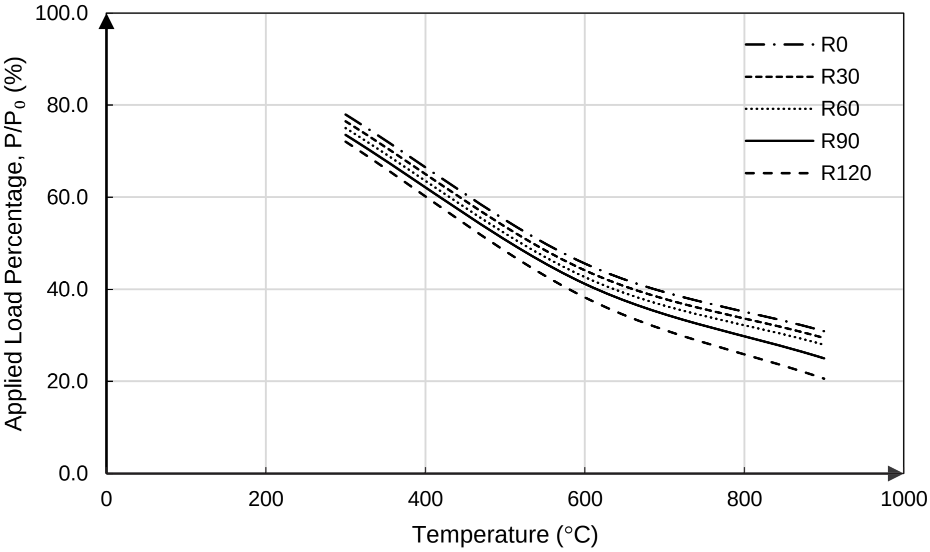

(b) f'c = 42MPa, Cover = 50mm

Figure-4.39: Applied Load Percentage Vs Temperature Graph for F_y = 500MPa

ii. With 0 minute rating *i.e.* just after reaching a temperature, about 20% to 30% reduction in capacity is noticed.

iii. For 28 MPa concrete, the reduction in capacities are dispersed from 65% to 83% for rating of 120 minutes (R120) to R0. Whereas, the reduced initial capacities are less dispersed (70% to 78%) in case of higher strength concrete (42 MPa).

iv. Almost for all strength, at 900°C, beams loaded at 20% of full capacity can withstand the temperature for large duration of 120 minutes (R120).

4.3 Results of Portal Frame Models

In parametric study of portal, the concrete and steel strength were fixed, only the temperature and duration of burning were the variables. A lateral load on top left corner of the portal was applied and analyzed for results. Rising temperature pattern was applied up to target temperature, but then a steady temperature was maintained for the desired duration.

4.3.1 Temperature profiles

The application of temperature for definite period of times gave specific temperature profiles of both the columns and beam of portal. The temperature profile of beam sized 300mm x 400mm with a cover of 50mm is presented in Figures 4.40 to 4.42 for temperature of 300°C, 600°C and 900°C respectively.

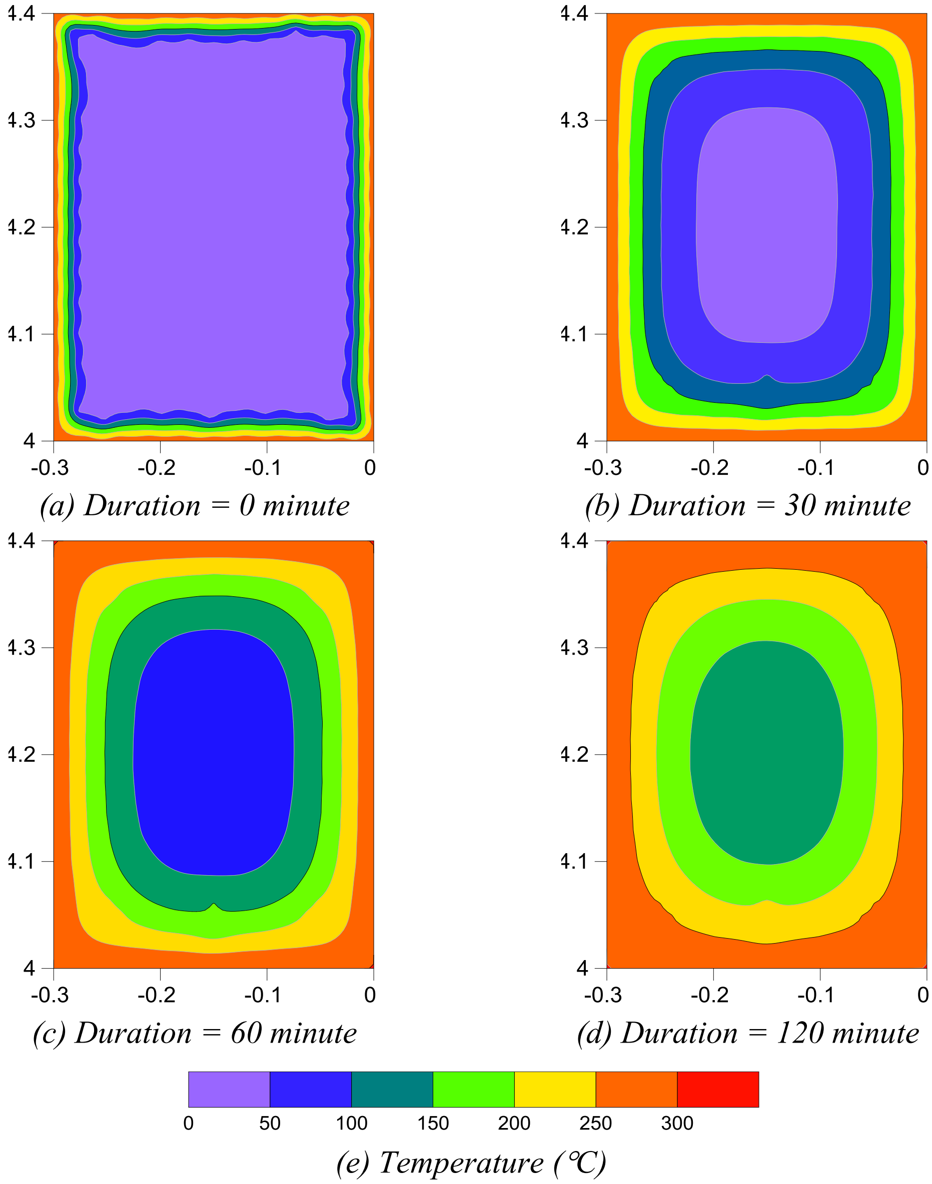

Figure-4.40: Temperature profiles for beam (300mm x 400mm) of portal frame for applied temperature of 300°C

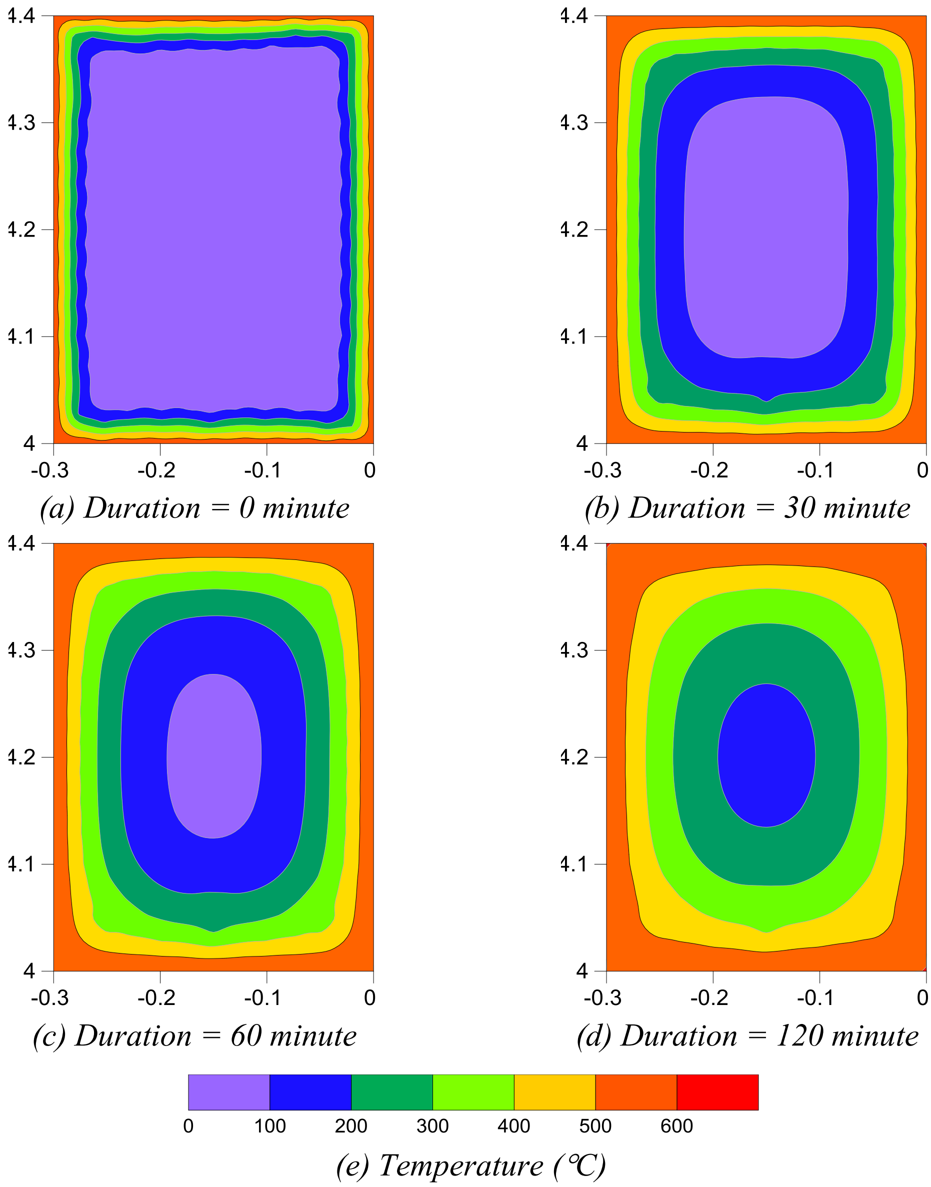

Figure-4.41: Temperature profiles for beam (300mm x 400mm) of portal frame for applied temperature of 600°C

In Figure 4.40, at a temperature level of 300°C maintained for 30minutes, 100°C temperature achieved at 50mm depth of the section, while after 60minutes and 120minutes this value rises to 100mm and 200mm respectively. At 120minutes the temperature fully penetrates the beam section. The reinforcement region is at a temperature of 120°C, 170°C and 220°C after 30minutes, 60minutes and 120minutes respectively.

Figure 4.41 shows the temperature propagated for burning temperature of 600°C. After 30minutes, 60minutes and 120minutes of burning a temperature of 100°C was achieved at a depth of 80mm, 120mm and 200mm respectively. A temperature of 170°C, 280°C and 300°C is observed in reinforcement level after 30, 60 and 120 minutes of burning duration.

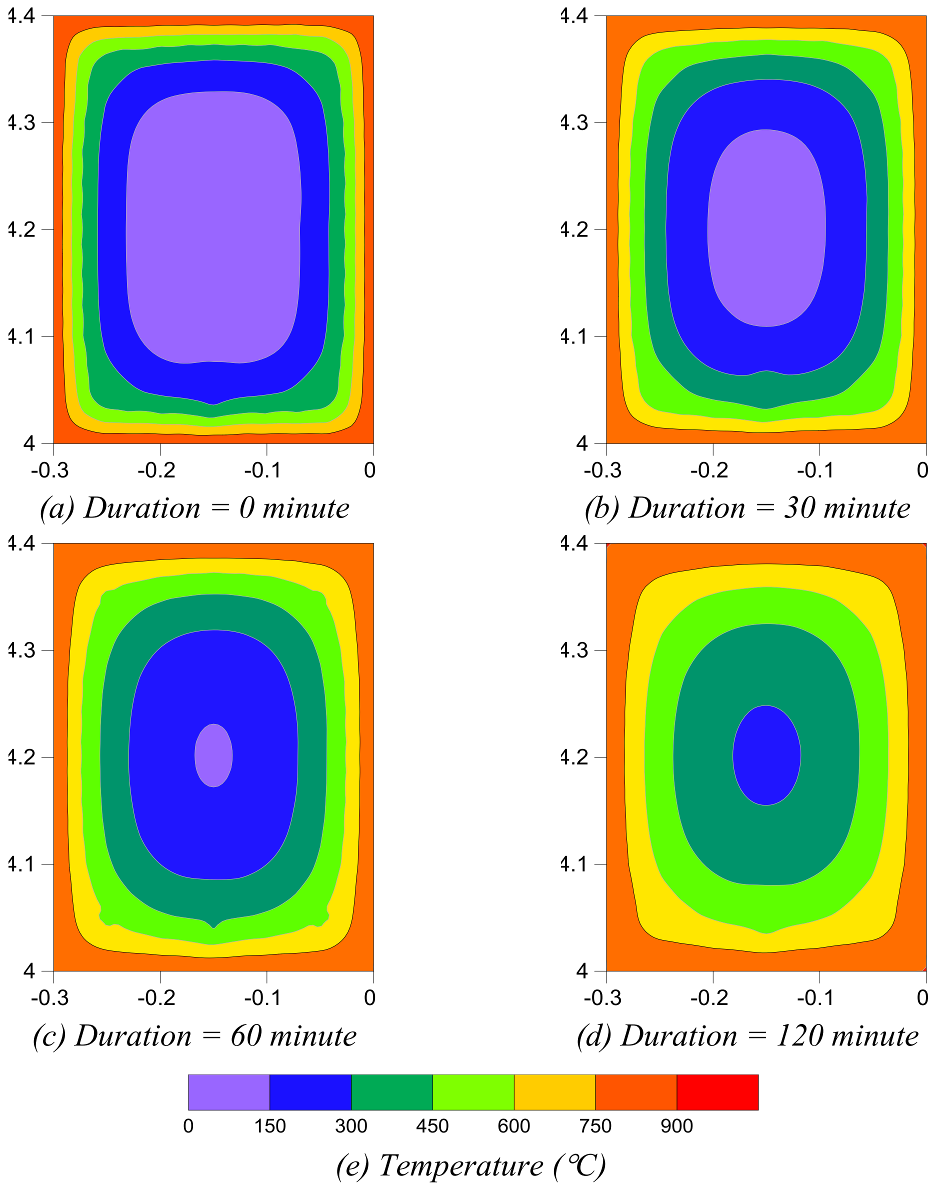

Figure-4.42: Temperature profiles for beam (300mm x 400mm) of portal frame for applied temperature of 900°C

At 900°C temperature, a level of 150°C was achieved at 110mm, 170mm and 200mm depth of the beam section for burning duration of 30, 60 and 120 minutes respectively as shown in Figure 4.42. Reinforcements were at 350°C, 470°C and 620°C temperature level after 30, 60 and 120 minutes respectively.

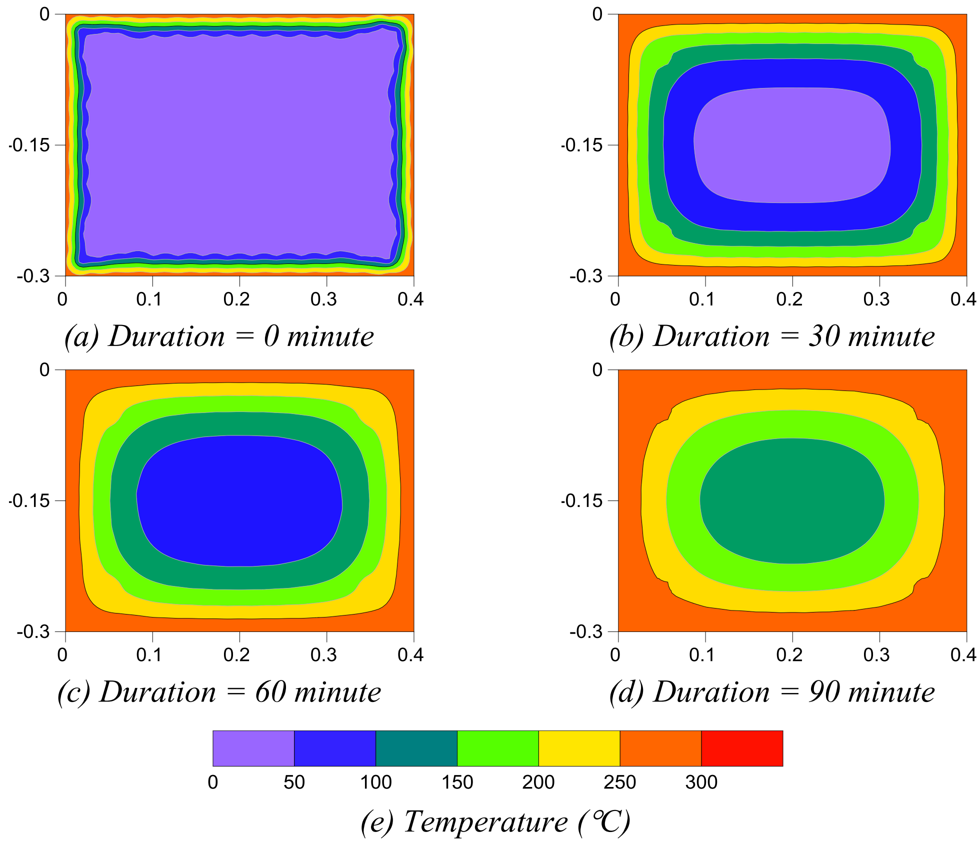

Figure-4.43: Temperature profiles for column (300mm x 400mm) of portal frame for applied temperature of 300°C

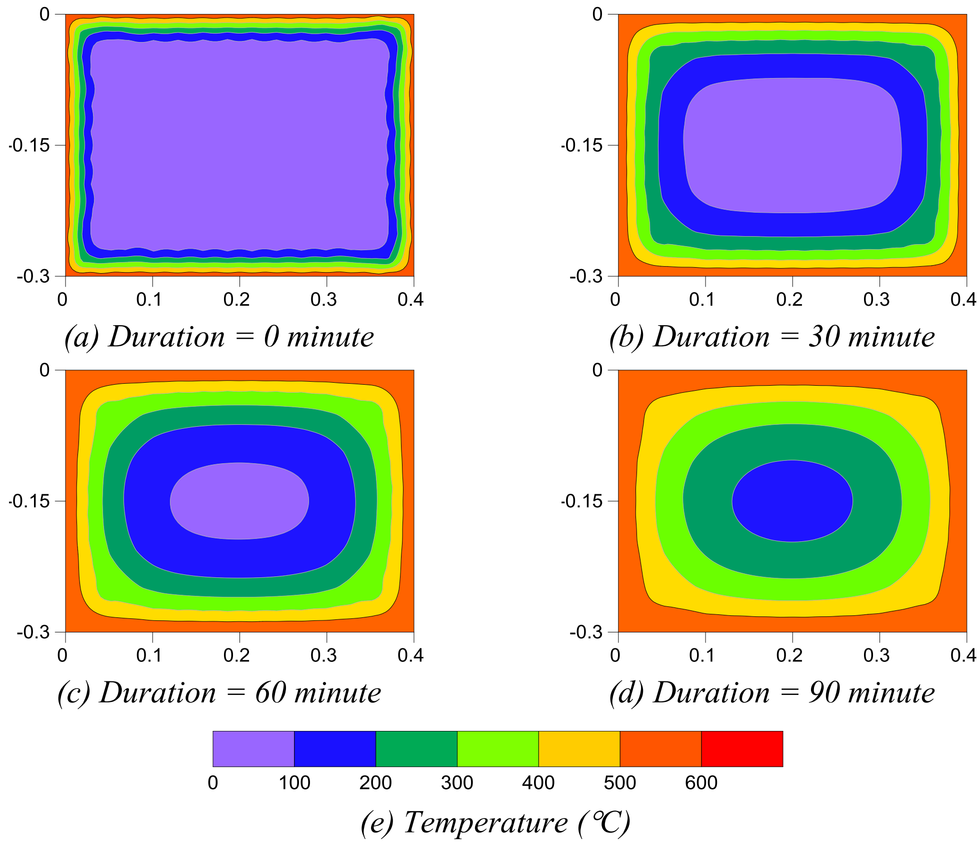

Figure-4.44: Temperature profiles for column (300mm x 400mm) of portal frame for applied temperature of 600°C

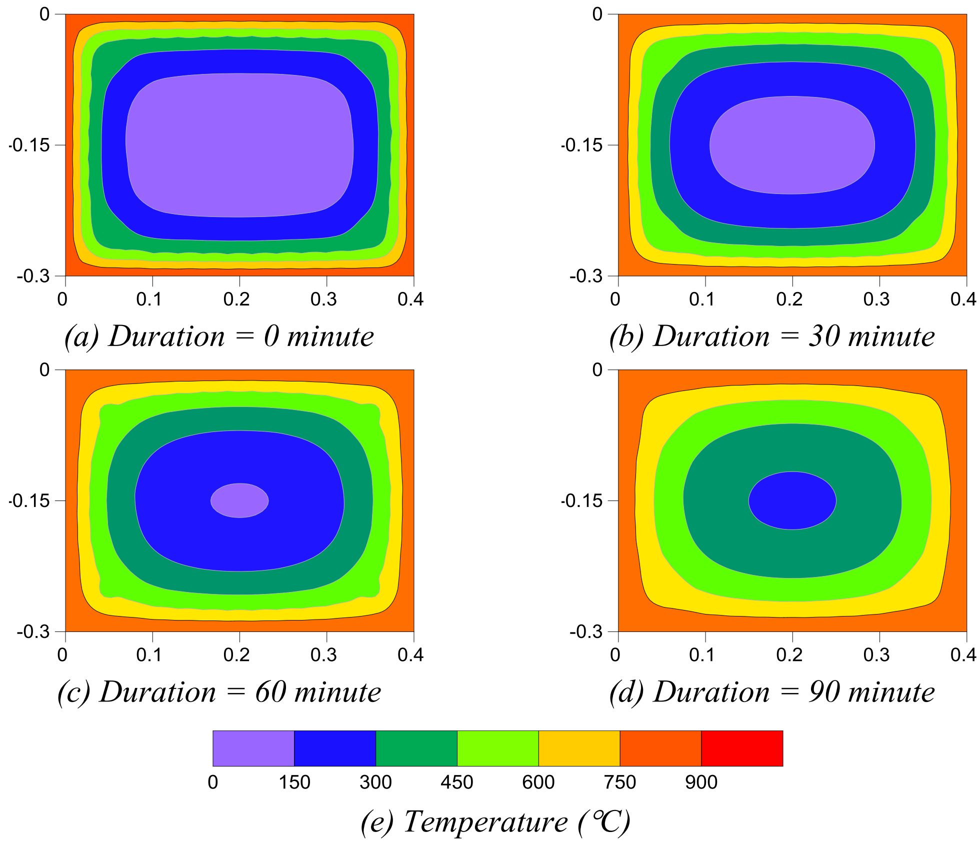

Figure-4.45: Temperature profiles for column (300mm x 400mm) of portal frame for applied temperature of 900°C

The columns of the portal shows the same temperature level throughout the section at specific temperature and duration as visualized in Figures 4.43 to 4.45 for temperature of 300°C, 600°C and 900°C respectively. Since the material properties were same for both beam and columns, the temperature propagated to same level in column section as in beam.

4.3.2 Lateral sway

The lateral sway resulted from the applied lateral load at top left corner of the portal is recorded and plotted in Figure 4.46. Though initially up to 60minutes of burning duration, the sway decreased with the increase in temperature, after 60minutes sway increased for 600°C and 900°C due to thermal action in effect. The deflected shapes of these analyses are given in Appendix-C of this report.

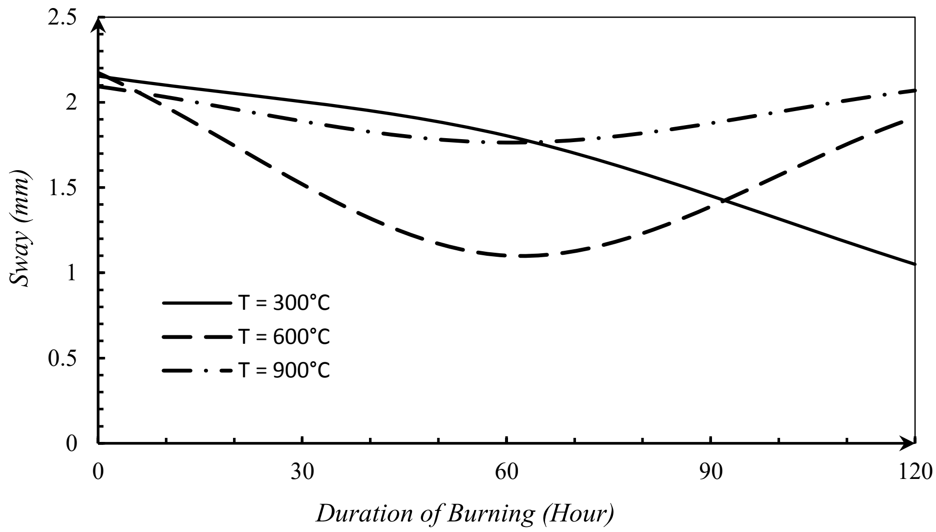

Figure-4.46: Sway Vs Duration of Burning Graph

4.4 Summary

The effect of temperatures depends not only on the intensity and duration of the heat but also on some geometric features such as the location of burning, direction of application of load etc. In this research, the most common scenario of burning from all direction and application of load in direction of gravity was used.

Chapter 5
CONCLUSION AND SUGGESTIONS

5.1 General

A number of numerical analyses was performed to study the effect of temperature on reinforced concrete members. As major component of frame structure, beams of different sectional dimensions and covers were modelled with multiple concrete and steel strength. To closely observe the temperature effect, 300°C, 600°C and 900°C temperatures were applied for a duration as high as 120minutes. Heated beams were loaded to their respective maximum capacity to obtain the compressive and tensile stress generated in concrete and steel both. A wide range of output data was put together to compare the results.

5.2 Conclusion

As basic parameters, compressive and tensile stress of concrete and steel were extracted and compared with input variables to obtain patterns and trends regarding mechanical and thermal action. Considering the data produced from the numerical analysis, few concluding remarks can be made:

(i) For initial 30minutes, reinforcing steels with cover as low as 50mm can withstand temperature as high as 900°C.

(ii) At 900°C, though reinforcing steel shows 150°C temperature, as per BS-EN1992-1-2:2004, steel strength does not degrade significantly.

(iii) For initial 60minutes, concrete in compression is stressed rapidly due to compressive force developed by the thermal action on flexural member.

(iv) For initial 30minutes with any temperature, the concrete can maintain its stress level in the elastic range.

(v) For any combination of concrete and reinforcing steel, flexural members, loaded at less than 20% of its maximum capacity, can withstand large temperature as high as 900°C for 120 minutes (R120).

(vi) Reinforcement ratio has little effect on the thermal degradation.

5.3 Suggestions

During modelling and result compilation, some points were noticed and on basis of these points following suggestions are made:

a) Ideal conditions were considered in the numerical model used in the research. More rigorous and intricate modelling to include the real life scenario is recommended to understand the thermal action completely.

b) The applied temperature and the applied mechanical loads acted in opposite direction in bending. Different configurations for direction of both mechanical and thermal loading must be analyzed to fully comprehend the effect of temperature on reinforced concrete members.

REFERENCES

[1] Islam, M. M. and Adri, N., “Fire Hazard Management of Dhaka City: Addressing Issues Relating to Institutional Capacity and Public Perception”, *Jahangirnagar Planning Review*, vol. 6, June 2008, Jahangirnagar University, pp. 57-67, *(2008)*

[2] Lambert, P., “Cement and Concrete - History and Development”, *World Wide Web: http://www.azom.com/article.aspx?ArticleID=1317#_Background* [02 July 2012], *(2002)*

[3] Isaac, N., “Building History - Cementing History”, in *BUILD*, June/July 2008, pp. 88-89, *(2008)*

[4] Blezard, R. G., “The History of Calcareous Cements”, *Amsterdam: Elsevier Butterworth-Heinemann*, 4th ed., ISBN 9780080535418, pp. 1-24, *(2004)*

[5] Schneider, U., “Concrete at High Temperature - A General Review”, *Fire Safety Journal*, Netherlands, pp. 55-68, *(1988)*

[6] Phan, L. T., “Fire Performance of High Strength Concrete: A Report of the State-of-the-Art”, *National Institute of Standard and Technology*, Gaithersburg University, Maryland, *(1996)*

[7] Castillo, C. and Durrani, A. J., “Effect of Transient High Temperature on High Strength Concrete”, *ACI Materials Journal*, vol.: 87 no. 1, January-February 1990, pp 47-53, *(1990)*

[8] Hertz, K., “Heat Induced Explosion of Dense Concrete”, *Report No.: 166*, Institute of Building Design, Technical University of Denmark, *(1984)*

[9] Hertz, K., “Danish Investigations on Silica Fume Concrete at Elevated Temperature”, *Proceedings, ACI 1991 Spring Convention*, Boston, MA, March 17-21, *(1991)*

[10] Bailey, C., “Holistic Behaviour of Concrete Buildings in Fire”, *Institute of Civil Engineering*, Structures and Buildings 152, Issue 3, pp. 199-212, *(2002)*

[11] Morita, T.; Saito, H. and Kumagai, H., “Residual Mechanical Properties of HSC Members Exposed to High Temperature-Part 1: Test on Material Properties”, *Summaries of Annual Meeting*, Architectural Institute of Japan, Niigata, *(1992)*

[12] Furumura, F.; Abe, T. and Shinohara, Y., “Mechanical Properties of HSC at High Temperatures”, *Proceedings, 4th Weimar Workshop on HSC: Material Properties and Design*, Hochschule fur Architekturund Bauwesen (HAB), Weimar, Germany, pp. 237 - 254, *(1995)*

[13] Felicetti, R.; Gambarova, P.G.; Rosati, G.P.; Corsi, F. and Giannuzzi, G., "Residual Mechanical Properties of HSC Subjected to High-Temperature Cycles", *Proceedings, 4th International Symposium on Utilization of HS/ HPC*, Paris, France, 579-588, *(1996)*

[14] Noumowé, A.; Clastres, P.; Debicki, G. and Costaz, J., "Thermal stresses and water vapor pressure of high performance concrete at high temperature," *in Proceedings of the 4th International Symposium on Utilization of High-Strength/High-Performance Concrete*, Paris, France, *(1996)*

[15] Jensen, J.J; Hammer, T.A; Opheim, E; Hansen, P.A., "Fire Resistance of Lightweight Aggregate Concrete". *Paper presented at the International Symposium on Structural Lightweight Aggregate Concrete*, Sandeford 1995, pp. 192-203, *(1995)*

[16] Sanjayan, G. and Stocks, L., "Spalling of High Strength Concrete in Fire", *ACI Spring Convention*, March 1991, Boston, M. A., *(1991)*

[17] Diederichs, U.; Jumppanen, U. M. and Schneider, U., „„High Temperature Properties and Spalling Behaviour of High Strength Concrete.‟‟ *Proceedings of 4th Weimar Workshop on High Performance Concrete*, HAB Weimar, Germany, pp. 219-236, *(1995)*

[18] Rashidi, M. R. K. S. R., "Fire Effect of the Behaviour of Reinforced Concrete with variable Strengths", *Thesis for M.Sc. in Civil Engineering*, Bangladesh University of Engineering and Technology, *(2013)*

[19] Kadhum, M.M., "Fire Resistance of Reinforced Concrete Rigid Beams", *Journal of Civil Engineering and Construction Technology*, Vol.-5(5), August 2014, pp. 35-48, *(2014)*

[20] Kodur, V. K. R.; Dwaikat, M., "A numerical model for predicting the fire resistance of reinforced concrete beams", *Cement & Concrete Composites*, Elsevier Ltd., Vol. 30, pp. 431-443, *(2008)*

[21] Mundhada, A.R.; Pofale, A.D., "Effect of High Temperature on Compressive Strength of Concrete", *IOSR Journal of Mechanical and Civil Engineering*, Vol.-12, Issue I, Version II, January-February 2015, pp. 66-70, *(2015)*

[22] Lee, J.; Harada, K.; Kang, S.; Kwon, Y. and Yamazaki, M., "Entire and Partial Heating Tests of High Strength Concrete Small Columns", *Proceedings on the 9th Asia-Oceania Symposium on Fire Science and Technology*, International Association for Fire Safety Science, Elsevier Ltd., Vol.-62, pp. 804-812, *(2013)*

[23] Willam, K. J. and Warnke, E. D. "Constitutive Model for the Triaxial Behavior of Concrete", *Proceedings, International Association for Bridge and Structural Engineering*, Vol. 19, ISMES. Bergamo, Italy, pp.174, *(1975)*

Appendix - A

REVIEW ON BS-EN1992-1-2:2004

A.1 General

The Eurocode standards provide common structural design rules for everyday use for the design of whole structures and component products of both a traditional and an innovative nature. Unusual forms of construction or design conditions are not specifically covered and additional expert consideration will be required by the designer in such cases. Eurocode standards recognise the responsibility of regulatory authorities in each Member State and have safeguarded their right to determine values related to regulatory safety matters at national level where these continue to vary from State to State. EN 1992-1-2 describes the Principles, requirements and rules for the structural design of buildings exposed to fire.

A.2 Concrete

The strength and deformation properties of uniaxially stressed concrete at elevated temperatures shall be obtained from the stress-strain relationships as presented in Figure A.1. The stress-strain relationships given in Figure A.1 are defined by two parameters: the compressive strength $f_{c,\theta}$ and the strain $\varepsilon_{c1,\theta}$ corresponding to $f_{c,\theta}$.

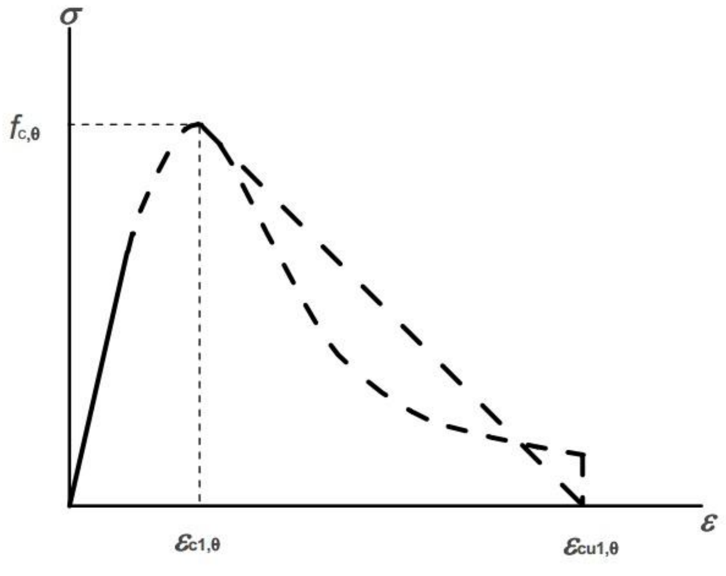

Figure-A.1: Stress-strain relationships of concrete under compression at elevated temperatures

Values for each of these parameters are given in Table A.1 as a function of concrete temperatures. For intermediate values of the temperature, linear interpolation is permitted. Values for $\varepsilon_{cu1,\theta}$ defining the range of the descending branch may be taken from Table A.1.

The ascending branch of the Figure A.1 is governed by the relation:

$$\sigma_\theta = \frac{3\varepsilon f_{c,\theta}}{\varepsilon_{c1,\theta}(2 + (\frac{\varepsilon}{\varepsilon_{c1,\theta}})^3)}; \varepsilon \leq \varepsilon_{c1,\theta} \tag{A.2.1}$$

For $\varepsilon_{c1,\theta} < \varepsilon \leq \varepsilon_{cu1,\theta}$, linear or nonlinear models are permitted, possible strength gain in cooling phase should not be taken into account.

Table-A.1: Values for the main parameters of the stress-strain relationships of normal weight concrete with siliceous or calcareous aggregates concrete at elevated temperatures

Concrete Temp, θ	Siliceous aggregates			Calcareous aggregates		
	$f_{c,\theta}/f_{ck}$	$\varepsilon_{c1,\theta}$	$\varepsilon_{cu1,\theta}$	$f_{c,\theta}/f_{ck}$	$\varepsilon_{c1,\theta}$	$\varepsilon_{cu1,\theta}$
[°C]	[-]	[-]	[-]	[-]	[-]	[-]
20	1.00	0.0025	0.0200	1.00	0.0025	0.0200
100	1.00	0.0040	0.0225	1.00	0.0040	0.0225
200	0.95	0.0055	0.0250	0.97	0.0055	0.0250
300	0.85	0.0070	0.0275	0.91	0.0070	0.0275
400	0.75	0.0100	0.0300	0.85	0.0100	0.0300
500	0.60	0.0150	0.0325	0.74	0.0150	0.0325
600	0.45	0.0250	0.0350	0.60	0.0250	0.0350
700	0.30	0.0250	0.0375	0.43	0.0250	0.0375
800	0.15	0.0250	0.0400	0.27	0.0250	0.0400
900	0.08	0.0250	0.0425	0.15	0.0250	0.0425
1000	0.04	0.0250	0.0450	0.06	0.0250	0.0450
1100	0.01	0.0250	0.0475	0.02	0.0250	0.0475
1200	0.00	-	-	0.00	-	-

The thermal strain $\varepsilon_c(\theta)$ of concrete may be determined from the following with reference to the length at 20°C:

Siliceous aggregate:

$$\varepsilon_c(\theta) = -1.8 \times 10^{-4} + 9 \times 10^{-6}\theta + 2.3 \times 10^{-11}\theta^3; \quad for\ 20°\mathrm{C} \leq \theta \leq 700°\mathrm{C} \tag{A.2.2}$$

$$\varepsilon_c(\theta) = 14 \times 10^{-3}; \quad for\ 700°\mathrm{C} < \theta \leq 1200°\mathrm{C} \tag{A.2.3}$$

Calcareous aggregate:

$$\varepsilon_c(\theta) = -1.2 \times 10^{-4} + 6 \times 10^{-6}\theta + 1.4 \times 10^{-11}\theta^3; \quad for\ 20°\mathrm{C} \leq \theta \leq 805°\mathrm{C} \tag{A.2.4}$$

$$\varepsilon_c(\theta) = 12 \times 10^{-3}; \quad for\ 805°\mathrm{C} < \theta \leq 1200°\mathrm{C} \tag{A.2.5}$$

where θ is the concrete temperature (°C).

The specific heat $c_p(\theta)$ of dry concrete may be determined from the following:

$$c_p(\theta) = 900(\mathrm{JKg^{-1}K^{-1}}); \quad for\ 20°\mathrm{C} \leq \theta \leq 100°\mathrm{C} \tag{A.2.6}$$

$$c_p(\theta) = 900 + (\theta - 100)\ (\mathrm{JKg^{-1}K^{-1}}); \quad for\ 100°\mathrm{C} < \theta \leq 200°\mathrm{C} \tag{A.2.7}$$

$$c_p(\theta) = 1000 + (\theta - 200)/2 \text{ (JKg}^{-1}\text{K}^{-1}\text{)}; \quad for\ 200°C < \theta \leq 400°C \tag{A.2.8}$$

$$c_p(\theta) = 1100 \text{(JKg}^{-1}\text{K}^{-1}\text{)}; \quad for\ 400°C < \theta \leq 1200°C \tag{A.2.9}$$

where θ is the concrete temperature (°C).

Where the moisture content is not considered explicitly in the calculation method, the function given for the specific heat of concrete with siliceous or calcareous aggregates may be modelled by a constant value, $c_{p.peak}$, situated between 100°C and 115°C with linear decrease between 115°C and 200°C.

$$c_{p.peak} = 900 \text{(JKg}^{-1}\text{K}^{-1}\text{)}; \quad \text{for moist. content = 0\% of concrete wt} \tag{A.2.10}$$

$$c_{p.peak} = 1470 \text{ (JKg}^{-1}\text{K}^{-1}\text{)}; \quad \text{for moist. content = 1.5\% of concrete wt} \tag{A.2.11}$$

$$c_{p.peak} = 2020 \text{ (JKg}^{-1}\text{K}^{-1}\text{)}; \quad \text{for moist. content = 3.0\% of concrete wt} \tag{A.2.12}$$

The variation of density with temperature is influenced by the water loss and is defined as follows:

$$\rho(\theta) = \rho(20°C); \quad for\ 20°C \leq \theta \leq 115°C \tag{A.2.13}$$

$$\rho(\theta) = \rho(20°C).\{1 - \frac{0.02(\theta - 115)}{85}\}; \quad for\ 115°C < \theta \leq 200°C \tag{A.2.14}$$

$$\rho(\theta) = \rho(20°C).\{0.98 - \frac{0.03(\theta - 200)}{200}\}; \quad for\ 200°C < \theta \leq 400°C \tag{A.2.15}$$

$$\rho(\theta) = \rho(20°C).\{0.95 - \frac{0.07(\theta - 400)}{800}\}; \quad for\ 400°C < \theta \leq 1200°C \tag{A.2.16}$$

where θ is the concrete temperature (°C).

The thermal conductivity λ_c of concrete may be determined between lower and upper limit values of the following:

The upper limit:

$$\lambda_c = 2 - 0.2451\left(\frac{\theta}{100}\right) + 0.0107\left(\frac{\theta}{100}\right)^2 \text{Wm}^{-1}\text{K}^{-1}; \quad for\ 20°C \leq \theta \leq 1200°C \tag{A.2.17}$$

where θ is the concrete temperature (°C).

The lower limit:

$$\lambda_c = 1.36 - 0.136\left(\frac{\theta}{100}\right) + 0.0057\left(\frac{\theta}{100}\right)^2 \text{Wm}^{-1}\text{K}^{-1}; \quad for\ 20°C \leq \theta \leq 1200°C \tag{A.2.18}$$

where θ is the concrete temperature (°C).

A.3 Reinforcing Steel

The strength and deformation properties of reinforcing steel at elevated temperatures shall be obtained from the stress-strain relationships specified in Figure A.2 and Table A.2. The stress-strain relationships given in Figure A.2 are defined by three parameters: the slope of the linear elastic range $E_{s,\theta}$, the proportional limit $f_{sp,\theta}$ and the maximum stress level $f_{sy,\theta}$. Values for these parameters for hot rolled and cold worked reinforcing steel at elevated temperatures are given in Table A.2.

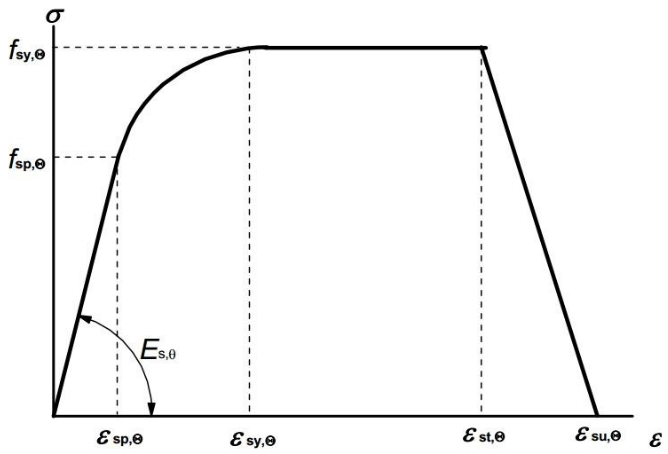

Figure-A.2: Stress-strain relationships of reinforcing steel at elevated temperatures

Table-A.2: Values for the parameters of the stress-strain relationship of hot rolled and cold worked reinforcing steel at elevated temperatures

Steel Temp, θ[°C]	$f_{sy,\theta}/f_{yk}$		$f_{sp,\theta}/f_{yk}$		$E_{s,\theta}/E_s$	
	hot rolled	cold worked	hot rolled	cold worked	hot rolled	cold worked
20	1.00	1.00	1.00	1.00	1.00	1.00
100	1.00	1.00	1.00	0.96	1.00	1.00
200	1.00	1.00	0.81	0.92	0.90	0.87
300	1.00	1.00	0.61	0.81	0.80	0.72
400	1.00	0.94	0.42	0.63	0.70	0.56
500	0.78	0.67	0.36	0.44	0.60	0.40
600	0.47	0.40	0.18	0.26	0.31	0.24
700	0.23	0.12	0.07	0.08	0.13	0.08
800	0.11	0.11	0.05	0.06	0.09	0.06
900	0.06	0.08	0.04	0.05	0.07	0.05
1000	0.04	0.05	0.02	0.03	0.04	0.03
1100	0.02	0.03	0.01	0.02	0.02	0.02
1200	0.00	0.00	0.00	0.00	0.00	0.00

For intermediate values of the temperature, linear interpolation may be used. The formulation of stress-strain relationships may also be applied for reinforcing steel in compression.

The stress for different parts of the stress-strain relationship as depicted in Figure A.2 are as follow:

$$\sigma(\theta) = \varepsilon E_{s,\theta} \text{ for } 0 \leq \varepsilon \leq \varepsilon_{sp,\theta} \tag{A.3.1}$$

$$\sigma(\theta) = f_{sp,\theta} - c + (b/a)\left[a^2 - (\varepsilon_{sy,\theta} - \varepsilon)^2\right]^{0.5} \text{ for } \varepsilon_{sp,\theta} \leq \varepsilon \leq \varepsilon_{sy,\theta} \tag{A.3.2}$$

$$\sigma(\theta) = f_{sy,\theta} \text{ for } \varepsilon_{sy,\theta} \leq \varepsilon \leq \varepsilon_{st,\theta} \tag{A.3.3}$$

$$\sigma(\theta) = f_{sy,\theta}\left[1 - \left(\varepsilon - \varepsilon_{st,\theta}\right)/\left(\varepsilon_{su,\theta} - \varepsilon_{st,\theta}\right)\right] \text{ for } \varepsilon_{st,\theta} \leq \varepsilon \leq \varepsilon_{su,\theta} \tag{A.3.4}$$

$$\sigma(\theta) = 0.00 \text{ for } \varepsilon = \varepsilon_{su,\theta} \tag{A.3.5}$$

The tangent modulus for part of Figure-2.7.4 is:

$$Tangent\ Modulus = E_{s,\theta} \text{ for } 0 \leq \varepsilon \leq \varepsilon_{sp,\theta} \tag{A.3.6}$$

$$Tangent\ Modulus = \frac{b(\varepsilon_{sy,\theta} - \varepsilon)}{a\left[a^2 - (\varepsilon - \varepsilon_{sy,\theta})^2\right]^{0.5}} \text{ for } \varepsilon_{sp,\theta} \leq \varepsilon \leq \varepsilon_{sy,\theta} \tag{A.3.7}$$

$$Tangent\ Modulus = 0 \text{ for } \varepsilon_{sy,\theta} \leq \varepsilon \leq \varepsilon_{st,\theta} \tag{A.3.8}$$

where:

$\varepsilon_{sp,\theta}$ = $f_{sp,\theta}/E_{s,\theta}$

$\varepsilon_{sy,\theta}$ = 0.02

$\varepsilon_{st,\theta}$ = 0.15

$\varepsilon_{su,\theta}$ = 0.20

$$c = \frac{\left(f_{sy,\theta} - f_{sp,\theta}\right)^2}{\left(\varepsilon_{sy,\theta} - \varepsilon_{sp,\theta}\right)E_{s,\theta} - 2(f_{sy,\theta} - f_{sp,\theta})}$$

$$a^2 = \left(\varepsilon_{sy,\theta} - \varepsilon_{sp,\theta}\right)\left(\varepsilon_{sy,\theta} - \varepsilon_{sp,\theta} + c/E_{s,\theta}\right)$$

$$b^2 = c\left(\varepsilon_{sy,\theta} - \varepsilon_{sp,\theta}\right)E_{s,\theta} + c^2$$

The thermal strain $\varepsilon_s(\theta)$ of reinforcing steel may be determined from the following with reference to the length at 20°C:

$$\varepsilon_s(\theta) = -2.416 \times 10^{-4} + 1.2 \times 10^{-5}\theta + 0.4 \times 10^{-8}\theta^2; \quad for\ 20℃ \leq \theta \leq 750℃ \tag{A.3.9}$$

$$\varepsilon_s(\theta) = 11 \times 10^{-3}; \qquad for\ 750℃ < \theta \leq 860℃ \tag{A.3.10}$$

$$\varepsilon_s(\theta) = -6.2 \times 10^{-3} + 2 \times 10^{-5}\theta; for\ 860℃ < \theta \leq 1200℃ \tag{A.3.11}$$

Appendix - B

ANSYS LITERATURE REVIEW

B.1 General

Ansys, Inc. is an American public company based in Canonsburg, Pennsylvania. It develops and markets engineering simulation software. Though initially, Ansys software is used to design products and semiconductors, as well as to create simulations that test a product's durability, temperature distribution, fluid movements, and electromagnetic properties; Ansys develops and markets finite element analysis software used to simulate engineering problems. The software creates simulated computer models of structures, electronics, or machine components to simulate strength, toughness, elasticity, temperature distribution, electromagnetism, fluid flow, and other attributes. Ansys is used to determine how a product will function with different specifications, without building test products or conducting crash tests.

B.2 Structural Fundamentals

ANSYS uses some fundamental structural properties.

B.2.1 Stress-strain relationship

The stress induced in linear materials is related to the strains by:

$$\{\sigma\} = [D]\{\varepsilon^{el}\} \qquad \text{(B.2.1)}$$

Where:

$\{\sigma\}$	=	stress vector = $[\sigma_x\ \sigma_y\ \sigma_z\ \sigma_{xy}\ \sigma_{yz}\ \sigma_{xz}]^T$
$[D]$	=	elasticity or elastic stiffness matrix or stress-strain matrix
$\{\varepsilon^{el}\}$	=	$\{\varepsilon\} - \{\varepsilon^{th}\}$ = elastic strain vector
$\{\varepsilon\}$	=	total strain vector = $[\varepsilon_x\ \varepsilon_y\ \varepsilon_z\ \varepsilon_{xy}\ \varepsilon_{yz}\ \varepsilon_{xz}]^T$
$\{\varepsilon^{th}\}$	=	thermal strain vector (defined in Eqaution-2.1.3)

The stress vector is shown in the Figure B.1 below:

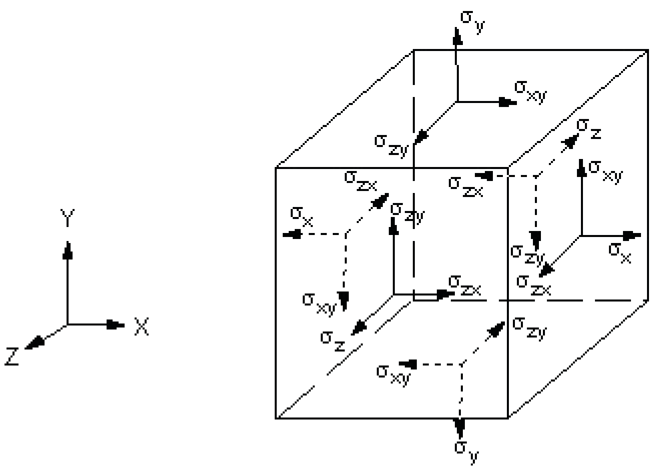

Figure-B.1: Stress vector definition

Equation-B.2.1 may also be inverted to:

$$\{\varepsilon\} = \{\varepsilon^{th}\} + [D]^{-1}\{\sigma\} \tag{B.2.2}$$

For the 3-D case, the thermal strain vector is:

$$\{\varepsilon^{th}\} = \Delta T[\alpha_x^{se} \quad \alpha_y^{se} \quad \alpha_z^{se} \quad 0 \quad 0 \quad 0]^T \tag{B.2.3}$$

where:

α_x^{se} = secant coefficient of thermal expansion in the x-direction

ΔT = $T - T_{ref}$

T = current temperature at the point of question

T_{ref} = reference (strain-free) temperature

The flexibility or compliance matrix, $[D]^{-1}$ is:

$$[D]^{-1} = \Delta T \begin{bmatrix} 1/E_x & -\nu_{xy}/E_x & -\nu_{xz}/E_x & 0 & 0 & 0 \\ -\nu_{yx}/E_y & 1/E_y & -\nu_{yz}/E_y & 0 & 0 & 0 \\ -\nu_{zx}/E_z & -\nu_{zy}/E_z & 1/E_z & 0 & 0 & 0 \\ 0 & 0 & 0 & 1/G_{xy} & 0 & 0 \\ 0 & 0 & 0 & 0 & 1/G_{yz} & 0 \\ 0 & 0 & 0 & 0 & 0 & 1/G_{xz} \end{bmatrix}^T \tag{B.2.4}$$

Where typical terms are:

E_x = Young's modulus in the x-direction

ν_{xy} = major Poisson's ratio

ν_{yx} = minor Poisson's ratio

G_{xy} = shear modulus in the xy-plane

Also, $[D]^{-1}$ matrix is presumed to be symmetric, so that:

$$\frac{\nu_{yx}}{E_y} = \frac{\nu_{xy}}{E_x} \tag{B.2.5}$$

$$\frac{\nu_{zx}}{E_z} = \frac{\nu_{xz}}{E_x} \tag{B.2.6}$$

$$\frac{\nu_{zy}}{E_z} = \frac{\nu_{yz}}{E_y} \tag{B.2.7}$$

Expanding Equation-B.2.2 with Equation-B.2.3 through Equation-B.2.7 and writing out the six equations explicitly,

$$\varepsilon_x = \alpha_x \Delta T + \frac{\sigma_x}{E_x} - \frac{\nu_{xy}\sigma_y}{E_x} - \frac{\nu_{xz}\sigma_z}{E_x} \tag{B.2.8}$$

$$\varepsilon_y = \alpha_y \Delta T - \frac{\nu_{xy}\sigma_x}{E_x} + \frac{\sigma_y}{E_y} - \frac{\nu_{yz}\sigma_z}{E_y} \tag{B.2.9}$$

$$\varepsilon_z = \alpha_z \Delta T - \frac{\nu_{xz}\sigma_x}{E_x} - \frac{\nu_{yz}\sigma_y}{E_y} + \frac{\sigma_z}{E_z} \tag{B.2.10}$$

$$\varepsilon_{xy} = \frac{\sigma_{xy}}{G_{xy}} \tag{B.2.11}$$

$$\varepsilon_{yz} = \frac{\sigma_{yz}}{G_{yz}} \tag{B.2.12}$$

$$\varepsilon_{xz} = \frac{\sigma_{xz}}{G_{xz}} \tag{B.2.13}$$

Where typical terms are:

ε_x	=	direct strain in the x-direction
σ_x	=	direct stress in the x-direction
ε_{xy}	=	shear strain in the xy-plane
σ_{xy}	=	shear stress in the xy-plane

Alternatively, Equation-B.2.1 may be expanded by first inverting Equation-B.2.4 and then combining the result with Equation-B.2.3 and Equation-B.2.5 through Equation-B.2.7 to give six explicit equations:

$$\begin{aligned}\sigma_x = {} & \frac{E_x}{h}\left(1-\left(\nu_{yz}\right)^2\frac{E_z}{E_y}\right)(\varepsilon_x-\alpha_x\Delta T) \\ & +\frac{E_y}{h}\left(\nu_{xy}+\nu_{xz}\nu_{yz}\frac{E_z}{E_y}\right)\left(\varepsilon_y-\alpha_y\Delta T\right) \\ & +\frac{E_z}{h}\left(\nu_{xz}+\nu_{yz}\nu_{xy}\right)(\varepsilon_z-\alpha_z\Delta T)\end{aligned} \tag{B.2.14}$$

$$\begin{aligned}\sigma_y = {} & \frac{E_y}{h}\left(\nu_{xy}+\nu_{xz}\nu_{yz}\frac{E_z}{E_y}\right)(\varepsilon_x-\alpha_x\Delta T) \\ & +\frac{E_y}{h}\left(1-(\nu_{xz})^2\frac{E_z}{E_x}\right)\left(\varepsilon_y-\alpha_y\Delta T\right) \\ & +\frac{E_z}{h}\left(\nu_{yz}+\nu_{xz}\nu_{xy}\frac{E_y}{E_x}\right)(\varepsilon_z-\alpha_z\Delta T)\end{aligned} \tag{B.2.15}$$

$$\begin{aligned}\sigma_z = {} & \frac{E_z}{h}\left(\nu_{xz}+\nu_{yz}\nu_{xy}\right)(\varepsilon_x-\alpha_x\Delta T) \\ & +\frac{E_z}{h}\left(\nu_{yz}+\nu_{xz}\nu_{xy}\frac{E_y}{E_x}\right)\left(\varepsilon_y-\alpha_y\Delta T\right) \\ & +\frac{E_z}{h}\left(1-\left(\nu_{xy}\right)^2\frac{E_y}{E_x}\right)(\varepsilon_z-\alpha_z\Delta T)\end{aligned} \tag{B.2.16}$$

$$\sigma_{xy} = G_{xy}\varepsilon_{xy} \tag{B.2.17}$$

$$\sigma_{yz} = G_{yz}\varepsilon_{yz} \tag{B.2.18}$$

$$\sigma_{xz} = G_{xz}\varepsilon_{xz} \tag{B.2.19}$$

Where,

$$h = 1-\left(\nu_{xy}\right)^2\frac{E_y}{E_x}-\left(\nu_{yz}\right)^2\frac{E_z}{E_y}-(\nu_{xz})^2\frac{E_z}{E_x}-2\nu_{xy}\nu_{yz}\nu_{xz}\frac{E_z}{E_x} \tag{B.2.20}$$

The shear moduli G_{xy}, G_{yz} and G_{xz} may be derived by:

$$G_{xy} = G_{yz} = G_{xz} = \frac{E_x}{2\left(1 + \nu_{xy}\right)} \tag{B.2.20}$$

B.2.2 Temperature-dependent coefficient of thermal expansion

Considering a typical component, the thermal strain from Equation-B.2.3 is:

$$\varepsilon^{th} = \alpha^{se}(T)(T - T_{ref}) \tag{B.2.21}$$

Where,

$\alpha^{se}(T)$ = temperature-dependent secant coefficient of thermal expansion

$\alpha^{se}(T)$ is computed from $\varepsilon^{ith}(T)$ by rearranging Equation-B.2.21:

$$\alpha^{se} = \frac{\varepsilon^{ith}(T)}{(T - T_{ref})} \tag{B.2.21}$$

Equation-B.1.21 assumes that, when $T = T_{ref}$, $\varepsilon^{ith} = 0$. If this is not the case, the ε^{ith} data is shifted automatically by a constant so that it is true. α^{se} at T_{ref} is calculated based on the slopes data points. Hence, if the slopes of the ε^{ith} above and below T_{ref} are not identical, a step change in α^{se} at T_{ref} will be computed.

$\varepsilon^{ith}(T)$ (thermal strain) is related to $\alpha^{in}(T)$ by:

$$\varepsilon^{ith}(T) = \int_{T_{ref}}^{T} \alpha^{in}(T)dT \tag{B.2.22}$$

Combining Equation-B.2.21 and Equation-B.2.22,

$$\alpha^{se} = \frac{\int_{T_{ref}}^{T} \alpha^{in}(T)dT}{(T - T_{ref})} \tag{B.2.23}$$

Again,

$$\varepsilon_0^{th} = \alpha_0^{se}(T)(T - T_0) = \int_{T_0}^{T} \alpha^{in} dT \tag{B.2.24}$$

$$\varepsilon_r^{th} = \alpha_r^{se}(T)\left(T - T_{ref}\right) = \int_{T_{ref}}^{T} \alpha^{in} dT \tag{B.2.25}$$

Equation-B.2.24 and Equation-B.2.25 represent the thermal strain at a temperature T for two different starting points, T_0 and T_{ref}. The right hand side of the Equation-B.2.24 may be expanded as:

$$\int_{T_0}^{T} \alpha^{in} dT = \int_{T_0}^{T_{ref}} \alpha^{in} dT + \int_{T_{ref}}^{T} \alpha^{in} dT \tag{B.2.26}$$

also,

$$\int_{T_0}^{T_{ref}} \alpha^{in} dT = \alpha_0^{se}(T_{ref})(T_{ref} - T_0) \quad \text{(B.2.27)}$$

or,

$$\int_{T_0}^{T_{ref}} \alpha^{in} dT = \alpha_r^{se}(T_0)(T_{ref} - T_0) \quad \text{(B.2.28)}$$

Combining Equation-B.2.24 through Equation-B.2.27,

$$\alpha_r^{se}(T) = \alpha_0^{se}(T) + \frac{T_{ref} - T_0}{T - T_{ref}}\left(\alpha_0^{se}(T) - \alpha_0^{se}(T_{ref})\right) \quad \text{(B.2.29)}$$

Equation-B.2.29 is non-linear. If $T_{ref} = T_0$, Equation-B.2.29 is trivial. If $T = T_{ref}$, Equation-B.2.29 is undefined.

B.3 Derivation of Structural Matrices

The principle of virtual work states that a virtual (very small) change of the internal strain energy must be offset by an identical change in external work due to the applied loads, or:

$$\delta U = \delta V \quad \text{(B.3.1)}$$

where:

U	=	strain energy (internal work) = $U_1 + U_2$
V	=	external work = $V_1 + V_2 + V_3$
δ	=	virtual operator

The virtual strain energy is:

$$\delta U_1 = \int_0^{vol} \{\delta\varepsilon\}\{\sigma\} d(vol)^T \quad \text{(B.3.2)}$$

where:

$\{\varepsilon\}$	=	strain vector
$\{\sigma\}$	=	stress vector
vol	=	volume of element

Continuing the derivation assuming linear material and geometry, Equation-B.3.1 and Equation-B.3.2 are combined as:

$$\delta U_1 = \int_0^{vol} (\{\delta\varepsilon\}^T[D]\{\varepsilon\} - \{\delta\varepsilon\}^T[D]\{\varepsilon^{th}\}) d(vol) \quad \text{(B.3.3)}$$

The strains may be related to the nodal displacement by:

$$\{\varepsilon\} = [B]\{u\} \quad \text{(B.3.4)}$$

where:

$[B]$	=	strain-displacement matrix, based on the element shape functions
$\{u\}$	=	nodal displacement vector

It is assumed that all effects are in global Cartesian system. Combining Equation-B.3.3 with Equation-B.3.4, and noting that $\{u\}$ does not vary over the volume:

$$\begin{aligned}\delta U_1 = \{\delta u\}^T \int_0^{vol} [B]^T[D][B]d(vol)\{u\} \\ - \{\delta u\}^T \int_0^{vol} [B]^T[D][\varepsilon^{th}]d(vol)\end{aligned} \tag{B.3.5}$$

Another form of virtual strain energy is when a surface moves against a distributed resistance, as in a foundation stiffness. This may be written as:

$$\delta U_2 = \int_0^{area_f} \{\delta w_n\}^T\{\sigma\}d(area_f) \tag{B.3.6}$$

where:

$\{w_n\}$	=	motion normal to the surface
$\{\sigma\}$	=	stress (or pressure) carried by the surface
$area_f$	=	area of the distributed resistance

Both $\{w_n\}$ and $\{\sigma\}$ usually have only one nonzero component. The point-wise normal displacement is related to the nodal displacements by:

$$\{w_n\} = [N_n]\{u\} \tag{B.3.7}$$

where:

$[N_n]$	=	matrix of shape functions for normal motions at the surface

The stress, $\{\sigma\}$, is

$$\{\sigma\} = k\{w_n\} \tag{B.3.8}$$

where:

k	=	the foundation stiffness in units of force per length per unit area

Combining Equation-B.3.6 through Equation-B.3.8, assuming that k is constant over the area,

$$\delta U_2 = \{\delta u\}^{T k} \int_0^{area_f} [N_n]^T[N_n]d\left(area_f\right)\{u\} \tag{B.3.9}$$

Next, the external virtual work is considered. The inertial effect is studied first:

$$\delta V_1 = -\int_0^{vol} \{\delta w\}^T \frac{\{F^a\}}{vol} d(vol) \tag{B.3.10}$$

where:

$\{w\}$	=	vector of displacement of a general point

$\{F^a\}$ = acceleration (D'Alembert) force vector

According to Newton's second law:

$$\frac{\{F^a\}}{vol} = \rho \frac{\partial^2}{\partial t^2}\{w\} \tag{B.3.11}$$

where:

ρ = density

t = time

The displacements within the element are related to the nodal displacements by:

$$\{w\} = [N]\{u\} \tag{B.3.12}$$

where

$[N]$ = matrix of shape functions

Combining Equation-B.3.10 through Equation-B.3.12, and assuming that ρ is constant over the volume,

$$\delta V_1 = -\{\delta u\}^T \rho \int_0^{vol} N^T [N] d(vol) \frac{\partial^2}{\partial t^2}\{u\} \tag{B.3.13}$$

The pressure force vector formulation starts with:

$$\delta V_2 = \int_0^{area_p} \{\delta w_n\}^T \{P\} d(area_p) \tag{B.3.14}$$

where:

$\{P\}$ = the applied pressure vector (normally contains only one nonzero component)

$area_p$ = area over which pressure acts

Combining equations Equation-B.3.12 and Equation-B.3.14,

$$\delta V_2 = \{\delta u\}^T \int_0^{area_p} [N_n]^T \{P\} d\left(area_p\right) \tag{B.3.15}$$

Nodal forces applied to the element can be accounted for by:

$$\delta V_3 = \{\delta u\}^T \{F_e^{nd}\} \tag{B.3.16}$$

where:

$\{F_e^{nd}\}$ = nodal forces applied to the element

Finally, Equation-B.3.1, Equation-B.3.5, Equation-B.3.9, Equation-B.3.13, Equation-B.3.15 and Equation-B.3.16 may be combined to give:

$$\{\delta u\}^T \int_0^{vol} [B]^T[D][B]d(vol)\{u\} - \{\delta u\}^T \int_0^{vol} [B]^T[D][\varepsilon^{th}]d(vol) + \{\delta u\}^{Tk} \int_0^{area_f} [N_n]^T[N_n]d(area_f)\{u\} = -\{\delta u\}^T \rho \int_0^{vol} N^T[N]d(vol)\frac{\partial^2}{\partial t^2}\{u\} + \{\delta u\}^T \int_0^{area_p} [N_n]^T\{P\}d(area_p) + \{\delta u\}^T\{F_e^{nd}\} \quad \text{(B.3.17)}$$

Noting that the $\{\delta u\}^T$ vector is a set of arbitrary virtual displacements common in all of the above terms, the condition required to satisfy the Equation-B.3.17 reduces to:

$$\left([K_e + K_e^f]\right)\{u\} - \{F_e^{th}\} = [M_e]\{\ddot{u}\} + \{F_e^{pr}\} + \{F_e^{nd}\} \quad \text{(B.3.18)}$$

where:

$[K_e]$	=	$\int_0^{vol}[B]^T[D][B]d(vol)$ = element stiffness matrix
$[K_e^f]$	=	$k\int_0^{area_f}[N_n]^T[N_n]d(area_f)$ = element foundation stiffness matrix
$\{F_e^{th}\}$	=	$\int_0^{vol}[B]^T[D][\varepsilon^{th}]d(vol)$ = element thermal load vector
$[M_e]$	=	$\rho\int_0^{vol} N^T[N]d(vol)$ = element mass matrix
$\{\ddot{u}\}$	=	$\frac{\partial^2}{\partial t^2}\{u\}$ = acceleration vector (such as gravity effects)
$\{F_e^{pr}\}$	=	$\int_0^{area_p}[N_n]^T\{P\}d(area_p)$ = element pressure vector

Equation-B.3.18 represents the equilibrium equation on a one element basis.

B.4 Structural Strain and Stress Evaluation

B.4.1 Integration point strain and stresses

The element integration point strain and stresses are computed by combining equations Equation-B.2.1 and Equation-B.3.4 to get:

$$\{\varepsilon^{el}\} = [B]\{u\} - \{\varepsilon^{th}\} \quad \text{(B.4.1)}$$

$$\{\sigma\} = [D]\{\varepsilon^{el}\} \quad \text{(B.4.2)}$$

where:

$\{\varepsilon^{el}\}$	=	strains that causes stresses
$[B]$	=	strain-displacement matrix evaluated at integration point
$\{u\}$	=	nodal displacement vector
$\{\varepsilon^{th}\}$	=	thermal strain vector
$\{\sigma\}$	=	stress vector
$[D]$	=	elasticity matrix

B.4.2 Surface stresses

Surface stress output on "free" faces ("free" means not connected to other elements as well as not having any imposed displacements or nodal forces normal to the surface) can be calculated using the following steps.

Computation of in-plain strains of the surface at an integration point using:

$$\{\acute{\varepsilon}\} = [\acute{B}]\{\acute{u}\} - \{\acute{\varepsilon^{th}}\} \tag{B.4.3}$$

Hence, $\acute{\varepsilon}_x$, $\acute{\varepsilon}_y$ and $\acute{\varepsilon}_{xy}$ are known. The prime (') represents the surface coordinate system, with z being normal to the surface. At each point, assuming

$$\{\acute{\sigma}_z\} = -P \tag{B.4.4}$$

$$\{\acute{\sigma}_{xz}\} = 0 \tag{B.4.5}$$

$$\{\acute{\sigma}_{yz}\} = 0 \tag{B.4.6}$$

where P is the applied pressure.

At each point, the six material property equations are formed as:

$$\{\acute{\sigma}\} = [\acute{D}]\{\acute{\varepsilon}\} \tag{B.4.7}$$

to compute the strain and stress components ($\acute{\varepsilon}_z$, $\acute{\varepsilon}_{xz}$, $\acute{\varepsilon}_{yz}$, $\acute{\sigma}_x$, $\acute{\sigma}_y$ and $\acute{\sigma}_{xy}$) at all integration points.

B.4.3 Shell element output

For elastic shell elements, the forces and moments per unit length are as:

$$T_x = \int_{-t/2}^{t/2} \sigma_x dz \tag{B.4.8}$$

$$T_y = \int_{-t/2}^{t/2} \sigma_y dz \tag{B.4.9}$$

$$T_{xy} = \int_{-t/2}^{t/2} \sigma_{xy} dz \tag{B.4.10}$$

$$M_x = \int_{-t/2}^{t/2} z\sigma_x dz \tag{B.4.11}$$

$$M_y = \int_{-t/2}^{t/2} z\sigma_y dz \tag{B.4.12}$$

$$M_{xy} = \int_{-t/2}^{t/2} z\sigma_{xy} dz \tag{B.4.13}$$

$$N_x = \int_{-t/2}^{t/2} \sigma_{xz} dz \tag{B.4.14}$$

$$N_y = \int_{-t/2}^{t/2} \sigma_{yz} dz \quad \text{(B.4.15)}$$

where:

T_x, T_y, T_{xy}	=	in-plane forces per unit length
M_x, M_y, M_{xy}	=	bending moments per unit length
N_x, N_y	=	transverse shear forces per unit length
t	=	thickness at midpoint of element
σ_x, etc.	=	direct stress
σ_{xy}, etc.	=	shear stress

For shell elements with linearly elastic material, Equation-B.4.8 to Equation-B.4.15 reduce to:

$$T_x = \frac{t(\sigma_{x,top} + 4\sigma_{x,mid} + \sigma_{x,bot})}{6} \quad \text{(B.4.16)}$$

$$T_y = \frac{t(\sigma_{y,top} + 4\sigma_{y,mid} + \sigma_{y,bot})}{6} \quad \text{(B.4.17)}$$

$$T_{xy} = \frac{t(\sigma_{xy,top} + 4\sigma_{xy,mid} + \sigma_{xy,bot})}{6} \quad \text{(B.4.18)}$$

$$M_x = \frac{t^2(\sigma_{x,top} - \sigma_{x,bot})}{12} \quad \text{(B.4.19)}$$

$$M_y = \frac{t^2(\sigma_{y,top} - \sigma_{y,bot})}{12} \quad \text{(B.4.20)}$$

$$M_{xy} = \frac{t^2(\sigma_{xy,top} - \sigma_{xy,bot})}{12} \quad \text{(B.4.21)}$$

$$N_x = \frac{t(\sigma_{xz,top} + 4\sigma_{xz,mid} + \sigma_{xz,bot})}{6} \quad \text{(B.4.22)}$$

$$N_y = \frac{t(\sigma_{yz,top} + 4\sigma_{yz,mid} + \sigma_{yz,bot})}{6} \quad \text{(B.4.23)}$$

B.5 Combined Stresses and Strains

When a model has only one functional direction of strains and stress, comparison with an allowable value is straightforward. But when there is more than one component, the components are normally combined into one number to allow a comparison with an allowable.

B.5.1 Combined strains

The principal strains are calculated from the strain components by the cubic equation:

$$\begin{vmatrix} \varepsilon_x - \varepsilon_0 & \frac{1}{2}\varepsilon_{xy} & \frac{1}{2}\varepsilon_{xz} \\ \frac{1}{2}\varepsilon_{xy} & \varepsilon_y - \varepsilon_0 & \frac{1}{2}\varepsilon_{yz} \\ \frac{1}{2}\varepsilon_{xz} & \frac{1}{2}\varepsilon_{yz} & \varepsilon_z - \varepsilon_0 \end{vmatrix} = 0 \qquad \text{(B.5.1)}$$

where:

ε_0 = principal strain (3 values)

The three principal strains are labeled ε_1, ε_2 and ε_3. The principal strains are ordered so that ε_1 is the most positive and ε_3 is the most negative.

The strain intensity ε_I is the largest of the absolute values of $\varepsilon_1 - \varepsilon_2$, $\varepsilon_2 - \varepsilon_3$ and $\varepsilon_3 - \varepsilon_1$. That is:

$$\varepsilon_I = MAX(|\varepsilon_1 - \varepsilon_2|, |\varepsilon_2 - \varepsilon_3|, |\varepsilon_3 - \varepsilon_1|) \qquad \text{(B.5.2)}$$

The von Mises or equivalent strain ε_e is computed as:

$$\varepsilon_e = \frac{1}{1+\nu'}(\frac{1}{2}[(\varepsilon_1 - \varepsilon_2)^2 + (\varepsilon_1 - \varepsilon_2)^2 + (\varepsilon_1 - \varepsilon_2)^2])^{\frac{1}{2}} \qquad \text{(B.5.3)}$$

where:

ν' = effective Poisson's ratio

B.5.2 Combined stresses

The principal stresses $(\sigma_1, \sigma_2, \sigma_3)$ are calculated from the stress components by the cubic equation:

$$\begin{vmatrix} \sigma_x - \sigma_0 & \sigma_{xy} & \sigma_{xz} \\ \sigma_{xy} & \sigma_y - \sigma_0 & \sigma_{yz} \\ \sigma_{xz} & \sigma_{yz} & \sigma_z - \sigma_0 \end{vmatrix} = 0 \qquad \text{(B.5.4)}$$

where:

σ_0 = principal stress (3 values)

The three principal stresses are labeled σ_1, σ_2 and σ_3. The principal stresses are ordered so that σ_1 is the most positive (tensile) and σ_3 is the most negative (compressive).

The stress intensity σ_I is the largest of the absolute values of $\sigma_1 - \sigma_2$, $\sigma_2 - \sigma_3$ and $\sigma_3 - \sigma_1$. That is:

$$\sigma_I = MAX(|\sigma_1 - \sigma_2|, |\sigma_2 - \sigma_3|, |\sigma_3 - \sigma_1|) \qquad \text{(B.5.5)}$$

The von Mises or equivalent strain ε_e is computed as:

$$\sigma_e = (\frac{1}{2}[(\sigma_1 - \sigma_2)^2 + (\sigma_1 - \sigma_2)^2 + (\sigma_1 - \sigma_2)^2])^{\frac{1}{2}} \qquad \text{(B.5.6)}$$

or:

$$\sigma_e = \left(\frac{1}{2}\left[(\sigma_x - \sigma_y)^2 + (\sigma_y - \sigma_z)^2 + (\sigma_z - \sigma_x)^2 + 6(\sigma_{xy}^2 + \sigma_{yz}^2 + \sigma_{xz}^2)\right]\right)^{\frac{1}{2}} \tag{B.5.7}$$

when $\nu' = \nu$, the equivalent stress is related to the equivalent strain through

$$\sigma_e = E\varepsilon_e \tag{B.5.8}$$

where:

E = Young's modulus

B.6 Concrete

The concrete material model predicts the failure of brittle materials. The criterion for failure of concrete due to a multi-axial stress state can be expressed in the form:

$$\frac{F}{f_c} - S \geq 0 \tag{B.6.1}$$

where:

F = a function of the principal stress state (σ_{xp}, σ_{yp}, σ_{zp})

S = failure surface expressed in terms of principal stresses and five input parameters f_t, f_c, f_{cb}, f_1 and f_2

f_t = ultimate uniaxial tensile strength

f_c = ultimate uniaxial compressive strength

f_{cb} = ultimate biaxial compressive strength

f_1 = ultimate compressive strength for a state of biaxial compression superimposed on hydrostatic stress state σ_h^a

f_2 = ultimate compressive strength for a state of uniaxial compression superimposed on hydrostatic stress state σ_h^a

σ_h^a = ambient hydrostatic stress state

σ_{xp}, σ_{yp}, σ_{zp} = principal stresses in principal directions

If Equation-B.6.1 is satisfied, the material will crack or crush. However, the failure surface can be specified with a minimum of two constants f_t and f_c. The other three constants default to *Willam et. al.* [23]:

$$f_{cb} = 1.2f_c \tag{B.6.2}$$

$$f_1 = 1.45f_c \tag{B.6.3}$$

$$f_2 = 1.725f_c \tag{B.6.4}$$

However, these default values are valid only for stress states where these conditions are satisfied:

$$|\sigma_h| \leq \sqrt{3}f_c \tag{B.6.5}$$

$$\sigma_h = \frac{1}{3}(\sigma_{xp} + \sigma_{yp} + \sigma_{zp}) = \text{hydrostatic stress state} \tag{B.6.6}$$

Thus condition (Equation-B.6.5) applies to stress situations with a low hydrostatic stress component. All five failure parameters should be specified when a large hydrostatic stress component is expected. If condition Equation-B.6.5 is not satisfied and the default values shown in Equation-B.6.2 thru Equation-B.6.4 are assumed, the strength of the concrete material may be incorrectly evaluated.

When the crushing capability is suppressed with f_c = -1.0, the material cracks whenever a principal stress component exceeds f_t.

Both the function F and the failure surface S are expressed in terms of principal stresses denoted as σ_1, σ_2, and σ_3 where:

$$\sigma_1 = \max(\sigma_{xp}, \sigma_{yp}, \sigma_{zp}) \tag{B.6.7}$$

$$\sigma_3 = \min(\sigma_{xp}, \sigma_{yp}, \sigma_{zp}) \tag{B.6.8}$$

and $\sigma_1 \geq \sigma_2 \geq \sigma_3$. The failure of concrete is categorized into four domains:

1. $0 \geq \sigma_1 \geq \sigma_2 \geq \sigma_3$ (compression-compression-compression)
2. $\sigma_1 \geq 0 \geq \sigma_2 \geq \sigma_3$ (tension-compression-compression)
3. $\sigma_1 \geq \sigma_2 \geq 0 \geq \sigma_3$ (tension-tension-compression)
4. $\sigma_1 \geq \sigma_2 \geq \sigma_3 \geq 0$ (tension-tension-tension)

In each domain, independent functions describe F and the failure surface S. The four functions describing the general function F are denoted as $F_1, F_2, F_3\ and\ F_4$ while the functions describing S are denoted as $S_1, S_2, S_3\ and\ S_4$. The functions $S_i\ (i = 1,4)$ have the properties that the surface they describe is continuous while the surface gradients are not continuous when any one of the principal stresses changes sign. The surface will be shown in Figure-B.6.1 and Figure-B.6.3.

B.6.1 The failure domain (compression-compression-compression)

The characteristics equation for this domain is: $0 \geq \sigma_1 \geq \sigma_2 \geq \sigma_3$. In this case, F takes the form

$$F = F_1 = \frac{1}{\sqrt{15}}[(\sigma_1 - \sigma_2)^2 + (\sigma_2 - \sigma_3)^2 + (\sigma_3 - \sigma_1)^2]^{\frac{1}{2}} \tag{B.6.8}$$

and S is defined as

$$S = S_1 = \frac{2r_2(r_2^2 - r_1^2)cos\eta + r_2(2r_1 - r_2)[4(r_2^2 - r_1^2)cos^2\eta + 5r_1^2 - 4r_1r_2]^{\frac{1}{2}}}{4(r_2^2 - r_1^2)cos^2\eta + (r_2 - 2r_1)^2} \tag{B.6.9}$$

Terms used to define S are:

$$cos\eta = \frac{2\sigma_1 - \sigma_2 - \sigma_3}{\sqrt{2}[(\sigma_1 - \sigma_2)^2 + (\sigma_2 - \sigma_3)^2 + (\sigma_3 - \sigma_1)^2]^{\frac{1}{2}}} \tag{B.6.10}$$

$$r_1 = a_0 + a_1\xi + a_2\xi^2 \tag{B.6.11}$$

$$r_2 = b_0 + b_1\xi + b_2\xi^2 \tag{B.6.12}$$

$$\xi = \frac{\sigma_h}{f_c} \tag{B.6.13}$$

σ_h is defined by Equation-2.6.6 and the undermined coefficients a_0, a_1, a_2, b_0, b_1 and b_2 are discussed below.

This failure surface is shown as Figure-B.6.1. The angle of similarity η describes the relative magnitudes of the principal stresses. From Equation-B.6.10, $\eta = 0°$ refers to any stress state such that $\sigma_3 = \sigma_2 > \sigma_1$ (e.g. uniaxial compression, biaxial tension) while $\xi = 60°$ for any stress state where $\sigma_3 > \sigma_2 = \sigma_1$ (e.g. uniaxial tension, biaxial compression). All other multiaxial stress states have angles of similarity such that $0° \le \eta \le 60°$. When $\eta = 0°$, S_1 (Equation-2.6.9) equals r_1 while if $\eta = 60°$, S_1 equals r_2. Therefore, the function r_1 represents the failure surface of all stress states with $\eta = 0°$. The functions r_1, r_1 and the angle η are depicted on Figure B.2.

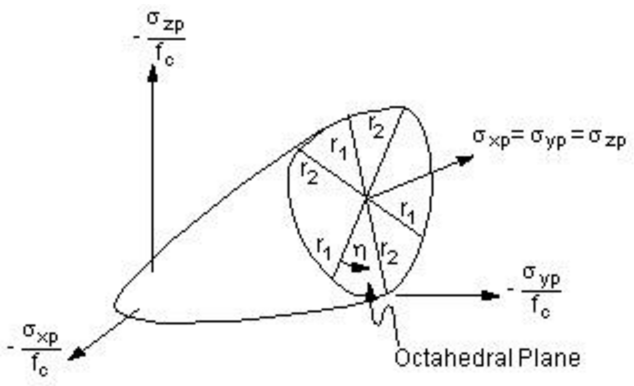

Figure-B.2: 3-D Failure Surface in Principal Stress Space

It may be seen that the cross-section of the failure plane has cyclic symmetry about each 120° sector of the octahedral plane due to the range $0° < \eta < 60°$ of the angle of similitude. The function r_1 is determined by adjusting a_0, a_1, and a_2 such that f_t, f_{cb} and f_1 all lie on the failure surface. The proper values for these coefficients are determined through solution of the simultaneous equations:

$$\left\{\begin{array}{c} \frac{F_1}{f_c}(\sigma_1 = f_t, \sigma_2 = \sigma_3 = 0) \\ \frac{F_1}{f_c}(\sigma_1 = 0, \sigma_2 = \sigma_3 = -f_{cb}) \\ \frac{F_1}{f_c}(\sigma_1 = -\sigma_h^a, \sigma_2 = \sigma_3 = -\sigma_h^a - f_1) \end{array}\right\} = \begin{bmatrix} 1 & \xi_t & \xi_t^2 \\ 1 & \xi_{cb} & \xi_{cb}^2 \\ 1 & \xi_1 & \xi_1^2 \end{bmatrix} \begin{Bmatrix} a_0 \\ a_1 \\ a_2 \end{Bmatrix} \tag{B.6.14}$$

with

$$\xi_t = \frac{f_t}{3f_c}, \xi_{cb} = -\frac{2f_{cb}}{3f_c}, \xi_1 = -\frac{\sigma_h^a}{f_c} - \frac{2f_1}{3f_c} \tag{B.6.15}$$

The function r_2 is calculated by adjusting b_0, b_1, and b_2 to satisfy the conditions:

$$\begin{Bmatrix} \frac{F_1}{f_c}(\sigma_1 = \sigma_2 = 0, \sigma_3 = -f_c) \\ \frac{F_1}{f_c}(\sigma_1 = \sigma_2 = -\sigma_h^a, \sigma_3 = -\sigma_h^a - f_1) \\ \frac{F_1}{f_c}(0) \end{Bmatrix} = \begin{bmatrix} 1 & -\frac{1}{3} & \frac{1}{9} \\ 1 & \xi_2 & \xi_2^2 \\ 1 & \xi_0 & \xi_0^2 \end{bmatrix} \begin{Bmatrix} b_0 \\ b_1 \\ b_2 \end{Bmatrix} \qquad \text{(B.6.16)}$$

ξ_2 is defined by:

$$\xi_2 = -\frac{\sigma_h^a}{f_c} - \frac{f_2}{3f_c} \qquad \text{(B.6.17)}$$

and ξ_0 is the positive root of the equation:

$$r_2(\xi_0) = a_0 + a_1\xi_0 + a_2\xi_0^2 = 0 \qquad \text{(B.6.18)}$$

where a_0, a_1, and a_2 are evaluated by Equation-B.6.14.

Since the failure surface must remain convex, the ratio r_1/r_2 is restricted to the range

$$0.5 < r_1/r_2 < 1.25 \qquad \text{(B.6.19)}$$

although the upper bound is not considered to be restrictive since $r_1/r_2 < 1$ for most materials. Also, the coefficients a_0, a_1, a_2, b_0, b_1 and b_2 must satisfy the conditions:

$$a_0 > 0, a_1 \leq 0, a_2 \leq 0 \qquad \text{(B.6.20)}$$

$$b_0 > 0, b_1 \leq 0, b_2 \leq 0 \qquad \text{(B.6.21)}$$

Therefore, the failure surface is closed and predicts failure under high hydrostatic pressure ($\xi > \xi_2$). This closure of the failure surface has not been verified experimentally and it has been suggested that a von Mises type cylinder is a more valid failure surface for large compressive σ_h values.

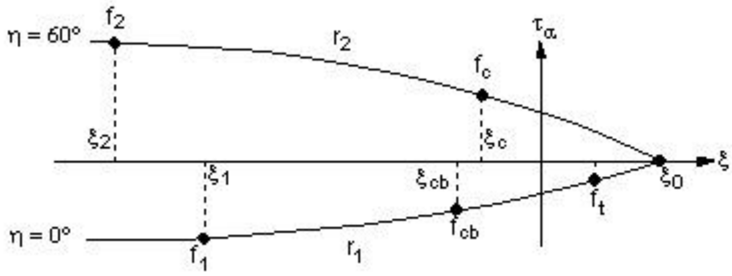

Figure-B.3: A profile of the failure surface

Consequently, it is recommended that values of f_1 and f_2 are selected at a hydrostatic stress level (σ_h^a) in the vicinity of or above the expected maximum hydrostatic stress encountered in the structure. Equation-B.6.18 expresses the condition that the failure surface has an apex at $\xi = \xi_0$. A profile of r_1 and r_2 as a function of ξ is shown in Figure B.3. The lower curve represents all stress states such that $\eta = 0°$ while the upper curve represents stress states such that $\eta = 60°$. If the failure criterion is satisfied, the material is assumed to crush.

B.6.2 The failure domain (tension-compression-compression)

The characteristics equation for this domain is: $\sigma_1 \geq 0 \geq \sigma_2 \geq \sigma_3$. In the regime, F takes the form:

$$F = F_2 = \frac{1}{\sqrt{15}}[(\sigma_2 - \sigma_3)^2 + \sigma_2^2 + \sigma_3^2]^{\frac{1}{2}} \tag{B.6.22}$$

and S is defined as:

$$S = S_2 = \left(1 - \frac{\sigma_1}{f_t}\right) \times \frac{2p_2(p_2^2 - p_1^2)cos\eta + p_2(2p_1 - p_2)[4(p_2^2 - p_1^2)cos^2\eta + 5p_1^2 - 4p_1p_2]}{4(p_2^2 - p_1^2)cos^2\eta + (p_2 - 2p_1)^2} \tag{B.6.23}$$

where $cos\eta$ is defined by Equation-B.6.10 and

$$p_1 = a_0 + a_1\chi + a_2\chi^2 \tag{B.6.24}$$

$$p_2 = b_0 + b_1\chi + b_2\chi^2 \tag{B.6.25}$$

The coefficients a_0, a_1, a_2, b_0, b_1 and b_2 are defined by Equation-B.6.14 and Equation-B.6.16 while

$$\chi = \frac{(\sigma_2 + \sigma_3)}{3f_c} \tag{B.6.26}$$

If the failure criterion is satisfied, cracking occurs in the plane perpendicular to principal stress σ_1.

B.6.3 The failure domain (tension-tension-compression)

The characteristics equation for this domain is: $\sigma_1 \geq \sigma_2 \geq 0 \geq \sigma_3$. In the tension-tension-compression regime, F takes the form:

$$F = F_3 = \sigma_i; i = 1, 2 \tag{B.6.27}$$

If the failure criterion for both $i = 1, 2$ is satisfied, cracking occurs in the planes perpendicular to principal stresses σ_1 and σ_2. If the failure criterion is satisfied only for $i = 1$, cracking occurs only in the plane perpendicular to principal stress σ_1.

B.6.4 The failure domain (tension-tension-tension)

The characteristics equation for this domain is: $\sigma_1 \geq \sigma_2 \geq \sigma_3 \geq 0$. In the tension-tension-tension regime, F takes the form:

$$F = F_4 = \sigma_i; i = 1, 2, 3 \tag{B.6.28}$$

and the S is defined as

$$S = S_4 = \frac{f_t}{f_c} \tag{B.6.29}$$

If the failure criterion is satisfied in directions 1, 2, and 3, cracking occurs in the planes perpendicular to principal stresses σ_1, σ_2 and σ_3. If the failure criterion is satisfied in directions 1 and 2, cracking occurs in the plane perpendicular to principal stresses σ_1 and σ_2. If the failure criterion is satisfied only in direction 1, cracking occurs in the plane perpendicular to principal stress σ_1.

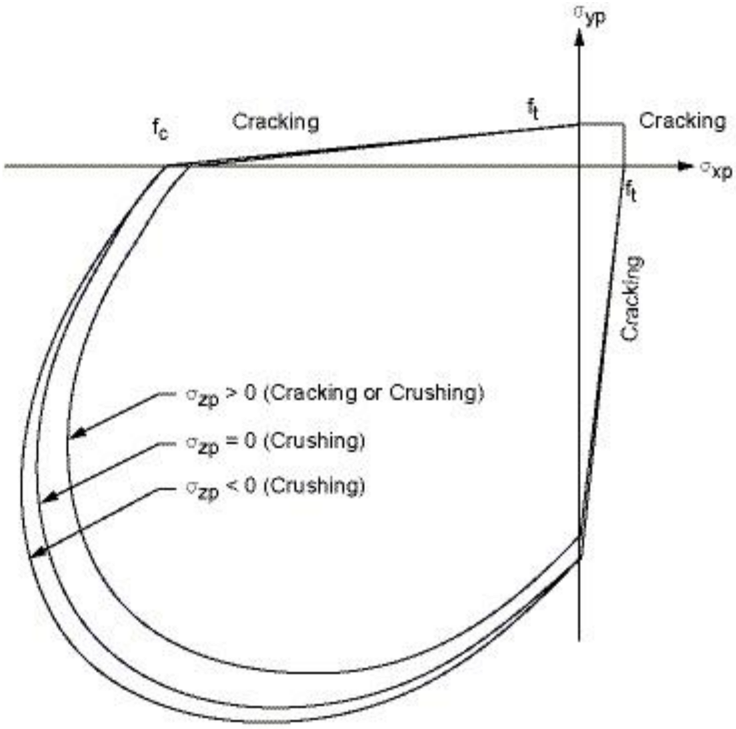

Figure-B.4: Failure Surface in Principal Stress Space with Nearly Biaxial Stress

Figure B.4 represents the 3-D failure surface for states of stress that are biaxial or nearly biaxial. If the most significant nonzero principal stresses are in the σ_{xp} and σ_{yp} directions, the three surfaces presented are for σ_{zp} slightly greater than zero, σ_{zp} equal to zero and σ_{zp} slightly less than zero. Although the three surfaces, shown as projections on the $\sigma_{xp} - \sigma_{yp}$ plane, are nearly equivalent and the 3-D failure surface is continuous, the mode of material failure is a function of the sign of σ_{zp}. For example, if σ_{xp} and σ_{yp} are both negative and σ_{zp} is slightly positive, cracking would be predicted in a direction perpendicular to the σ_{zp} direction. However, if σ_{zp} is zero or slightly negative, the material is assumed to crush.

B.7 Reinforcing Steel

The model assumes isotropic elastic behavior, and the elastic behavior is assumed to be the same in tension and compression. The plastic yielding and hardening in tension may be different from that in compression. The plastic behavior is assumed to harden isotropically and that restricts the model to monotonic loading only.

A composite yield surface is used to describe the different behavior in tension and compression. The tension behavior is pressure dependent and the Rankine maximum stress criterion is used. The compression behavior is pressure independent and the von Mises yield criterion is used. The yield surface is a cylinder with a tension cutoff (cap).

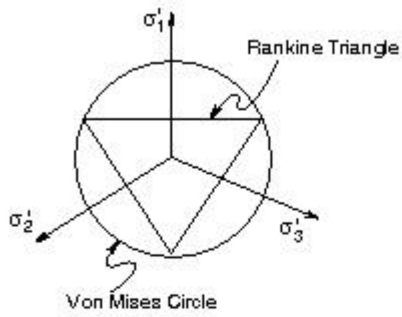

Figure-B.5: Cross-Section of Yield Surface (viewed along the hydrostatic pressure axis)

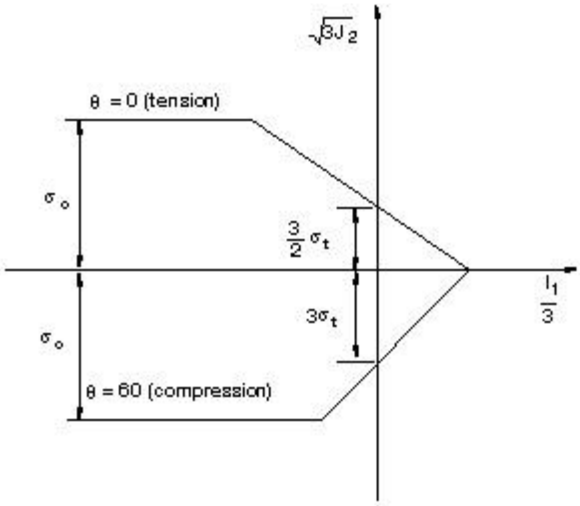

Figure-B.6: Meridian Section of Yield Surface (von Mises cylinder with tension cutoff)

Figure B.5 shows a cross section of the yield surface on principal deviatoric-stress space and Figure B.6 shows a meridional section of the yield surface for two different stress states, compression (θ = 60) and tension (θ = 0).

The yield function for the tension cap is:

$$f_t = \frac{2}{3}\cos(\theta)\,\sigma_e + p - \sigma_t = 0 \qquad \text{(B.7.1)}$$

and the yield function for the compression regime is:

$$f_c = \sigma_e - \sigma_c = 0 \qquad \text{(B.7.2)}$$

where:

p = $I_1/3 = tr(\sigma)/3$ = hydrostatic pressure

σ_e = $\left(\frac{3}{2}S{:}S\right)^{\frac{1}{2}}$ = von Mises equivalent stress

S = deviatoric stress tensor

θ	=	$\frac{1}{3} arccos \left(\frac{3\sqrt{3}J_3}{2J_2^{3/2}}\right)^{\frac{1}{2}}$ = Lode angle
J_2	=	$\frac{1}{2} S{:}S$ = second invariant of deviatoric stress tensor
J_3	=	$\det(S)$ = third invariant of deviatoric stress tensor
σ_t	=	tension yield stress
σ_c	=	compression yield stress

The plastic strain increments are defined as:

$$\bar{\varepsilon}^{pl} = \bar{\lambda}\frac{\partial Q}{\partial \sigma} \quad \text{(B.7.3)}$$

where Q is the so-called plastic flow potential, which consists of the von Mises cylinder in compression and modified to account for the plastic Poisson's ratio in tension, and takes the form:

$$Q = \sigma_e - \sigma_c \text{ for } p < -\bar{\sigma}_c/3 \quad \text{(B.7.4)}$$

$$\frac{(p-Q)^2}{c^2} + \sigma_e^2 = 9Q^2 \text{ for } p \geq -\bar{\sigma}_c/3 \quad \text{(B.7.5)}$$

where:

c	=	$\sqrt{\frac{9(1-2\nu)^{pl}}{5+2\nu^{pl}}}$
ν^{pl}	=	plastic Poisson's ratio

When $\nu^{pl} = 0.5$, the equation reduces to the von Mises cylinder. This is shown below:

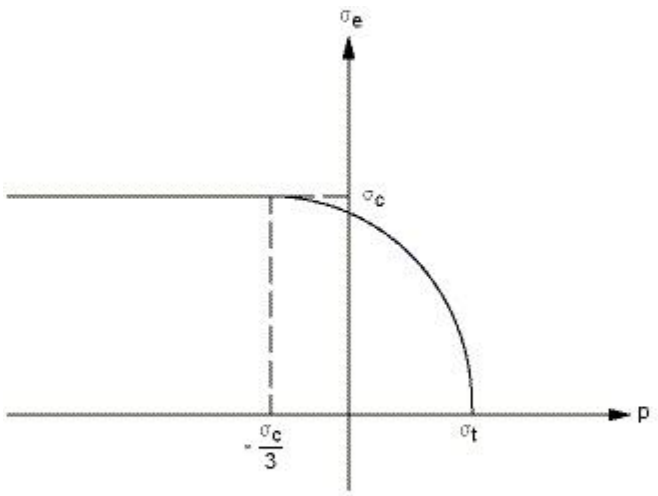

Figure-B.7: Flow Potential for Cast Iron

As the flow potential is different from the yield function, nonassociated flow rule, the resulting material Jacobian is unsymmetric.

The yield stress in uniaxial tension, σ_t, depends on the equivalent uniaxial plastic strain in tension, $\bar{\varepsilon}_t^{pl}$, and the temperature T. Also the yield stress in uniaxial compression, σ_c, depends on the equivalent uniaxial plastic strain in compression, $\bar{\varepsilon}_c^{pl}$, and the temperature T.

To calculate the change in the equivalent plastic strain in tension, the plastic work expression in the uniaxial tension case is equated to general plastic work expression as:

$$\sigma_t \Delta\bar{\varepsilon}_t^{pl} = \{\sigma\}^T\{\Delta\varepsilon^{pl}\} \tag{B.7.6}$$

where:

$\{\Delta\varepsilon^{pl}\}$ = plastic strain vector increment

Equation-B.7.3 leads to:

$$\Delta\bar{\varepsilon}_t^{pl} = \frac{1}{\sigma_t}\{\sigma\}^T\{\Delta\varepsilon^{pl}\} \tag{B.7.7}$$

In contrast, the change in the equivalent plastic strain in compression is defined as:

$$\Delta\bar{\varepsilon}_c^{pl} = \Delta\hat{\varepsilon}^{pl} \tag{B.7.8}$$

where:

$\Delta\hat{\varepsilon}^{pl}$ = equivalent plastic strain increment

Appendix - C

RESULTS

C.1 Temperature Profiles of Beams

C.1.1 Beam size: 300mmx400mm, cover=50mm

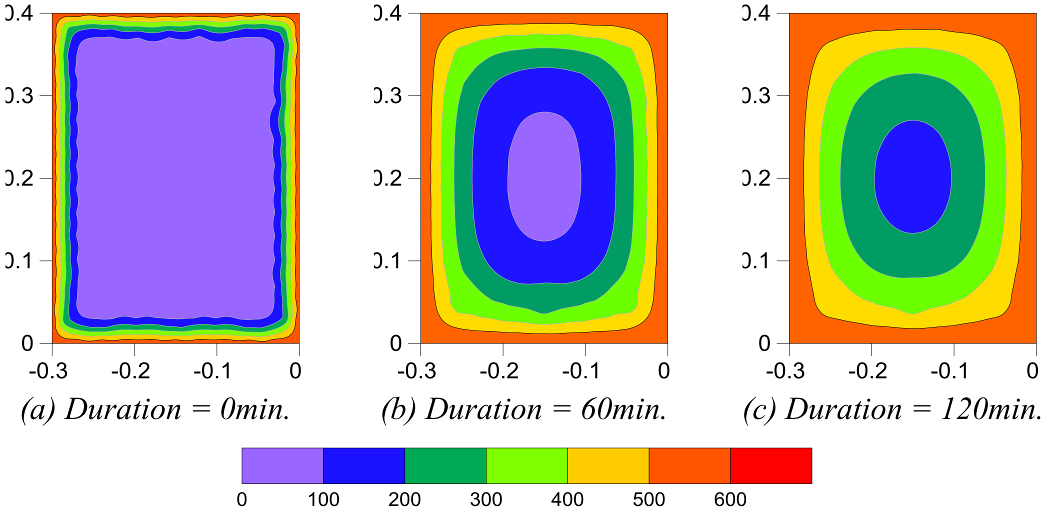

Figure-C.1: Temperature profiles for beam for applied temperature of 600°C

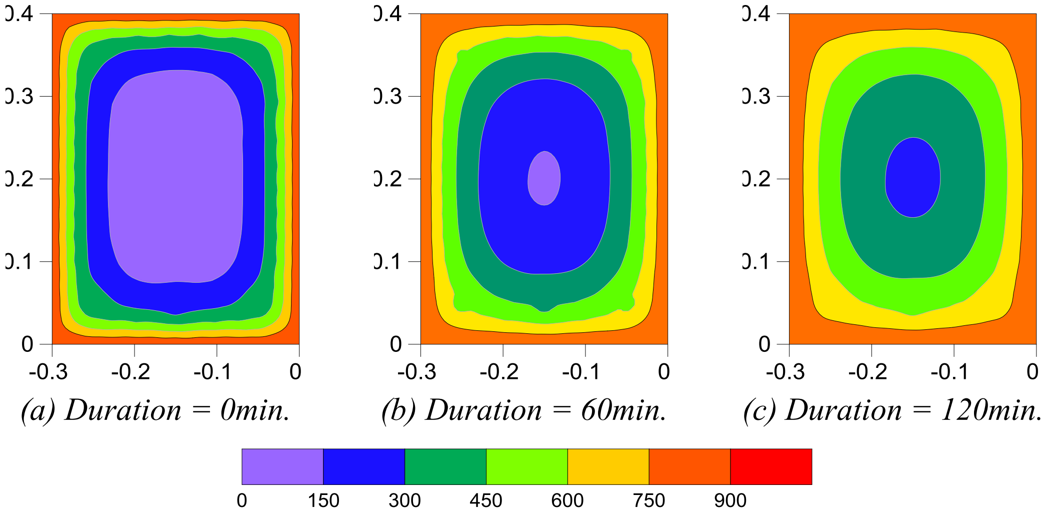

Figure-C.2: Temperature profiles for beam for applied temperature of 900°C

C.1.2 Beam size: 300mmx400mm, cover=75mm

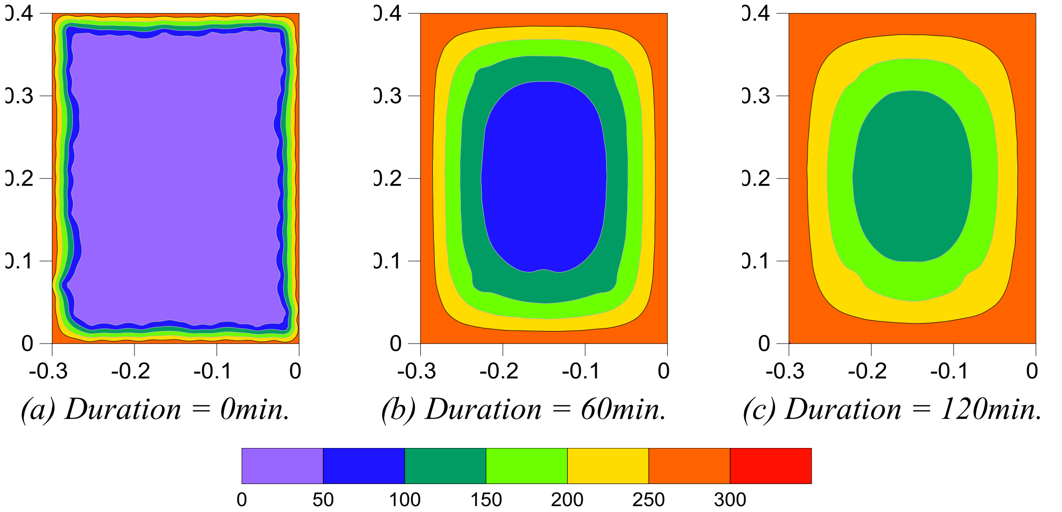

(a) Duration = 0min. (b) Duration = 60min. (c) Duration = 120min.

Figure-C.3: Temperature profiles for beam for applied temperature of 300°C

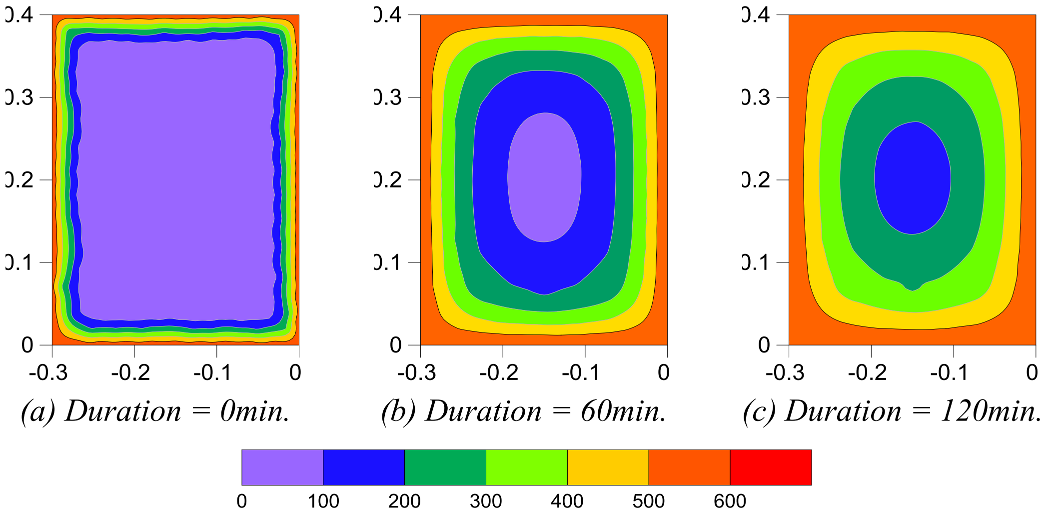

(a) Duration = 0min. (b) Duration = 60min. (c) Duration = 120min.

Figure-C.4: Temperature profiles for beam for applied temperature of 600°C

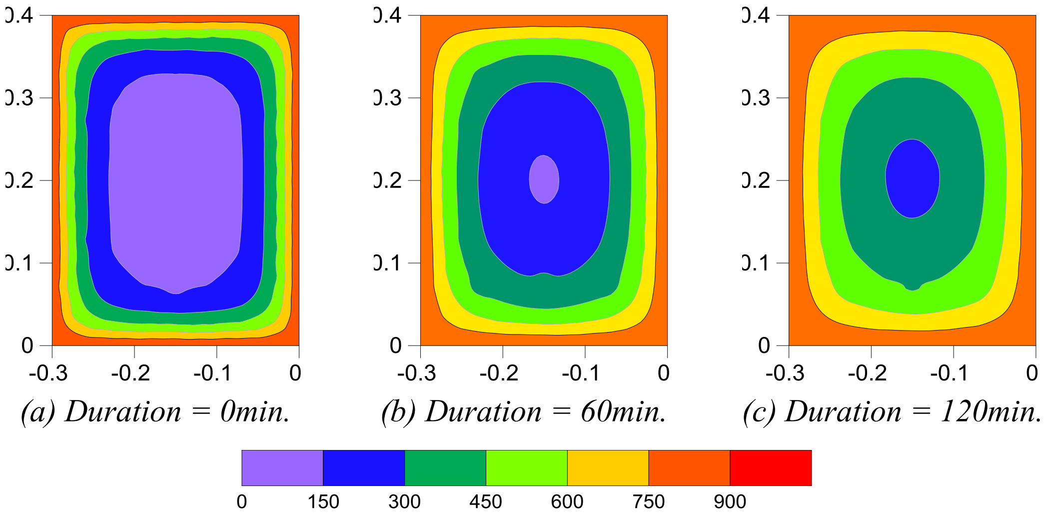

(a) Duration = 0min. (b) Duration = 60min. (c) Duration = 120min.

Figure-C.5: Temperature profiles for beam for applied temperature of 900°C

C.2.3 Beam size: 300mmx600mm, cover=50mm

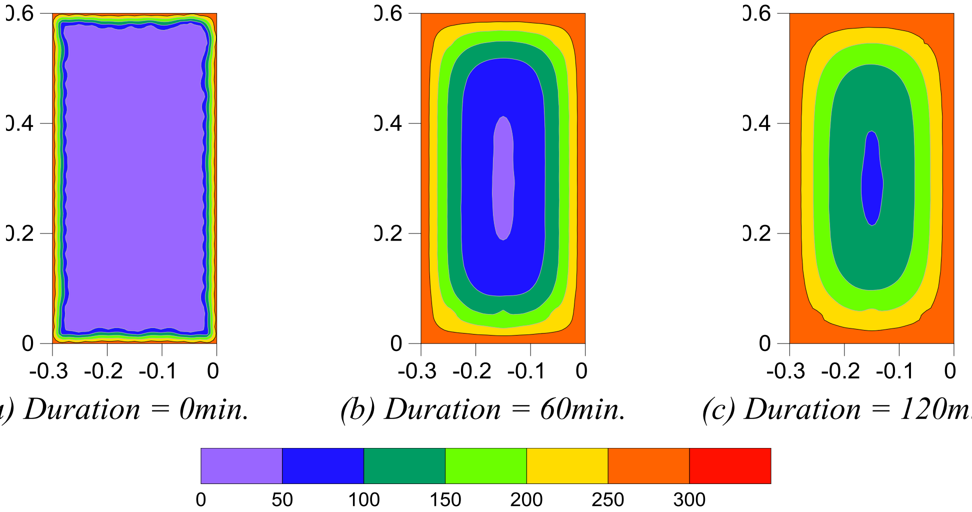

(a) Duration = 0min. *(b) Duration = 60min.* *(c) Duration = 120min.*

Figure-C.6: Temperature profiles for beam for applied temperature of 300°C

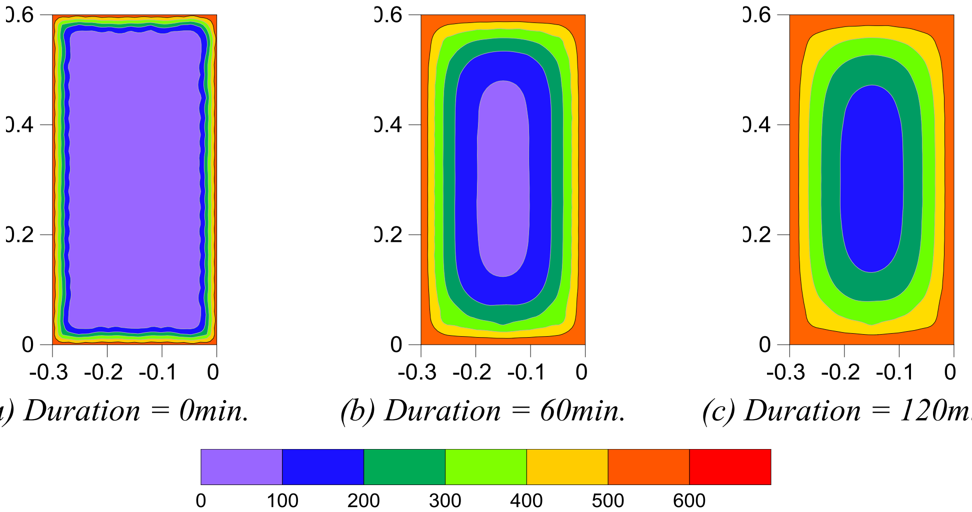

(a) Duration = 0min. *(b) Duration = 60min.* *(c) Duration = 120min.*

Figure-C.7: Temperature profiles for beam for applied temperature of 600°C

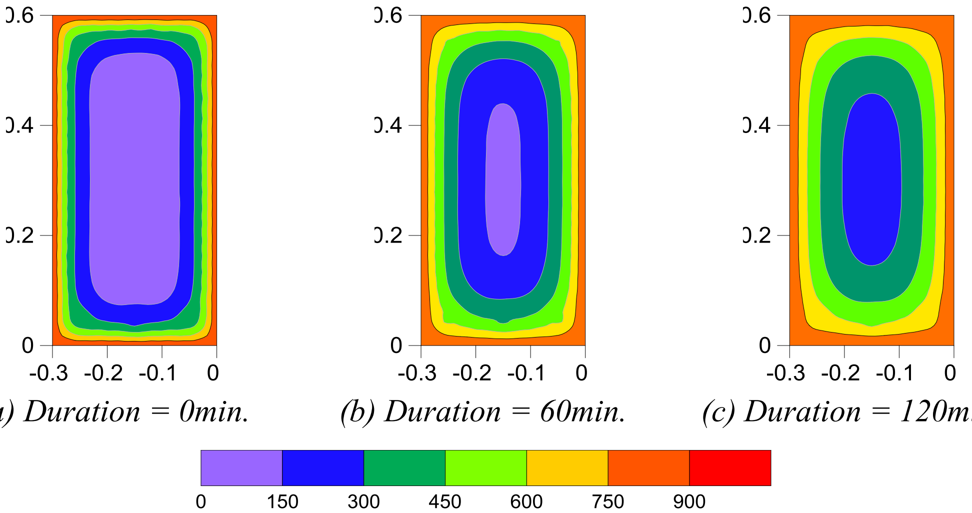

(a) Duration = 0min. *(b) Duration = 60min.* *(c) Duration = 120min.*

Figure-C.8: Temperature profiles for beam for applied temperature of 900°C

C.2 Lateral Sway of Portals

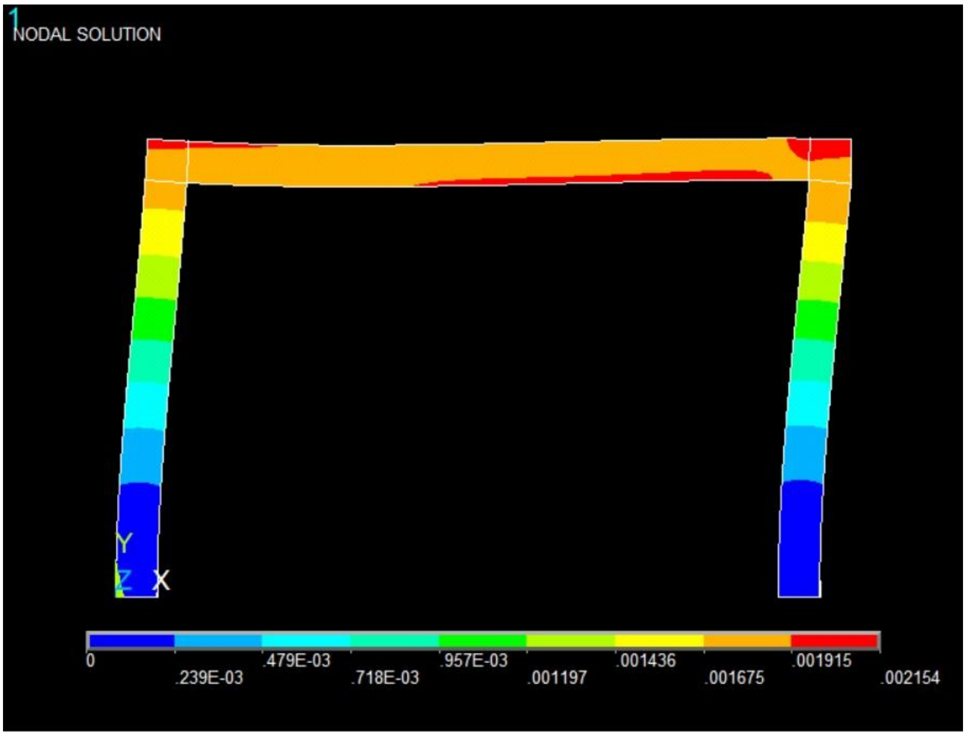

Figure-C.9: Lateral sway (mm) for 300°C with burning duration of 0 min

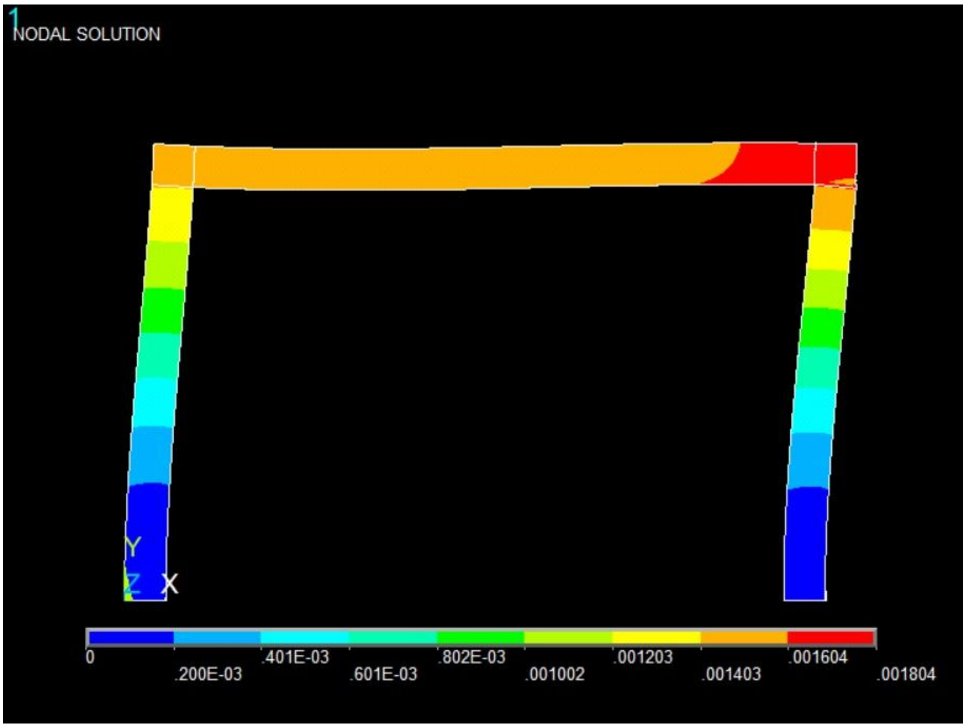

Figure-C.10: Lateral sway (mm) for 300°C with burning duration of 60 min

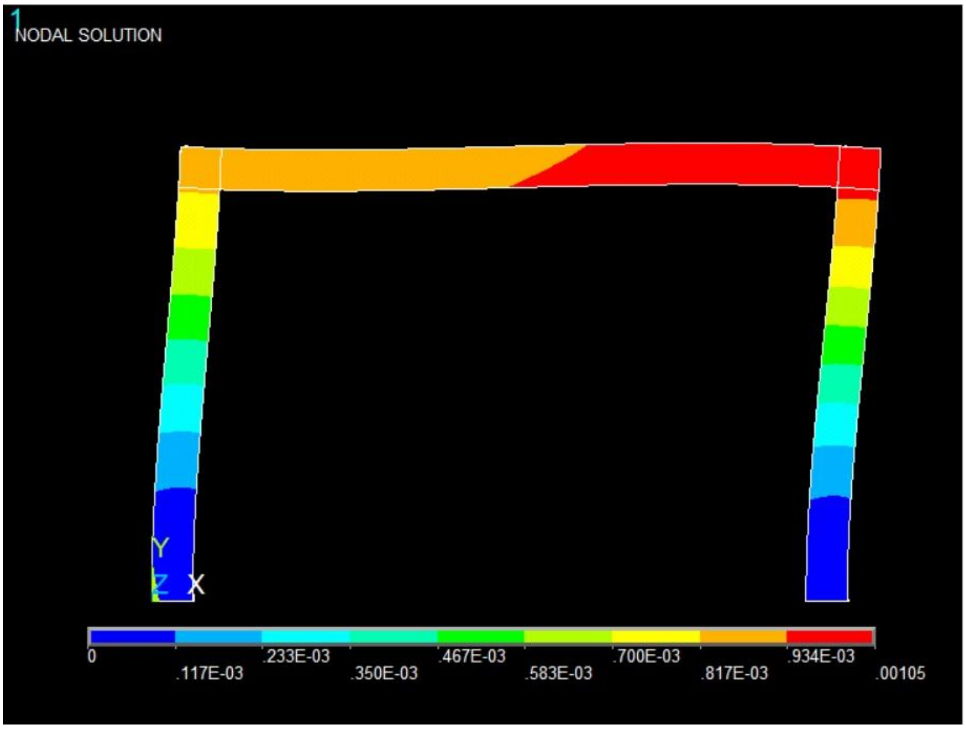

Figure-C.11: Lateral sway (mm) for 300°C with burning duration of 120 min

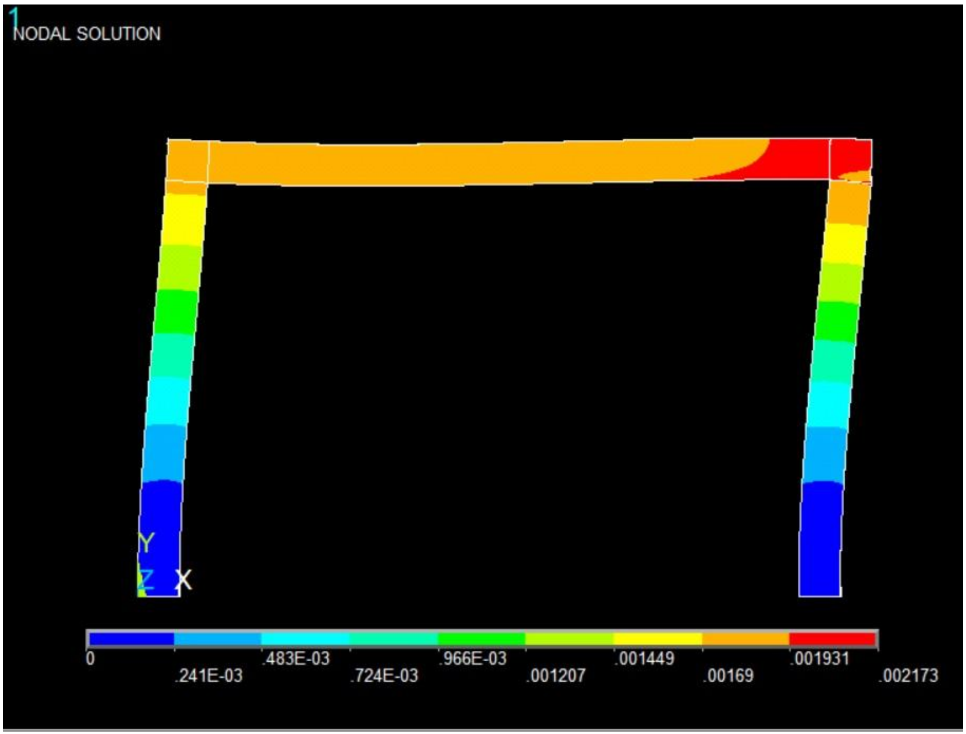

Figure-C.12: Lateral sway (mm) for 600°C with burning duration of 0 min

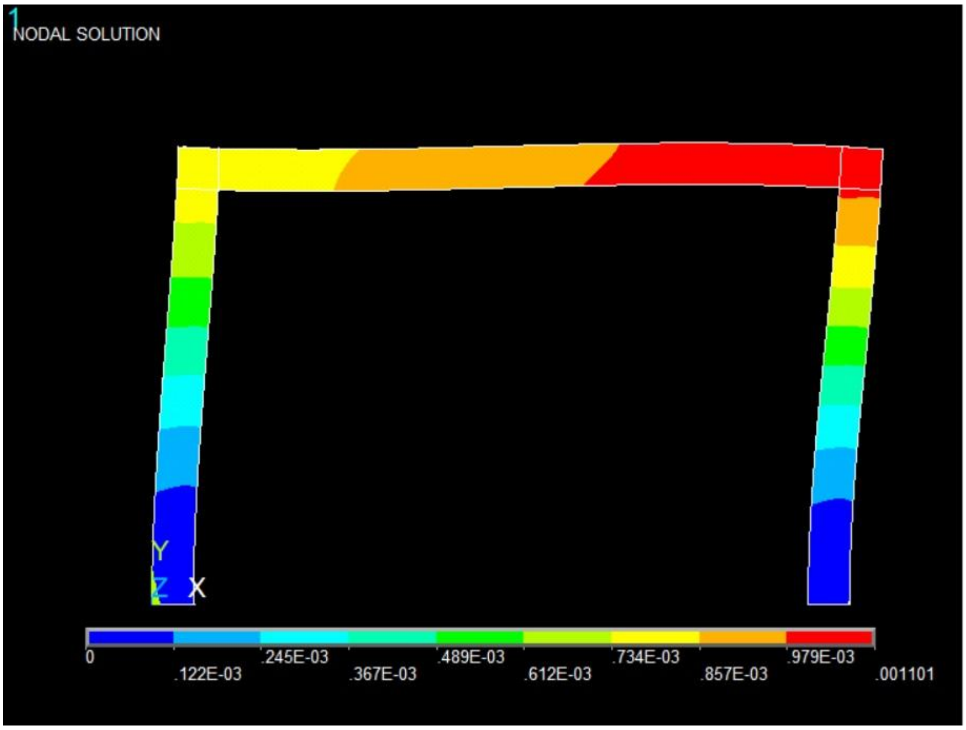

Figure-C.13: Lateral sway (mm) for 600°C with burning duration of 60 min

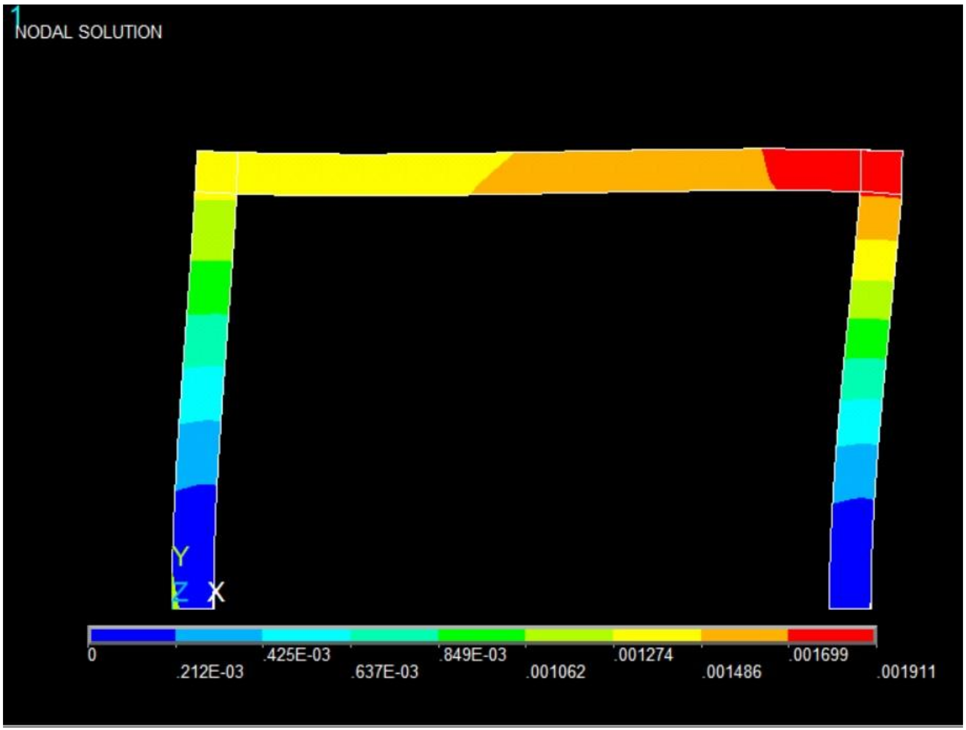

Figure-C.14: Lateral sway (mm) for 600°C with burning duration of 120 min

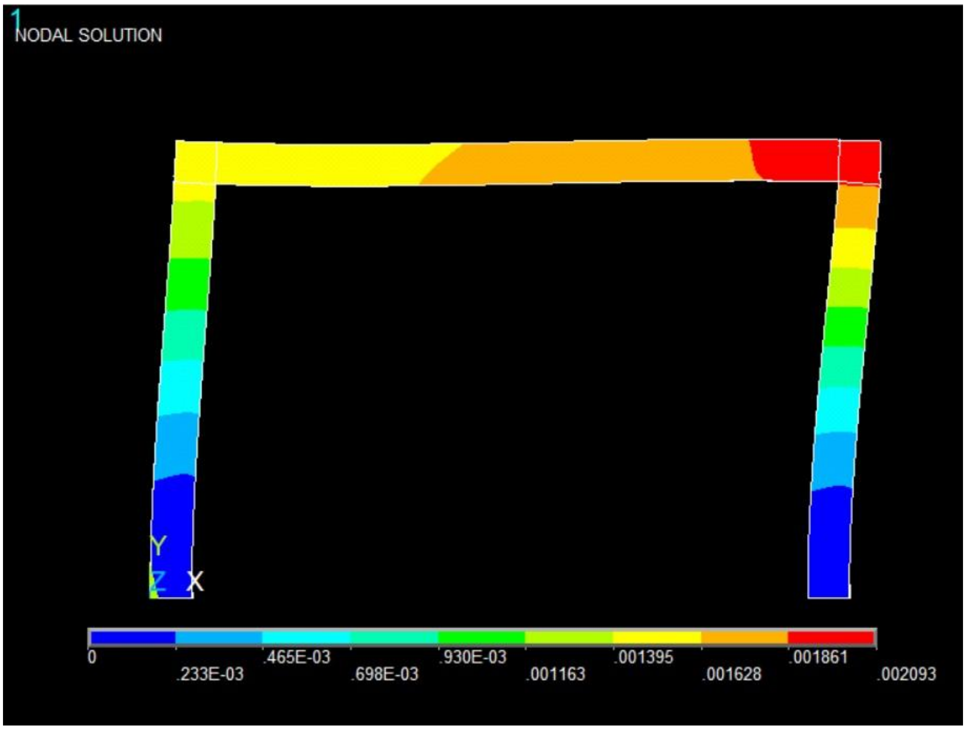

Figure-C.15: Lateral sway (mm) for 900°C with burning duration of 0 min

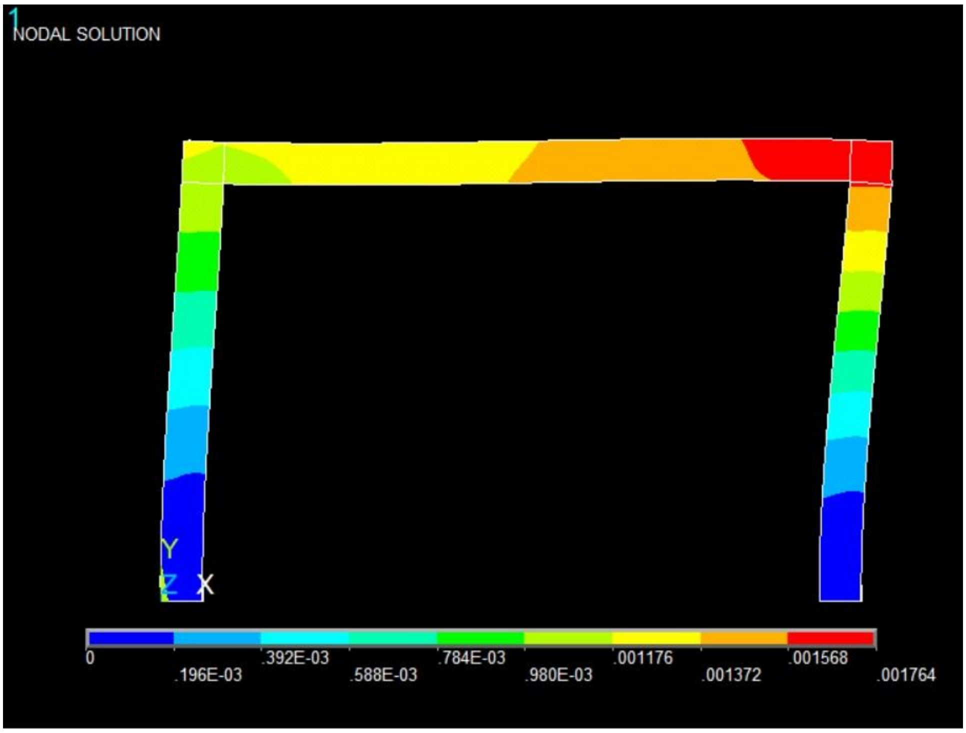

Figure-C.16: Lateral sway (mm) for 900°C with burning duration of 60 min

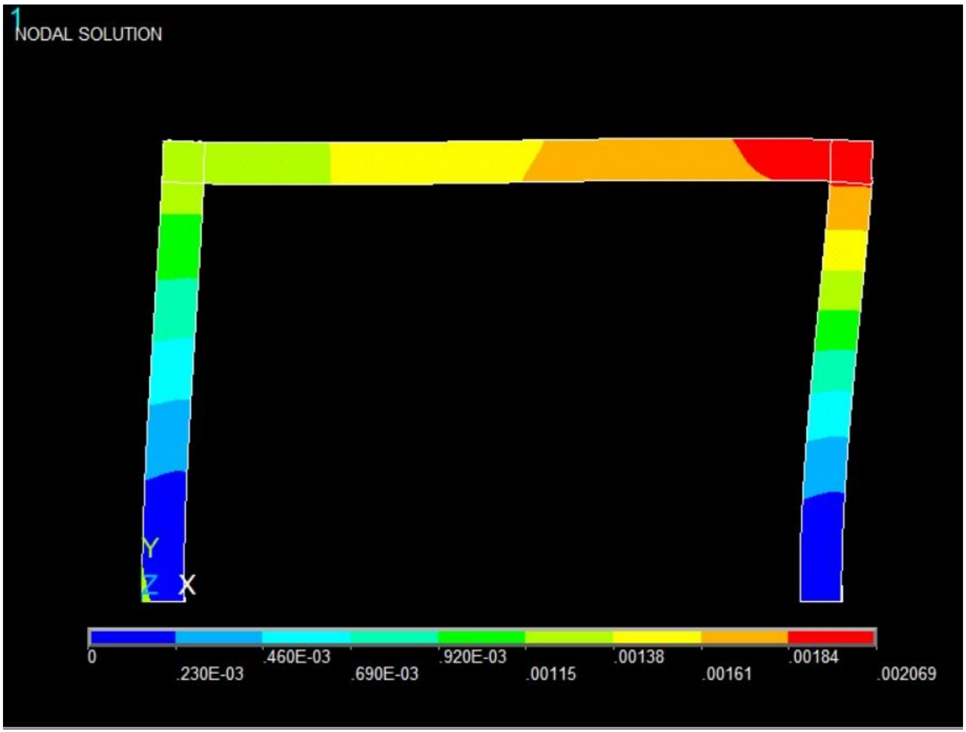

Figure-C.17: Lateral sway (mm) for 900°C with burning duration of 120 min